MODELLING AND MODEL REDUCTION OF VISCOELASTIC COMPOSITE ROTORS – AN OPERATOR BASED APPROACH

Saurabh Chandraker

Department of Mechanical Engineering
National Institute of Technology, Rourkela

MODELLING AND MODEL REDUCTION OF VISCOELASTIC COMPOSITE ROTORS – AN OPERATOR BASED APPROACH

Dissertation submitted to the

National Institute of Technology, Rourkela

in partial fulfillment of the requirements

of the degree of

Doctor of Philosophy

in

Mechanical Engineering

by

SAURABH CHANDRAKER

(Roll Number: 511ME106)

under the supervision of

Dr. Haraprasad Roy

and

Dr. Tarapada Roy

Department of Mechanical Engineering
National Institute of Technology, Rourkela (India)
February, 2016

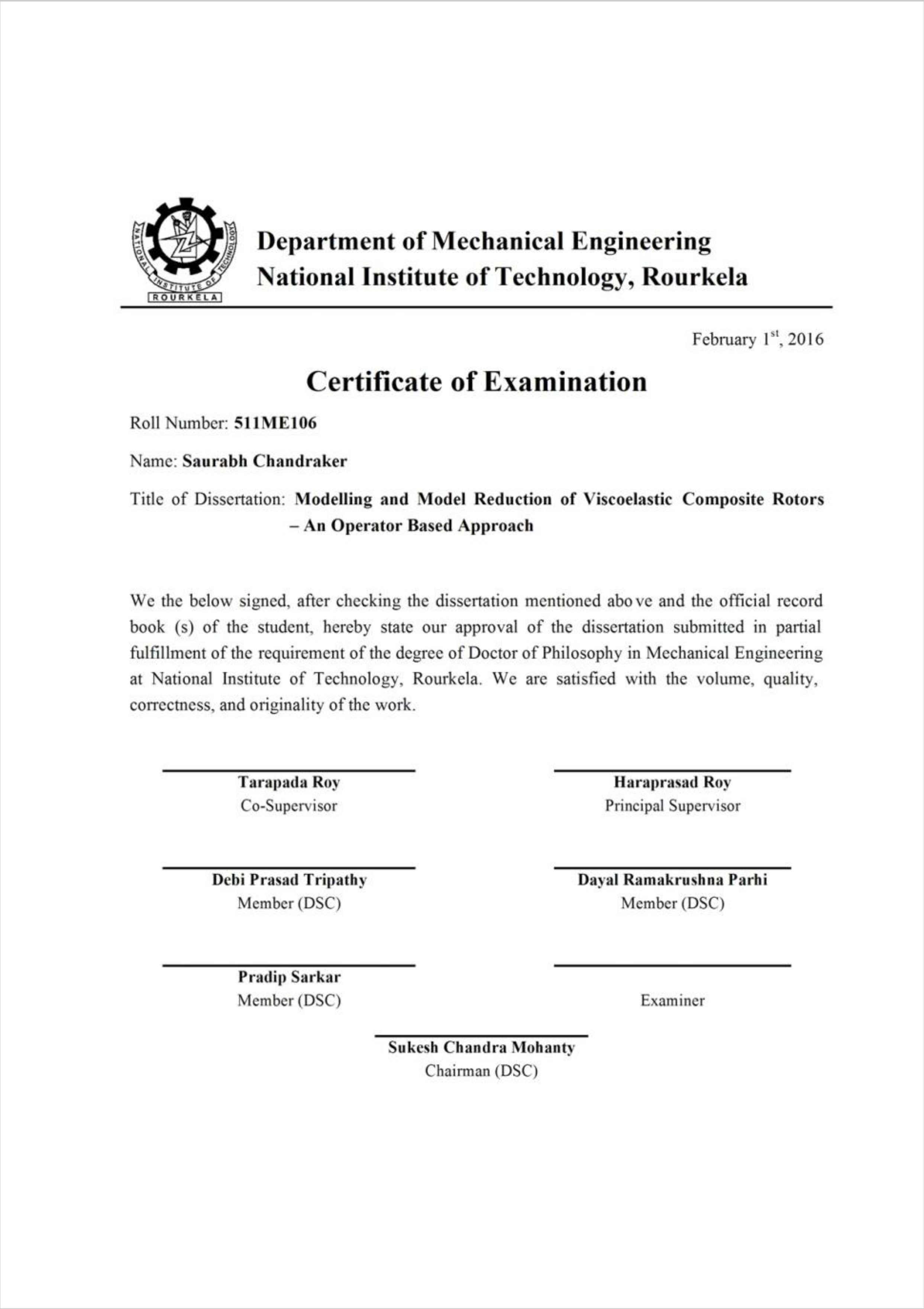

Department of Mechanical Engineering
National Institute of Technology, Rourkela

February 1st, 2016

Certificate of Examination

Roll Number: **511ME106**

Name: **Saurabh Chandraker**

Title of Dissertation: **Modelling and Model Reduction of Viscoelastic Composite Rotors – An Operator Based Approach**

We the below signed, after checking the dissertation mentioned above and the official record book (s) of the student, hereby state our approval of the dissertation submitted in partial fulfillment of the requirement of the degree of Doctor of Philosophy in Mechanical Engineering at National Institute of Technology, Rourkela. We are satisfied with the volume, quality, correctness, and originality of the work.

Tarapada Roy
Co-Supervisor

Haraprasad Roy
Principal Supervisor

Debi Prasad Tripathy
Member (DSC)

Dayal Ramakrushna Parhi
Member (DSC)

Pradip Sarkar
Member (DSC)

Examiner

Sukesh Chandra Mohanty
Chairman (DSC)

Department of Mechanical Engineering
National Institute of Technology, Rourkela

February 1st, 2016

Supervisors' Certificate

This is to certify that the work presented in this dissertation entitled **"*Modelling and Model Reduction of Viscoelastic Composite Rotors – An Operator Based Approach*"** by **"Saurabh Chandraker"**, **Roll Number: 511ME106**, is a record of original research carried out by him under our supervision and guidance in partial fulfillment of the requirements of the degree of *Doctor of philosophy in Mechanical Engineering*. Neither this dissertation nor any part of it has been submitted for any degree or diploma to any institute or university in India or abroad.

Tarapada Roy
(Co-Supervisor)
Department of Mechanical Engineering
National Institute of Technology, Rourkela

Haraprasad Roy
(Principal Supervisor)
Department of Mechanical Engineering
National Institute of Technology, Rourkela

To my Parents,
Kalindri Devi & Channu Lal Chandraker,
with all my love

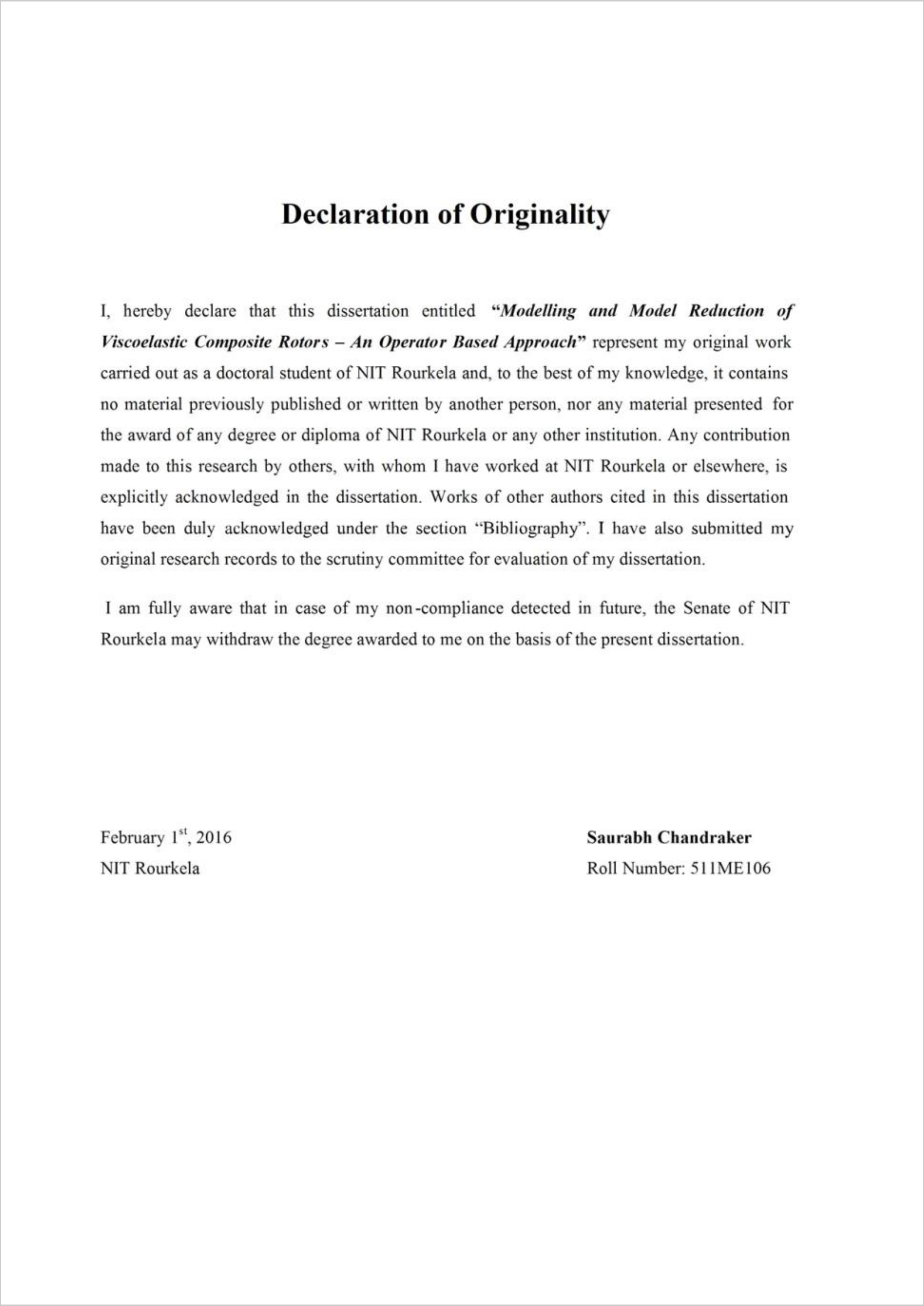

Declaration of Originality

I, hereby declare that this dissertation entitled ***"Modelling and Model Reduction of Viscoelastic Composite Rotors – An Operator Based Approach"*** represent my original work carried out as a doctoral student of NIT Rourkela and, to the best of my knowledge, it contains no material previously published or written by another person, nor any material presented for the award of any degree or diploma of NIT Rourkela or any other institution. Any contribution made to this research by others, with whom I have worked at NIT Rourkela or elsewhere, is explicitly acknowledged in the dissertation. Works of other authors cited in this dissertation have been duly acknowledged under the section "Bibliography". I have also submitted my original research records to the scrutiny committee for evaluation of my dissertation.

I am fully aware that in case of my non-compliance detected in future, the Senate of NIT Rourkela may withdraw the degree awarded to me on the basis of the present dissertation.

February 1st, 2016
NIT Rourkela

Saurabh Chandraker
Roll Number: 511ME106

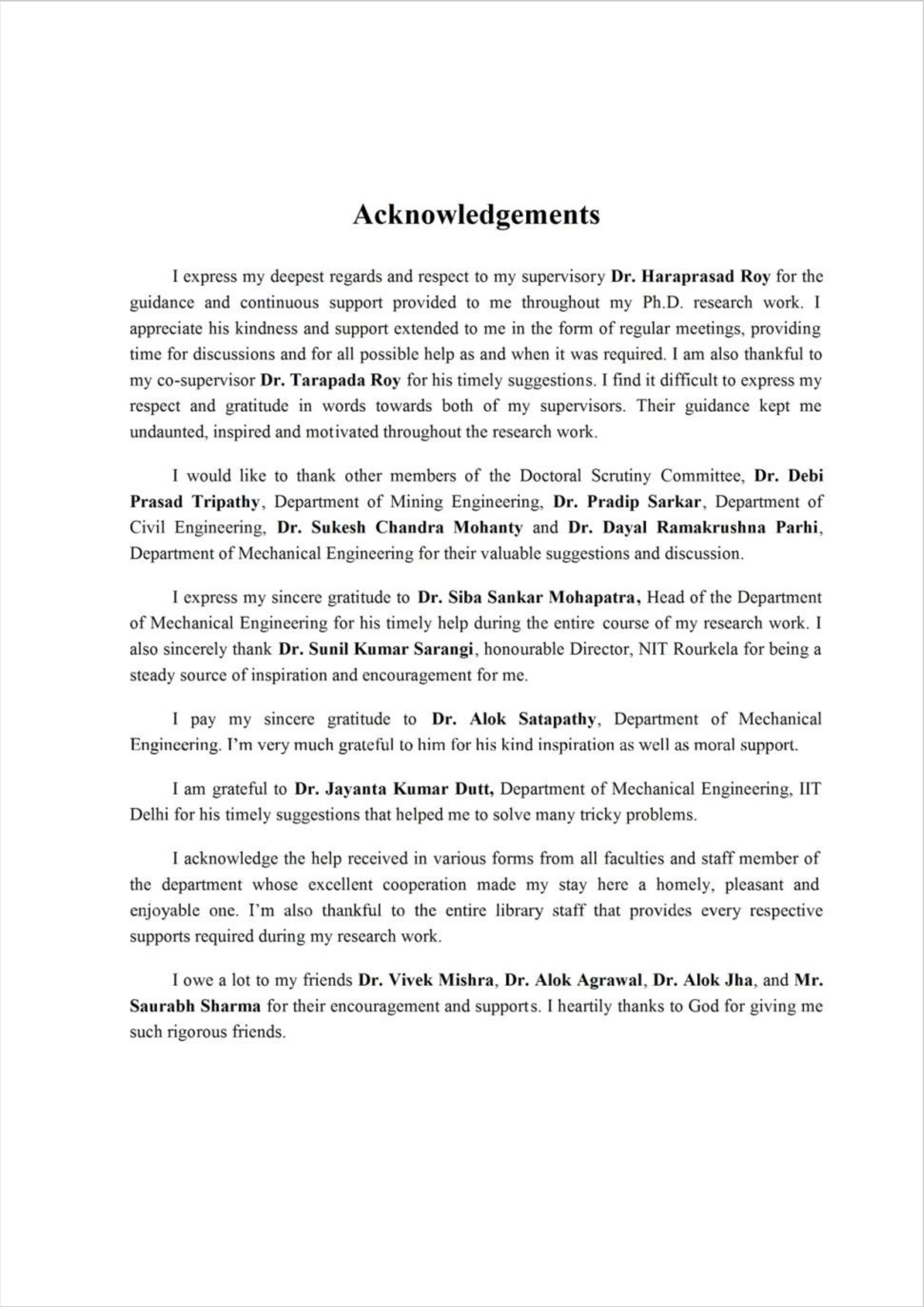

Acknowledgements

I express my deepest regards and respect to my supervisory **Dr. Haraprasad Roy** for the guidance and continuous support provided to me throughout my Ph.D. research work. I appreciate his kindness and support extended to me in the form of regular meetings, providing time for discussions and for all possible help as and when it was required. I am also thankful to my co-supervisor **Dr. Tarapada Roy** for his timely suggestions. I find it difficult to express my respect and gratitude in words towards both of my supervisors. Their guidance kept me undaunted, inspired and motivated throughout the research work.

I would like to thank other members of the Doctoral Scrutiny Committee, **Dr. Debi Prasad Tripathy**, Department of Mining Engineering, **Dr. Pradip Sarkar**, Department of Civil Engineering, **Dr. Sukesh Chandra Mohanty** and **Dr. Dayal Ramakrushna Parhi**, Department of Mechanical Engineering for their valuable suggestions and discussion.

I express my sincere gratitude to **Dr. Siba Sankar Mohapatra,** Head of the Department of Mechanical Engineering for his timely help during the entire course of my research work. I also sincerely thank **Dr. Sunil Kumar Sarangi**, honourable Director, NIT Rourkela for being a steady source of inspiration and encouragement for me.

I pay my sincere gratitude to **Dr. Alok Satapathy**, Department of Mechanical Engineering. I'm very much grateful to him for his kind inspiration as well as moral support.

I am grateful to **Dr. Jayanta Kumar Dutt,** Department of Mechanical Engineering, IIT Delhi for his timely suggestions that helped me to solve many tricky problems.

I acknowledge the help received in various forms from all faculties and staff member of the department whose excellent cooperation made my stay here a homely, pleasant and enjoyable one. I'm also thankful to the entire library staff that provides every respective supports required during my research work.

I owe a lot to my friends **Dr. Vivek Mishra**, **Dr. Alok Agrawal**, **Dr. Alok Jha**, and **Mr. Saurabh Sharma** for their encouragement and supports. I heartily thanks to God for giving me such rigorous friends.

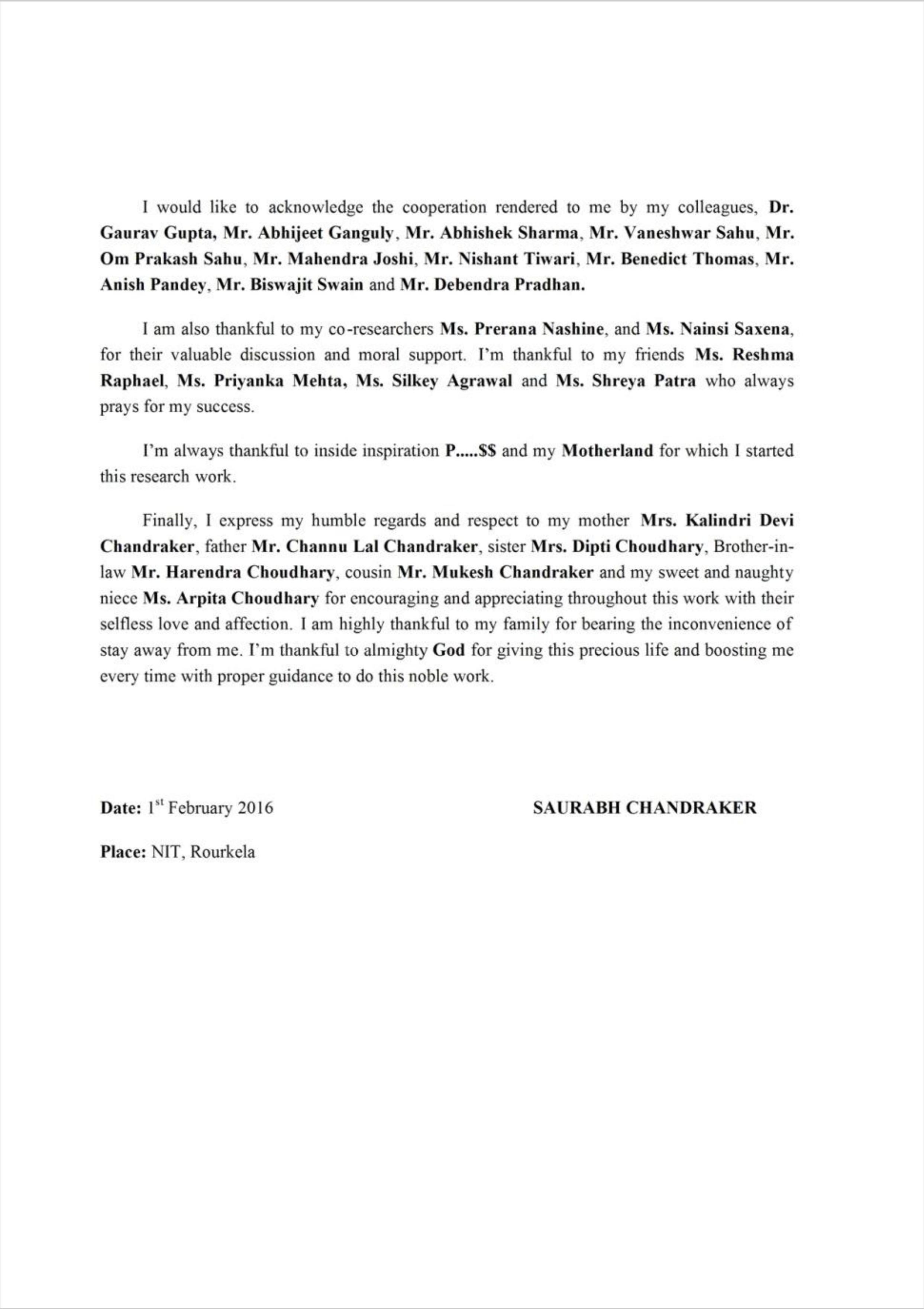

I would like to acknowledge the cooperation rendered to me by my colleagues, **Dr. Gaurav Gupta, Mr. Abhijeet Ganguly**, **Mr. Abhishek Sharma**, **Mr. Vaneshwar Sahu**, **Mr. Om Prakash Sahu**, **Mr. Mahendra Joshi**, **Mr. Nishant Tiwari**, **Mr. Benedict Thomas**, **Mr. Anish Pandey**, **Mr. Biswajit Swain** and **Mr. Debendra Pradhan.**

I am also thankful to my co-researchers **Ms. Prerana Nashine**, and **Ms. Nainsi Saxena**, for their valuable discussion and moral support. I'm thankful to my friends **Ms. Reshma Raphael**, **Ms. Priyanka Mehta, Ms. Silkey Agrawal** and **Ms. Shreya Patra** who always prays for my success.

I'm always thankful to inside inspiration **P.....$$** and my **Motherland** for which I started this research work.

Finally, I express my humble regards and respect to my mother **Mrs. Kalindri Devi Chandraker**, father **Mr. Channu Lal Chandraker**, sister **Mrs. Dipti Choudhary**, Brother-in-law **Mr. Harendra Choudhary**, cousin **Mr. Mukesh Chandraker** and my sweet and naughty niece **Ms. Arpita Choudhary** for encouraging and appreciating throughout this work with their selfless love and affection. I am highly thankful to my family for bearing the inconvenience of stay away from me. I'm thankful to almighty **God** for giving this precious life and boosting me every time with proper guidance to do this noble work.

Date: 1st February 2016

SAURABH CHANDRAKER

Place: NIT, Rourkela

Abstract

Material damping in rotating structure plays a crucial role in dynamics. It produces a tangential force and acts towards whirl direction. This force is also proportional to spin speed, after certain speed it destabilizes the system, and corresponding speed is known as stability limit of spin speed. Thus, a reliable model is indeed essential for the correct assessment of stability. Modelling was done by many researchers and incorporated material damping through frequency dependent viscous or frequency independent hysteretic behaviour. Both of these damping models are not sufficient to predict the exact dynamic characteristic. The motivation for using general viscoelastic model arises from a need to capture the influence of both types of damping behaviours. The operator based constitutive relationship is used to incorporate such type of damping. The instantaneous stress of the linear viscoelastic material is obtained by operating instantaneous strain. The numerator and denominator of material modulus are a polynomial of differential time operator, and polynomial coefficients are known as viscoelastic parameters. Those parameters are obtained from frequency-dependent storage modulus and loss factor by using any optimization tool or curve fitting technique. Two types of material (low and high damped) are chosen for a case study.

The operator based constitutive relationship is further used to bring down higher order equations of motion of an isotropic viscoelastic rotor by using two distinct approaches, i.e. (a) Classical model (CM) and (b) Finite element model (FEM). Lumped mass approximation is adopted in the CM approach thus it is also known as lumped mass classical model. Whereas, in FEM approach, the distributed effect of the continuum is considered. The Euler-Bernoulli beam theory is used here. The shear deformation effect may easily be included; however, it has been left out for simplicity. The shaft material damping has been tackled in such a way that to consider dissipation effect through all coordinates. The order of the differential equation exclusively depends on the material behaviour and explained by modulus operator. For better understanding the dynamic characteristics of the rotating system, a comparative study is done by using following parameters such as decay rate, campbell diagram, modal damping factor, stability limit of spin-speed, unbalance frequency response, and also time response. This study is affirming compatibility between two approaches with each other up to some extent.

According to industrial demand, heavy and bulky rotors are replaced by a light yet strong rotor, where the composite material is only supplementary. This composite is achieved either by reinforcing fibre or multi-layering arrangements. The present idea is also extended to develop multi-layer, multi-disc rotor system with the help of CM and FEM. All layers are isotropic viscoelastic material and assumed to be perfectly bonded. The effect of placement of material and their radius ratio in multi-layering of rotor is being well justified by taking an example of aluminium/steel (as low damped material) and PVC/LORD LD-400 (as high damped material). In general rotor shafts made of composite material are used in aerospace, helicopter rotor, under water vehicle soft toys etc.

Since all dynamic behaviours of the rotating system are interlinked with rotation. The present study focuses on finding directivity and some other modal characteristics through complex modal analysis. A complex modal coordinate creates a platform to indicate the directivity of modes and provides better information about the whirl direction. The study of natural modes and directional frequency response function is obtained from free and force vibration analysis. The modal analysis also distinguishes the significance of higher order model over conventional second order model. For achieving a complete study, modal analysis is done under consideration of both rolling and sliding contact bearings.

Higher-order finite element model involves a large number of coordinates as well as various types of asymmetry in different orders, resulting a complicated system again. Such problem is overcome by reducing the matrix size. For the sake of finding best methodology to reduce the higher order model, two different reduction techniques are applied here, i.e. a) Iterative Improved Reduction System (IIRS) b) Balanced Realization System (BRS). In the first case, an iterative algorithm is used to improve the transformation matrix by achieving convergence. Whereas, in the second case, Hankel singular value decomposition assures to predict the most controllable and most observable states that help to reduce the system matrices accurately. The dynamic study justifies the effectiveness of the reduced model.

The presented work purely shows the mathematical modelling of various viscoelastic rotor bearing system. The mathematical procedure and formulations can be used for any rotors as per their applications.

Keywords: *Viscoelastic rotors, Classical model, Finite element model, Operator parameter, Multi layer rotor, Multi disc analysis, Stability threshold, Model order reduction.*

Contents

S. No. **Title** **Page No.**

Certificate of Examination .... **iii**

Supervisors' Certificate .... **iv**

Dedication .... **v**

Declaration of Originality .... **vi**

Acknowledgements .... **vii**

Abstract .... **ix**

List of Figures .... **xiv**

List of Tables .... **xvii**

List of Symbols .... **xviii**

Chapter-1 **Introduction** **1-19**
1.1 Preamble and research motivation 1
1.2 Modelling of viscoelastic material and its application 2
1.3 Dynamics of damped rotor bearing system 6
1.4 Dynamics of composite rotors 10
1.5 Modal analysis of rotor-bearing system 12
1.6 Model order reduction 13
1.7 Objective and scope of present work 16
1.8 Thesis layout 18

Chapter-2 **Modelling of Viscoelastic Rotor: Isotropic Material** **20-76**
2.1 Preamble 20
2.2 Operator based constitutive relationship 20
2.3 Classical approach 23
2.4 Finite element approach 28
2.5 Incorporation of disc effects 34
2.6 Incorporation of bearing effects 34
2.7 State space representation 35
2.8 Modal analysis of rotor bearing model 37
  2.8.1 Eigen analysis of the system 38
  2.8.2 Directional frequency response functions 39
  2.8.3 Mode shapes 41

2.9 Response calculation due to mass unbalance 42
2.10 Validation of numerical results 43
2.10.1 Classical approach 43
2.10.2 Finite element approach 44
2.11 Model implementation 48
2.11.1 Numerical problem of rotor made of low damped material: Case – 1 48
2.11.2 Numerical problem of rotor made of high damped material: Case – 2 54
2.11.3 Numerical problem for rotor with various asymmetry: Case – 3 59
2.11.3.1 Rotor model with rolling contact bearings 59
2.11.3.2 Rotor model with sliding contact bearings 68
2.12 Summary 75

Chapter-3 Modelling of Viscoelastic Rotor: Layered Composite Material 77-105
3.1 Preamble 77
3.2 Constitutive relationship 77
3.3 Classical approach 78
3.4 Finite element approach 83
3.5 State space representation 86
3.6 Model implementation 87
3.7 Result simulation and discussion 88
3.7.1 Simulated results obtained from aluminium and steel composite rotor: Case – 1 89
3.7.2 Simulated results obtained from PVC and Lord LD-400 composite rotor: Case – 2 97
3.8 Summary 104

Chapter-4 Reduction of Higher Order Models 106-127
4.1 Introduction 106
4.2 Higher order finite element model 106
4.3 Iterative improve reduction system 107
4.4 Balanced realization system 110
4.5 Model implementation 112
4.5.1 Numerical illustration for reducing third order model: Case-1 113
4.5.2 Numerical illustration for reducing fourth order model: Case-2 120
4.6 Summary 126

Chapter-5 Conclusion and Future Work 128-133
5.1 Conclusions 128
5.2 Potential applications of present work 131
5.3 Future scopes 132

Bibliography 134-146

Appendices ……………………………………………………………………..…. **147-170**
Appendix-A Extraction of viscoelastic parameters ……………………. 147
Appendix-B Effective mass of a simply supported beam for non-central loading ………………………………………………. 151
Appendix-C Stiffness coefficient of multi-disc rotor ………………….. 157
Appendix-D Different matrices in finite element approach ………….. 165
Appendix-E Coefficients of sliding contact bearing …………………... 168

Dissemination ……………………………………………………………….. **171-172**
List of publications ……………………………………………………………... 171
Vitae ………………………………………………………………………………... 173

List of Figures

Figure No.	Title	Page No.
Fig. 2.1	Rheological model: (a) Maxwell model (b) Kelvin-Voigt model (c) Three-element standard model (d) Four-element standard model	22
Fig. 2.2	Schematic diagram of multi-disc rotor bearing system	23
Fig. 2.3	Cross-sectional view of deformed rotor	24
Fig. 2.4	Rotating and stationary coordinate systems	25
Fig. 2.5	Nodal displacement of a beam element in two coordinate planes	29
Fig. 2.6	Campbell diagram	44
Fig. 2.7	Unbalance response amplitude	44
Fig. 2.8	Campbell diagram: (a) Rigid bearing case (b) Rolling contact bearing case (c) Sliding contact bearing case	46
Fig. 2.9	Modal damping factor: (a) Rigid bearing case (b) Rolling contact bearing case (c) Sliding contact bearing case	47
Fig. 2.10	Directional frequency response function: (a) Rolling contact bearing case (b) Sliding contact bearing case	48
Fig. 2.11	Schematic diagram of single disc rotor model on simply supported ends	49
Fig. 2.12	Decay rate	50
Fig. 2.13	Stability limit of spin speed	50
Fig. 2.14	Campbell diagram	51
Fig. 2.15	First natural frequency	51
Fig. 2.16	Modal damping factor	52
Fig. 2.17	Unbalance frequency response	52
Fig. 2.18	Time response: (a) Stable zone (b) Unstable zone	53
Fig. 2.19	Whirl orbit: (a) Stable region (b) Unstable region	54
Fig. 2.20	Schematic diagram of two disc rotor model on simply supported ends	55
Fig. 2.21	Decay rate	56
Fig. 2.22	Stability limit of spin speed	56
Fig. 2.23	Campbell diagram	57
Fig. 2.24	First natural frequency	57
Fig. 2.25	Modal damping factor	58
Fig. 2.26	Unbalance frequency response	58
Fig. 2.27	Whirl orbit: (a) Stable region (b) Unstable region	59
Fig. 2.28	Schematic diagram of the rotor mounted on rolling contact bearings	60
Fig. 2.29	Decay rate plot	61
Fig. 2.30	Campbell diagram	62
Fig. 2.31	Modal damping factor	62
Fig. 2.32	Comparative plots of uniaxial rod between SOM and TOM: (a) Hysteresis loop (b) Response plot (c) Energy dissipation plot	64
Fig. 2.33	dFRF at: (a) 200 rpm, (b) 800 rpm, (c) 1700 rpm	65
Fig. 2.34	Mode shapes for SOM at 200 rpm	66
Fig. 2.35	Mode shapes for TOM at 200 rpm	66
Fig. 2.36	Mode shapes for SOM at 800 rpm	67
Fig. 2.37	Mode shapes for TOM at 800 rpm	67
Fig. 2.38	Mode shapes for SOM at 1700 rpm	68
Fig. 2.39	Mode shapes for TOM at 1700 rpm	68

Fig. 2.40 Schematic diagram of the rotor 69
Fig. 2.41 Campbell diagram: (a) Full view (b) Zoomed view of curve veering zone 70
Fig. 2.42 Decay rate plot 71
Fig. 2.43 Modal mamping factor (a) Full view (b) Zoomed view of curve veering zone 72
Fig. 2.44 dFRF plot (a) At 1400 rpm (b) At 1900 rpm 73
Fig. 2.45 Mode shapes for SOM at 1400 rpm (a) 1F mode (b) 2F mode (c) 1B mode (d) 3F mode 74
Fig. 2.46 Mode shapes for TOM at 1400 rpm (a) 1F mode (b) 2F mode (c) 1B mode (d) 3Fmode 74
Fig. 2.47 Mode shapes for SOM at 1900rpm (a) 1F mode (b) 2F mode (c) 1B mode (d) 3F mode 74
Fig. 2.48 Mode shapes for TOM at 1900rpm (a) 1F mode (b) 2F mode (c) 3F mode (d) 1B mode 75
Fig. 3.1 Schematic diagram of multi layer, multi-disc rotor bearing system 78
Fig. 3.2 Cross-sectional view of deformed rotor 79
Fig. 3.3 Schematic diagram of the rotor: (a) A deformed rotor disc arrangement (b) Cross-sectional view of deformed rotor 88
Fig. 3.4 Decay rate plot 90
Fig. 3.5 Stability limit of spin speed: (a) For various disc position (b) For various radius ratio 91
Fig. 3.6 Campbell diagram for two displacement mode 92
Fig. 3.7 Campbell diagram for various radius ratio (a) Aluminium outside case (b) Aluminium inside case 92
Fig. 3.8 First natural frequency: (a) For various disc positions (b) For various radius ratio 93
Fig. 3.9 Modal damping factor: (a) For three radius ratio (b) For four consecutive modes 94
Fig. 3.10 Unbalance frequency response: (a) For three radius ratio (b) For Aluminium inside - outside case 95
Fig. 3.11 Time response plot: (a) Unstable zone (b) Stable zone 96
Fig. 3.12 Whirl orbit: (a) Unstable zone (b) Stable zone 97
Fig. 3.13 Decay rate plot 98
Fig. 3.14 SLS plot 98
Fig. 3.15 Campbell diagram 99
Fig. 3.16 FNF plot 99
Fig. 3.17 MDF plot 100
Fig. 3.18 UBR plot 100
Fig. 3.19 Time response for unstable zone 101
Fig. 3.20 Time response for stable zone 102
Fig. 3.21 Whirl orbit plot: (a) Unstable region (b) Stable region 102
Fig. 3.22 First mode shape at spin speed of 500 rpm: (a) Backward whirl (b) Forward whirl 103
Fig. 3.23 Second mode shape at spin speed of 500 rpm (a) Backward whirl (b) Forward whirl 104
Fig. 4.1 Schematic diagram of the simply-supported rotor 113
Fig. 4.2 Decay rate using IIRS 115
Fig. 4.3 SLS for various disc positions using IIRS 115

Fig. 4.4 Decay rate using BRS 115
Fig. 4.5 SLS for various disc positions using BRS 115
Fig. 4.6 Campbell diagram using IIRS 116
Fig. 4.7 FNF for various disc positions using IIRS 116
Fig. 4.8 Campbell diagram using BRS 117
Fig. 4.9 FNF for various disc positions using BRS 117
Fig. 4.10 MDF plot using IIRS 117
Fig. 4.11 MDF plot using BRS 117
Fig. 4.12 UBR plot using IIRS 118
Fig. 4.13 UBR plot using BRS 118
Fig. 4.14 Time response for stable zone using BRS 119
Fig. 4.15 Time response for unstable zone using BRS 119
Fig. 4.16 Orbit plot showing stable region using BRS 120
Fig. 4.17 Orbit plot showing unstable region using BRS 120
Fig. 4.18 Schematic diagram of deformed rotor disc arrangement 121
Fig. 4.19 Decay rate plot 122
Fig. 4.20 SLS for various radius ratio 122
Fig. 4.21 Campbell diagram 123
Fig. 4.22 FNF for various radius ratio 123
Fig. 4.23 MDF plot 124
Fig. 4.24 UBR plot 124
Fig. 4.25 Time response for unstable zone 125
Fig. 4.26 Time response for stable zone 125
Fig. 4.27 Orbit plot showing unstable region 126
Fig. 4.28 Orbit plot showing stable region 126
Fig. A.1 Schematic diagram of an uni-axial circular rod 147
Fig. A.2 Data validation for mild steel (a) Hysteresis loop (b) Response plot (c) Energy dissipation plot 150
Fig. A.3 Data validation for aluminium (a) Hysteresis loop (b) Response plot (c) Energy dissipation plot 150
Fig. B.1 Simply supported beam with single point loading condition 151
Fig. B.2 Effective mass factor for various loading positions 154
Fig. B.3 Effective diamertal moment of inertia factor for various loading position .. 155
Fig. C.1 Simply supported beam at two point loading condition 159
Fig. E.1 Bearing geometry 168

List of Tables

Table No.	Title	Page No.
Table 2.1	Various rheological model and modulus operator ………………………	22
Table 2.2	Material properties and extracted viscoelastic parameters of Mild steel …	49
Table 2.3	Material properties and viscoelastic parameters of PVC ………………..	55
Table 2.4	Disc parameter ………………………………………………………….	55
Table 2.5	Disc parameter ………………………………………………………….	60
Table 2.6	Comparison of modal parameters for low damped material: Case – 1 ………………………………………………………………….	75
Table 2.7	Comparison of modal parameters for high damped material: Case – 2 ………………………………………………………………….	76
Table 3.1	Disc parameter ………………………………………………………….	89
Table 3.2	Material properties and extracted viscoelastic parameters ……………….	89
Table 3.3	Material properties of the rotor ………………………………………..	97
Table 3.4	Disc parameter ………………………………………………………….	98
Table 3.5	Comparison of modal parameters for low damped material: Case – 1 $(\mathfrak{R} = 0.3)$ ……………………………………………………….	104
Table 3.6	Modal parameters for high damped material: Case – 2 ………………….	105
Table 4.1	Disc parameter ………………………………………………………….	113
Table 4.2	Material properties of mild steel ………………………………………	114
Table 4.3	Discs parameter ……………………………………………………….	121
Table 4.4	Material properties of the rotor ………………………………………..	121
Table 4.5	Comparison of modal parameters at $L^* = 0.3$ using BRS technique: Case -1 ………………………………………………………………….	127
Table 4.6	Comparison of modal parameters using BRS technique: Case -2 ……….	127

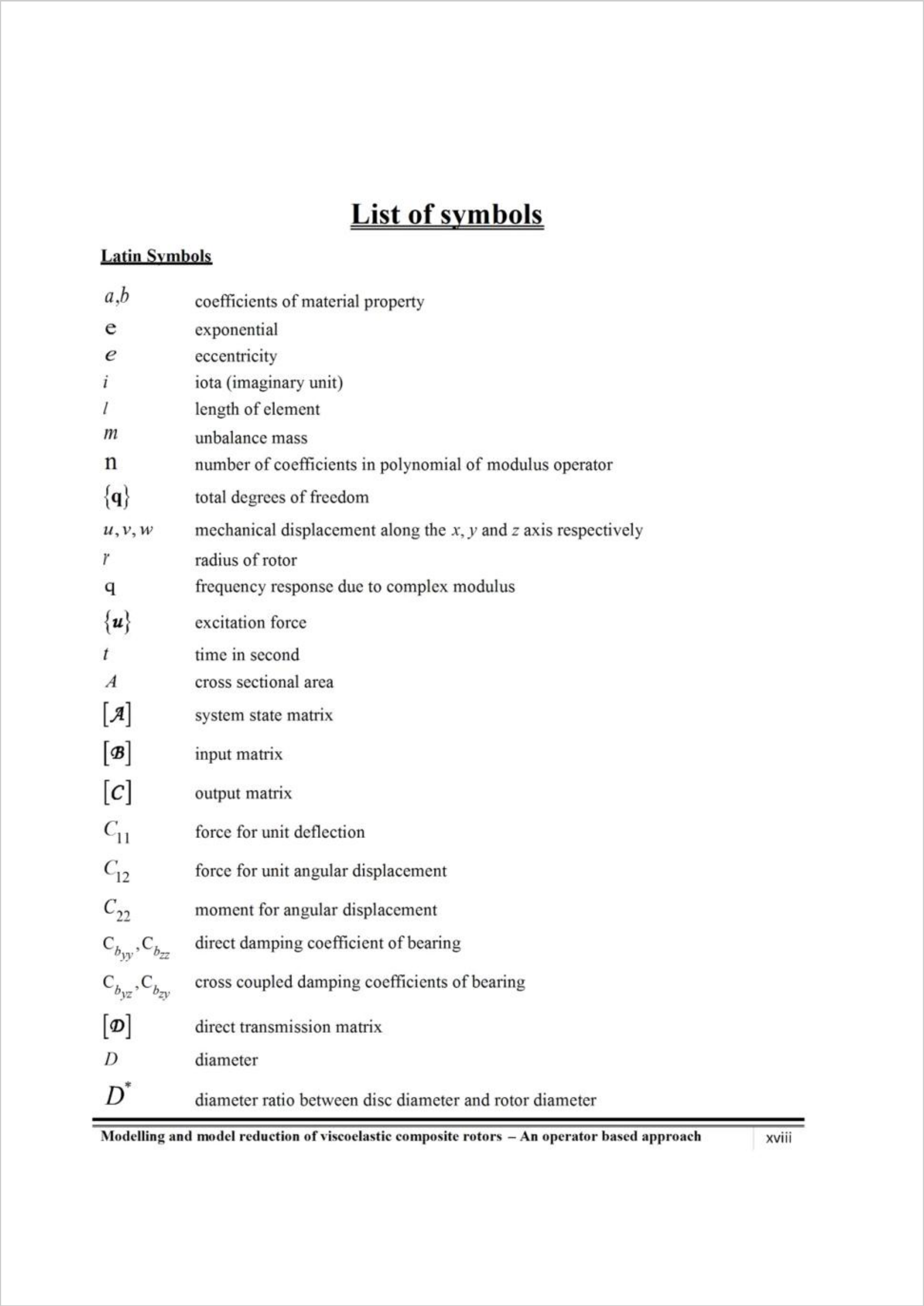

List of symbols

Latin Symbols

a,b	coefficients of material property
e	exponential
e	eccentricity
i	iota (imaginary unit)
l	length of element
m	unbalance mass
n	number of coefficients in polynomial of modulus operator
$\{\mathbf{q}\}$	total degrees of freedom
u, v, w	mechanical displacement along the x, y and z axis respectively
r	radius of rotor
q	frequency response due to complex modulus
$\{\boldsymbol{u}\}$	excitation force
t	time in second
A	cross sectional area
$[\mathcal{A}]$	system state matrix
$[\mathcal{B}]$	input matrix
$[\mathcal{C}]$	output matrix
C_{11}	force for unit deflection
C_{12}	force for unit angular displacement
C_{22}	moment for angular displacement
$\mathrm{C}_{b_{yy}}, \mathrm{C}_{b_{zz}}$	direct damping coefficient of bearing
$\mathrm{C}_{b_{yz}}, \mathrm{C}_{b_{zy}}$	cross coupled damping coefficients of bearing
$[\mathcal{D}]$	direct transmission matrix
D	diameter
D^*	diameter ratio between disc diameter and rotor diameter

D	first order differential time operator, i.e. $\frac{d(\ )}{dt}$
$E(\ )$	modulus operator
E	modulus of elasticity
$[\mathcal{E}]$	descriptor Matrix
$\mathcal{F}$	objective function
$[\mathbf{H}]$	frequency response function matrix
$[\mathbf{G}]$	gyroscopic matrix
I	area moment of inertia
$\mathbf{I}$	identity Matrix
J_P	polar moment of inertia
J_D	diametral moment of inertia
$[\mathbf{K}]$	stiffness matrix
L	length of rotor
L^*	disc position
$[M_{yy}]$	bending moment about y-axis
$[M_{zz}]$	bending moment about z-axis
$[\mathbf{M}]$	mass matrix
$\mathcal{M}$	mass
N_d	number of disc
N_l	number of layer
$\{\mathbf{P}\}$	external nodal force vector
$[\mathcal{P}]$	controllability gramian
$[\mathcal{Q}]$	observability gramian
R	deformation of the rotor center line
$\mathbf{T}$	transfer function
$[\mathcal{T}]$	transformation matrix

T	kinetic Energy
V	potential Energy
$\{x\}$	state vector
$\{\mathbf{y}\}$	output vector

Abbreviation

dFRF	directional Frequency Response Function
r-dFRF	reverse directional Frequency Response Function
BRS	Balances Reduction System
CM	Classical Model
FEM	Finite Element Model
FNF	First Natural Frequency
IIRS	Iterative Improved Reduction System
MDF	Modal Damping Factor
PVC	Poly Vinyl Chloride
SLS	Stability Limit of Spin Speed
SNF	Second Natural Frequency
SOM	Second Order Model
SWL	Synchronous Whirl Line
TOM	Third Order Model
UBR	Unbalance Response

Hellenic Symbols

α	hankel singular value
φ, ϑ	rotation about y and z- axis respectively
θ	phase angle
$\Re$	radius ratio
σ	mechanical stress
β	factor for calculating for effective mass and diametral moment of inertia of the rotor
ε	mechanical strain
$\boldsymbol{\phi}$	hermite shape function
ρ	mass density
Ψ	deformation of the rotor along rotational axis

$\boldsymbol{\lambda}$	eigenvalues
$[\boldsymbol{\Lambda}]$	eigenvalues
$[\boldsymbol{\psi}]$	eigenvectors
$[\boldsymbol{\Psi}]$	eigenvectors
ω	excitation frequency / whirl speed
Ω	spin speed
η	loss factor

Subscript

b	balanced
br	balanced reduction
brg	bearing
cr	critical
d	disc
eff	effective
i	iteration
i, j, k	indices
$\mathbf{r}$	reduced
l	layer
m	master
n	total number of degrees of freedom
N	indicate matrix size
p, g	complex displacement and force rotating in same direction as shaft
$\bar{p}, \bar{g}$	complex displacement and force rotating in opposite direction as shaft
r	rotor
s	static
s	slave
D	diametral
P	polar
x, y, z	conventional coordinate axis
B	bending
C	circulatory
R	rotational

T	translational

Superscript

e	element
T	transpose

Mathematical operators

$(\ )$	operator
$(\bullet)$	order of differential equation
$(\sim)$	vector is in rotating coordinate
$(*)$	non dimensional term
$(\wedge)$	assumed quantity

Chapter-1

Introduction

1.1 Preamble and research motivation

Rotating machine is a mechanical system that is used in many applications such as engines, electrical generators, hydraulic turbines, pumps, compressors, etc., well established in Vance (1988), Lee (1993) and Rao (2009). Rotordynamic has a very long back history; it started when Rankine (1869) wrote a paper on the subject of centrifugal forces of a rotating shaft solely. The author determined that rotors experience large amplitude vibrations at certain running speed, called critical speed. A statement was highlighted that rotor is impossible to run faster than the critical speed without experiencing machine failure. After some time, Dunkerley (1895) and Foppl (1895) improved the understanding of operating speeds greater than the first critical speed. It was discovered that rotor has multiple critical speeds and that some of them correspond to the natural frequencies of a non-rotating shaft.

After some time, most simple and efficient rotor bearing model was developed by Jeffcott (1919), which was used to improve the understanding of dynamics of rotor behaviour using lumped mass parameter approach. Dimentberg (1961) introduced a term instability caused due to material damping that has a greater influence on the system dynamics, it has been found that rotor shaft becomes unstable after first critical speed. Today's highly complex rotors running at increasingly faster speeds in varied environments require more sophisticated methods to understand their dynamics. With the development of computers, there have been new computational techniques that allow for more complex and accurate analysis. The Newtonian approach, transfer matrix method and finite element method are various such methods.

The high-speed rotor operation causes two major problems, i.e., 1) high transverse response due to resonance and 2) instability of the rotor shaft system over a spin speed, both of which set a limitation on the operating speed of a rotor. Vibration in any structure is very dangerous, not only affects the portion where it happens but also hampers the supporting structures. Vibration present in rotating machinery also causes severe effects and controlling them is one of the biggest challenges, established by many researchers Tondl (1965), Meirovitch (1986), Kramer (1993), Genta (2005), Thomson et al. (2008), and Kiciński (2010). It is essential to have a vibration free system for the smooth and efficient operation of machines. However, in reality, no rotor operation can be made vibration-free due to the presence of various types of excitations viz. self and external excitation to the rotor shaft system. The harmonic force of excitation due to mass unbalance is the most common source of rotor vibration among several external excitations (e.g., misalignment, rubbing, impact), reported by Muszynska and Goldman (1995, 2005), although the amount of mass unbalances in a rotor may at best be minimized by balancing the rotor. However, there always remains some residual mass-unbalance even after the most precise balancing technique has been adopted. Therefore, the primary aim of the researchers is to minimize the vibrational energy of the system as small as possible. Viscoelastic materials are one of an alternative to dilute the problem such as excessive vibrations and instability of the system. Thus, modelling of the rotor shaft system considering damping effect is very crucial.

1.2 Modelling of viscoelastic material and its application

In the last few decades, intensive research has been carried out on viscoelastic materials, and they are extensively applied to engineering structures and equipment s (Kapur et al. (1977), Nakra (1998)). Viscoelasticity of any material can be understood as the material that exhibits both viscous and elastic behaviour. Here, stress at a point is not only proportional to strain , but in general, stress and its derivatives are proportional to strain and their derivatives; the Hookean behaviour of a material, where stress is proportional to strain forms a particular case of viscoelastic material. Ideally, every material may be treated as viscoelastic because every material store as well as dissipates some energy under deformation as damping is inherent. In this regard, metals may be classified as weakly viscoelastic as the amount of energy dissipated is much less than the energy stored. Whereas, polymers are generally strongly viscoelastic as the energy dissipation is substantial. Viscoelastic behaviour is represented either by viscous or by hysteretic damping to include frequency dependent and independent behaviour of materials. Under dynamic deformation the stress and strain are not in phase, the current stress state depends on both past and present deformation states and causes energy dissipation where the dissipated energy per cycle depends on the frequency of excitation (Christensen (1982)). Therefore, in a case of periodic loading, the modulus is a complex quantity, whose real part is storage modulus and the ratio between imaginary and real part is loss factor. For polymeric materials, both storage modulus and loss factor are frequency dependent. It is quite obvious to mention that the frequency functions are varying with material to material. The frequency dependent behaviour of storage modulus and loss factor for different polymeric material was presented by Lazan (1968), Ferry (1980), Nashif et al. (1985), and Nashif and Lewis (1991) reported system damping value for different structural materials under different types of deformation. These databases were generated after performing several experiments and reconsidered for simulation of various viscoelastic materials through complex modulus approach. In the end, it is commented as the complex modulus method is suitable for finding frequency response under mono-frequency excitation. But it faces difficulty in obtaining a frequency response under multi frequency excitation and transient response also (Bert (1973)). This is overcome by using a time domain model where the parameters used in material modulus are the function of differential time operator. But obtaining those parameters from frequency dependent values of storage modulus and loss factor are not straight forward.

Time domain representation of viscoelastic behaviour is done through the rheological model, which is a network formed by linear springs and linear dashpots. Various rheological models made of a spring-dashpot combination like 2, 3, 4, elements are presented by Bland (1960), Shames and Cozzarelli (1992). These texts serve as a real serious beginning to get conceptions about the dynamic behaviour of viscoelastic solids. Different basic models with a spring-dashpot combination are Voigt (one spring and one dashpot are in parallel), and Maxwell (one spring and one dashpot are in series) model are suitable to predict creep and stress relaxation behaviour respectively. Both creep and stress relaxation behaviour of a viscoelastic material can closely represent by three or higher element model. The standard 3-element linear model consists of a Maxwell model and a linear spring in parallel, is also known as Zener model and was firstly introduced by Zener (1948). Authors like Wang and Chen (2009), Palmeri and Muscolino (2011), Lei et al. (2013), Alves et al. (2013) and others used Zener model to find the stability of an axially accelerating viscoelastic beam and numerically validated the parametric resonances. The 4-element standard linear model was also used to model the viscoelastic material depending on its material behaviour. A series of spring and dashpot combination was investigated by Friedrich (1991) and developed a generalized Maxwell (GM) model also known as Maxwell-Wiechert model. This model has several advantageous features and predicts accurate dynamic characteristics of the viscoelastic model.

Another way of time domain representation of linear viscoelastic behaviour is an internal variable approach. Likewise, mechanical variable, a separate variable is incorporated to take care of dissipation effect, known as an internal variable. In the category of internal variable, Fractional Derivative Model (FDM) is another necessary approach of study which was done by Bagley and Torvik (1983, 1985, and 1986). Sometime FDM is also known as fractional calculus, where differentiation is done on the fractional level. In this technique, constitutive relationships of viscoelastic material are demonstrated concerning strain -stress, which process the viscoelastic modulus into complex values. This model also describes the mechanical properties of the viscoelastic material, but leads to closed-form solution of the finite element equation of motion of damped structures. Mainardi (2010) explained the important features of fractional derivatives as had the capability to capture the frequency dependent viscoelastic material by using few model parameters, generally three to six. FDM also satisfies the second law of thermodynamics and predict elliptic stress-strain hysteresis loop for viscoelastic damped material. Maxwell model is further extended as the Fractional Derivative Maxwell Model (FDMM), in which the previous model is combined with fractional derivatives as an operator that generalizes the differentiation to fractional order of range 0 to 1. Modified version fits well with experimental data of viscoelastic behaviour of material over a broad range of frequency, referred from Lewandowski and Chorazyczewski (2010) and Lu et al. (2012). Based on the non-negative rate of internal work and non-negative rate of energy dissipation, Jia et al. (2007) applied fractional derivative to examine the creep compliance and relaxation modulus of the viscoelastic material. The authors also compared the result with classical model and analyzed the fractional derivative by the sinusoidal response. Makris and Constantinou (1991) used fractional derivative to study the effect of viscous dampers applied for vibration isolation and reduction in the piping system and calibrated with dynamic experiments.

In late 80's, Golla and Hughes (1985) developed a frequency-domain model that predicts the dynamic properties of large and flexible viscoelastic material structures. In this model integer, derivative model and the hereditary integral used to form the constitutive relationships law. McTavish et al. (1992), McTavish and Hughes (1992, 1993), extended the proposed model for linear viscoelastic structures and named as the Golla -Hughes-McTavish model (GHM). Several studies have been performed on the application of GHM model to calculate the dynamic response of viscoelastic beams, plates and shells reported by many researchers like Lam et al. (1995, 1997, and 2000), Trindade et al. (1999), and McTavish (2003). GHM model has an advantage that it has a higher capability to match experimental data and excellent compatibility with finite element method. It also has a drawback in predicting the dynamic parameters by FEM that it produces a large matrix system depending on the discretization of finite element model.

Likewise, different internal variable models, viz. Augmenting Thermodynamic Field (ATF) and Anelastic Displacement Field (ADF) were reported by Lesieutre (1989) and Lesieutre and Bianchini (1995) respectively. ATF modelling is based on energy dissipation in solid materials using thermodynamic principles. ATF utilizes the time domain continuum of viscoelastic material that preserves the characteristic frequency-dependent damping and modulus of real materials. Lesieutre and Mingori (1990), and Lesieutre (1992) applied ATF to model linear viscoelastic structures using finite element and found that ATF is easily compatible with FE structural analysis methods. Using an ATF modelling technique has a significant advantage that the elastic modulus and dissipated energy can be obtained by the fixed matrix of structure and the modal damping is calculated using the modal frequency. Lesieutre et al. (1996) extended the ATF method to three-dimensional case. Lesieutre and Bianchini (1995) developed Anelastic Displacement Field (ADF) models. ADF is a special type of ATF model, in which displacement field is composed of both elastic and anelastic component that takes into account the dissipation. Lesieutre and Govindswamy (1996) modified the ADF to take into account the temperature-dependent characteristics and also used this approach to estimate the local temperature changes in viscoelastic continuum due to self-heating caused by deformation. The main advantage of ADF model is that it tends to a straightforward development of time-domain viscoelastic damped material in the finite element method, and does not require explicit time dependence in the material constitutive equation. After several years of development ATF and ADF are used to model viscoelastic material for structural vibration control using Active Constrained Layer Damping (ACLD) techniques reported by Lesieutre and Lee (1996). For enhancing dynamic performance of beam, Roy et al. (2009, 2013) used a multilayer architecture, where each layer is assumed to be viscoelastic material. ATF and ADF approach were used to develop finite element model of the multilayer viscoelastic beam.

The common way of incorporating the damping effect is so called frequency dependent viscous damping, where instantaneous velocity is only state variable. However, this cannot be a damping mechanism for structural material. Frequency independent hysteretic damping also faces difficulty in time domain dynamic simulation. A new method named non viscous damping (NVD) was proposed by Adhikari (1999, 2001, and 2002) for applying damping on such structural materials. Here the damping force depends on past history of velocities and measured through convolution integrals over some kernel function. This method does not require any additional dissipation coordinate. Recently, Zhou et al. (2015) served a valuable review on the past and present researches of viscoelastic material.

All these models depict same conclusion, i.e. instantaneous stress for linear viscoelastic materials is achieved by operating the instantaneous strain. Thus, by correlating Hook's law, a modulus operator which is a function of differential time operator, is used to represent the constitutive relationship. For exclusive elastic material, it is once again a constant term, known as Young's modulus. The numerator and denominator of material modulus are a polynomial of differential time operator and the order of the polynomial depends on material behaviour. The polynomial coefficients are known as viscoelastic parameters, which are found from frequency dependent values of storage modulus and loss factor. Therefore, the present work concentrates to first develop a mathematical model of generally viscoelastic rotor shaft system using operator based approach.

1.3 Dynamics of damped rotor bearing system

To study the exact dynamics of any rotor bearing system, it is very important to model the system with its sufficient parameter consideration. From the past to present several advancements have been occurred in the modelling of rotor bearing system using different modelling techniques such as force-Newtonian method, transfer matrix methods, energy methods and some others too. They all are some sort of classical approach, i.e. distributed effects of the continuous system are assumed to concentrate on single or few points through which the force analysis is done to get the dynamics of that system. Firstly, Jeffcott (1919), introduced a simple classical method to model the rotor bearing system, where the rotor shaft was taken as simply supported ends and total mass was concentrated at the middle. Many more have followed the same path and generated various model considering rotating disc, bearings, foundations and other parameters too, some are reported here as Tondl (1965), Vance (1988), Lee (1993), Kramer (1995), Lalanne and Ferraris (1998). After some time, many researchers faced difficulties to model complex rotor shaft system through this technique. Thus, an advance modelling technique known as finite element method is adopted for increasing accuracy. In this regard, formulation by Ruhl and Booker (1971), Nelson and McVaugh (1976) put a remarkable impression and were useful for the society. In that research, the authors used Euler-Bernoulli beam theory in finite element models of turbo rotor system. Further Zorzi and Nelson (1980) developed a finite element model considering Euler-Bernoulli beam theory when the rotor is subjected to an axial torque. Nelson (1980) modelled the rotor bearing system using an FEM technique, in which rotor was considered as Timoshenko beam. In recent trend Satyanarayana et al. (2003) used complex coordinates in FE model and explained the whirling effect of the rotor. All those models did not account for rotary inertia, axial load, gyroscopic moment, shear deformation or internal damping. While applying this model in an actual working environment, several researchers have noticed that these models are not sufficient to predict the actual system dynamics. They have also found that rotor bearing system has a greater influence of other parts which are attached to it and the material used to model the whole system. Concluding with this fact, it is necessary to study the effect of damping present in the form of internal as well as an external in the rotor bearing system.

Damping plays a significant role in the dynamics of the rotor bearing system. In general, it can be classified into two categories as internal damping (rotating damping) and external damping (non-rotating damping). Rotating damping appears due to shaft material damping, friction forces in bolted and riveted joints in built up rotors, the force generated by shrink fitted rotor assemblies. The viscoelastic rotor is acted upon by rotating damping force generated by the internal material damping, which tends to destabilize the rotor shaft system by generating a tangential force proportional to the rotor spin speed (Dimentberg (1961)). This tangential force has a major influence on dynamic performance as it tends to destabilize the system. Thus, for perfect assessment of dynamics or exact evaluation of the stability limit of spin speed (SLS), it is very important to consider the tangential forces that are generated due to material internal damping, well stated by Kandil (2004).

Non-rotating damping is present due to joint damping, air damping, and bearing support. Bearing is a machine element which supports another moving element and permits relative motion through contact surface. Bearings are mainly categorized as rolling contact bearing and sliding contact bearing. In the first type, the force is transferred through some rolling elements such as ball and roller. Due to less contact area, rolling friction is much lesser than sliding friction, thus it is also known as the antifriction bearing. In sliding contact bearing, a load is transferred through a thin film of lubricant such as fluid film journal bearing. Various sources of damping present in bearing are hydrodynamic lubrication, bearing interface between bearing rings and rotor, material damping due to deformation of the rolling element and raceway well explained in Walford and Stone (1983), Harris (2001), Horney (2003), Rao (2009), Guo and Parker (2012). The rolling contact bearings are simulated as linear springs and linear dashpots. Stiffness and damping coefficients are independent of spin speed and oppose the tangential forces generated due to internal friction and in this way helps in improving the stability of the rotor system, referred from Gunter (1967), Kirk & Gunter (1972), and Ku (1998). The fluid film forces of journal bearing depend on many parameters like clearance, lubricant viscosity and spin speed. It also provides asymmetry to the system model and has a major effect on dynamics. Detail derivation of these forces in terms of four stiffness and four damping coefficients are available in Hamrock et al. (2004), Genta (2005), Rao (2009), Friswell et al. (2010b). Though these hydrodynamic forces are actually nonlinear functions of displacement and velocity of the journal with respect to its bearing housing, but sometimes linear forcing function is assumed for simplicity (Holmes (1963)). A negatively cross couple term exists in the forcing function. Thus, it also provides a tangential force in the direction of the whirl and proportional to spin speed. This tangential force is dissipative in nature and has a destabilizing effect. After certain spin speed, this tangential force is sufficient to overcome the restoring force, the rotor is subjected to instability and corresponding oil whirl is known as an 'oil whip' (Crandall (1983), Muszynska (1986), Stepan et al. (1995)). A detailed survey of finding the bearing parameter and their effect was reported by Tiwari et al. (2004). Therefore, modelling and identification of such forces are very important in investigating the dynamics of the rotor-bearing system.

After getting the actual idea of the importance of both types of damping, it is necessary to develop a reliable model to represent the constitutive relationship for understanding the dynamic behaviour of a viscoelastic rotor. In the past, many researchers like Dimentberg (1961), Ehrich (1964), Gunter (1967), Gunter and Trumpler (1969), Kramer (1993), Genta (2005), and Friswell et al. (2010b) developed rotor model either by lump mass system approach or by finite element approach and considered internal or external damping effect. The authors like, Zorzi and Nelson (1977), Ozguven and Ozkan (1984), Ku (1998) presented a finite element model for damped rotor bearing system. They incorporated internal damping either viscous and hysteretic form or a combination of two for presenting the characteristic behaviour of structural materials. It has been found that the system becomes unstable after first critical speed due to viscous damping, but hysteretic damping has a destabilizing effect from the beginning of speed. With this regard, some interesting interpretation and utilization of hysteretic damping model are also shown in Genta (2004). Since hysteretic damping model faces difficulty in time domain dynamic simulation, Genta and Amati (2009, 2010) used an alternative solution by using Non-Viscous Damping (NVD) model to derive the equation of motion for limited degrees of freedom.

A brief report on the historical background of rotor dynamics and their latest trends are available in Tiwari (2006). Bavastri et al. (2008) also developed a rotor model with flexible bearings made of a viscoelastic material that helps in reducing shock and vibration. They used an energy method to derive the equation of motion and for designing the bearing portion viscoelastic layer was added between an external layer of the roller bearing and the bearing housing. Combescure and Lazarus (2008) developed a refined finite element model for dynamic analysis of large rotating machine. Viscous form of internal damping was considered either through 2D Fourier model or 3D shell model. Carrera et al. (2013) proposed a new technique as Carrera's unified formulation (CUF) to perform a free vibrational analysis. In this method, hierarchical formulation was used to obtain refined structural theories for explaining variable kinematic description. This can be achieved by expanding the unknown displacement variable over a section by adopting Taylor's polynomial for Nth order parameter.

Some of the classical models were developed by Dutt (1992), Dutt and Nakra (1992, 1995, and 1996), and Dutt and Toi (2003), where viscoelastic supports were used to enhance the stability. Multi-element rheological model was used for viscoelastic support and consequently higher order equations of motion were derived. Tiwari (2013) had also developed several methodologies to design rotor model using traditional and finite element approaches.

Several finite element packages have also been developed to investigate the dynamic behaviour of the rotor bearing model. Chatelet et al. (2005) developed a rotating assembly of turbo machines, where they had created a 3D finite element model and used a programmable package named ROTORINSA which was based on beam type 1D finite elements to analysis that model. Liu et al. (2013) investigated the stability of a flexible rotor bearing 3D system using Floquet theory, in which periodic motion and stability margin were obtained by shooting methods and path following techniques. Jalali et al. (2014) used ANSYS to model the 3D rotor bearing system and modal analysis has also been done to get the insight dynamic of the system. Chávez et al. (2015) presented a new mathematical model which uses snubber with isotropic bearings to enhance dynamics of the modified Jeffcott rotor. MATLAB has been used to generate the simulated results and experimental setup is also done to demonstrate the predictive capabilities of snubbers ring.

Both viscous and hysteretic models are not sufficient to predict the dynamic behaviour of the real system. The motivation for using general viscoelastic model arises from the need to capture the influence of both types of damping. Modelling of rotor continuum made of generally viscoelastic materials and the study of dynamics are not sufficient. Grybos (1991) studied the dynamics of a viscoelastic rotor-shaft by considering a lumped 3-element rheological model (Hooke's and Kelvin-Voigt element are in series). Roy et al. (2008) used the ATF approach for predicting stability limit of spin speed and unbalanced response amplitude of an aluminium rotor. Aluminium considered to be generally viscoelastic and various parametric values reported by Lesieutre and Mingori (1990) were used here. Roy (2008) did a detailed study for modelling the generally viscoelastic rotor shaft. Friswell et al. (2010a) reported an internal variable based approach to study the dynamic characteristics of a viscoelastic rotor. Dutt and Roy (2011) proposed an operator-based approach to write the equations of motion of a viscoelastic rotor-shaft continuum after discretizing it with finite Timoshenko beam elements.

From various literature, it has been seen that the researchers have used either classical approach or finite element approach. In classical form, the equations of motion are drawn up by considering lumped mass approximation of the rotor-shaft-system. Whereas in finite element approach, the distributed effect of continuum is considered. The latter is elegant but results in many equations which need heavy computational effort. However the former is brief, handy and may be used for a quick prediction of dynamic behaviour. But it captures few modes and fails to predict correct result in some cases.

1.4 Dynamics of composite rotors

Within few decades enormous research activities are aimed at enhancing the dynamic behaviour of structures. Nowadays, most of the heavy and bulky structures are replaced by viscoelastic materials, especially polymers and polymer-composites for many physical advantages. By virtue of lesser density and proficient material damping mechanism, plenty of examples are found where viscoelastic substances are used for structural vibration minimization (Nakra (1998)). However, low elastic modulus is one of the major disadvantages of these materials, which can be overcome adequately through reinforcement. Motivated by this occurrence, polymer matrix reinforced with acceptable viscoelastic fibres is used to fabricate composite rotor.

Following the same fact, researchers like Zinberg and Symonds (1970), Reis et al. (1987), Bert and their colleagues (1992, 1993, and 1995) developed numerous numerical models of rotating composite shaft. Firstly, the equivalent modulus beam theory (EMBT) was used by Zinberg and Symonds (1970) to obtain critical speed of a composite shaft and compared with experimental data. Asnani and Nakra (1976) suggested the effectiveness of damping to reduce flexural vibration using the concept of multi-layered beam with constrained viscoelastic layers. Reis et al. (1987) utilized Timoshenko beam theory (TBT) with Donnell thin shell theory (DTST) to derive stiffness matrix for spinning composite shaft. Bert (1992) started to model the composite shaft with Euler Bernoulli beam theory (EBBT) and incorporated all effects (i.e . gyroscopic, bending and torsion coupling) that helped to predict the actual dynamics of rotor system. Later on, Kim and Bert (1993) applied the Sanders best first order approximation of shell theory to obtain the equation of motion and determined the critical speed of a spinning cylindrical hollow composite shaft. It was extended by Bert and Kim (1995) with Bresse-Timoshenko beam theory and Hamilton principle to establish the governing equation of composite shaft. Either boron-epoxy or graphite-epoxy was utilized for composite material. Chandramouli et al. (1994) developed an experimental setup to study the crack propagation of a composite shaft (carbon-epoxy) based on the laminated plate theory. Singh and Gupta (1994) employed first order shear deformation theory (FSDT) to achieve governing equation and investigated natural frequencies, loss factor and damping ratio in flexural mode of a cylindrical composite shaft. EMBT and LBT (layerwise beam theory) were used by Singh and Gupta (1996) to do the dynamic analysis of composite rotor. Effect of stacking sequence in carbon-epoxy composite rotor-shaft was also studied. An experiment (rap test) was conducted by Gupta and Singh (1998) on a composite shaft made of carbon fibre (Hercules 929-6h) and epoxy resin (Ciba Geigy LY-556 and HT-992), to measure damping from decay curve.

In present scenario, Chang et al. (2004a) applied first order shear deformation theory and extended Hamilton principle to develop an equation of motion for laminated com posite shaft (boron/epoxy and graphite/epoxy). Later on Chang et al. (2004b) adopted Mori-Tanaka mean field theory to study the interaction of randomly oriented reinforced composite material (E - glass/epoxy). Effective elastic modulus of the composite material was considered as a function of phase properties, volume fraction and orientation angles of its constituents. Among all other effects, (gyroscopic couple, rotary inertia and shear deformation), coupling effect due to the lamination of composite layers was also taken care of. Gubran and Gupta (2005) analysed the natural frequencies of a tubular composite shaft. A different coupling effect caused due to ply - stacking sequence present in graphite/epoxy composite material was incorporated. Sino et al. (2008) used simplified homogenized beam theory (SHBT) to obtain the sensitivity of frequencies and stability threshold of a fibre reinforced composite rotor shaft. Several effects like fibre orientation, stacking sequence and shear between carbon/epoxy were also analyzed.

Recently, Montagnier and Hochard (2014) developed a composite drive shaft mounted by viscoelastic supports to operate at supercritical regime, where carbon/epoxy was used. The damping in carbon fibre reinforced plastic (CFRP) is hysteretic in nature. Material damping was incorporated in finite element model through equivalent viscous damping. The critical speeds were found considering various effects such as rotary inertia, gyroscopic forces, transverse shear, supports stiffness and coupling effect due to unsymmetrical composite laminate. Carrera and Filippi (2014) utilized Carrera's unified formulation (CUF) to derive the governing equation of multi-layered composite rotor and obtained the dynamic response. Boron/epoxy were used to estimate anisotropic and laminated composite rotor shaft. Roy and Chandraker (2015) presented a multilayered viscoelastic rotor and used Voigt model for each viscoelastic layer.

Many such applications are aimed to design light yet strong rotor which are capable of running at high speed for obtaining high power in spite of heavy rotors that are available in the market. The surveyed literature shows a lack of consideration of the layered rotor shaft where the effect of internal damping are taken care for each layer. In this regard, the work by Roy et al. (2014) was important as in this work all layers were perfectly bonded and assumed to be viscoelastic. Operator based constitutive relationship for each layer was used to derive the higher order equation of motion in the finite element form. The same concept was again used by Roy and Dutt (2016) to develop finite element model of the viscoelastic composite rotor. Composite was formed by reinforcing long unidirectional fibre into the matrix material, where both fibre and matrix were assumed to be viscoelastic. It is seen from both works, that the order of the differential equation depends on the number of layers as well as their constituent materials. The number of viscoelastic parameters exists in constitutive relationship, vary from material to material. Thus, a large number of coordinates appear when the higher order equation is converted to state space form. This may lead to increase computational effort.

1.5 Modal analysis of rotor-bearing system

Since all dynamic behaviour of rotors is interlinked with a rotation of the rotor (Lee (1991)), the concept of directivity becomes very important in rotor dynamics. Thus, modal analysis of such rotating system is an essential tool to get an insight of dynamic behaviour. Eigen analysis is only useful way for getting modal behaviour. For a damped system, eigenvalues and eigenvectors are generally complex quantity. Thus, for a damped rotor system,it is also known as complex modal analysis, where complex refers to complex variable representation in terms of either excitation or response (Kessler and Kim (2002) and Mesquita et al. (2002)).

Modal analysis is a numerical technique to determine the modal parameter of a system. Mathematical models only describe the dynamic behaviour of the system and they are constrained with some assumptions and boundary condition. Most of the vibration analyses on rotor-dynamics are using a traditional concept which is based on natural modes, natural frequencies, and critical speed (Nakra (1998), Genta (2005) and Friswell et al. (2010b)). The major distinction comes into picture when the vibration analysis is done on a rotating system. Due to the existence of asymmetry, which arises from gyroscopic and circulatory forces, the rotor shaft system is generally non-self-adjoint nature. The equation of motion of such non-self-adjoint system is solved by transforming it into state space form. Two kinds (left and right) of eigenvectors are obtained through eigen-analysis, which help to proceed for modal analysis (Ewins (2000a, 2000b)). Firstly, it was notified by Lee (1991) after considering asymmetric system due to the gyroscopic stiffening effect and explained the backward, forward whirling. Following the same theory Jei and Kim (1993) started the modal analysis of a rigid rotor supported by a flexible bearing using a classical model with two displacements and two rotational degrees of freedom. Due to the conjugate even property of traditional coordinate, directivity of modes is lost, while it is protected under complex coordinate. A modal parameter like modal frequency, modal damping, mode shapes, and direction of whirl were well explained with the use of complex modal analysis by Crandal and Yeh (1989), Jei and Lee (1992), Joh and Lee (1996), Lee and Lee (1997), and Kessler (1999). Mesquita et al. (2002) did a comparative study between traditional frequency response function and directional frequency response function (dFRF) of the rotor shaft system. Kessler and Kim (2006, 2007) showed that general planer motion and forces can be represented as the linear superposition of forward and backward rotating vectors. The forward and backward component of complex displacement and excitation function were interpreted by d-FRF.

Most of the researchers considered asymmetry due to gyroscopic effect and studied the modal behaviour. But another source of asymmetry is the internal friction of the rotor, as discussed in the previous section. Chouksey et al. (2010) obtained mode shape and dFRF for a flexible damped rotor shaft supported by antifriction (ball or roller) bearings. Shaft material damping was included through two elements Voigt model. Journal bearings are frequently used to support heavy rotors in the power plant industry, railway car and others. Very few reports on modal analysis considering fluid film bearing are noticed in literature. Lee and Jei (1988) did the modal analysis of a flexible non-uniform shaft supported by an anisotropic bearing. But rotary inertia and gyroscopic moment were only considered. Relative work by Chouksey (2012) and Chouksey et al. (2012), found modes shape, d-FRF of flexible rotor mounted by short oil film bearing. Internal material damping of the rotor shaft was included in the finite element formulation through two elements Voigt model. Chandraker et al. (2013) did the modal analysis of a multi-layer viscoelastic rotor and found modal damping factor and mode shape. Chen and Jiang (2015) expressed an analytical solution for addressing the effect of forward/backward whirl mechanism on stability through multiple nonlinear normal modes (NNMs). The concept of NNMs arose for modal analysis of nonlinear system. Wang et al. (2015) suggested a new method of modal analysis to predict the damping ratio of the rotor bearing system. Rational polynomial method (RPM) was used to predict stability analysis of a centrifugal compressor supported by magnetic bearing. dFRF and modal damping ratio were estimated through weighted instrumental variables (WIV).

Previously, most of the researcher did modal analysis for the conventional second order system. While, considering the general viscoelastic model of the rotor shaft, the equations of motion reach to a higher order and order of differential equation depends on the nature of the material. Adopting this approach for the higher order system is very complex and complicated because asymmetry exists in higher order also.

1.6 Model order reduction

Modelling of viscoelastic rotor has been done in several ways, but some stumbling block came at the time of computational simulation because of the matrix size. It is just not a problem of big matrices, but it generates a computational error due to the presence of skew-symmetric circulatory stiffness and gyroscopic matrices. In the interest of reducing computational effort and simulation time, model order reduction is essential for bulky system. Many model order reduction techniques are available for reducing the size of matrices. But the selection of reduction methods varies with the dependence of the application. In viscoelastic rotor same problem arises.

Firstly, Guyan (1965) communicated the concept of reduction methods for the static condition case. In this technique, the inertia terms interconnected with the unwanted degrees of freedom were considered as a slave. On a contrary, the valuable degrees of freedom were known as master. Although Guyan method is specifically used for static problem, on the other side if it is implemented to a dynamic model, the cut-down model is insufficient to generate a precise result. After sometime Carig and Bampton (1968) introduced another reduction method which was extensively used in the aerospace industry to re-characterize large finite element models into a set of relatively small matrices contain mass and stiffness that captured fundamental low-frequency response modes only. In this technique, mass, damping and stiffness matrices are truncated using Craig-Bampton transformation matrix, the transformation is successful because the modes become uncoupled from each other as the system matrices are symmetric in nature. The major drawback of this technique is that if the interface of substructure is changed, the entire reduction basis needs to be recomputed.

To overcome the problem faced in above techniques another revised reduction technique was introduced by O'Callaghan et al. (1989), known as SEREP (System Equivalent Reduction Expansion Process). SEREP provides improved accuracy for applications such as cross-orthogonality checks between computational and experimental modal vectors. O'Callaghan (1989) also introduced another technique which is called as Improved Reduced system (IRS). It is also a static condensation procedure and involves potential energy minimization. To take into account inertia effect, a supplemental factor is incorporated to the static reduction transformation by adjusting modal matrix. IRS does not require full system eigenvalue like SEREP. Few studies using IRS and balanced truncation model were done by Friswell et al. (1995, 1996, 2000) and Friswell and Inman (1999). In both methods, the transformation matrix is formed by the proper arrangement of masters and slave coordinates and used to reduce system matrix. Friswell et al. (1998) did several implementations for the improvement of IRS method and reintroduced a new technique known as Iterative Improved Reduction system (IIRS). An iterative algorithm is used to improve the transformation matrix by achieving convergence. Recently, Chandraker and Roy, (2014) implemented IIRS technique on the damped rotor bearing system, where both external and internal damping were considered. Due to consideration of internal damping, cross couple stiffness arises and system matrices become asymmetric. Das and Dutt, (2008, 2012) and Das (2009) introduced modified SEREP technique to reduce externally and internally damped rotor by taking into account both left and right modal matrices of the full model.

Another model order reduction technique is the Balanced Realization System (BRS). It can also be recognized as Balanced truncation technique and accomplished through Dynamic condensation process. Researchers like Pernebo and Silverman (1982), Fernando and Nicholson (1982), Saksena et al. (1984), Subbaiah et al. (1989) gave the clear idea about the balanced order reduction based on the stability of modes. The unstable modes are controlled with the use of weighted function or by system feedback control filters. Moore (1981), Liu and Anderson (1989), Al-Saggaf et al. (1993) presented the principal theory for the controllability and observability based on the Lyapunov stability criteria. Balance Realization System was utilized by Mohiuddin et al. (1998) to reduce a bulky model of damped rotor. A detailed explanation for most of the reduction techniques is available in Qu Z-Q (2004). The literature review by Matthew et al. (2010) showed different reduced model of rotor bearing system. The difficulty and success in several reduction techniques were reported here. Furthermore, Banner and Saak (2011) developed a reduced model for second order damped system of spindle by using BRS technique, where proportional damping was used to compute damping matrix. Some recent work by Zhang et al. (2015), where BRS technique was applied to nonstructural case.

Among other reduction technique, Han (2014) applied Kryov subspace method via moment matching to reduce the large-scale rotor. In this method, repeated dynamic simulation was done with the reduced system by changing the operating speed, which can be preserved as a parameter in the process of model reduction. Recently, Zghal et al. (2015), developed a reduced viscoelastic sandwich structures models, in which first order shear deformation theory (FSDT) along with Golla Hughes Mc Tavish (GHM) were applied. On the basis of different coordinate systems (i.e., physical coordinates, generalized coordinates and hybrid coordinates), different model order reduction techniques were applied. Primarily, Guyan reduction was applied to an undamped system and sub vector corresponds to slave degrees of freedom were further used to generate the transformation matrix for the dynamic reduction method.

Most of the research works are being noticed in the available literature indicating model reduction considering symmetric inertia matrices and symmetric stiffness matrices and analysis up to conventional second order system only. In state space representation, system matrices of the higher order model are fully populated due to the presence of a large number of states. It is difficult to derive explicit mass, damping, and stiffness matrices of the reduced model defined in the displacement state, which are very useful in many dynamic analyses. While implementing any reduction technique to the defined problem, one of the biggest challenge is to select the proper reduction technique that will generate an accurate result, which matches with the existing full model.

1.7 Objective and scope of present work

After substantial literature survey, it is seen that time domain model of generally viscoelastic rotor is insufficient. This leads to primary inspiration for the present research work.

By and large, every material is termed as viscoelastic as damping is inherent. Frequency domain model, which is done through complex modulus approach, is insufficient for Eigen analysis. In this regards, time domain model is compatible with transient as well as frequency response analysis. On the contrary, neither viscous nor hysteretic damping is accurate. Keeping these key factors, the present modelling is done through operator based constitutive relationship. Both numerator and denominator of modulus operator are polynomial of differential time operator and order of the polynomial varies from material to material. Polynomial coefficients are known as a viscoelastic parameter, and those are found from experimentally obtained values of storage modulus and loss factor.

In the present work, whole research concentrates on the modelling and studying the dynamics of axisymmetric rotor made of generally viscoelastic material. To achieve this, two types of approaches are taken 1) Classical model and 2) Finite Element model. Higher order equations of motion are derived by using Euler-Bernoulli beam theory. The important contribution of this dissertation is to generate skew symmetric stiffness matrix and damping matrix so that dissipation effect has been considered through all coordinates. While considering classical modelling, effective mass and effective diametral moment of inertia is evaluated for non-central loading situation. To obtain a comprehensive view on the dynamic characteristics of the system, a comparative study is done by using following parameters such as decay rate, campbell diagram, stability limit of spin-speed, unbalance frequency response, and also time response. This study is affirming the compatibility between two approaches with each other up to some extent.

Since modelling is dependent on the material property the development of models are being categorized as two distinct material viz. low and high damped material. In both cases, materials are assumed to be isotropic and modelling is done on single layer rotor. Later it has extended for composite material, where composite is formed by multi layering of those isotropic materials.

After perfect modelling it is necessary to study the actual dynamics of the rotor. For this modal analysis is the best tool to analyze dynamic behaviour. Here, a study has been done using modal analysis of higher order finite element model for a generally viscoelastic rotor supported by bearings. Both rolling and sliding contact bearings are used in this purpose. Gyroscopic couple, internal damping and fluid film forces of journal bearings have major asymmetric influences on rotor-dynamics. A complex modal coordinates create a platform to indicate the directivity of modes as well as the direction of whirl. In which, study of natural modes and directional frequency response function (dFRF) are obtained from free and force vibration analysis. Modal analysis also helps to distinguish the importance of higher order model over conventional second order model.

Based on the material behaviour, various models are achieved here. With substantial advantages of such modelling, some stumbling block appears at the time of computational simulation because of the higher order differential equation and due to heavy/bulky size of matrices. It is just not a problem of big matrices, but it generates a computational error due to presence of asymmetry. Therefore, it is necessary to impose the best reduction technique to reduce the size of model without distorting any dynamic characteristic. For the sake of finding the best methodology to reduce the higher order model, two different reduction techniques are used here, i.e. (a) Iterative Improved Reduction System (IIRS) and (b) Balanced Realization System (BRS). Under both these reduction procedures, a comparative study has been done, where model order reduction is examined for the different complex modal behaviour. Nice agreement between reduced and original system predict the usefulness of this study .

Absentia of these works in the field of modal analysis and model order reduction for the higher order system is the greatest motivation to take initiative in this direction.

The main objectives of the research work are as follows:

1) To develop the mathematical model of a rotor bearing system for isotropic and composite viscoelastic material using an operator based approach.
2) To design a formulation of model order reduction for the higher order system.

Several intermediate objectives lead to the achievement of the main objectives. These are:

i. To develop a method for the extraction of viscoelastic parameters for various materials using optimization technique.
ii. Two types of approaches, i.e., a) classical model and b) finite element model are used to develop the desired form of governing equation for the first objective.
iii. To derive the effective mass and effective diametral moment of inertia for non-central loading condition that is used in classical formulation.
iv. To express a generalized formulation for the estimation of stiffness coefficients of multi-disc rotor model.
v. To design a method for the modal characterization of higher order models that can be used to estimate the insight dynamic of the rotor bearing system.

vi. To perform a model order reduction in the higher order system to overcome the limitations of classical and finite element models.

1.8 Thesis layout

For the ease of presentation, present work is divided into the following chapters.

Chapter 1: Introduction

This chapter deals with general outlines about the research work. Further, the research motivation is provoked through relevant literature surveys, which reveals several important and interesting facts in this chapter. This also helps author to find scopes and overall conclusions.

Chapter 2: Modelling of viscoelastic rotor - isotropic material

In this chapter, firstly a constitutive relationship is developed for generally viscoelastic material using an operator based constitutive relationship. Continuing with classical and finite element approaches, higher order equations of motion are derived for viscoelastic isotropic single layer rotor. A comparative study between two models shows their effectiveness and limitation. After that modal analysis is used as a tool to explain the significance of higher order model over conventional second order model.

Chapter 3: Modelling of viscoelastic rotor - composite material

For better dynamic performance and to replace heavy and bulky rotors, an alternative hybrid material is proposed here. Composite material is only supplementary, which is done through multi-layering arrangement. Modelling has been done for generalized multi-layer, multi-disc viscoelastic rotor with the help of classical approach as well as finite element approach. The predicted dynamic behaviours from both approaches are used to validate the correctness of perfect modelling. Higher order differential equations are also established due to the different material properties present in distinct layers.

Chapter 4: Reduction of higher order models

In this chapter, higher order differential equations based on finite element formulation are firstly reduced with the help of state space representation. In state space representation, system matrices of the higher order model are fully populated due to the presence of a large number of states. It is difficult to derive explicit mass, damping, and stiffness matrices of the reduced model defined by the displacement state, which are very useful in many dynamic analysis. Thus a necessary reduction is done by keeping invariant dynamic properties. The primary focus of the research is to implement IIRS and BRS techniques for reducing the higher order asymmetric system. With respect to this, some comparative study is also carried out for both techniques to show their usefulness.

Chapter 5: Conclusions and future work

This chapter summarizes the basic conclusions arrived from this work and some subsequent work are presented.

Bibliography

A list of references is given.

Appendix

Appendix-A	Extraction of viscoelastic parameters
Appendix-B	Effective mass of a simply supported beam for non-central loading
Appendix-C	Stiffness coefficient of multi-disc rotor
Appendix-D	Different matrices in finite element approaches
Appendix-E	Coefficients of sliding contact bearing

Chapter-2

Modelling of Viscoelastic Rotors: Isotropic Material

2.1 Preamble

This chapter deals with the modelling of isotropic, linear viscoelastic rotor. In which two distinct approaches are used as follows.

- Classical Model (CM)
- Finite Element Model (FEM)

In the CM approach, the total mass is considered to be concentrated on a single point of the rotor where the disc is located and the remaining portion is assumed to be massless. Thus, it is also known as a lumped system approach. Whereas, in FE approach, rotor shaft is discretized into small finite elements to capture distributed effect of continuum and modelling is done on a single element. Later on, all elements are assembled to get the whole system behaviour.

2.2 Operator based constitutive relationship

By and large, every material is considered to be viscoelastic, unlike elastic materials, the strain produced in viscoelastic materials causes simultaneous energy storage and dissipation when subjected to dynamic loading. Here, stress at a point is not only proportional to strain, but in general the stress and its derivatives are proportional to strain and their derivatives; the

Hookean behaviour of a material, where stress is proportional to strain forms a special case of viscoelastic material.

For generally linear viscoelastic material, instantaneous stress (σ) is obtained by operating instantaneous strain (ε). Following Bland (1960), the generic form of constitutive relationship is written as,

$$\sigma = E(\ )\varepsilon \tag{2.1}$$

Here, $E(\ )$ is the modulus operator whose numerator and denominator are the functions of $'\mathrm{D}'$, where $'\mathrm{D}'$ is the differential time operator. The generic form of the modulus operator is given by

$$E(\ ) = \frac{\mathrm{Nu(D)}}{\mathrm{Dn(D)}} = \frac{\sum_{j=0}^{\mathrm{n_n}} a_j \mathrm{D}^j}{\sum_{j=0}^{\mathrm{n_d}} b_j \mathrm{D}^j} \tag{2.2}$$

where, subscripts 'n' and 'd' are used for numerator and denominator respectively, $'\mathrm{D}^j'$ indicates the j^{th} order of differentiation i.e. $\mathrm{D}^j = \dfrac{d^j(\ )}{dt^j}$., $'a_j'$ and $'b_j'$ are the polynomial coefficients present in numerator and denominator respectively.

According to the presence of damping the viscoelastic material is divided into two categories viz. low and high damped viscoelastic materials. For low damped material, lower order polynomial is used, whereas higher order polynomial is necessary to capture the frequency dependent behaviour of high damped material. Polynomial coefficients are also known as viscoelastic parameters and obtained from frequency-dependent storage modulus and loss factor by using any optimization tool or curve fitting technique, which is well explained in Appendix-A. The modulus operator and various viscoelastic parameters for various rheological models are given in Table 2.1.

Table 2.1 Various rheological models and modulus operator

Rheological Model	Operator	Coefficients
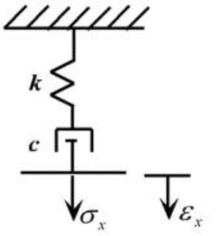 Fig. 2.1 (a) Maxwell model	$E(\ )=\dfrac{a_1\mathrm{D}}{b_0+b_1\mathrm{D}}$	$a_1=c, b_0=1, b_1=\dfrac{c}{k}$
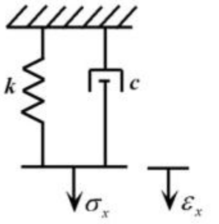 Fig. 2.1 (b) Kelvin-Voigt model	$E(\ )=a_0+a_1\mathrm{D}$	$a_0=k, a_1=c$
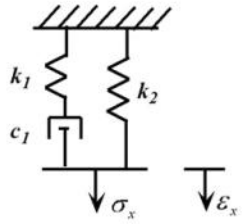 Fig. 2.1 (c) Three-element standard model	$E(\ )=\dfrac{a_0+a_1\mathrm{D}}{b_0+b_1\mathrm{D}}$	$a_0=k_2, a_1=c_1+\dfrac{k_2c_1}{k_1}$ $b_0=1, b_1=\dfrac{c_1}{k_1}$
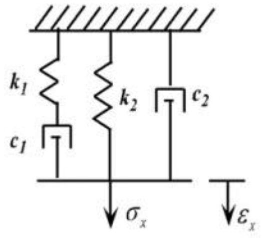 Fig. 2.1 (d) Four-element standard model	$E(\ )\dfrac{a_0+a_1\mathrm{D}+a_2\mathrm{D}^2}{b_0+b_1\mathrm{D}}$	$a_0=k_2, a_1=c_1+c_2+\dfrac{k_2c_1}{k_1}$ $a_2=\dfrac{c_1c_2}{k_1}, b_0=1, b_1=\dfrac{c_1}{k_1}$

From the Table 2.1 it is seen that the order of polynomial increases for different types of spring and dashpot arrangements. Therefore, it can be concluded that for low damped material simple Voigt and Zener models are sufficient to represent the constitutive relationship. But for high damped materials like polymers and polymeric composites, higher version network is used. In the present study two cases are carried out viz. low and high damped material. The expressions of modulus operator are procured by assuming a different polynomial order.

$$\text{if,}\quad n_n = 1 \text{ and } n_d = 1;\quad E(\ ) = \frac{a_0 + a_1 D}{b_0 + b_1 D} \tag{2.3(a)}$$

$$\text{if,}\quad n_n = 2 \text{ and } n_d = 1;\quad E(\ ) = \frac{a_0 + a_1 D + a_2 D^2}{b_0 + b_1 D} \tag{2.3(b)}$$

2.3 Classical approach

The classical approach is a traditional technique used to derive the equations of motion of rotor shaft system and studying the dynamics. The total mass is considered to be concentrated on a single point of the rotor where the disc is located and the remaining portion is assumed massless. A same assumption can be valid for the multi-disc rotor system. Therefore, if the rotor system is having N_d -disc, then at each disc location, the total mass is the sum of disc mass and the associated portion of shaft mass. Fig 2.2 shows the schematic diagram of a single layer, multi disc rotor bearing model.

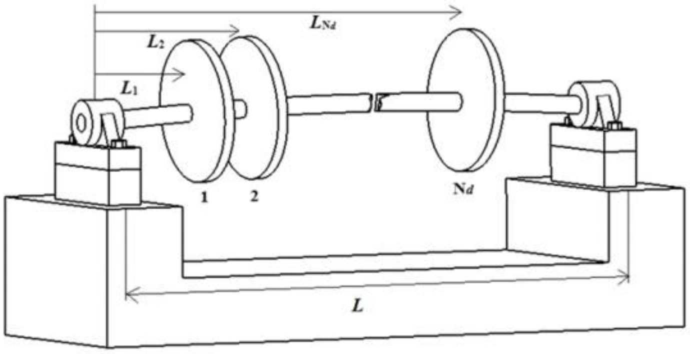

Fig. 2.2 Schematic diagram of multi-disc rotor bearing system

Fig. 2.3 indicates the cross sectional view of the deformed rotor-shaft of the radius. The instantaneous deflection of the shaft centre is denoted as '$R(x,t)$, whose components along 'y'

and 'z' direction are '$v(x,t)$' and '$w(x,t)$' , where 'x' and 't' are the spatial and temporal variables. These represent the shaft centre coordinates at any instant of time. For further analysis, a small radial element of thickness 'dr', and subtending angle '$d\Omega t$' , at an angular location 'Ωt' and 'r' distance from centre, is considered. Here, 'ω'and 'Ω'are termed as whirl and spin frequencies of rotor respectively.

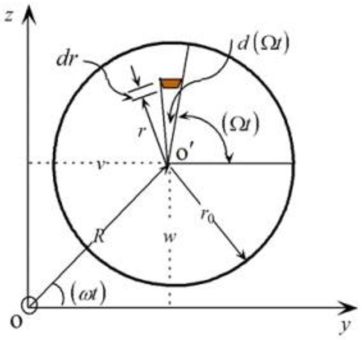

Fig. 2.3 Cross-sectional view of deformed rotor

A rotating frame of reference as shown in Fig. (2.4) has been considered to capture damping force exerted by the rotating parts. Rotating frame rotates with same speed of rotor (Ω) and about an axis passing through the origin of stationary frame. For a constant rotational speed, at any instant of time 't', angle between two frames is 'Ωt'. The coordinates in rotating frame are expressed with '$\sim$'.

Following Tondl (1965) and Thomson et al. (2012), expression of potential energy 'V' for 'N_d' disc rotor in a rotating frame of reference is given below.

$$V = \frac{1}{2}\{\tilde{\mathbf{q}}\}^T\left[\mathbf{C}_{ij}\right]\{\tilde{\mathbf{q}}\} \qquad i, j = 1, 2, \ldots, 4\mathrm{N}_d \tag{2.4}$$

where, $\left[\mathbf{C}_{ij}\right]$ is stiffness matrix, the expression of various stiffness coefficients of the shaft are available in Appendix-C. The generalized coordinate, $\{\tilde{\mathbf{q}}\}$ is written as $\{\tilde{\mathbf{q}}\} = \left\{\tilde{v}_1 \quad \tilde{\varphi}_1 \quad \tilde{w}_1 \quad \tilde{\vartheta}_1 \quad \cdots \quad \tilde{v}_{\mathrm{N}_d} \quad \tilde{\varphi}_{\mathrm{N}_d} \quad \tilde{w}_{\mathrm{N}_d} \quad \tilde{\vartheta}_{\mathrm{N}_d}\right\}^T$. In which, $(\tilde{v}),(\tilde{w})$ and $(\tilde{\varphi}),(\tilde{\vartheta})$ are the lateral and angular deformations along and about '$\tilde{y}$' and '$\tilde{z}$' direction respectively.

Lagrange's equation is employed to the potential energy expression to obtain expression of force. Using complex coordinate, force vector $\{\tilde{\mathbf{F}}\}$ in a rotating frame of reference is given as,

$$\begin{aligned}\{\tilde{\mathbf{F}}\}_{(2\mathrm{N}_d\times 1)} &= \left[\mathbf{C}_{ij}\right]\{\tilde{\mathbf{x}}_i\} \\ &= EI\left[\mathbf{K}_{ij}\right]\{\tilde{\mathbf{x}}_i\} \qquad i,j=1,2,\ldots,2\mathrm{N}_d\end{aligned} \tag{2.5}$$

$'E'$ is material modulus, $'I'$ is area moment of inertia, and $\{\tilde{x}_i\}$ is the complex coordinate, viz. $\tilde{\mathbf{x}}_{(2\mathrm{N}_d-1)}=\tilde{v}_{\mathrm{N}_d}+i\tilde{w}_{\mathrm{N}_d}$, $\tilde{\mathbf{x}}_{2\mathrm{N}_d}=\tilde{\varphi}_{\mathrm{N}_d}+i\tilde{\vartheta}_{\mathrm{N}_d}$. $'i'$ is imaginary unit, $i=\sqrt{-1}$. The indices (*i, j*) are dropped in subsequent analysis for convenience.

The coordinates in rotating frames can be transformed to stationary frame and are written in Eq. (2.6). Though this transformation is developed by looking at displacements and forces in $'y'$ and $'z'$ direction, but same transformation is used for rotations and moments about $'y'$ and $'z'$ axis (Friswell et al. (2010b)). This is possible due to the fact that the generalized force expressed in Eq. (2.5) contains the components of force and moment along $\tilde{y}$ and $\tilde{z}$ directions. So these components can be coupled by using complex coordinates. Though physically coupling two angles $\tilde{\varphi}$ and $\tilde{\vartheta}$ does not mean anything as angles are not vectorial quantities. This is done for a mathematical purpose.

$$\{\tilde{\mathbf{x}}\}=\{\mathbf{x}\}\mathrm{e}^{-i\Omega t} \tag{2.6}$$

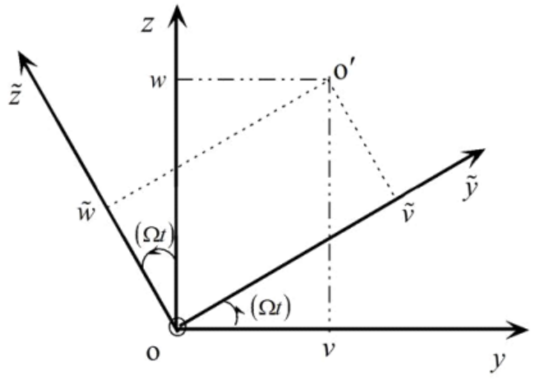

Fig. 2.4 Rotating and stationary coordinate systems

If material damping in rotor shaft is considered, Young's modulus E in Eq. (2.5) is replaced by the modulus operator from Eq. (2.3) and the reformed equations are

$$\text{For } n_n = 1,\ \left\{\tilde{\mathbf{F}}\right\}_{(2\mathrm{N}_d\times 1)} = \left(\frac{a_0 + a_1\mathrm{D}}{b_0 + b_1\mathrm{D}}\right)[\mathbf{K}]\{x\}\,\mathrm{e}^{-i\Omega t}, \qquad (2.7(a))$$

$$\text{For } n_n = 2,\ \left\{\tilde{\mathbf{F}}\right\}_{(2\mathrm{N}_d\times 1)} = \left(\frac{a_0 + a_1\mathrm{D} + a_2\mathrm{D}^2}{b_0 + b_1\mathrm{D}}\right)[\mathbf{K}]\{x\}\,\mathrm{e}^{-i\Omega t}, \qquad (2.7(b))$$

This differential time operator only operates on complex coordinates and exponential term while other terms remain as it is because they are independent of time quantity. After differentiating with time operator, the above equation is again written as ,

$$\begin{aligned}\text{For } n_n = 1,\ \left\{\tilde{\mathbf{F}}\right\}_{(2\mathrm{N}_d\times 1)} &= \left(\frac{1}{b_0 + b_1\mathrm{D}}\right)\Big(\left(a_0 - i\Omega a_1\right)[\mathbf{K}]\{x\} + a_1[\mathbf{K}]\{\dot{x}\}\Big)\mathrm{e}^{-i\Omega t} \\ &= \{\mathbf{F}\}\,\mathrm{e}^{-i\Omega t}\end{aligned} \qquad (2.8(a))$$

$$\begin{aligned}\text{For } n_n = 2,\ \left\{\tilde{\mathbf{F}}\right\}_{(2\mathrm{N}_d\times 1)} &= \left(\frac{1}{b_0 + b_1\mathrm{D}}\right)\left(\begin{aligned}&\left(a_0 - \Omega^2 a_2\right)[\mathbf{K}]\{x\} + a_1(-i\Omega)[\mathbf{K}]\{x\} + a_1[\mathbf{K}]\{\dot{x}\} \\ &\qquad + 2a_2(-i\Omega)[\mathbf{K}]\{\dot{x}\} + a_2[\mathbf{K}]\{\ddot{x}\}\end{aligned}\right)\mathrm{e}^{-i\Omega t} \\ &= \{\mathbf{F}\}\,\mathrm{e}^{-i\Omega t}\end{aligned} \qquad (2.8(b))$$

$\{\mathbf{F}\}$ is the generalized force due to stiffness and rotating damping measured in stationary frame. Rearranging the complex coordinate $\{x\}$ with its original coordinate $\{\mathbf{q}\}$, the force vector is written in a simplified form as,

$$\text{For } n_n = 1,\ \{\mathbf{F}\}_{(4\mathrm{N}_d\times 1)} = \left(\frac{1}{b_0 + b_1\mathrm{D}}\right)\left[a_0\left[\mathbf{K}_B\right]\{\mathbf{q}\} + a_1\Omega\left[\mathbf{K}_C\right]\{\mathbf{q}\} + a_1\left[\mathbf{K}_B\right]\{\dot{\mathbf{q}}\}\right] \qquad (2.9(a))$$

$$\text{For } n_n = 2,\ \{\mathbf{F}\}_{(4\mathrm{N}_d\times 1)} = \left(\frac{1}{b_0 + b_1\mathrm{D}}\right)\left[\begin{aligned}&\left(a_0 - \Omega^2 a_2\right)\left[\mathbf{K}_B\right]\{\mathbf{q}\} + a_1\Omega\left[\mathbf{K}_C\right]\{\mathbf{q}\} + a_1\left[\mathbf{K}_B\right]\{\dot{\mathbf{q}}\} \\ &\qquad + 2a_2\left[\mathbf{K}_C\right]\{\dot{\mathbf{q}}\} + a_2\left[\mathbf{K}_B\right]\{\ddot{\mathbf{q}}\}\end{aligned}\right] \qquad (2.9(b))$$

where, $\left[\mathbf{K}_B\right]$ is the bending stiffness matrix and $\left[\mathbf{K}_C\right]$ is the skew symmetric circulatory matrix, their expression are given in Appendix-C. All three matrices, viz. damping matrix, bending stiffness matrix and circulatory matrix, are developed from stiffness matrix. As stiffness matrix covers all coordinates, dissipation effects are taken care through all coordinates.

Equation of motion is obtained by adding this force with all other forces, viz. forces from kinetic energy and external force, and is given below.

$$[\mathbf{M}]\{\ddot{\mathbf{q}}\}+[\mathbf{G}]\{\dot{\mathbf{q}}\}+\{\mathbf{F}\}=[\mathbf{P}]\{\boldsymbol{u}\} \tag{2.10}$$

In the preceding equation, $\{\boldsymbol{u}\}$ is the force vector originates due to some external disturbances, $[\mathbf{P}]$ defines the appropriate position of external forces, whose number of columns indicate the total disturbances and elements are chosen either zero or one to distribute the forces at the correct location. $[\mathbf{M}]$ is the symmetric mass matrix and $[\mathbf{G}]$ is the skew symmetric gyroscopic matrix.

After operating the operand in denominator with other terms in Eq. (2.11), final equation of motion of the multi-disc isotropic viscoelastic rotor, rotating at constant angular speed is written as:

$$\begin{aligned}[][\mathbf{A}_0]_{(4\mathrm{N}_d\times 4\mathrm{N}_d)}\{\mathbf{q}\}_{(4\mathrm{N}_d\times 1)}+[\mathbf{A}_1]_{(4\mathrm{N}_d\times 4\mathrm{N}_d)}\{\dot{\mathbf{q}}\}_{(4\mathrm{N}_d\times 1)}+[\mathbf{A}_2]_{(4\mathrm{N}_d\times 4\mathrm{N}_d)}\{\ddot{\mathbf{q}}\}_{(4\mathrm{N}_d\times 1)}\\ +[\mathbf{A}_3]_{(4\mathrm{N}_d\times 4\mathrm{N}_d)}\{\dddot{\mathbf{q}}\}_{(4\mathrm{N}_d\times 1)}=[\mathbf{B}]_{(4\mathrm{N}_d\times r)}\{\boldsymbol{u}\}_{(r\times 1)}\end{aligned} \tag{2.11}$$

The preceding equation shows the equations of motion of a damped rotor, where the rotor shaft is made of either low or high damped material. The coefficients in Eq. (2.11), are elaborated as follows.

For low damped viscoelastic material ($\mathrm{n}_\mathrm{n}=1$, $\mathrm{n}_\mathrm{d}=1$):

$$[\mathbf{A}_0]_{(4\mathrm{N}_d\times 4\mathrm{N}_d)}=(a_0)[\mathbf{K}_B]+\Omega(a_1)[\mathbf{K}_C],$$

$$[\mathbf{A}_1]_{(4\mathrm{N}_d\times 4\mathrm{N}_d)}=(b_0)[\mathbf{G}]+(a_1)[\mathbf{K}_B],$$

$$[\mathbf{A}_2]_{(4\mathrm{N}_d\times 4\mathrm{N}_d)}=(b_0)[\mathbf{M}]+(b_1)[\mathbf{G}],$$

$$[\mathbf{A}_3]_{(4\mathrm{N}_d\times 4\mathrm{N}_d)}=(b_1)[\mathbf{M}],$$

$[\mathbf{B}]_{(4\mathrm{N}_d\times r)}=(b_0+b_1\mathrm{D})[\mathbf{P}]$, '$r$' is the number of inputs.

For high damped viscoelastic material ($\mathrm{n}_\mathrm{n}=2$, $\mathrm{n}_\mathrm{d}=1$):

$$[\mathbf{A}_0]_{(4\mathrm{N}_d\times 4\mathrm{N}_d)}=(a_0-a_2\Omega^2)[\mathbf{K}_B]+\Omega(a_1)[\mathbf{K}_C],$$

$$[\mathbf{A}_1]_{(4\mathrm{N}_d\times 4\mathrm{N}_d)}=(b_0)[\mathbf{G}]+(a_1)[\mathbf{K}_B]+2\Omega(a_2)[\mathbf{K}_C],$$

$$\left[\mathbf{A}_2\right]_{\left(4\mathrm{N}_d\times 4\mathrm{N}_d\right)}=\left(b_0\right)[\mathbf{M}]+\left(b_1\right)[\mathbf{G}]+\left(a_2\right)\left[\mathbf{K}_B\right],$$

$$\left[\mathbf{A}_3\right]_{\left(4\mathrm{N}_d\times 4\mathrm{N}_d\right)}=\left(b_1\right)[\mathbf{M}],$$

$[\mathbf{B}]_{\left(4\mathrm{N}_d\times r\right)}=\left(b_0+b_1\mathrm{D}\right)[\mathbf{P}]$, '$r$' is the number of inputs.

Here, $\{\mathbf{q}\}_{\left(4\mathrm{N}_d\times 1\right)}$ is total degree of freedom and its size depends on the number of disc 'N_d'. The significance of using classical approach to develop the equation of motion is that the size of the matrices is very small, i.e. $\left(4\mathrm{N}_d\times 4\mathrm{N}_d\right)$.

The above expressions are valid for the generalized single layer, multi-disc rotor shaft system. But, some important points are to be remembered while implementing this model for solving the numerical problems. In the present context, two sets of numerical problem are considered, i.e., simply supported rotor shaft mounted with single and double disc. In first case, for non-central location of disc the loading point is not at centre. Due to this reason it is inappropriate to use the expression of Rayleigh effective mass $\left(0.4857M_r\right)$. Therefore, it is necessary to derive the expression for effective mass $\left(M_{r_{eff}}\right)$ and effective diametral moment of inertia $\left(J_{D_{r_{eff}}}\right)$ of the rotor shaft for non-central loading condition. These expressions are solely derived in Appendix-B and are further used to form the mass and gyroscopic matrices. The expressions of various matrices (mass, gyroscopic, bending and circulatory stiffness) for the multi disc rotor are well explained in Appendix-C.

2.4 Finite element approach

Finite element method is used to take care the distributed effect of continuum. In this approach, rotor shaft is discretized into small finite elements and modelling is done on a single element. Later assembling of all elements to form global matrices that capture the whole system behaviour. The rotor is discretized using Euler Bernoulli beam theory. The shear deformation effect can easily be added, however the same has been discarded at present for the sake of simplicity. The elemental length 'l' of a beam with nodal displacement variables is presented in Fig. 2.5. Forces due to bending action are obtained first. Ordinary differential equation of motion is developed by incorporating this force to other forces like inertia force and force due to gyroscopic action Zorzi and Nelson (1977).

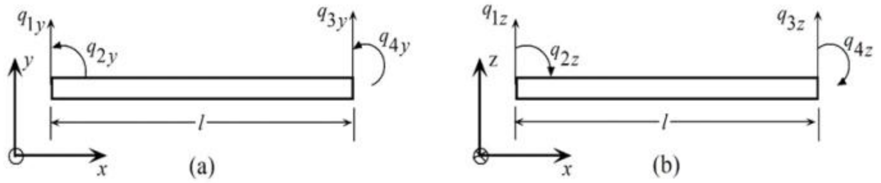

Fig. 2.5 Nodal displacement of a beam element in two coordinate plane

Let σ_x and ε_x denote respectively the dynamic normal mechanical stress and strain induced in the infinitesimal element at the t^{th} instant of time. Zorzi and Nelson (1977) expressed the mechanical strain in the 'x' direction, which is along the length of the shaft as

$$\varepsilon_x = -r\cos\left[(\Omega-\omega)t\right]\frac{\partial^2 R(x,t)}{\partial x^2} \tag{2.12}$$

$R(x,t)$ is the instantaneous deflection of the shaft center. At any instant of time, the bending moments 'M_{yy}' and 'M_{zz}' about 'y' and 'z' axes are as follows:

$$\begin{aligned} M_{zz} &= \int_0^{2\pi}\int_0^{r_o} -\left(v + r\cos(\Omega t)\right)\sigma_x r dr d(\Omega t) \\ M_{yy} &= \int_0^{2\pi}\int_0^{r_o} \left(w + r\sin(\Omega t)\right)\sigma_x r dr d(\Omega t) \end{aligned} \tag{2.13}$$

The expression of 'σ_x' from Eq. (2.1) is substituted in Eq. (2.13). Later, substituting the expressions of $E(\ )$ and 'ε_x' given in Eq. (2.3) and Eq. (2.12), the bending moment expressions are rewritten as.

For low damped material ($\mathrm{n}_{\mathrm{n}} = 1$),

$$\begin{aligned} M_{zz} &= \int_0^{2\pi}\int_0^{r_o} -\left(v + r\cos(\Omega t)\right)\left(\frac{a_0 + a_1\mathrm{D}}{b_0 + b_1\mathrm{D}}\right)\left[-r\cos(\Omega t - \omega t)\frac{\partial^2 R(x,t)}{\partial x^2}\right] r dr d(\Omega t) \\ M_{yy} &= \int_0^{2\pi}\int_0^{r_o} \left(w + r\sin(\Omega t)\right)\left(\frac{a_0 + a_1\mathrm{D}}{b_0 + b_1\mathrm{D}}\right)\left[-r\cos(\Omega t - \omega t)\frac{\partial^2 R(x,t)}{\partial x^2}\right] r dr d(\Omega t) \end{aligned} \tag{2.14(a)}$$

For high damped material ($\mathrm{n}_{\mathrm{n}} = 2$),

$$M_{zz} = \int_0^{2\pi}\int_0^{r_o} -\left(v + r\cos(\Omega t)\right)\left(\frac{a_0 + a_1\mathrm{D} + a_2\mathrm{D}^2}{b_0 + b_1\mathrm{D}}\right)\left[-r\cos(\Omega t - \omega t)\frac{\partial^2 R(x,t)}{\partial x^2}\right] r dr d(\Omega t)$$

$$M_{yy} = \int_0^{2\pi}\int_0^{r_o} \left(w + r\sin(\Omega t)\right)\left(\frac{a_0 + a_1\mathrm{D} + a_2\mathrm{D}^2}{b_0 + b_1\mathrm{D}}\right)\left[-r\cos(\Omega t - \omega t)\frac{\partial^2 R(x,t)}{\partial x^2}\right] r dr d(\Omega t) \qquad (2.14(b))$$

After simplifying the above Eq. (2.14), that can be written as

For $\mathrm{n}_{\mathrm{n}} = 1$,

$$M_{zz} = \left(\frac{1}{b_0 + b_1\mathrm{D}}\right)\int_0^{2\pi}\int_0^{r_o} r^2\left(v + r\cos\Omega t\right)[a_0\cos(\Omega t - \omega t)\frac{\partial^2 R}{\partial x^2} + a_1\cos(\Omega t - \omega t)\frac{\partial^3 R}{\partial x^2 \partial t}$$
$$- a_1(\Omega - \omega)\sin(\Omega t - \omega t)\frac{\partial^2 R}{\partial x^2}] dr d(\Omega t) \qquad (2.15(a))$$

$$M_{yy} = -\left(\frac{1}{b_0 + b_1\mathrm{D}}\right)\int_0^{2\pi}\int_0^{r_o} r^2\left(w + r\sin\Omega t\right)[a_0\cos(\Omega t - \omega t)\frac{\partial^2 R}{\partial x^2} + a_1\cos(\Omega t - \omega t)\frac{\partial^3 R}{\partial x^2 \partial t}$$
$$- a_1(\Omega - \omega)\sin(\Omega t - \omega t)\frac{\partial^2 R}{\partial x^2}] dr d(\Omega t)$$

For $\mathrm{n}_{\mathrm{n}} = 2$,

$$M_{zz} = \left(\frac{1}{b_0 + b_1\mathrm{D}}\right)\int_0^{2\pi}\int_0^{r_o} r^2\left(v + r\cos\Omega t\right)[a_0\cos(\Omega t - \omega t)\frac{\partial^2 R}{\partial x^2} + a_1\cos(\Omega t - \omega t)\frac{\partial^3 R}{\partial x^2 \partial t}$$
$$- a_1(\Omega - \omega)\sin(\Omega t - \omega t)\frac{\partial^2 R}{\partial x^2} + a_2\cos(\Omega t - \omega t)\frac{\partial^4 R}{\partial x^2 \partial t^2}$$
$$- 2a_2(\Omega - \omega)\sin(\Omega t - \omega t)\frac{\partial^3 R}{\partial x^2 \partial t} - a_2(\Omega - \omega)^2 cos(\Omega t - \omega t)\frac{\partial^2 R}{\partial x^2}] dr d(\Omega t) \qquad (2.15(b))$$

$$M_{yy} = -\left(\frac{1}{b_0 + b_1\mathrm{D}}\right)\int_0^{2\pi}\int_0^{r_o} r^2\left(w + r\sin\Omega t\right)[a_0\cos(\Omega t - \omega t)\frac{\partial^2 R}{\partial x^2} + a_1\cos(\Omega t - \omega t)\frac{\partial^3 R}{\partial x^2 \partial t}$$
$$- a_1(\Omega - \omega)\sin(\Omega t - \omega t)\frac{\partial^2 R}{\partial x^2} + a_2\cos(\Omega t - \omega t)\frac{\partial^4 R}{\partial x^2 \partial t^2}$$
$$- 2a_2(\Omega - \omega)\sin(\Omega t - \omega t)\frac{\partial^3 R}{\partial x^2 \partial t} - -a_2(\Omega - \omega)^2 cos(\Omega t - \omega t)\frac{\partial^2 R}{\partial x^2}] dr d(\Omega t)$$

After integrating Eq. (2.15), the bending moment expressions are again written as.

For $\mathrm{n}_{\mathrm{n}} = 1$,

$$M_{zz} = \left(\frac{I}{b_0 + b_1\mathrm{D}}\right)[a_0 v'' + a_1\dot{v}'' + \Omega a_1 w'']$$
$$M_{yy} = -\left(\frac{I}{b_0 + b_1\mathrm{D}}\right)[a_0 w'' + a_1\dot{w}'' - \Omega a_1 v''] \qquad (2.16(a))$$

For $\mathrm{n}_\mathrm{n} = 2$,

$$\begin{aligned} M_{zz} &= \left(\frac{I}{b_0 + b_1 \mathrm{D}}\right)[a_0 v'' + a_1 \dot{v}'' + \Omega a_1 w'' + a_2 \ddot{v}'' + 2\Omega a_2 \dot{w}'' - \Omega^2 a_2 v''] \\ M_{yy} &= -\left(\frac{I}{b_0 + b_1 \mathrm{D}}\right)[a_0 w'' + a_1 \dot{w}'' - \Omega a_1 v'' + a_2 \ddot{w}'' - 2\Omega a_2 \dot{v}'' - \Omega^2 a_2 w''] \end{aligned} \tag{2.16(b)}$$

where, area moment of inertia is given by $I = \int_A y^2 dA$, the symbols '.' and ''' (dot and prime over a variable) denote single differentiation with respect to time 't' and space 'x' respectively. The above Eq. (2.16) are rearranged in matrix form.

For $\mathrm{n}_\mathrm{n} = 1$,

$$\begin{Bmatrix} M_{zz} \\ M_{yy} \end{Bmatrix} = \left(\frac{I}{b_0 + b_1 \mathrm{D}}\right)\left(\begin{bmatrix} a_0 & a_1\Omega \\ a_1\Omega & -a_0 \end{bmatrix}\begin{Bmatrix} v'' \\ w'' \end{Bmatrix} + \begin{bmatrix} a_1 & 0 \\ 0 & -a_1 \end{bmatrix}\begin{Bmatrix} \dot{v}'' \\ \dot{w}'' \end{Bmatrix}\right) \tag{2.17(a)}$$

For $\mathrm{n}_\mathrm{n} = 2$,

$$\begin{Bmatrix} M_{zz} \\ M_{yy} \end{Bmatrix} = \left(\frac{I}{b_0 + b_1 \mathrm{D}}\right)\left(\begin{aligned} &\begin{bmatrix} (a_0 - a_2\Omega^2) & a_1\Omega \\ a_1\Omega & (-a_0 + a_2\Omega^2) \end{bmatrix}\begin{Bmatrix} v'' \\ w'' \end{Bmatrix} + \begin{bmatrix} a_1 & 2a_2\Omega \\ 2a_2\Omega & -a_1 \end{bmatrix}\begin{Bmatrix} \dot{v}'' \\ \dot{w}'' \end{Bmatrix} \\ &+ \begin{bmatrix} a_2 & 0 \\ 0 & -a_2 \end{bmatrix}\begin{Bmatrix} \ddot{v}'' \\ \ddot{w}'' \end{Bmatrix} \end{aligned}\right) \tag{2.17(b)}$$

2- noded beam element is used to discretize the rotor. In which two displacements ($v(x,t)$ and $w(x,t)$) and two slopes ($\varphi(x,t)$ and $\vartheta(x,t)$) along and about 'y' and 'z' axes are the four degrees of freedom per node.

$$\begin{Bmatrix} v \\ w \end{Bmatrix} = [\boldsymbol{\phi}(x)]^T\{\mathbf{q}(t)\}; \quad \varphi = -\frac{\partial w}{\partial x}; \quad \vartheta = \frac{\partial v}{\partial x} \tag{2.18}$$

where, $\{\mathbf{q}(t)\}$ is the nodal displacement vector and $\boldsymbol{\phi}(x)$ is Hermite shape function.

The bending moment expression also helps to find the three common matrices (viz. stiffness, circulatory and damping matrices) of any rotating system. The diagonal elements of bending moment expression give rise to direct elements (e.g. direct stiffness, direct damping matrix) whereas the off-diagonal elements give rise to cross coupled elements i.e. circulatory matrix. The total bending energy is obtained after integrating the differential bending energy $\left(dP_B^e = \frac{1}{2}\begin{Bmatrix} \vartheta' \\ \varphi' \end{Bmatrix}^T \begin{Bmatrix} M_{zz} \\ M_{yy} \end{Bmatrix}\right)$ over elemental length. This contains the strain energy and dissipation function, and is expressed as:

$$P_B^e = \frac{1}{2}\int_0^l \begin{Bmatrix} v'' \\ -w'' \end{Bmatrix}^T \begin{Bmatrix} M_{zz} \\ M_{yy} \end{Bmatrix} dx \tag{2.19}$$

Putting the terms of Eq. (2.17) and Eq. (2.18) in Eq. (2.19), and Lagrangian concept is applied to obtain generalized force, which is expressed in terms of nodal displacement vector and time derivatives. The generalized force vector in $'xy'$ and $'xz'$ plane are givens as:

For $\mathrm{n}_{\mathrm{n}} = 1$,

$$\{\mathbf{F}\} = \begin{Bmatrix} \{\mathbf{F}_{xy}\} \\ \{\mathbf{F}_{zx}\} \end{Bmatrix} = \left(\frac{I}{b_0 + b_1\mathrm{D}}\right)\left(a_0\left[\mathbf{K}_B\right]\{\mathbf{q}\} + \Omega a_1\left[\mathbf{K}_C\right]\{\mathbf{q}\} + a_1\left[\mathbf{K}_B\right]\{\dot{\mathbf{q}}\}\right) \tag{2.20(a)}$$

For $\mathrm{n}_{\mathrm{n}} = 2$,

$$\{\mathbf{F}\} = \begin{Bmatrix} \{\mathbf{F}_{xy}\} \\ \{\mathbf{F}_{zx}\} \end{Bmatrix} = \left(\frac{I}{b_0 + b_1\mathrm{D}}\right)\begin{pmatrix} (a_0 - a_2\Omega^2)\left[\mathbf{K}_B\right]\{q\} + a_1\Omega\left[\mathbf{K}_C\right]\{q\} + a_1\left[\mathbf{K}_B\right]\{\dot{q}\} \\ + 2a_2\Omega\left[\mathbf{K}_C\right]\{\dot{q}\} + a_2\left[\mathbf{K}_B\right]\{\ddot{q}\} \end{pmatrix} \tag{2.20(b)}$$

The expression of $\left[\mathbf{K}_B\right]$ and $\left[\mathbf{K}_C\right]$ are given as

$\left[\mathbf{K}_B\right] = \int_0^l \left[\boldsymbol{\phi}''(x)\right]\left[\boldsymbol{\phi}''(x)\right]^T dx,$ and $\left[\mathbf{K}_C\right] = \int_0^l \left[\boldsymbol{\phi}''(x)\right]\begin{bmatrix} 0 & 1 \\ -1 & 0 \end{bmatrix}\left[\boldsymbol{\phi}''(x)\right]^T dx$ in which, Hermite shape function matrix is given as $\left[\boldsymbol{\phi}(x)\right] = \begin{bmatrix} \{\boldsymbol{\phi}_{xy}(x)\} & \{0\} \\ \{0\} & \{\boldsymbol{\phi}_{zx}(x)\} \end{bmatrix}$ (refer to Rao (2009)) with subscripts in the elements showing the respective planes. The Hermite shape function expressions of 2- noded beam element are shown in Appendix-D.

Following Rao (2009), inertia force and force due to gyroscopic couple are obtained after utilizing kinetic energy expression. These forces are incorporated with the above generalized force to get the equation of motion for generally viscoelastic rotor.

$$[\mathbf{M}]\{\ddot{\mathbf{q}}\} + [\mathbf{G}]\{\dot{\mathbf{q}}\} + \{\mathbf{F}\} = [\mathbf{P}]\{\boldsymbol{u}\} \tag{2.21}$$

In the preceding equation, $\{\boldsymbol{u}\}$ is the force vector originates due to some external disturbances, $[\mathbf{P}]$ defines the nodal position of external forces, whose number of columns indicate the total disturbances and elements are chosen either zero or one to distribute the forces at various desired nodal locations. The mass matrix is given as, $[\mathbf{M}]_{(8\times8)} = \left[\mathbf{M}_T\right]_{(8\times8)} + \left[\mathbf{M}_R\right]_{(8\times8)}$, where, $\left[\mathbf{M}_T\right]_{(8\times8)}$ and $\left[\mathbf{M}_R\right]_{(8\times8)}$ are translational and rotary inertia matrix respectively. $[\mathbf{G}]_{(8\times 8)}$ is the gyroscopic matrix. Following Rao (2009), these expressions are given as:

$$[\mathbf{M}_T]=\int_0^l \rho A\boldsymbol{\phi}(x)\boldsymbol{\phi}(x)^T\,dx,$$

$$[\mathbf{M}_R]=\int_0^l \rho I\boldsymbol{\phi}'(x)\boldsymbol{\phi}'(x)^T\,dx,$$

$$[\mathbf{G}]=\int_0^l 2\rho I\Omega\boldsymbol{\phi}'(x)\begin{bmatrix}0 & 1\\ -1 & 0\end{bmatrix}\boldsymbol{\phi}'(x)^T\,dx,$$

After operating the operand, the final form of governing differential equation of the full model at constant angular speed is written as:

$$[\mathbf{A}_0]_{n\times n}\{\mathbf{q}\}_{n\times 1}+[\mathbf{A}_1]_{n\times n}\{\dot{\mathbf{q}}\}_{n\times 1}+[\mathbf{A}_2]_{n\times n}\{\ddot{\mathbf{q}}\}_{n\times 1}+[\mathbf{A}_3]_{n\times n}\{\dddot{\mathbf{q}}\}_{n\times 1}=[\mathbf{B}]_{n\times r}\{\boldsymbol{u}\}_{r\times 1} \tag{2.22}$$

Therefore, for low damped viscoelastic material ($\mathfrak{n}_\mathrm{n}=1,\ \mathfrak{n}_\mathrm{d}=1$):

$$[\mathbf{A}_0]_{n\times n}=(a_0)[\mathbf{K}_B]_{n\times n}+\Omega(a_1)[\mathbf{K}_C]_{n\times n},$$

$$[\mathbf{A}_1]_{n\times n}=(b_0)[\mathbf{G}]_{n\times n}+(a_1)[\mathbf{K}_B]_{n\times n},$$

$$[\mathbf{A}_2]_{n\times n}=(b_0)[\mathbf{M}]_{n\times n}+(b_1)[\mathbf{G}]_{n\times n},$$

$$[\mathbf{A}_3]_{n\times n}=(b_1)[\mathbf{M}]_{n\times n},$$

$$[\mathbf{B}]_{n\times r}=(b_0+b_1\mathrm{D})[\mathbf{P}]_{n\times r},$$

$\{\mathbf{q}\}_{n\times 1}=\{v_1\ \ \varphi_1\ \ w_1\ \ \vartheta_1\ \ \cdots\ \ v_{\mathcal{N}}\ \ \varphi_{\mathcal{N}}\ \ w_{\mathcal{N}}\ \ \vartheta_{\mathcal{N}}\}^T$, '$\mathcal{N}$' is the total number of nodes.

Similarly, for high damped material ($\mathfrak{n}_\mathrm{n}=2,\ \mathfrak{n}_\mathrm{d}=1$):

$$[\mathbf{A}_0]_{n\times n}=(a_0-a_2\Omega^2)[\mathbf{K}_B]_{n\times n}+\Omega(a_1)[\mathbf{K}_C]_{n\times n},$$

$$[\mathbf{A}_1]_{n\times n}=(b_0)[\mathbf{G}]_{n\times n}+(a_1)[\mathbf{K}_B]_{n\times n}+2\Omega(a_2)[\mathbf{K}_C]_{n\times n},$$

$$[\mathbf{A}_2]_{n\times n}=(b_0)[\mathbf{M}]_{n\times n}+(b_1)[\mathbf{G}]_{n\times n}+(a_2)[\mathbf{K}_B]_{n\times n},$$

$\left[\mathbf{A}_3\right]_{n\times n} = \left(b_1\right)\left[\mathbf{M}\right]_{n\times n}$,

$\left[\mathbf{B}\right]_{n\times r} = \left(b_0 + b_1\mathrm{D}\right)\left[\mathbf{P}\right]$, '$r$' is the number of inputs.

With keen observation, it is noted that the order of the equation depends on the viscoelastic material model. 'n' is the total degree of freedom. The associated mass, gyroscopic and stiffness matrices are shown in Appendix-D.

2.5 Incorporation of disc effect

For a rotor disc system, inclusion of disc effect is done separately. The disc is assumed to be a rigid body and its mobility is similar to the shaft mobility at the disc location. In classical model, the shaft continuum behaviour is considered to accumulate on various disc locations. Whereas in finite element model the shaft is discretized with finite number of elements and discs are located at different nodal positions. Assuming N_d discs are mounted on the shaft, the total degrees of freedom of all discs are $4\mathrm{N}_d$.

The disc effects are accounted through mass and gyroscopic matrix, which are calculated using kinetic energy expression. Following Lalanne and Ferraris (1998), the equation of motion in complex coordinates for N_d disc is written as.

$$\left[\mathbf{M}_d\right]\left\{\ddot{\mathbf{x}}\right\} + \left[\mathbf{G}_d\right]\left\{\dot{\mathbf{x}}\right\} = \left\{\mathbf{F}_d\right\} \tag{2.23}$$

where, $\left[\mathbf{M}_d\right] = \mathrm{diag}\left[M_{d_1} \quad J_{D_{d_1}} \quad M_{d_2} \quad J_{D_{d_2}} \quad \cdots \quad M_{\mathrm{N}_d} \quad J_{D_{\mathrm{N}_d}}\right]$,

$\left[\mathbf{G}_d\right] = \mathrm{diag}\left[0 \quad i\Omega J_{P_{d_1}} \quad 0 \quad i\Omega J_{P_{d_2}} \quad \cdots \quad 0 \quad i\Omega J_{P_{\mathrm{N}_d}}\right]$,

M_d, J_{D_d}, and J_{P_d} ,are the disc mass, diametral, and polar moment of inertia, respectively. The expressions of mass and gyroscopic matrices in normal coordinate are presented in Appendix-C. According to disc location, the above mass and gyroscopic matrices are directly adjoined with the acceleration and velocity coefficients of shaft equation of motion.

2.6 Incorporation of bearing effect

Rotor systems are invariably mounted on bearings, as bearings bear both static and dynamic loads and facilitate spinning motion of the rotor shaft. Rolling and sliding contact bearings are widely used in many machinery. Rolling contact bearings are also called anti friction bearings, as the friction and wear are very small in these bearings due to the presence of rolling elements. A rolling contact bearing applies both restoring and dissipative forces due to radial deformation of the rolling elements as well as tilt of the rotor-shaft. These introduce radial and tilt stiffness and damping terms in the equations of motion. Meanwhile, in sliding contact bearing, the coefficients of the bearings are functions of several parameters like clearance, oil viscosity, and spin speed of the rotor shaft. As a result the fluid film forces acting on the journal are both conservative and dissipative in nature. Researchers like Vance (1988), Rao (2009), Friswell et al. (2010b), among others, have given theoretical derivations to obtain the bearing model in terms of four stiffness (two direct and two cross coupled) and four damping coefficients. These forces cause asymmetry in the stiffness matrix due to the anisotropy as well as cross coupled terms.

The bearing force in terms of stiffness and damping coefficients is given as,

$$\left[\mathbf{C}_{brg}\right]\begin{Bmatrix}\dot{v}\\ \dot{w}\end{Bmatrix}+\left[\mathbf{K}_{brg}\right]\begin{Bmatrix}v\\ w\end{Bmatrix}=\begin{Bmatrix}\mathbf{F}_{brg_y}\\ \mathbf{F}_{brg_z}\end{Bmatrix} \qquad (2.24(a))$$

$$\begin{bmatrix}C_{yy} & C_{yz}\\ C_{zy} & C_{zz}\end{bmatrix}\begin{Bmatrix}\dot{v}\\ \dot{w}\end{Bmatrix}+\begin{bmatrix}K_{yy} & K_{yz}\\ K_{zy} & K_{zz}\end{bmatrix}\begin{Bmatrix}v\\ w\end{Bmatrix}=\begin{Bmatrix}\mathbf{F}_{brg_y}\\ \mathbf{F}_{brg_z}\end{Bmatrix} \qquad (2.24(b))$$

The detail derivation of bearing forces is presented in Appendix-E. The damping and stiffness matrices are directly adjoined with the velocity and displacement coefficients of shaft equation of motion.

Some important point is to be noticed that the above expression is valid only for sliding contact bearing where all coefficients are added. But for the case of rolling contact bearing, the bearing force is independent of spin speed and cross couple coefficients are neglected (i.e. $C_{yz}=C_{zy}=0$ and $K_{yz}=K_{zy}=0$). If the stiffness of the rolling elements is sufficiently high, bearing deformation is negligible and it is termed as rigid bearing. In this situation, the bearing effects are incorporated either by penalty or elimination approach. In penalty approach high value of stiffness is inserted into the appropriate bearing location. Whereas, in elimination approach entire row and column of the matrices are deleted according to the bearing location.

2.7 State space representation

To solve the eigenvalue problem of higher order systems, one needs to use the state space representation of equations of motion. In this representation, the higher order equation is reduced to first order form. There are various ways of state space representation, as per need governing equations are to be modified. Some of them are presented here.

To establish the standard eigenvalue problem, Eq. (2.11) and Eq. (2.22) is conjoined with an identity equation to obtain the state space form as shown below.

$$[\boldsymbol{\mathcal{E}}]_{3h\times 3h}\{\dot{\boldsymbol{x}}\}_{3\mathrm{N}\times 1}=[\boldsymbol{\mathcal{A}}]_{3\mathrm{N}\times 3\mathrm{N}}\{\boldsymbol{x}\}_{3\mathrm{N}\times 1}+[\boldsymbol{\mathcal{B}}]_{3\mathrm{N}\times r}\{\boldsymbol{u}\}_{r\times 1} \tag{2.25(a)}$$

$$\{\boldsymbol{y}\}_{p\times 1}=[\boldsymbol{\mathcal{C}}]_{p\times 3\mathrm{N}}\{\boldsymbol{x}\}_{3\mathrm{N}\times 1}+[\boldsymbol{\mathcal{D}}]_{p\times r}\{\boldsymbol{u}\}_{r\times 1} \tag{2.25(b)}$$

where,

$$[\boldsymbol{\mathcal{E}}]_{3\mathrm{N}\times 3\mathrm{N}}=\begin{bmatrix}[\mathbf{I}] & [0] & [0]\\ [0] & [\mathbf{I}] & [0]\\ [0] & [0] & [\mathbf{A}_3]\end{bmatrix},\qquad [\boldsymbol{\mathcal{A}}]_{3\mathrm{N}\times 3\mathrm{N}}=\begin{bmatrix}[0] & [\mathbf{I}] & [0]\\ [0] & [0] & [\mathbf{I}]\\ -[\mathbf{A}_0] & -[\mathbf{A}_1] & -[\mathbf{A}_2]\end{bmatrix},$$

$$[\boldsymbol{\mathcal{B}}]_{3\mathrm{N}\times r}=\begin{bmatrix}[\mathbf{0}]_{\mathrm{N}\times r}\\ [\mathbf{0}]_{\mathrm{N}\times r}\\ [\mathbf{B}]_{\mathrm{N}\times r}\end{bmatrix},\qquad [\boldsymbol{\mathcal{C}}]_{p\times 3\mathrm{N}}=\begin{bmatrix}[\mathbf{L}]_{p\times\mathrm{N}} & [\mathbf{0}]_{p\times\mathrm{N}} & [\mathbf{0}]_{p\times\mathrm{N}}\end{bmatrix},$$

$$\{\boldsymbol{x}\}_{3\mathrm{N}\times 1}=\begin{Bmatrix}\mathbf{q}\\ \dot{\mathbf{q}}\\ \ddot{\mathbf{q}}\end{Bmatrix},\ \{\boldsymbol{u}\}_{r\times 1}=\begin{Bmatrix}\{\mathbf{0}\}\\ \{\mathbf{0}\}\\ \{\mathbf{B}\}\end{Bmatrix},$$

Here, $[\boldsymbol{\mathcal{E}}]$ is the descriptor matrix, $[\boldsymbol{\mathcal{A}}]$ is the system state matrix, $[\boldsymbol{\mathcal{B}}]$ is the input matrix, $[\boldsymbol{\mathcal{C}}]$ is the output matrix, $[\boldsymbol{\mathcal{D}}]$ is the direct transmission matrix. $\{\boldsymbol{x}\}$ is the state vector. $\{\boldsymbol{u}\}_{r\times 1}$ is the vector of $'r'$inputs, and $\{\mathbf{y}\}_{p\times 1}$is the vector of $'p'$ output quantities. Elements of matrix $[\mathbf{L}]_{p\times h}$ are chosen zero or one to select the correct output from all states. Subscript $'\mathrm{N}'$ is used to indicate the matrix size (i.e. for CM $(\mathrm{N}=\mathrm{N}_d)$and FEM $(\mathrm{N}=n)$)

Another style of state space representation is shown below, which will use in subsequent section.

$$\{\dot{\boldsymbol{x}}\}_{3\mathrm{N}\times 1}=[\boldsymbol{\mathcal{A}}]_{3\mathrm{N}\times 3\mathrm{N}}\{\boldsymbol{x}\}_{3\mathrm{N}\times 1}+[\boldsymbol{\mathcal{B}}]_{3\mathrm{N}\times r}\{\boldsymbol{u}\}_{r\times 1} \tag{2.26}$$

where,

$$[\boldsymbol{\mathcal{A}}]_{3\mathrm{N}\times 3\mathrm{N}} = \begin{bmatrix} [0] & [\mathbf{I}] & [0] \\ [0] & [0] & [\mathbf{I}] \\ \left[-\mathbf{A}_3^{-1}\mathbf{A}_0\right] & \left[-\mathbf{A}_3^{-1}\mathbf{A}_1\right] & \left[-\mathbf{A}_3^{-1}\mathbf{A}_2\right] \end{bmatrix}, \quad [\boldsymbol{\mathcal{B}}]_{3\mathrm{N}\times r} = \begin{bmatrix} [\mathbf{0}]_{\mathrm{N}\times\mathrm{N}} \\ [\mathbf{0}]_{\mathrm{N}\times\mathrm{N}} \\ \left[\mathbf{A}_3^{-1}\right]_{\mathrm{N}\times\mathrm{N}} \end{bmatrix} [\mathbf{B}]_{\mathrm{N}\times r},$$

$$\{\boldsymbol{x}\}_{3\mathrm{N}\times 1} = \begin{Bmatrix} \mathbf{q} \\ \dot{\mathbf{q}} \\ \ddot{\mathbf{q}} \end{Bmatrix},$$

2.8 Modal analysis of rotor bearing model

Modal analysis is one of the best tool that can completely describe the dynamic of a rotor bearing system. Referring to Lee and Lee (1997) it is justified that in the case of rotating structures two distinct modes are appearing, i.e. backward and forward modes due to its spin speed. If the direction of the whirl is same with the spin speed, then it is called forward whirl, otherwise it is backward whirl. In conventional modal characteristics, which are used in non-rotating structure, no such directivity of modes is found. The principle of reciprocity is not competent due to the imperative characteristic of rotating machinery, and therefore they are mentioned to as 'Non Self Adjoint System' (NSA). As a result of such characterization of the system, there is an evolution of two sets of an eigenvector, mentioned as left-hand and right-hand eigenvectors. Both eigenvectors are essential to evaluate the dynamics of the rotor system. Left-hand eigenvectors are procured by examining the transformed equation and help to demonstrate the arrangement of forces related to the single mode, established in Chouksey et al. (2012). On the other hand, right-hand eigenvectors contribute to evaluate mode shapes of the system.

In the traditional frequency response function no such technique has recommended to extract the characteristic about directivity of modes. Among various methods, complex modal analysis is a useful tool to determine the dynamic behaviour of the rotor system. Various advantages are also reported in Lee (1991) were complex coordinates for force and displacement has been used to preserve the characteristics achieved by the directivity of modes. Dynamics of rotor is studied with the help of various important parameters such as decay rate plot, campbell diagram and modal damping factor. Those parameters are found through eigen analysis. For the eigen analysis free vibration equation of classical and finite element model is used.

2.8.1 Eigen analysis of the system

After developing the desired governing equation for viscoelastic rotor model, eigen analysis is done to study the various modal parameters like natural frequencies, damping factors, stability limit of spin speed, mode shapes and directivity of the modes.

Eq. (2.26) is showing the state space reduced form of higher order differential equation to a first order differential equation. An assumed function $\{x\}=\{\hat{x}\}e^{\lambda t}$ is utilized in the free vibration equation of Eq. (2.26) for eigen analysis. Two consecutive equations, involving two kinds of eigenvectors, are written below.

$$\left([\mathbf{\Lambda}][\mathbf{I}]-[\mathcal{A}]\right)[\mathbf{\Psi}]=0 \tag{2.27(a)}$$

$$\left([\mathbf{\Lambda}][\mathbf{I}]-[\mathcal{A}]^T\right)[\mathbf{\Phi}]=0 \tag{2.27(b)}$$

$[\mathbf{\Lambda}]$, $[\mathbf{\Psi}]$ and $[\mathbf{\Phi}]$ are the compact form of eigenvalues, right eigenvectors and left eigenvector of different modes. These are expressed as

$$\begin{aligned}
[\mathbf{\Lambda}]_{(3N\times 3N)} &= \operatorname{diag}\begin{bmatrix}\lambda_1 & \lambda_2 & \dots & \lambda_{3N}\end{bmatrix} \\
[\mathbf{\Psi}]_{(3N\times 3N)} &= \begin{bmatrix}\{\psi\}_1 & \{\psi\}_2 & \dots & \{\psi\}_{3N}\end{bmatrix} \\
[\mathbf{\Phi}]_{(3N\times 3N)} &= \begin{bmatrix}\{\Phi\}_1 & \{\Phi\}_2 & \dots & \{\Phi\}_{3N}\end{bmatrix}
\end{aligned} \tag{2.28}$$

Each column of the full modal matrix represents single mode, whereas eigenvalues appear diagonally. $[\mathbf{\Psi}]$ and $[\mathbf{\Phi}]$ are bi-orthogonal to each other. Sometime eigen solvers are not providing normalized eigenvector. Then normalization is done to get the following equations.

$$[\mathbf{\Phi}]^T[\mathcal{A}][\mathbf{\Psi}]=[\mathbf{\Lambda}] \tag{2.29(a)}$$

$$[\mathbf{\Phi}]^T[\mathbf{\Psi}]=[\mathbf{I}], \tag{2.29(b)}$$

where, $[\mathbf{I}]$ is identity matrix.

Campbell diagram: The eigenvalues of a damped system are in general complex quantity. The imaginary parts of eigenvalues indicate whirl frequency. Campbell diagram is plotted between whirl frequency and spin speed. Diverging line in the figure gives the idea of forward and backward whirl, which are denoted as FW and BW. A 45^0 line is also drawn, which is known as 'Synchronous Whirl Line (SWL). Locations of natural frequencies are predicted through intersection between SWL and whirl frequency lines. First point of intersection indicates first natural frequency and is denoted as FNF. Resonance frequencies are reflected in the campbell diagram when the whirl frequency intersects SWL.

Decay rate: It is plotted between maximum real parts of all eigenvalues versus spin speed. For a Linear Time Invariant (LTI) system stability is determined from the Decay rate plot. A stability limit of the spin speed (SLS) is the maximum spin speed till which all the eigenvalues have negative real parts. Existence of purely imaginary eigenvalue signifies sustained oscillations in the system about the point of equilibrium and is also considered to be unstable.

Modal damping factor (MDF): It represents the damping in different modes and is written as the ratio between negative real parts of the eigenvalues to absolute value of the eigenvalues corresponds to any mode. The MDF is also a stability deciding parameter. The positive values of MDF show the system is in the stable region where the vibrational energy is dissipative nature. But when these modes intersect the zero line and reaches to the negative zone, rotary energy supports rotor whirl by adding vibrational energy and the system becomes unstable.

2.8.2 Directional frequency response functions

This section mainly highlights to estimate the directional frequency response function (dFRF), which is an important parameter for determining the directivity of mode. To estimate the directional frequency response function, the state vector $\{\boldsymbol{x}(t)\}$ in Eq. (2.26) is replaced with the modal coordinates $\{\xi(t)\}$ and the right hand eigenvector $[\boldsymbol{\Psi}]$. The state vector is written as,

$$\{\boldsymbol{x}(t)\} = [\boldsymbol{\Psi}]\{\boldsymbol{\xi}(t)\} = \sum_{j=1}^{3\mathrm{N}} \{\psi\}_j \boldsymbol{\xi}_j(t) \tag{2.30}$$

Substituting Eq. (2.30) it into Eq. (2.26) and pre-multiplying throughout by $[\boldsymbol{\Phi}]^T$, the Eq. (2.31) is rewritten as below,

$$[\boldsymbol{\Phi}]^T[\boldsymbol{\Psi}]\{\dot{\boldsymbol{\xi}}(t)\} - [\boldsymbol{\Phi}]^T[\mathcal{A}][\boldsymbol{\Psi}]\{\boldsymbol{\xi}(t)\} = [\boldsymbol{\Phi}]^T[\mathcal{B}]\{\boldsymbol{u}(t)\} \tag{2.31}$$

Using orthogonality relations, the above equation can be written as:

$$\{\dot{\boldsymbol{\xi}}(t)\} - [\boldsymbol{\Lambda}]\{\boldsymbol{\xi}(t)\} = \{\mathbf{U}(t)\} \tag{2.32}$$

where, $\{\mathbf{U}(t)\} = [\boldsymbol{\Phi}]^T[\mathcal{B}]\{\boldsymbol{u}(t)\}$ represent the modal excitation vector. A set of independent modal equations is also expressed from preceding equation.

$$\dot{\boldsymbol{\xi}}_j(t)-\boldsymbol{\lambda}_j\boldsymbol{\xi}_j(t)=\left\{\mathbf{U}_j(t)\right\},\ \left(j=1,2,....,3\mathrm{N}\right) \tag{2.33}$$

where $\left\{\mathbf{U}_j(t)\right\}=\{\boldsymbol{\Phi}\}_j^T\left[\boldsymbol{\mathcal{B}}\right]\{\boldsymbol{u}(t)\}$ is the generalized excitation force of the j^{th} mode.

Calculating the modal response from the Eq. (2.33) under harmonic force $\mathbf{U}_j(t)$ of frequency $'\omega'$ is given by:

$$\boldsymbol{\xi}_j(t)=\frac{\left\{\mathbf{U}_j(t)\right\}}{\left(i\omega-\boldsymbol{\lambda}_j\right)}=\frac{\{\boldsymbol{\Phi}\}_j^T\left[\boldsymbol{\mathcal{B}}\right]\{\boldsymbol{u}(t)\}}{\left(i\omega-\boldsymbol{\lambda}_j\right)} \tag{2.34}$$

Substituting Eq. (2.34) into Eq. (2.30) gives

$$\left\{\boldsymbol{x}(t)\right\}=\sum_{j=1}^{3\mathrm{N}}\frac{\{\boldsymbol{\Psi}\}_j\{\boldsymbol{\Phi}\}_j^T}{\left(i\omega-\boldsymbol{\lambda}_j\right)}\left[\boldsymbol{\mathcal{B}}\right]\{\boldsymbol{u}(t)\} \tag{2.35}$$

Therefore, Frequency Response Function matrix $\left[\mathbf{H}\right]$ in state space may be written as,

$$\left[\mathbf{H}\right]=\frac{\left\{\boldsymbol{x}(t)\right\}}{\{\boldsymbol{u}(t)\}}=\sum_{j=1}^{3\mathrm{N}}\frac{\{\boldsymbol{\Psi}\}_j\{\boldsymbol{\Phi}\}_j^T}{\left(i\omega-\boldsymbol{\lambda}_j\right)}\left[\boldsymbol{\mathcal{B}}\right] \tag{2.36}$$

It is seen in the preceding equation, natural frequency, both right and left eigenvectors are involved to deduce FRF matrix. Thus, for a non-self-adjoint system, any one row and any one column from a complete FRF are able to estimate modal behaviour. The F RF matrix, $\left[\mathbf{H}\right]$ relating generalized displacement, may be written as:

$$\mathbf{H}=\begin{bmatrix}\mathbf{H}_{yy} & \mathbf{H}_{yz}\\ \mathbf{H}_{zy} & \mathbf{H}_{zz}\end{bmatrix} \tag{2.37}$$

After following Lee (1991), the directional Frequency Response Function (dFRF) and reverse directional Frequency Response Function (r-dFRF) can be written as:

$$\begin{aligned}
\mathbf{H}_{pg}&=\frac{1}{2}\left(\mathbf{H}_{yy}+\mathbf{H}_{zz}-i\left(\mathbf{H}_{yz}-\mathbf{H}_{zy}\right)\right),\\
\mathbf{H}_{p\bar{g}}&=\frac{1}{2}\left(\mathbf{H}_{yy}-\mathbf{H}_{zz}+i\left(\mathbf{H}_{yz}+\mathbf{H}_{zy}\right)\right),\\
\mathbf{H}_{\bar{p}g}&=\frac{1}{2}\left(\mathbf{H}_{yy}-\mathbf{H}_{zz}-i\left(\mathbf{H}_{yz}+\mathbf{H}_{zy}\right)\right),\\
\mathbf{H}_{\overline{pg}}&=\frac{1}{2}\left(\mathbf{H}_{yy}+\mathbf{H}_{zz}+i\left(\mathbf{H}_{yz}-\mathbf{H}_{zy}\right)\right),
\end{aligned} \tag{2.38}$$

Here, '$\mathbf{H}_{pg}$' and '$\mathbf{H}_{\bar{p}\bar{g}}$' are dFRF matrix and '$\mathbf{H}_{\bar{p}g}$', '$\mathbf{H}_{p\bar{g}}$' are r-dFRF matrix. Where, over bar $(\bar{\ })$ represents complex conjugate of a vector or scalar. Complex linear displacement and complex force at any particular node are represented by '*p*' and '*g*' respectively. Those are written as.

$$p(t)=y(t)+iz(t),\ \ g(t)=f_y(t)+if_z(t), \tag{2.39}$$

The complex conjugate expression of dFRF and r-dFRF are related as.

$$\mathbf{H}_{pg}(i\omega)=\bar{\mathbf{H}}_{\bar{p}\bar{g}}(-i\omega);\ \ \mathbf{H}_{\bar{p}g}(i\omega)=\bar{\mathbf{H}}_{p\bar{g}}(-i\omega); \tag{2.40}$$

This complex frequency response function is also important for detecting anisotropy, asymmetry and cracks in rotating machinery.

2.8.3 Mode shapes

The mode shapes of a rotating shaft indicate the locus of any point of the shaft during whirling motion. Due to forward and backward whirling, two kinds of mode shape appear, known as forward and backward modes. The mode shapes and their direction can be obtained from the eigenvector by plotting the two perpendicular time varying displacement function. The eigenvector of the whole system is a matrix of size equal to the state space vector, is known as modal matrix. In which, the individual column indicates the each mode. The displacement function and its higher order derivative are arranged in each column according to the degree of freedom in the state space vector $\{X\}$.

In the eigenvector, let 'V', and 'W' are the two perpendicular complex displacement function of 'j^{th}' mode correspond to any spatial location. So time varying displacement function can be expressed as

$$\begin{aligned} v&=|V|\cos(\omega t+\theta_y); \\ w&=|W|\cos(\omega t+\theta_z); \end{aligned} \tag{2.41}$$

To have an incomplete circle of each locus, the angle (ωt) varies $0\le\omega t<2\pi$ and phase angle θ_y and θ_z are written as $\tan^{-1}\dfrac{\mathrm{imag}(V)}{\mathrm{real}(V)}$ and $\tan^{-1}\dfrac{\mathrm{imag}(W)}{\mathrm{real}(W)}$, respectively.

Direction of whirl can also be predicted by using vector algebra. The positive sign of cross product between displacement and velocity function indicates forward whirl, otherwise it is backward whirl.

$$\vec{\nabla} = \vec{R} \times \dot{\vec{R}} \tag{2.42}$$

where, $\begin{matrix} \vec{R} = \vec{V} + i\vec{W}; \\ \dot{\vec{R}} = \dot{\vec{V}} + i\dot{\vec{W}}; \end{matrix}$ and $\nabla = \begin{Bmatrix} > 0 \Rightarrow \text{forward whirl} \\ < 0 \Rightarrow \text{backward whirl} \end{Bmatrix}$

2.9 Response calculation due to mass unbalance

Unbalance Frequency Response: Unbalance frequency response for various rotational speeds helps to predict the critical speed of a system. It happens at the point of resonance (high response amplitude) when the spin speed of the rotating structure reaches to system's natural frequency.

Synchronous unbalance response amplitude (UBR) at any location of the shaft is obtained from the equation of motion. The induced vibration due to unbalance acts as an external disturbance force can be modelled by a vector $\{\boldsymbol{u}\} = \{\hat{\boldsymbol{u}}_r\}\mathrm{e}^{\mathrm{i}\Omega t}$, where, $r = 1, 2, \ldots\ldots, 2j$ and $j = 1, 2, \ldots\ldots, n$, specify all unbalance force in rotor section. The j^{th} nodal unbalance force vector is written as $\{\boldsymbol{u}_j\} = \{m_j e_j \Omega^2 \quad -i m_j e_j \Omega^2\}^T$, where $'m','e'$ are unbalance mass, eccentricity and $'i'$ is imaginary unit.

From Eq. (2.25), transfer function $'\mathbf{T}'$ can be calculated as follows:

$$\mathbf{T} = [\mathcal{C}]_{p\times 3\mathrm{N}} \left([\mathcal{E}]_{3\mathrm{N}\times 3\mathrm{N}}\, s - [\mathcal{A}]_{3\mathrm{N}\times 3\mathrm{N}}\right)^{-1} [\mathcal{B}]_{3\mathrm{N}\times r} \tag{2.43}$$

Then the output at k^{th} node is given as:

$$\{\mathbf{y}_p\} = \mathbf{T}\{\hat{\boldsymbol{u}}_r\}, \quad p = 1, 2, \ldots\ldots, 2k \tag{2.44}$$

The unbalance response amplitude at the same location is given by,

$\mathrm{UBR}_k = \max\left|\mathrm{Real}\left(\{\mathbf{y}_k\}_{y\text{-}disp}\,\mathrm{e}^{i\Omega t}\right) + i\mathrm{Real}\left(\{\mathbf{y}_k\}_{z\text{-}disp}\,\mathrm{e}^{i\Omega t}\right)\right|$ where, $y-disp$ and $z-disp$ are $'y'$ and $'z'$ directions displacement at k^{th} node.

Time Response: Stable and unstable behaviour of the system are predicted by time response over a particular time span. Whirl motion of the rotating shaft is observed through whirl orbit, which is a path traced by a point on rotor with time. It is obtained by plotting time response along the y- direction vs. the z- direction. For steady state operation in stable zone, whirl orbit remains constant. Whereas it enlarges monotonically when spin speed is above the stability limit of spin speed (SLS).

2.10 Validation of numerical results

The whole research work is based on some numerical simulation, obtained from programmable codes. For checking the correctness of these codes, initially some results are validated with published literature. These computer codes are written with the help of MATLAB (version- 7.10, R2010a) software. Best matches between the computed and published results prove the correctness of the present formulation.

2.10.1 Classical approach

Dutt and Nakra (1995) put an effort to determine the eigenvalues and unbalance response of a rotor with viscoelastic support. The disc is asymmetrically located, the rotor mass and the disc mass are concentrated at particular disc location. Some of the expressions and given data which are used here to validate the classical model are as follows,

$$\alpha = \mathrm{M}_1/\mathrm{M}_2, \quad \delta = \omega_{n_1}/\omega_n, \quad \omega_n = \sqrt{\mathrm{K}^*_{(F/d)}/\mathrm{M}_2}, \quad \delta_\mathrm{R} = \omega/\omega_n,$$

$$\mathrm{C} = \omega_n/\sqrt{(\mathrm{C}_{22}/\mathrm{I}_\mathrm{t})}, \quad \mathrm{R}=\mathrm{I}_\mathrm{p}/\mathrm{I}_\mathrm{t}, \quad \beta = \mathrm{K}_\mathrm{b}/\mathrm{K}^*_{(\mathrm{F/d})}, \quad \beta_1 = \mathrm{K}/\mathrm{K}^*_{(\mathrm{F/d})},$$

$$\mathrm{e}_1 = l_1/l, \quad \mathrm{M}_1/\mathrm{M}_2 = 0.4, \quad \mathrm{C}_{22}/\mathrm{I}_\mathrm{t} = 0.1, \quad \mathrm{K}_\mathrm{b}/\mathrm{K}_\mathrm{s} = 5.0,$$

$$\mathrm{K}/\mathrm{K}_\mathrm{s} = 0.1, \quad l_1/l = 0.1, \quad \mathrm{I}_\mathrm{p}/\mathrm{I}_\mathrm{t} = 1.8, \quad \beta = 5,$$

$$\beta_1 = 0.1,$$

where, M_1, K_s and l are the mass, stiffness and length of the rotor respectively. l_1 is the left end distance of disc, I_p and I_t are the polar and transverse moment of inertia of the disc, ω is the rotational speed of the rotor, ω_n is the first natural frequencies. M_2 and K are the mass and stiffness of each support, K_b is the stiffness of each bearing element, C_{22} and C_{12} are the angular stiffness and force/angular deflection of the shaft at rotor disc location.

Both the eigenvalues and the unbalance response have been calculated for the above sets of system parameters. Fig. 2.6 shows the campbell diagram, where a 45° line (which becomes a curve due to logarithmic scale in the vertical axis) cut the first three lines at point P, Q, R. The fourth line, i.e. the natural frequency line corresponding to the 4^{th} forward whirl is never intercepted. Fig 2.7 shows the unbalance response effect of the system with viscoelastic supports. The parameter K is the in-phase stiffness and is replaced by $\mathrm{K}(1+i\eta)$, where η is the loss factor of viscoelastic material. It is observed in the figure that the peaks occur at values corresponding to the point P and R. The point Q corresponds to second mode, which is due to the angular rotation effect, is not excited by unbalance excitation. The results obtained are accurately matched with the Dutt and Nakra (1995) model, which shows the authentication of the results.

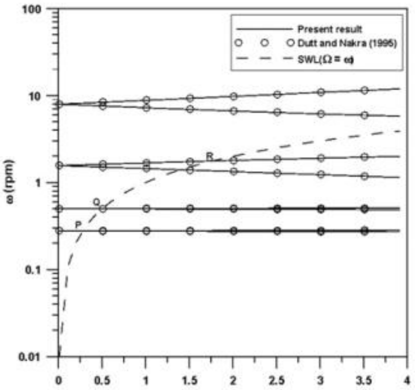

Fig. 2.6 Campbell diagram

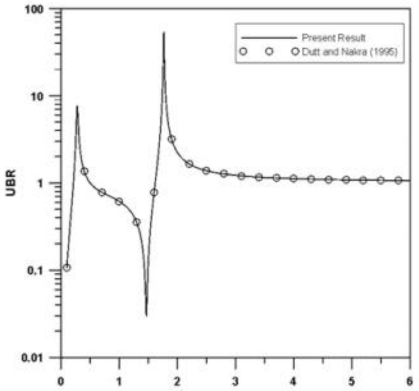

Fig. 2.7 Unbalance response amplitude

2.10.2 Finite element approach

A code based on finite element formulation is written to validate the results obtained for rotor model with different bearing support (i.e. rigid, rolling and sliding contact bearings). For this purpose three different research papers are used to validate such type of numerical problem. These codes are further modified as per the present model.

Rotor supported by rigid bearing

Combescure and Lazarus (2008) show the rotor model supported by rigid bearing. Data needed to validate the numerical problem are given below.

The rotor is made of mild steel and discretized into 16- node or 15- element. Length of the rotor is 0.4 m, diameter of rotor is 0.02 m, elastic modulus is 200 GPa and the density of material is 7800 kg/m^{3,} and the material damping coefficient is $\eta_v = 0.0002$. A disc is mounted at node 6 with its parameter as: diameter 0.3 m and thickness 0.005 m respectively.

Rotor supported by rolling contact bearing

Work by Chouksey et al. (2010) used the rolling contact bearing in damped rotor model and did the modal analysis. Data needed to validate the numerical problem are given below.

The rotor is made of mild steel and discretized into 15- node or 14- element. Similar properties of mild steel are used here. A disc is mounted at node 6 and its parameters are as: diameter 0.4 m, thickness 0.05 m and unbalance 200 gm-mm. The parameters of rolling contact bearing are $K_{yy} = K_{zz} = 1.75e7\,N/m$, and $C_{yy} = C_{zz} = 700\,N\text{-sec}/m$.

Rotor supported by sliding contact bearing

Chouksey et al. (2012) showed the modal analysis of a damped rotor supported by sliding contact bearing. Data needed to validate the numerical problem are given below

The steel shaft is mounted by two discs. The density of the shaft and discs is 7810 kg/m^3. Viscosity of oil and radial clearance between the journal and bearing are taken as 0.1 Pa-s and 0.0001 m respectively. Each bearing supports a static load of 648 N and has length to diameter ratio of 0.3. The viscous damping coefficient of rotor-shaft material is considered as 0.0002 s, other rotor parameters can be taken from refereed paper.

Here dynamic analysis is performed and the following results are obtained after simulation of codes. All results are fully satisfactory and precisely validated with the previously published results.

A. Campbell diagram

Fig. 2.8 shows the campbell diagram of the system where first four displacement modes are drawn. Diverging line in the figure gives the idea of forward and backward whirl, which are denoted as F and B. Nice matches in all the figures (i.e. Fig. 2.8(a), Fig. 2.8(b), and Fig. 2.8(c)) show the correctness of imaginary part of eigenvalues. The encircled portion in Fig. 2.8(c) highlights the curve veering zone. The detail explanation of this phenomenon is given later.

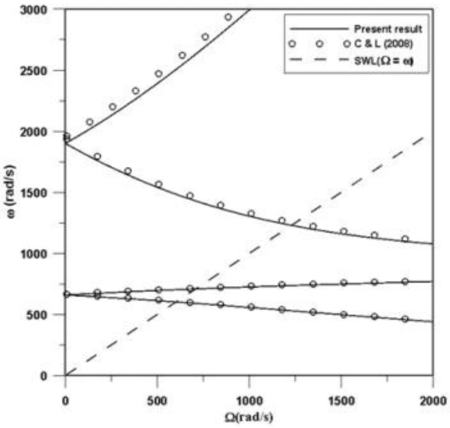

(a) Rigid bearing case

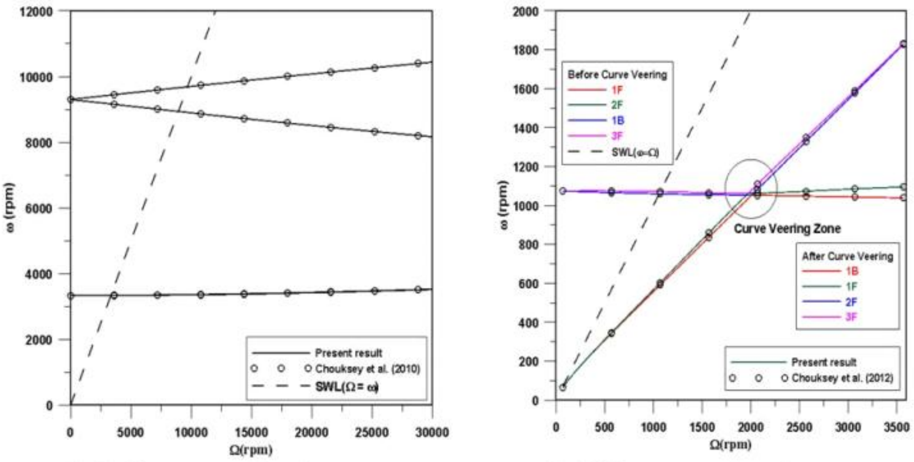

(b) Rolling contact bearing case (c) Sliding contact bearing case

Fig. 2.8 Campbell diagram

B. Modal damping factor

Fig. 2.9 shows the variation of modal damping factors in initial four modes as spin speed increases; this serves as a stability plot of the system. Fig. 2.9(a), Fig. 2.9(b) and Fig 2.9(c) justify the authentication of both real and imaginary parts of the eigenvalues.

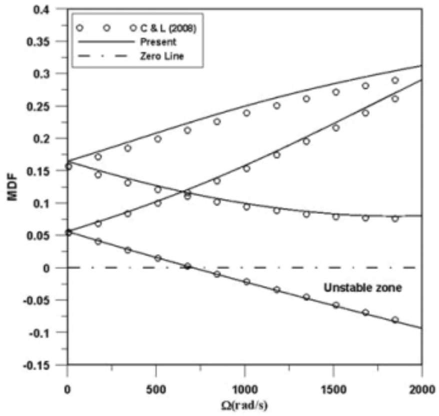

(a) Rigid bearing case

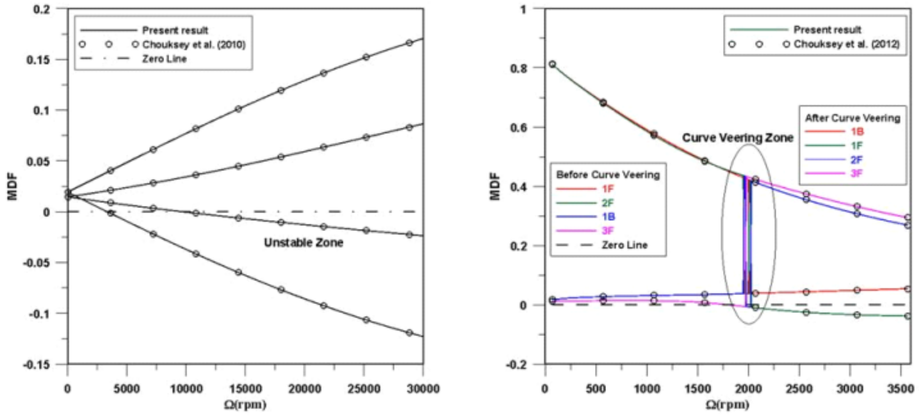

(b) Rolling contact bearing case (c) Sliding contact bearing case

Fig. 2.9 Modal damping factor

C. Directional frequency response functions

Fig. 2.10(a) and Fig. 2.10(b) show dFRF plot, which is plotted for two cases i.e. rolling and sliding contact bearing for the corresponding spin speed of 3000 rpm and 1800 rpm, respectively. To obtain dFRF, both eigenvalues and eigenvectors are required. Thus, a nice match in dFRF indicates the correctness of code from both sides.

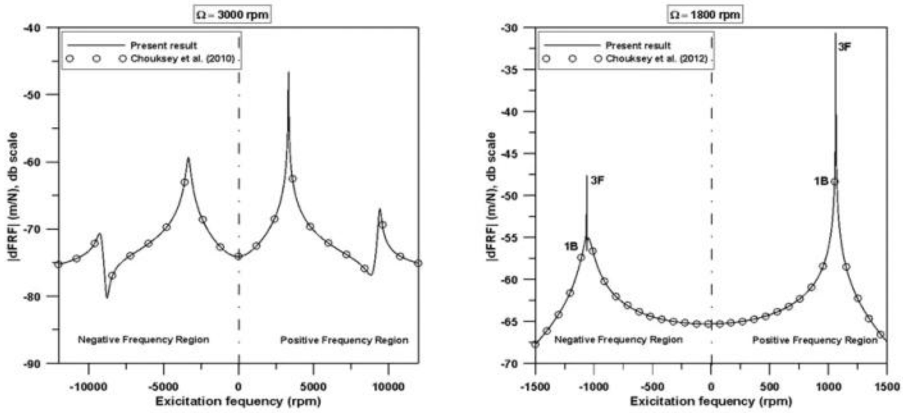

(a) Rolling contact bearing case **(b) Sliding contact bearing case**

Fig. 2.10 Directional frequency response function s

2.11 Model implementation

In this section, numerical simulation is done for various developed viscoelastic rotor models. A comparative study has also been done for both classical model and finite element model. For the simplicity of study three different numerical problems are considered.

- **Case-1:** rotor made of low damped material.
- **Case-2:** rotor made of high damped material.
- **Case-3:** rotor with various asymmetries.

2.11.1 Numerical problem of rotor made of low damped material: Case-1

It is already discussed in the literature section that all metals are considered as a low damped material. So, for simulation purpose mild steel is considered as a rotor material to get the actual dynamic behaviour of low damped material. The eigenvalue analysis can be performed on Eq. (2.27) for studying the dynamics of a designed rotor model. A schematic diagram of rotor shaft is shown in Fig. 2.11. The material properties and dimensional parameters are given as length $L = 1\ \mathrm{m}$, and diameter $D_r = 0.05\ \mathrm{m}$. It is mounted by rigid bearings at the ends, considered to generate simply supported boundary conditions. A disc of the same material is mounted non-centrally. For parametric study placement of the disc is changed from one end to another end. Diameter of the disc is also varied to show the effect of gyroscopic moment. The nondimensional position of the disc is denoted by $L^* = L_1/L$, where, L_1 is the disc position from the left end and L *is* the total length of the rotor. Another non-dimensional parameter, diameter ratio, is used to take into account the varying disc diameter, i.e. $D^* = D_d/D_r$, D_d is the disc diameter. Thickness of the disc is same as diameter of the rotor, T_d = 0.05 m. A mass unbalance is assumed to locate at disc and their value is 10e-06 kgm.

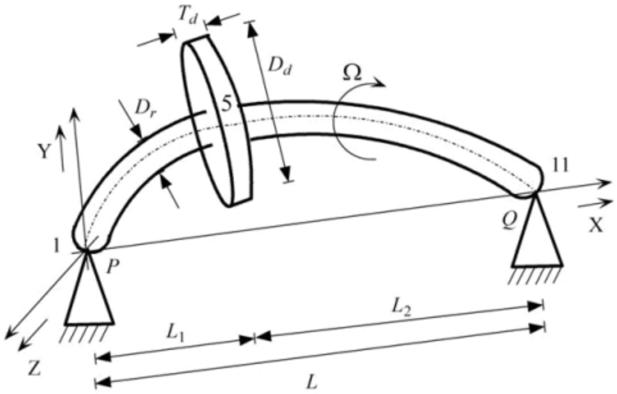

Fig. 2.11 Schematic diagram of single disc rotor model on simply supported ends

The viscoelastic parameters of mild steel are extracted from storage modulus and loss factor, which are clearly mentioned in Appendix-A. The extracted data are directly used here referring in Table 2.2.

Table 2.2 Material properties and extracted viscoelastic parameters of Mild steel

Density 'ρ' (kg/m^3)	Storage Modulus 'E' (Pa)	Loss Modulus 'η'	Fixed Parameters		Designed Parameters	
			a_0	b_0	a_1	b_1
7800	2.1e+11	2.9e-02	2.1e+11	1	7.51e+05	1.475e-9

A comparative study is done on various numerical results for both classical model (CM) and finite element model (FEM). Most of the results are obtained for $L^* = 0.2$ and $D^* = 5$, otherwise it has been mentioned. For better understanding of graphs, different legends and line styles are used to represent different analysis. Nice match in all figures between both models shows the correctness of this study.

A. Stability limit of spin speed

Decay rate plot is drawn in Fig. 2.12 to obtain stability region. In this example, the values of SLS for the CM and FEM are 4030 rpm, and 4490 rpm respectively.

SLS for three different values of D^* and various disc positions are shown in Fig. 2.13. Placement of the disc is changed from left to right end, or L^* varies from 0 to 1. SLS in non-central location of disc gives higher value than a central location. It is due to the stiffening effect of gyroscopic couple. It is also seen from the figure, SLS for both models are reflecting similar values up to the range of $L^* = 0.25 \text{ to } 0.75$, when D^* is 5. Beyond that range classical model fails to extract the correct values of SLS as FE model. It is the limitation of lumped system analysis.

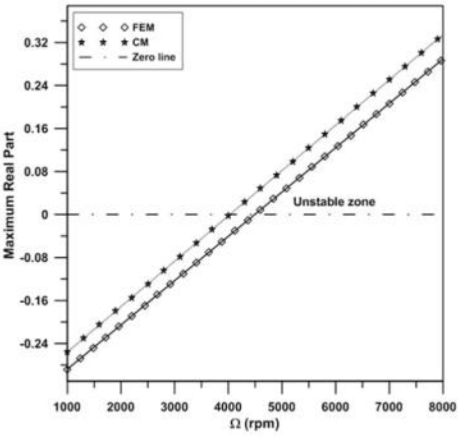

Fig. 2.12 Decay rate

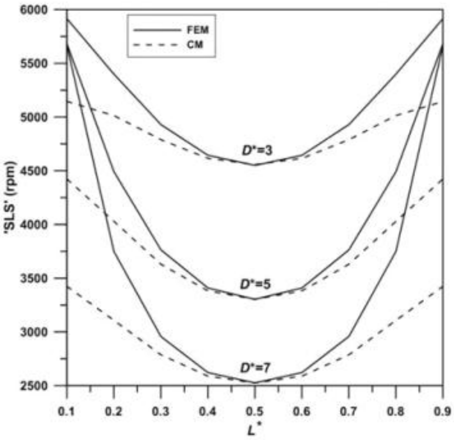

Fig. 2.13 Stability limit of spin speed

B. Campbell diagram

Fig. 2.14 demonstrates campbell diagram, which is plotted between the whirl-frequency and the rotor spin speed. Here only two displacement modes have been presented. Diverging line in the figure gives the idea of forward and backward whirl, which are denoted as FW and BW. Bifurcation is more at higher spin speed; it is due to the presence of gyroscopic effect.

SWL is also drawn here to locate natural frequencies. Fig. 2.15 represents the FNF for three different values of D^* and various disc positions. Likewise SLS, it also shows that there is an improvement in FNF when disc shifts from centre to offset position. It is seen in this figure that FNF from CM doesn't agree with FEM, when disc is near to boundary.

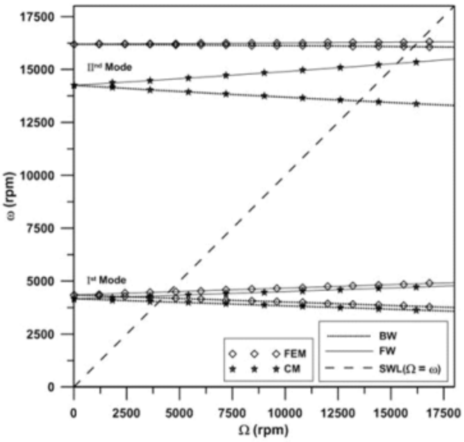

Fig. 2.14 Campbell diagram

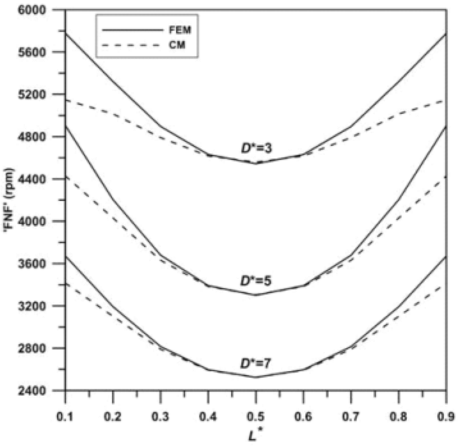

Fig. 2.15 First natural frequency

C. Modal damping factor

Fig. 2.16 represents the variation of MDF with the rotor spin speed for CM and FEM. The MDF is plotted here considering first and second mode only. It has the incremental value for backward whirl with respect to spin speed, whereas it has decrementing nature for fo rward whirl and after certain spin speed becomes negative. The system becomes unstable when any of the MDF reaches to negative zone and it occurs due to first forward whirl only.

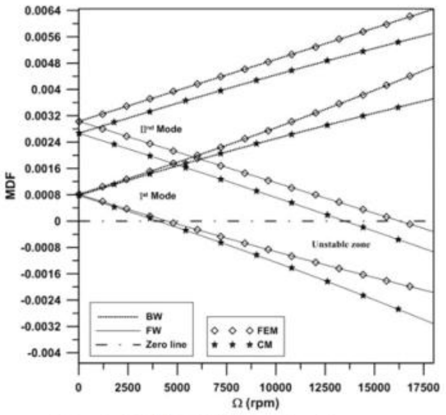

Fig. 2.16 Modal damping factor

D. Unbalance frequency response

Unbalance response for various rotational speeds is shown in Fig. 2.17. It is seen in the figure that, both the models have a good agreement upto first mode. At higher mode, though the nature of response amplitude is alike, but in classical model resonance is achieved sooner compare to FE model.

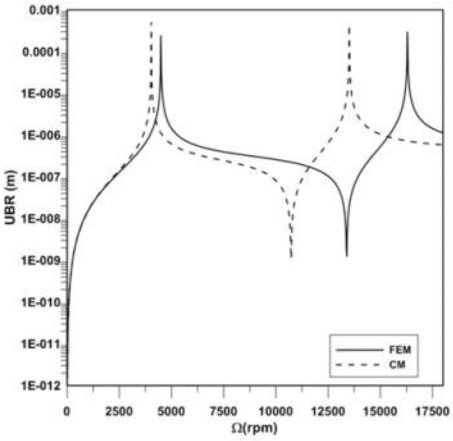

Fig. 2.17 Unbalance frequency response

E. Time response

Fig. 2.18(a) and Fig. 2.18(b) show the steady state time response of the disc due to unbalance for CM and FEM considering rotor spin speed at 3200 rpm and 4200 rpm. Fig. 2.20 has a stable nature as response magnitude is constant with time. As deformed rotor follows same path, the response in all cycles is a symmetric pattern. The hazy behaviour at beginning indicates transient effect. While, the plot in Fig. 2.18(b) represents the unstable nature, as response amplitude monotonically increases.

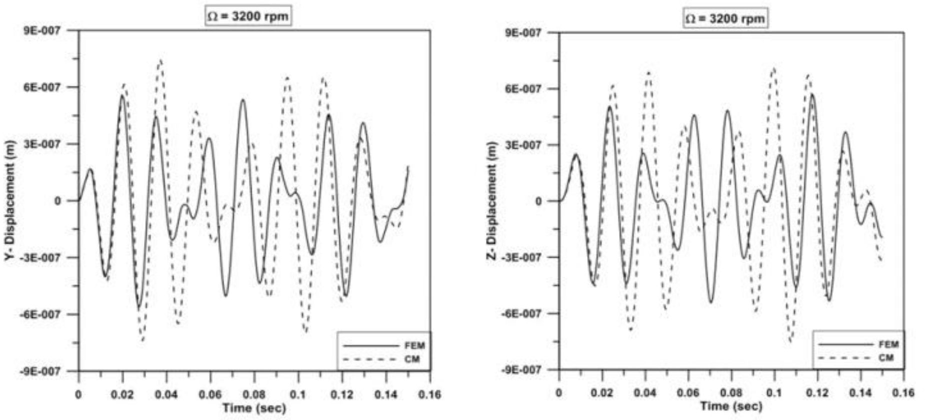

(a) Stable zone

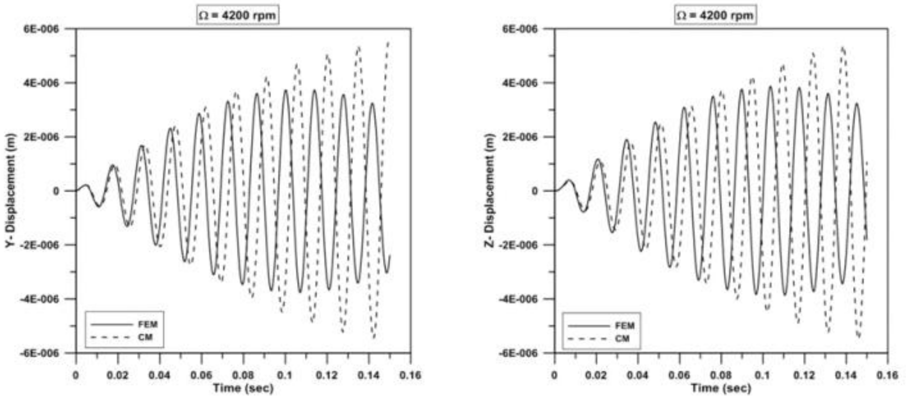

(b) Unstable zone

Fig. 2.18 Time response

F. Whirl orbit

Fig. 2.19(a) and Fig. 2.19(b) show whirl orbit due to unbalance. The same time responses as obtained in previous section are used to procure orbit plots. The rotor orbit in first case remains constant, whereas it increases monotonically in second case. In second case rotor spin speed is above the SLS and system shows unstable behaviour.

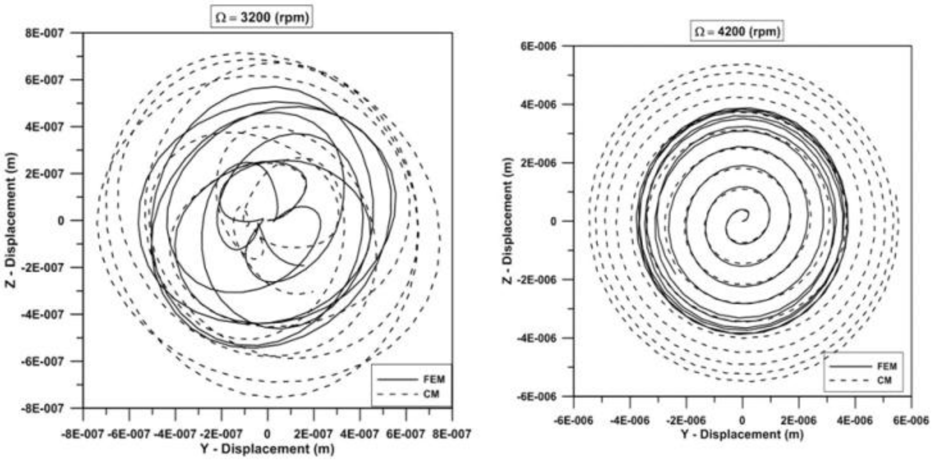

(a) Stable region **(b) Unstable region**

Fig. 2.19 Whirl orbit

2.11.2 Numerical problem of rotor made of high damped material: Case-2

All polymers and polymers based composites are treated as a high damped material. Therefore, for present simulation purpose Poly Vinyl Chloride (PVC) is considered for rotor material. A schematic diagram of rotor shaft is shown in Fig. 2.20, supported by a rigid bearing considered to generate simply supported ends. Dimensional parameters of the shaft are length $L = 0.35$ m and diameter $D_r = 0.035$ m. The material properties of PVC are taken from Roy (2008) and are shown in Table 2.3. Two identical discs are symmetrically located at distance 'L_1' and 'L_2' from the left end. The discs are made up of the same material (PVC) and their various geometric dimensions are shown in Table 2.4.

PVC is very soft and high damped material, due to this reason the nature of material properties varies with temperature change. Here, the comparative dynamic study of rotor behaviour for high damped material is done with three distinct temperature, i.e. 17 ° C, 24° C and 30° C. The eigenvalue analysis can be performed on Eq. (2.27) for studying the dynamics of a designed rotor model.

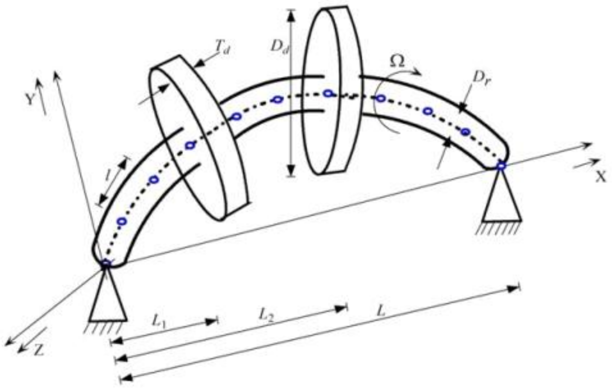

Fig. 2.20 Schematic diagram of two disc rotor model on simply supported ends

Table 2.3 Material properties and viscoelastic parameters of PVC

Density $'\rho'$ **(kg/m^3)**	**Temperature ‘T (^{o}C)’**	**Operator parameters**				
		a_0	a_1	a_2	b_0	b_1
	17	2.62e7	2.63e5	152.97	1	4.63e-3
1390	**24**	1.88e7	1.46e5	64.91	1	4.20e-3
	30	1.26e7	7.36e4	23.07	1	3.65e-3

Table 2.4 Disc parameter

Disc No.	**Diameter (m)**	**Thickness (m)**	**Mass un-balance (kg m)**	**Disc Positions**
Disc – 1	0.12	0.03	10e-06	$L_1 = 0.3$
Disc – 2	0.12	0.03	10e-06	$L_1 = 0.7$

A comparative study is also done on various numerical results for both classical model (CM) and finite element model (FEM). For better understanding of graphs, different legends and line styles are used for representation. Nice match in all figures between both models shows the correctness of this study.

A. *Stability limit of spin speed*

Fig. 2.21 shows the decay rate plot for three different temperature conditions. It is clear from figure that the SLS decreases with increase in temperature and their values (in rpm) are 387(407), 325(339), and 265(269) for CM(FEM) respectively. At high temperature, material properties degrade due to softening effect and system suffers earlier instability.

Fig. 2.22 is plotted between SLS and various disc positions for three different temperature conditions. Placement of the first disc shifts from left end to middle of shaft, while second disc changes its position from right end to the middle of the shaft. As the two identical discs are approaching from boundary to centre or vice versa, their position is represented by a single nondimensional parameter, $L^* = L_1/L$. From the figure, it is noticed that, SLS of the system varies with disc position, and non-central position gives higher value than central position, which is due to stiffening effect of gyroscopic couple. It is also seen from the figure that SLS for both CM and FEM are reflecting similar values up to the range of $L^* = 0.2 \text{ to } 0.8$. Beyond that range classical model fails to extract the correct values of SLS as same as FE model, due to data insufficiency. The stiffness coefficients for classical model predict incorrect result when L_1 is very small or L_2 is very large.

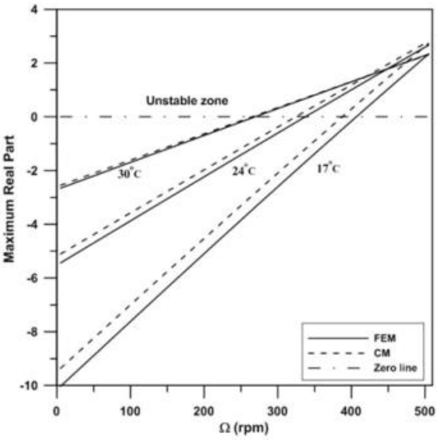

Fig. 2.21 Decay rate plot

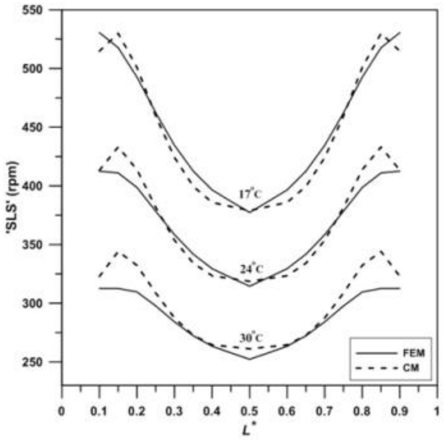

Fig. 2.22 Stability limit of spin speed

B. Campbell diagram

Fig. 2.23 shows the campbell diagram for three different temperature conditions and considering first displacement mode only. The first point of intersection between whirl line and SWL indicates the first natural frequency and is denoted by FNF. In the present case, the values of FNF (in rpm) for three different temperature condition are 441(449), 373(381), 305(311) for CM(FEM) respectively.

Fig. 2.24 shows the values of FNF for various disc positions. Due to gyroscopic stiffening effect, the system FNF is high when the discs are near the boundary . The figure also reveals that as the temperature increases the FNF of the system decreases, it is because the system stiffness reduces with an increase in temperature.

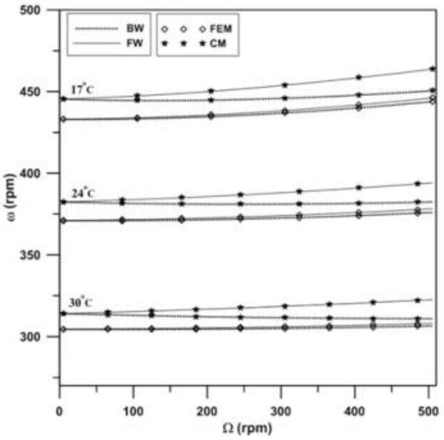

Fig. 2.23 Campbell diagram

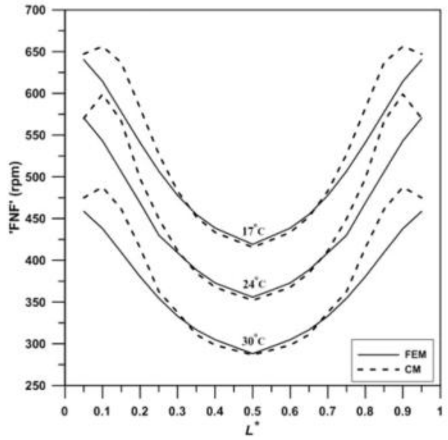

Fig. 2.24 First natural frequency

C. Modal damping factor

Fig. 2.25 represents the variation of MDF with the rotor spin speed for different temperature condition. The MDF in the plot is only for first mode. The values of SLS (in rpm) are 387(407), 325(339), and 265(269) for CM(FEM). SLS of the system decrease with increase in temperature due to the softening effect of polymeric material.

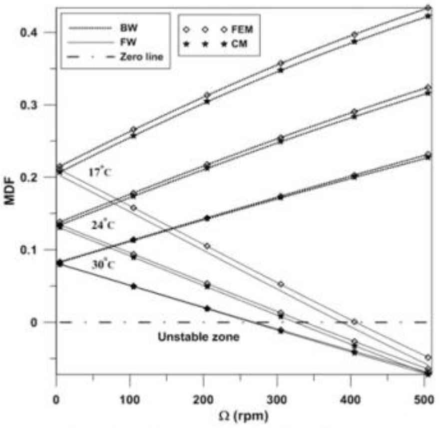

Fig. 2.25 Modal damping factor

D. Unbalance frequency response

Unbalance response (UBR) of the second disc is plotted for various rotational speeds as shown in Fig. 2.26. In which, the figure shows unbalance response for three different temperature condition. From the figure it is clearly visible that the resonance peak is shifted towards the left direction as well as increase in peak height, as the temperature increases. It is due to the reduction of system stiffness.

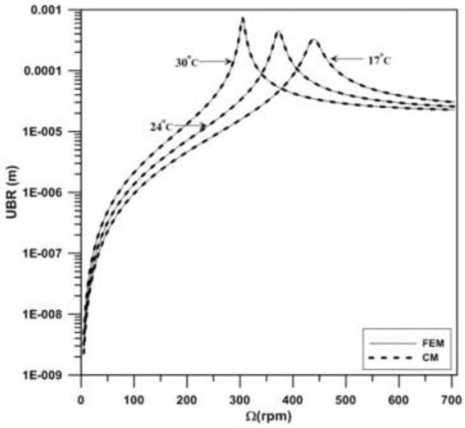

Fig. 2.26 Unbalance frequency response

E. Time Response

Fig. 2.27(a) and Fig. 2.27(b) show whirl orbit due to unbalance. The rotor orbit in second case increases monotonically for **T**= 24° C, whereas whirl orbit quenches in the first case for **T**= 17° C. This is because, the rotor spin speed is above SLS in second case and system shows unstable behaviour.

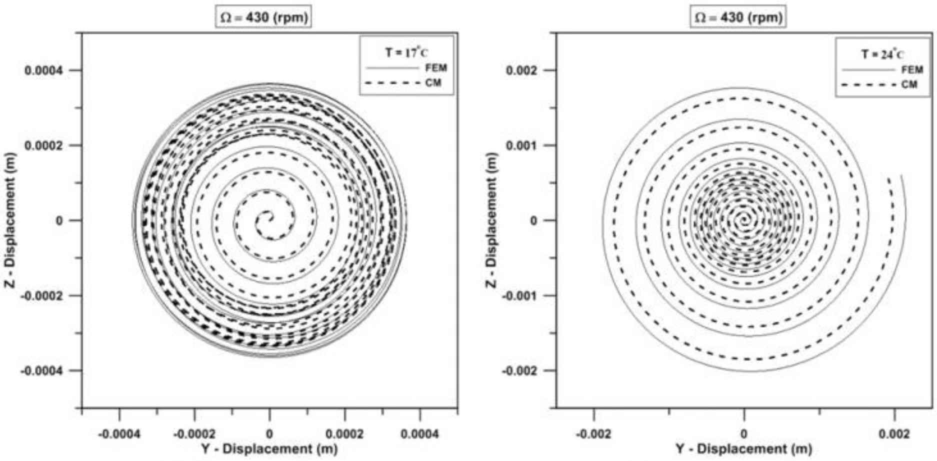

(a) Stable region **(b) Unstable region**

Fig. 2.27 Whirl orbit

2.11.3 Numerical problem of rotor with various asymmetry: Case-3

In this section, all types of asymmetries caused due to gyroscopic effect, circulatory stiffness and support condition. Those are incorporated into the generalized governing equation and modal analysis is performed for two sets of numerical problems i.e ,

1) Rotor with rolling contact bearings
2) Rotor with sliding contact bearings

2.11.3.1 Rotor with rolling contact bearings

In this numerical illustration, a flexible rotor shaft with circular cross section is considered which is supported by rolling contact bearings at the ends, as shown in Fig. 2.28. Two noded beam elements are considered in finite element analysis of the rotor shaft. The continuum is discretized into 10- elements or 11- nodes and each node has 4- degree of freedom, i.e. 2- displacements and 2- rotations. Length of the mild steel shaft is taken as $L = 1\,\mathrm{m}$. Diameter (D_r) of the boundary elements, which are mounted to two bearings, is taken as 0.1 m and rest of the portion is 0.05 m. Two identical discs of same material (mild steel) are located non symmetrically and the details are shown in the Table 2.5. While material properties and operator parameters of the rotor are taken from Table 2.2.

Following Lalanne and Ferraris (1998), the two stiffness and two damping coefficients of the rolling contact bearing are $\mathrm{K}_{b_{yy}} = 5e{+}07, \mathrm{K}_{b_{zz}} = 7e{+}07$ and $\mathrm{C}_{b_{yy}} = 5e+02, \mathrm{C}_{b_{zz}} = 7e{+}02$, respectively.

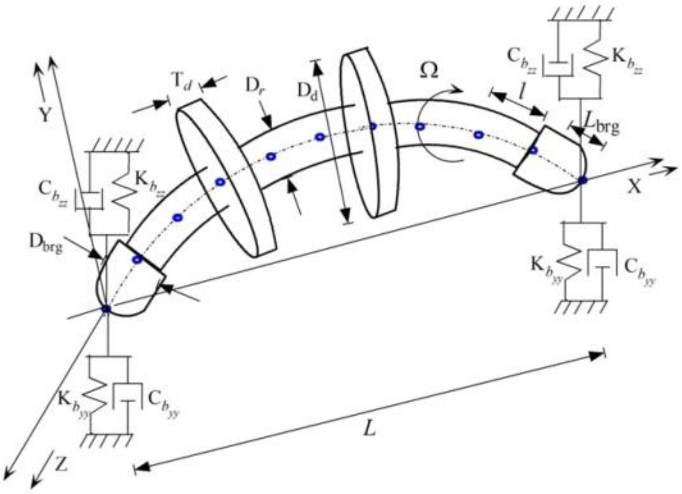

Fig. 2.28 Schematic diagram of the rotor mounted on rolling contact bearings

Table 2.5 Discs parameter

Disc No.	Diameter (m)	Thickness (m)	Disc Positions
Disc - 1	0.25	0.05	4
Disc - 2	0.25	0.05	7

For better understanding of graphs, different legends, and line styles are used for representation. Second and third order models are abbreviated as SOM and TOM respectively, are used as a legend in some figures.

A. *Decay rate*

Fig. 2.29 shows the decay rate plot for the rotor bearing model. Here only two displacement modes have been presented. Diverging line in the figure gives the idea of forward and backward whirl, which are denoted as FW and BW. The BW is stable and the FE cut the zero line and reaches to unstable zone. The SLS of the system is found to be 3820 rpm.

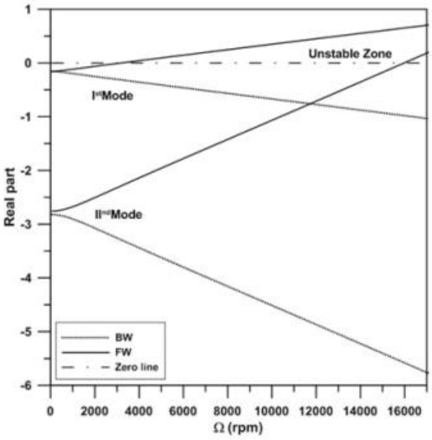

Fig. 2.29 Decay rate plot

B. *Campbell diagram*

Fig. 2.30 shows the campbell diagram. Here the first natural frequency of the system is calculated as 2710 rpm. Due to the presence of non-rotating damping stability increases and SLS is greater than FNF.

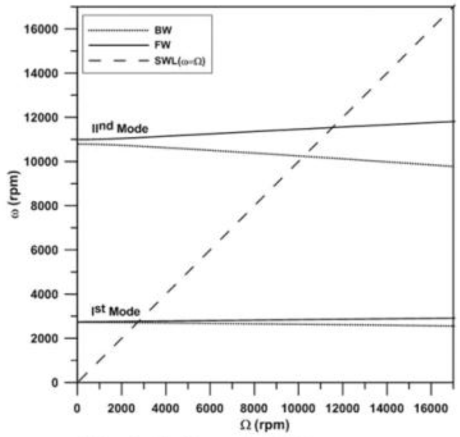

Fig. 2.30 Campbell diagram

C. *Modal damping factor*

Fig. 2.31 shows the MDF plot for the rotor bearing model. The MDF is plotted here considering first and second mode only. MDF also predicts the stability criteria and the value of SLS for the present system is 3820 rpm.

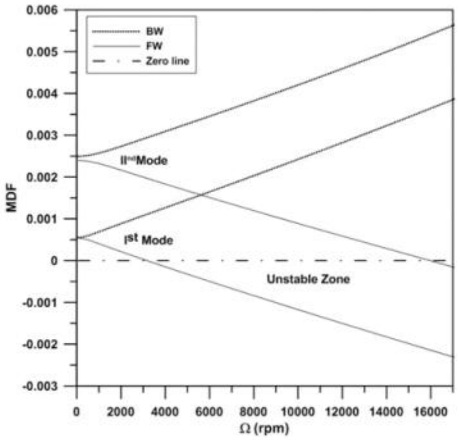

Fig. 2.31 Modal damping factor

D. Directional frequency response functions

This section illustrates the significance of third order model (TOM) over the conventional second order model (SOM) on rotor dynamics. TOM is developed after considering operator based constitutive relationship of a Zener model, which includes all types of asymmetry. Whereas SOM is done based on Voigt model, which is simplified version of Zener model and modulus operator is brought by assuming the denominator unity of previous one. Figs. 2.32(a), 2.32(b) and 2.32(c), below show a comparative results on hysteresis loop, response and energy dissipation plot respectively, of a uni-axial circular rod subjected to harmonic loading considering SOM and TOM. Length and diameter of the rod are same as rotor shaft and magnitude of harmonic excitation is 1 N. Finite element formulation of the viscoelastic rod is shown in Appendix-A. It is seen from all figures that SOM and TOM reflect same results as viscoelastic parameter appears in the denominator (b_1) is very small. But in rotor dynamics point of view, there may be a high impact of TOM that has seen in subsequent sections.

Since modelling of any rotating structure involves with rotation, th is study of directivity of modes is very important. The dFRF has an advantage of predicting the directivity by separating the modes in negative and positive excitation frequency region. The peaks of dFRFs achieve in positive (negative) zone is named as forward (backward) and directivity is decided by measuring both peak heights. For a symmetric rigid rotor dFRFs become an even function of spin speed as gyroscopic effect is neglected, the strength of cross dFRFs become s zero. While incorporating system anisotropy, the dFRFs are not an even function of frequency, the magnitude of cross dFRFs is non-zero and deviation becomes larger at high speed (Kessler and Kim (2002)). This is further illustrated here to show the influence of anisotropy using higher order model. For this reason dFRFs are plotted for different spin speeds considering SOM and TOM.

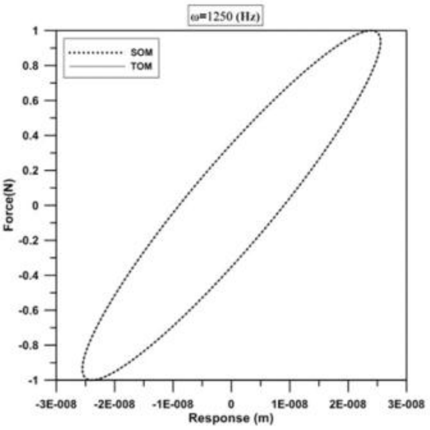

(a) Hysteresis loop

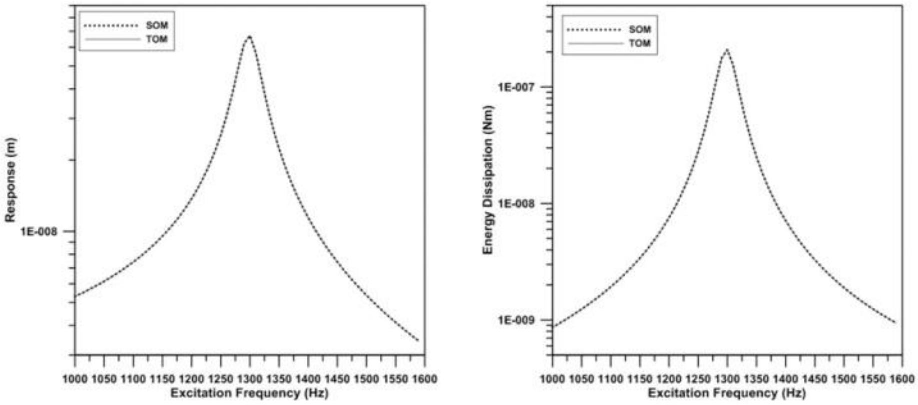

(b) Response plot (c) Energy dissipation plot

Fig. 2.32 Comparative plots of uniaxial rod between SOM and TOM

Fig. 2.33 shows the dFRF of the system considering second and third order model. These figures are plotted for three different values of spin speed , i.e. 200 rpm, 800 rpm and 1700 rpm. At low speed (Fig. 2.33(a)), both SOM and TOM are reflecting backward whirl. In Fig. 2.33(b), SOM (TOM) highlights backward (forward) whirl. But at high spin speed (Fig. 2.33(c)), SOM and TOM again show forward whirl. It is due to the presence of cross dFRFs generated by speed dependent gyroscopic matrix. In TOM, gyroscopic matrix appears in higher order term also, resulting a strongly dependent of cross dFRFs. With the help of dFRF it is easy to show the effectiveness of the third order model over the conventional second order model.

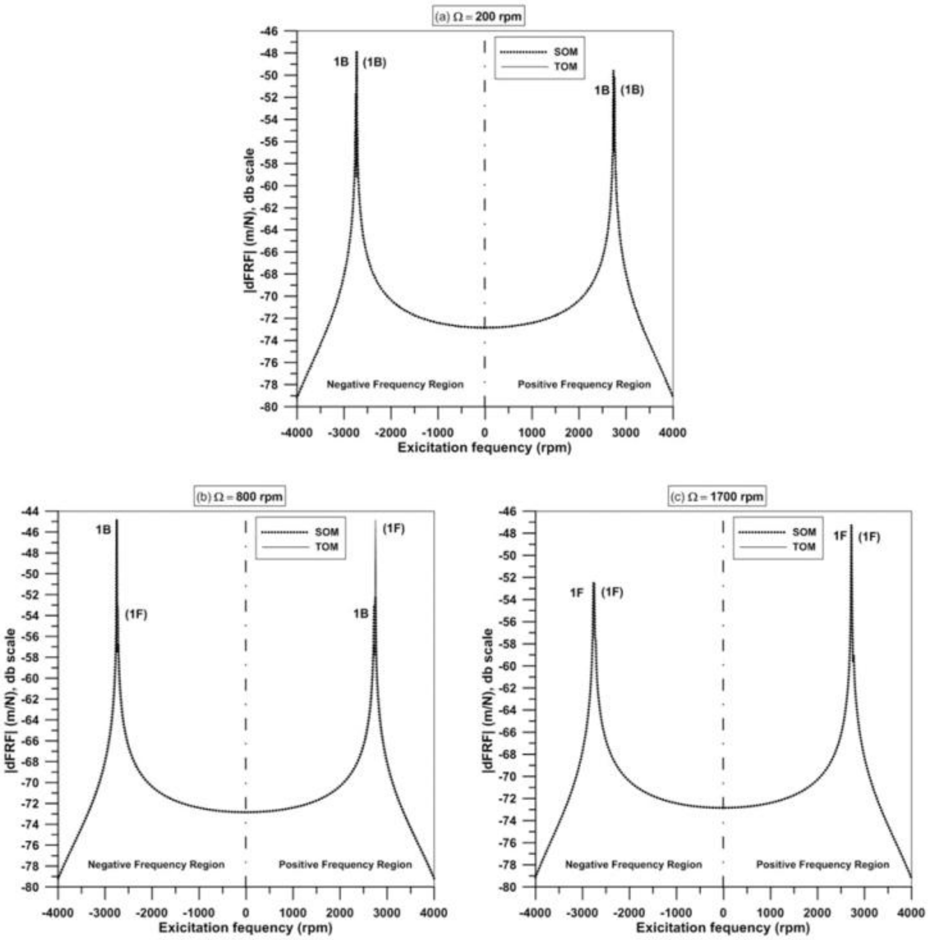

Fig. 2.33 dFRF at: (a) 200 rpm, (b) 800 rpm, (c) 1700 rpm

E. Mode shapes

Mode shapes have been shown in Figs. 2.34, 2.35, 2.36, 2.37, 2.38 and 2.39 at various spin speeds, i.e. for 200 rpm, 800 rpm and 1700 rpm considering SOM and TOM, respectively.

Clockwise rotations of the circles present in figure are considered as a backward whirl and counter clockwise rotation is the forward whirl. The starting point of each locus is marked by a marker (*) and the locus is kept incomplete to show its direction. In subsequent figures, same directivity of modes is seen for SOM and TOM, which is also correlating dFRF plot. At both speed, 200 rpm and 800 rpm 1B mode is dominant for SOM, whereas TOM changes its directivity from 1B to 1F. At higher speed of 1700 rpm SOM also changes its directivity from 1B to 1F. The tendency of cross dFRFs due to speed dependent gyroscopic matrix is high for TOM and its directivity changes earlier.

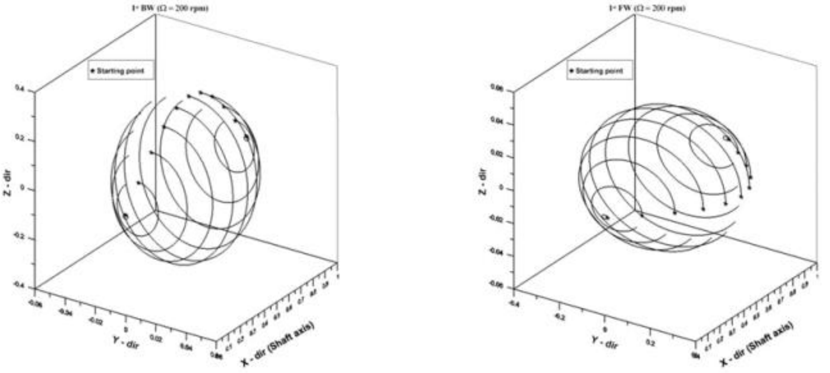

(a) 1B mode **(b) 1F mode**

Fig. 2.34 Mode shapes for SOM at 200rpm

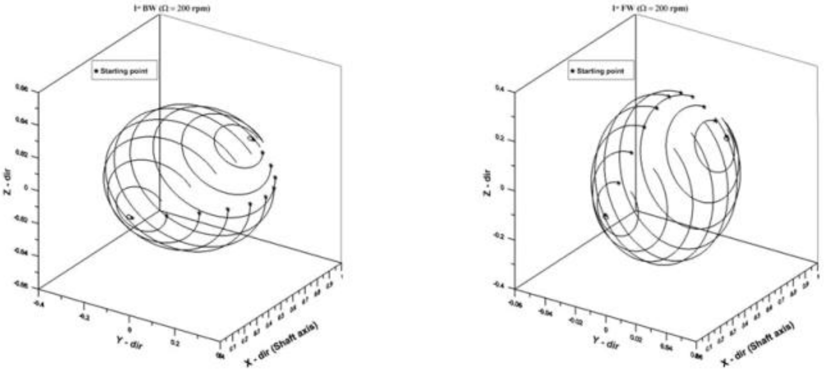

(a) 1B mode **(b) 1F mode**

Fig. 2.35 Mode shapes for TOM at 200rpm

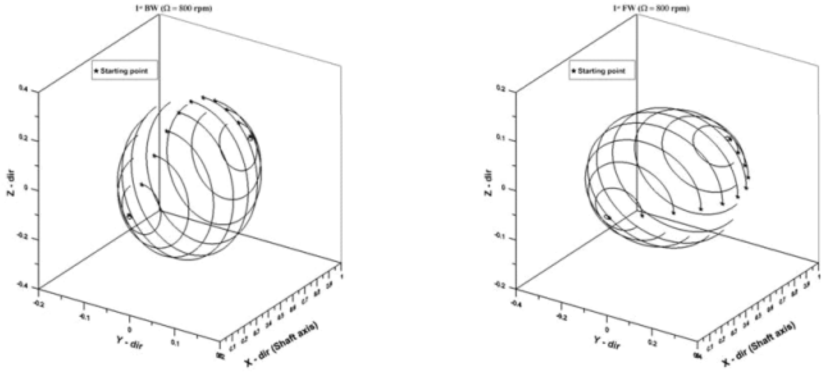

(a) 1B mode **(b) 1F mode**

Fig. 2.36 Mode shapes for SOM at 800rpm

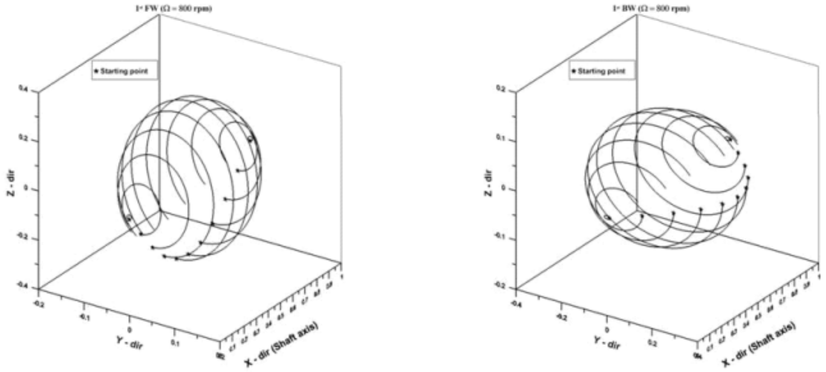

(a) 1F mode **(b) 1B mode**

Fig. 2.37 Mode shapes for TOM at 800rpm

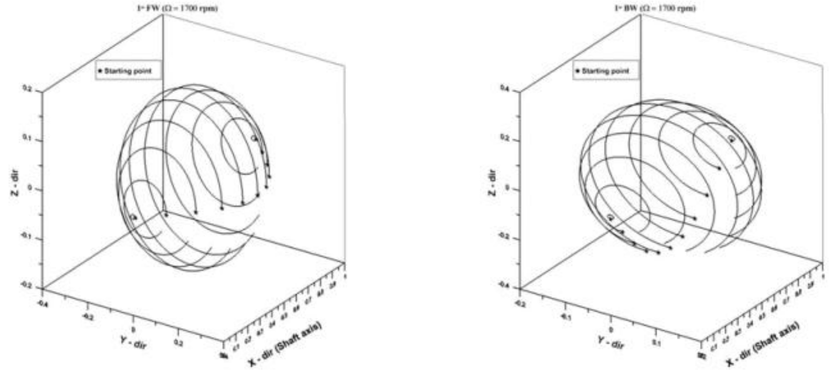

(a) 1F mode (b) 1B mode

Fig. 2.38 Mode shapes for SOM at 1700rpm

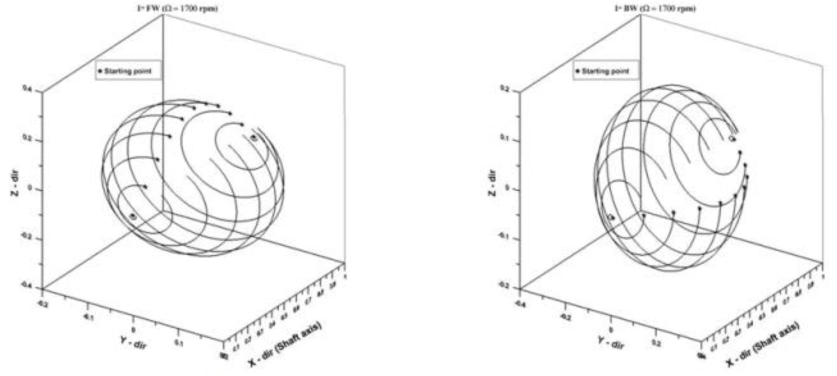

(a) 1F mode (b) 1B mode

Fig. 2.39 Mode shapes for TOM at 1700rpm

2.11.3.2 Rotor model with sliding contact bearings

For the simulation purpose, a flexible rotor shaft with circular cross section is supported by short sliding contact bearings at the ends, as shown schematically in Fig. 2.40. Two noded beam elements are considered in finite element analysis of the rotor shaft. The continuum is discretized into 10- elements or 11- nodes and each node has 4- degree of freedom, i.e. 2- displacements and 2- rotations. Length of the mild steel shaft is taken as $L = 1\ \mathrm{m}$. Diameter

(D_r) of the boundary elements, which are mounted to two bearings, is taken as 0.1 m and rest of the portion is 0.05 m. Two identical discs of same material (mild steel) are located non symmetrically and the details are shown in the Table 2.5. While material properties and operator parameters of the rotor are shown in Table 2.2.

$K_{b_{yy}}, K_{b_{yz}}, K_{b_{zy}}, K_{b_{zz}}$ and $C_{b_{yy}}, C_{b_{yz}}, C_{b_{zy}}, C_{b_{zz}}$ are the four stiffness and four damping coefficient of the sliding contact bearing are obtained after following Friswell et al. (2010). Other significant parameters for obtaining the sliding contact bearing coefficients are as follow: Length to diameter ratio of bearing $L_{brg}/D_{brg} = 0.3$, $D_{brg} = 0.1\text{m}$. Viscosity of oil inside bearing is 0.1 Pa-Sec, the radial clearance between the journal and the bearing is 0.0001 m. The static thrust force exerted on to the left (right) bearing is calculated through self-weight and their values are 318.514 N (282.456 N). These two unequal forces produce different bearing coefficients at two ends.

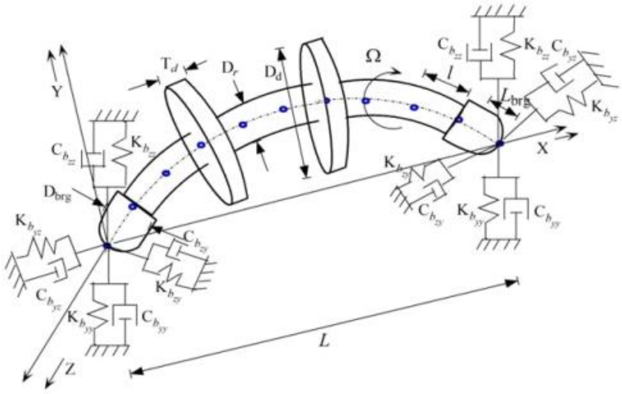

Fig. 2.40 Schematic diagram of the rotor

For better understanding of graphs, different legends, line styles and color lines are used for representation. Second and third order models are abbreviated as SOM and TOM respectively, are used as a legend in some figures.

A. Campbell diagram

Campbell diagram of rotor shaft is demonstrated in Fig. 2.41. Diverging line in the figure gives the idea of forward and backward whirl. In forward whirling, whirl and spin have a same sense, while it is opposite in backward whirling. Those are denoted as 'F' and 'B'. For better clarity, only four whirl lines are presented in the figures which are sufficient to predict basic characteristic. The four whirl lines indicate first four modes. Two rising lines are for oil motion and marked as 1F, 2F, as increase with spin speed. Oil motion for a particular spin speed is defined from these lines. From the figure, it is seen that the oil motion is almost half of the spin speed as noticed by Muszynska (1986). Two other whirl lines are almost parallel to abscissa and denoted as 1B, 3F. Those are due to bending of shaft. A 45^0 line is also drawn here, which is called as 'Synchronous Whirl Line (SWL). It helps to locate natural frequency for bending mode only through intersection between SWL and whirl frequency lines. First point of intersection indicates first natural frequency and is denoted as FNF. In this case FNF is 2768 rpm, where SWL intersect the 1B line. Operating region of the rotor is divided into super and sub critical zone, if the spin speed is above and below the FNF.

Curve veering phenomenon of the eigen frequencies occurs in the post-critical speed zone and encircled in the campbell diagram to show a zoomed view in Fig. 2.41(b). This phenomena ware illustrated by many researchers like Crandal and Yeh (1989) and Jei and Lee (1992). When a couple of modes approach, they do not intersect, but repel to each other and abruptly diverge by maintaining their continuity. The zoomed view of curve veering zone, gives the clear idea of veering nature of eigen frequency, swapping from one direction to the other. Firstly, a pair of eigen frequency due to oil motion, start below the SWL and increases with a spin speed marked as 1F (red line) and 2F (green line), They will veer after the interaction with the two bending modes i.e. represented as 1B (blue line) and 3F (magenta line). Two hypothetical lines (dash and dot) are drawn to show the actual trend of 2F and 3F whirl lines.

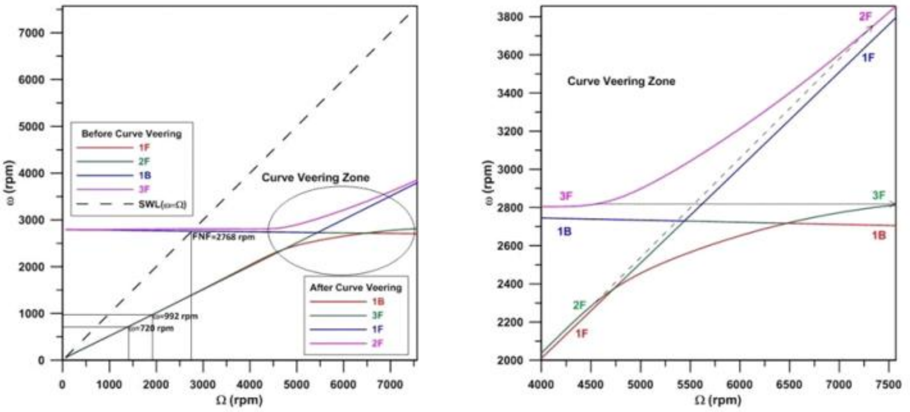

(a) Full view **(b) Zoomed View of the curve veering zone**

Fig. 2.41 Campbell diagram

B. Decay rate

Real parts of the first four modes are plotted with a spin speed in Fig. 2.42. Here real part of first mode (red line) touches the zero line at a speed of 4753 rpm and system instability starts. Likewise curve veering phenomena as seen in the campbell diagram, real part lines also change their trend at same frequency.

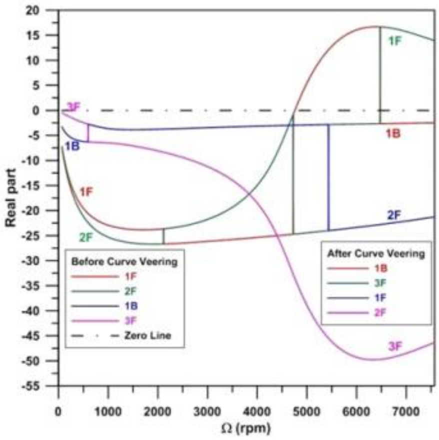

Fig. 2.42 Decay rate plot

C. Modal damping factor

Fig. 2.43(a) represents the variation of MDF with the rotor spin speed for four modes. The stability limit of spin speed (SLS) is found to be 4753 rpm when the MDF of 1F mode becomes negative. It is also seen from the figure, at low spin speed the value of MDF due to oil motion is very high and drastically reduces with high spin speed. It is due to inability to provide high viscous effect of oil seal at high speed. The veering characteristic also causes an exchange of trend in MDF plots too. A zoomed view of the curve veering zone is presented in Fig. 2.43(b) to show the swapping of modes. Veering phenomenon of the present system occurs near to SLS point.

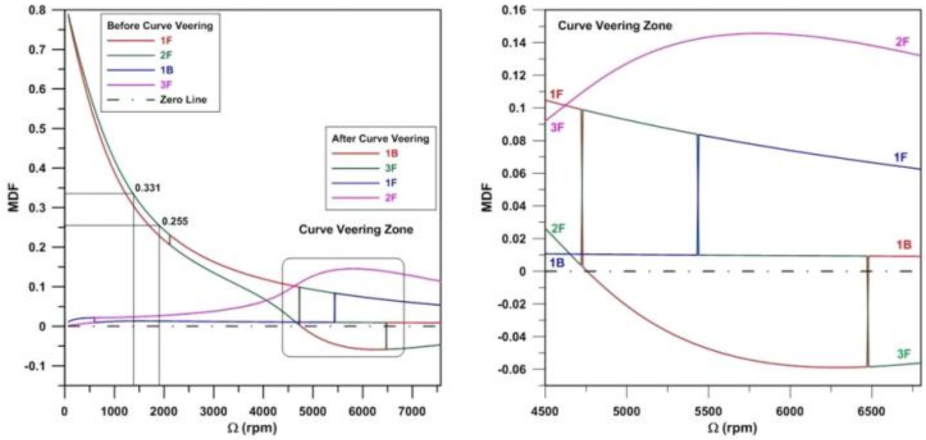

(a) Full view **(b) Zoomed view of the curve veering zone**

Fig. 2.43 Modal damping factor

D. Directional frequency response functions

Fig. 2.44(a) and Fig. 2.44(b) represent the dFRF plot at finite element node 2 for two individual speeds, i.e. 1400 rpm and 1900 rpm respectively. Two individual spin speeds are chosen to show the effect of cross dFRF considering SOM and TOM. Significance of plotting dFRF nearer to the bearing node helps to show the proper effect of oil whirl phenomena in figures. In both figures, first peak due to oil whirl appears at 720 rpm and 992 rpm respectively. Similarly, same kind of peak is also visible in negative zone at almost the same speed in TOM case, but in SOM case no such peak is found. With the incorporation of gyroscopic stiffening effect in higher order, TOM becomes stiffer than SOM, the solid line passes lower the dash line and negative zone oil peak slightly appears. The positive zone peak height is more and named as 1F (1F) for SOM (TOM) cases. The 2F mode is very close to 1F mode, but it does not appear, as lower mode (1F) is dominating. The oil whirl is achieved approximately at half of the spin speed. The oil seal has two boundary conditions one at the bearing end which is non - rotating surface and another at the journal end rotate at spin speed. Thus whole oil motion occurs at an average of the two surface speeds. The resonance frequency is also determined from campbell diagram by dropping projections from oil whirl line to abscissa and ordinate respectively. This phenomenon occurs up to curve veering phenomenon where swapping of modes occurs and oil whirl line becomes almost parallel to the abscissa. Further increase of spin speed, the shifting of peak does not happen.

As the excitation frequency increases the system gains another resonance due to bending mode at 2768 rpm. In Fig. 2.44(a), when the rotor rotates at 1400 rpm, dFRF of SOM and TOM has duplicate nature. The peak height in negative zone is more and named as 1B (1B). The 3F mode does not appear in SOM (TOM), as close to 1B, which is dominating. Major difference between SOM and TOM is visualized in Fig. 2.44(b), when the dFRF is plotted for a high spin speed. The magnitude of peak achieved is lower(higher) for SOM(TOM) case in the positive frequency region, therefore the directivity of modes is termed as 1B (3F). This is due to existence of anisotropy in TOM, becomes more prominent at high speed and changes its directivity. This verifies the significance of third order model over the second order model.

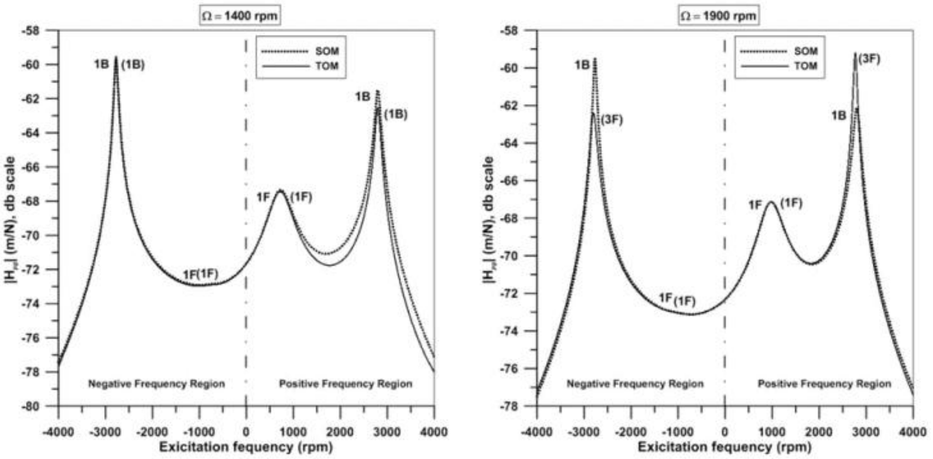

(a) At 1400 rpm (a) At 1900 rpm

Fig. 2.44 dFRF plot

E. Mode shapes

First four mode shapes have been shown in Fig. 2.45 and Fig. 2.46 at spin speed of 1400 rpm considering SOM and TOM respectively. In both figures mode shapes for SOM and TOM reflect same directivity. 1F and 2F mode are due to oil whirl and of conical shapes. Cylindrical type of mode does not achieve, as two bearings provide unequal thrust forces. These type s of shapes appear when rotor acts as a rigid body. Whereas bending of rotor is clearly visible in 1B and 3F modes.

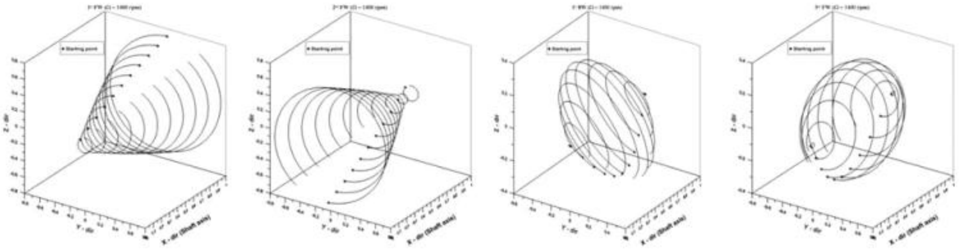

(a) 1F mode **(b) 2F mode** **(c) 1B mode** **(d) 3F mode**

Fig. 2.45 Mode shapes for SOM at 1400 rpm

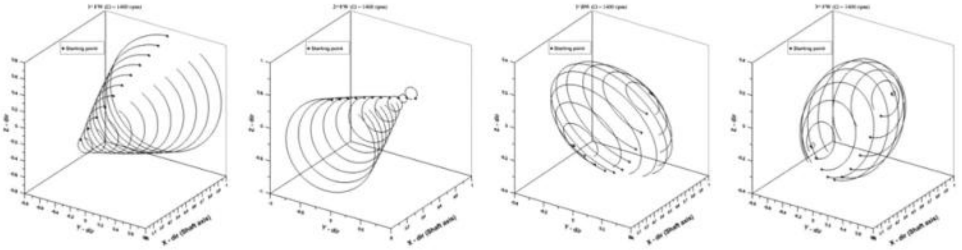

(a) 1F mode **(b) 2F mode** **(c) 1B mode** **(d) 3Fmode**

Fig. 2.46 Mode shapes for TOM at 1400 rpm

Fig. 2.47 and Fig. 2.48 show first four Mode shapes at 1900 rpm considering SOM and TOM respectively. Two consecutive conical shapes due to oil motion are found for both cases. Like dFRFs, a similar nature is found in bending modes. At high speed the cross dFRFs of TOM become powerful, forwards mode is dominating and appears first.

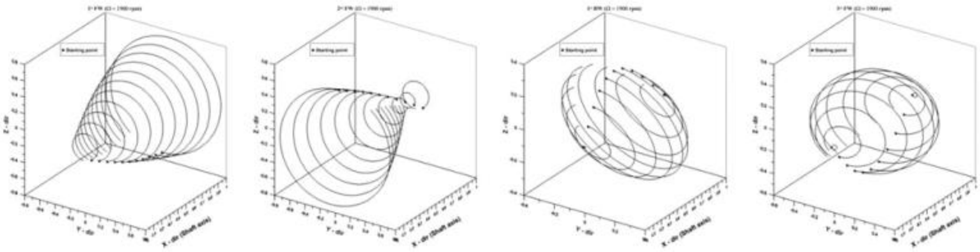

(a) 1F mode **(b) 2F mode** **(c) 1B mode** **(d) 3F mode**

Fig. 2.47 Mode shapes for SOM at 1900rpm

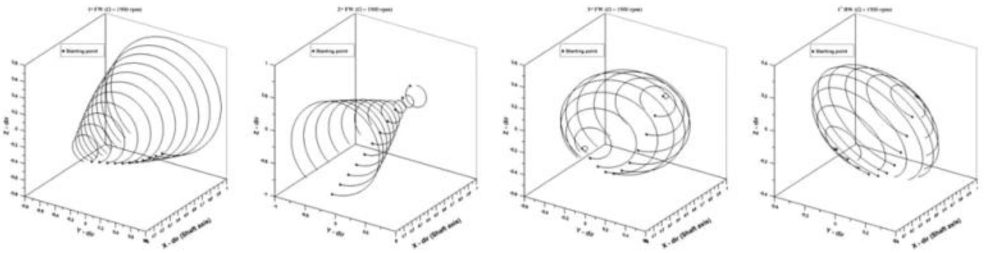

(a) 1F mode (b) 2F mode (c) 3F mode (d) 1B mode

Fig. 2.48 Mode shapes for TOM at 1900rpm

2.12 Summary

This chapter shows the mathematical modelling for isotropic viscoelastic rotor bearing system using an operator based approach. Two distinct techniques, i.e., classical model and finite element model are used here to achieve such type of modelling. The operator based constitutive relationship is used to bring down higher order equations of motion. The inherent material properties decide the number of viscoelastic parameters as well as the order of differential equation. Therefore, lower degree of polynomial is chosen to model the low damped material, whereas higher degree polynomial is appropriate for the high damped material. Taking an example of low and high damped material shows the effectiveness of modelling techniques. Modelling is done on a variety of support conditions, i.e. rigid bearing, rolling contact bearing and sliding contact bearing.

From the comparative study of CM and FEM, it concludes that in most of the cases, both models predict similar result, when the discs are kept within the range between $L^* = 0.2$ to 0.8. If the discs are kept outside of this range, then CM fails to extract the exact result as compared with FEM. Based on the several analyses, complete databases of the two methods are given in Table 2.6 and Table 2.7. There is a small difference between CM and FEM in the tabulated values.

Table 2.6 Comparison of modal parameters for low damped material: Case - 1

Modelling Approach	'Ω_{cr}' (rpm)				SLS (rpm)
	1st BW	1st FW	2nd BW	2nd FW	
CM	4030	4312	13512	15283	4030
FEM	4200	4490	16070	16294	4490

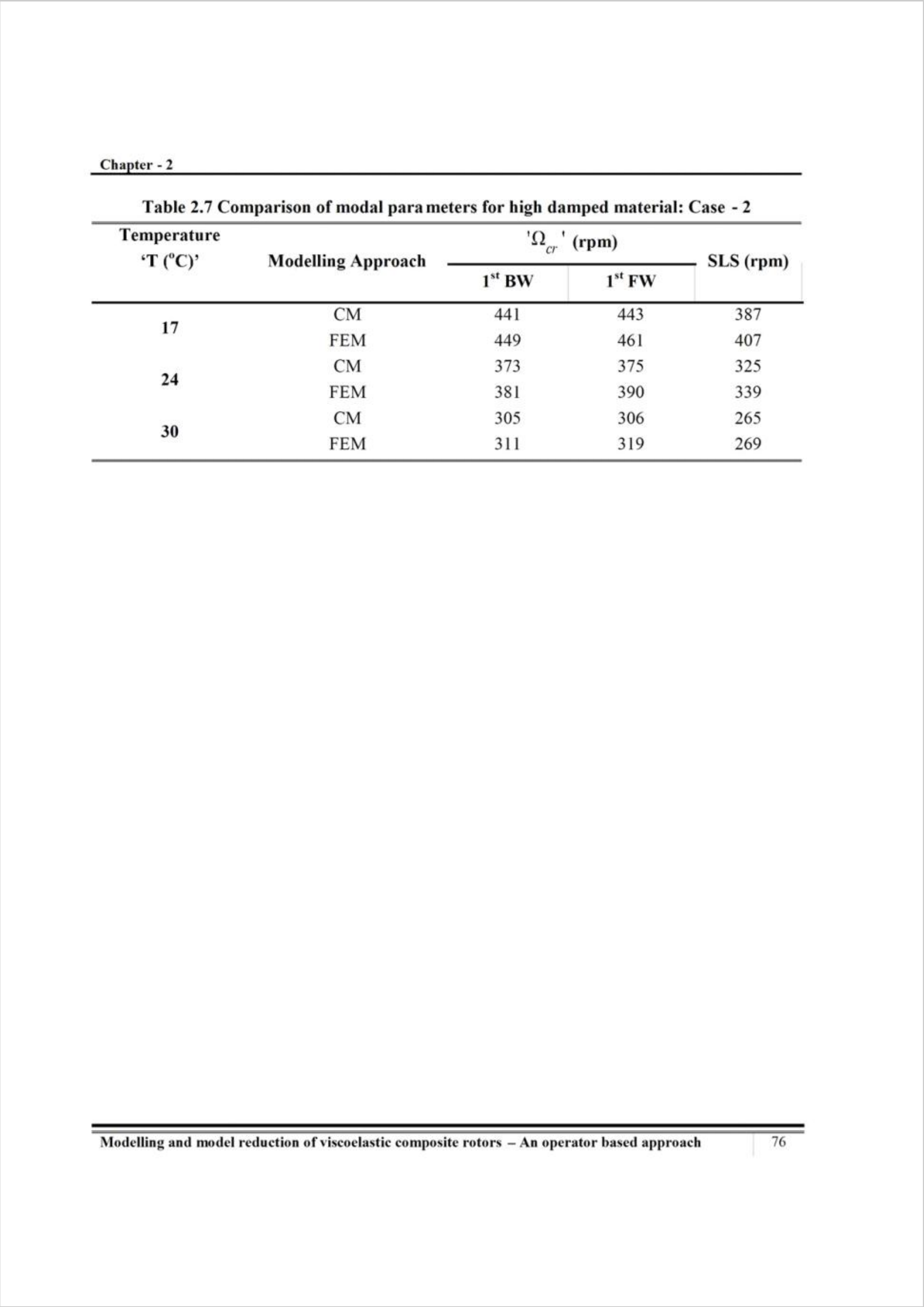

Table 2.7 Comparison of modal parameters for high damped material: Case - 2

Temperature 'T (°C)'	**Modelling Approach**	**'Ω_{cr}' (rpm)**		**SLS (rpm)**
		1st BW	**1st FW**	
17	CM	441	443	387
	FEM	449	461	407
24	CM	373	375	325
	FEM	381	390	339
30	CM	305	306	265
	FEM	311	319	269

Chapter-3

Modelling of Viscoelastic Rotor: Layered Composite Material

3.1 Preamble

Nowadays, composite material is a good alternative for heavy structural material. This also helps to reduce noise and vibration due to its light weight and high damping properties as seen in many literatures. The composite is formed either by fibre reinforcing or by layering several isotropic materials. The concept of using composite material in the field of rotor dynamics is also a new trend. This section covers to develop a composite rotor, where the composite is formed by perfect alignment of several viscoelastic isotropic materials. For this purpose both classical and finite element approaches are used and modelling is done using Euler-Bernoulli beam theory. Effectiveness of modelling is clarified through a comparative study.

3.2 Constitutive relationship

Viscoelastic material has a tendency to show both viscous and elastic properties. For generally linear viscoelastic material, instantaneous stress $(\sigma)$is directly proportional to instantaneous strain (ε). The generic form of constitutive relationship is written as

$$\sigma = E(\ )\varepsilon \tag{3.1}$$

$E(\ )$ is the modulus operator, whose numerator and denominator are a function of the differential time operator. Depending upon the material behaviour, order of the modulus operator is decided. In subsequent sections, the polynomial degree for both numerator and denominator is assumed to be unity, i.e. n=1. This correlates three element standard Zener model and expression of modulus operator is written as below.

$$E(\ )=\frac{a_0+a_1D}{b_0+b_1D} \tag{3.2}$$

3.3 Classical approach

Present section deals to develop a mathematical formulation of a multi layer, multi disc viscoelastic rotor using classical approach. The classical approach is also known as a lumped system approach, where total mass of the system is assumed to be concentrated at a single or few points and another portion is massless. A multi disc rotor is treated as a shaft with a multi point loading condition as shown in Fig. 3.1. The rotor shaft with N_d - disc is subjected to N_d loading points, and disc mass and an associated portion of shaft mass are accumulated at each disc location.

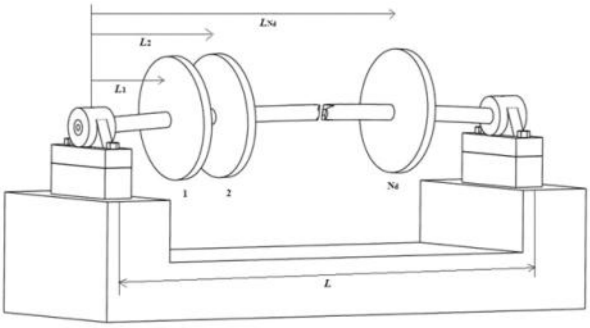

Fig. 3.1 Schematic diagram of multi layer, multi disc rotor bearing system

Fig. 3.2 indicates the cross sectional view of deformed multilayer rotor-shaft at some distance 'x' from the left end, where different layer's have been expressed in various shades of circle. An important assumption for the modelling of multilayer viscoelastic rotor is that all layers are perfectly bonded and no slippage takes place within layers during deformation . 'r_{i_k}' and 'r_{o_k}' are inner and outer radiuses of 'k^{th}' layer respectively. $v(x,t)$ and $w(x,t)$ represent the shaft centre coordinates along 'y' and 'z' direction at any instant of time; where 'x' and 't' are the spatial and temporal variables. For further analysis, a small radial element of thickness

'dr', with subtending angle '$d\Omega t$' at an angular location of 'Ωt' and 'r' distance from centre is considered. Here, 'ω' and 'Ω' are termed as whirl and spin frequencies of rotor respectively.

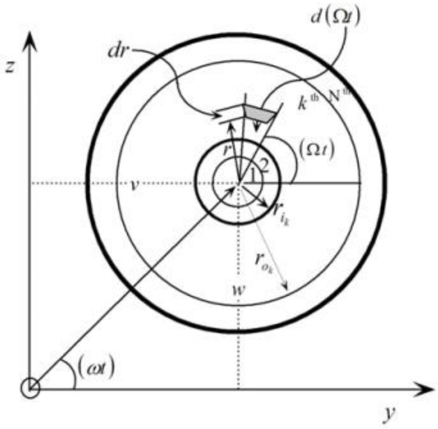

Fig. 3.2 Cross-sectional view of deformed rotor

To develop a model for viscoelastic rotor through classical formulation, four degrees of freedom are assumed at each disc location, in which, two translations and two rotations along and about 'y' and 'z' axis respectively. Therefore, in case of N_d-disc, $4 \times N_d$-degrees of freedom are to be considered.

A rotating frame of reference as shown in Fig. (2.4), has been considered to capture damping force exerted by the rotating parts. Rotating frame rotates with same speed of rotor (Ω) and about an axis passing through the origin of stationary frame. For a constant rotational speed, at any instant of time 't', angle between two frames is 'Ωt'. The coordinate in rotating frame are expressed with '$\sim$'.

Following Tondl (1965) and Thomson et al. (2012), expression of potential energy 'V' for N_d disc rotor in a rotating frame of reference is given below.

$$V = \frac{1}{2}\{\tilde{\mathbf{q}}\}^T \left[\mathbf{C}_{ij}\right]\{\tilde{\mathbf{q}}\} \qquad i, j = 1, 2, \ldots, 4N_d \tag{3.3}$$

Where, $\left[\mathbf{C}_{ij}\right]$ is stiffness matrix. The expressions of various stiffness coefficients of the shaft are derived separately and are available in Appendix-C. The generalized coordinate, $\{\tilde{\mathbf{q}}\}$

is written as $\{\tilde{\mathbf{q}}\}=\{\tilde{v}_1 \quad \tilde{\varphi}_1 \quad \tilde{w}_1 \quad \tilde{\vartheta}_1 \quad \cdots \quad \tilde{v}_{\mathrm{N}_d} \quad \tilde{\varphi}_{\mathrm{N}_d} \quad \tilde{w}_{\mathrm{N}_d} \quad \tilde{\vartheta}_{\mathrm{N}_d}\}^T$. $(\tilde{v}),(\tilde{w})$ and $(\tilde{\varphi}),(\tilde{\vartheta})$ are the lateral and angular deformations along and about $'\tilde{y}'$ and $'\tilde{z}'$ direction respectively.

Lagrange's equation is employed to the potential energy expression to obtain expression of force. Using complex coordinate, force vector $\{\tilde{\mathbf{F}}\}$ in a rotating frame of reference is given as,

$$\begin{aligned}\{\tilde{\mathbf{F}}\}_{(2\mathrm{N}_d\times 1)} &= \left[\mathbf{C}_{ij}\right]\{\tilde{\mathbf{x}}_i\} \\ &= EI\left[\mathbf{K}_{ij}\right]\{\tilde{\mathbf{x}}_i\} \qquad i,j=1,2,\ldots,2\mathrm{N}_d\end{aligned} \tag{3.4}$$

$'E'$ is material modulus, $'I'$ is area moment of inertia, and $\{\tilde{x}_i\}$ is the generalized complex coordinate, viz. $\tilde{x}_{(2\mathrm{N}_d-1)}=\tilde{v}_{\mathrm{N}_d}+i\tilde{w}_{\mathrm{N}_d}$, $\tilde{x}_{2\mathrm{N}_d}=\tilde{\varphi}_{\mathrm{N}_d}+i\tilde{\vartheta}_{\mathrm{N}_d}$. $'i'$ is imaginary unit, $i=\sqrt{-1}$. The indices (i, j) are dropped in subsequent analysis for convenience.

The coordinates in rotating frames can be transformed to stationary frame and are written in Eq. (3.5). Though this transformation is developed by looking at displacements and forces in $'y'$ and $'z'$ direction, but same transformation is used for rotations and moments about $'y'$ and $'z'$ axis (Friswell et al. (2010b)). This is possible due to the fact that the generalized force expressed in Eq. (3.4) contains the components of force and moment along $\tilde{y}$ and $\tilde{z}$ directions. So these components can be coupled by using complex coordinates. Though physically coupling two angles $\tilde{\varphi}$ and $\tilde{\vartheta}$ does not mean anything as angles are not vectorial quantities. This is done for a mathematical purpose.

$$\{\tilde{\mathbf{x}}\}=\{\mathbf{x}\}\,\mathrm{e}^{-i\Omega t}, \tag{3.5}$$

Instead of isotropic elastic material, rotor shaft is made of several layers of viscoelastic materials. Assuming, $'\mathrm{N}_l'$ as the number of concentric layers and are perfectly bonded, as shown in Fig. (3.2).

To incorporate the material damping for each layer, Young's modulus $'E'$ and moment of inertia $'I'$ in Eq. (3.4) is replaced by modulus operator from Eq. (3.2) and modified equation is written for $'\mathrm{N}_l'$layers as:

$$\{\tilde{\mathbf{F}}\}_{(2\mathrm{N}_d\times 1)}=\sum_{k=1}^{\mathrm{N}_l}\left(\frac{a_{0_k} I_k + a_{1_k} I_k \mathrm{D}}{b_{0_k} + b_{1_k}\mathrm{D}}\right)[\mathbf{K}]\{x\}\,\mathrm{e}^{-i\Omega t}, \tag{3.6}$$

This differential time operator only operates on complex coordinates and exponential term. Because other terms are not time dependent. After differentiating with time operator, the above equation is again written as,

$$\left\{\tilde{\mathbf{F}}\right\}_{(2\mathrm{N}_d\times 1)}=\left(\left(\sum_{k=1}^{\mathrm{N}_l}\frac{a_{0_k}I_k}{b_{0_k}+b_{1_k}\mathrm{D}}-i\Omega\sum_{k=1}^{\mathrm{N}_l}\frac{a_{1_k}I_k}{b_{0_k}+b_{1_k}\mathrm{D}}\right)\left[\mathbf{K}\right]\{x\}+\sum_{k=1}^{\mathrm{N}_l}\frac{a_{1_k}I_k}{b_{0_k}+b_{1_k}\mathrm{D}}\left[\mathbf{K}\right]\{\dot{x}\}\right)\mathrm{e}^{-i\Omega t} \tag{3.7}$$

$$=\{\mathbf{F}\}\mathrm{e}^{-i\Omega t}$$

$\{\mathbf{F}\}$ is the generalized force due to stiffness and rotating damping measured in stationary frame. Rearranging the complex coordinate $\{x\}$ to its original coordinate $\{\mathbf{q}\}$, the force vector is written as,

$$\{\mathbf{F}\}_{(4\mathrm{N}_d\times 1)}=\left[\sum_{k=1}^{\mathrm{N}_l}\frac{a_{0_k}I_k}{b_{0_k}+b_{1_k}\mathrm{D}}\left[\mathbf{K}_B\right]\{\mathbf{q}\}+\sum_{k=1}^{\mathrm{N}_l}\frac{a_{1_k}I_k}{b_{0_k}+b_{1_k}\mathrm{D}}\Omega\left[\mathbf{K}_C\right]\{\mathbf{q}\}+\sum_{k=1}^{\mathrm{N}_l}\frac{a_{1_k}I_k}{b_{0_k}+b_{1_k}\mathrm{D}}\left[\mathbf{K}_B\right]\{\dot{\mathbf{q}}\}\right] \tag{3.8}$$

After multiplying imaginary unit with stiffness matrix, a new matrix $\left[\mathbf{K}_C\right]$ appears, which is skew symmetric in nature and known as a skew symmetric circulatory matrix. Here, $\left[\mathbf{K}_B\right]$ is a symmetric matrix, called as bending stiffness matrix. The expressions of $\left[\mathbf{K}_B\right]$ and $\left[\mathbf{K}_C\right]$ are given in Appendix-C. All three matrices, viz. damping matrix, bending stiffness matrix and circulatory matrix, are developed from stiffness matrix. Since stiffness matrix covers all coordinates, dissipation effects are taken care through all coordinates.

It is seen from the above equation that the degree of 'D' depends on the nature of viscoelastic material as well as the number of constituent material exists in the multi layering arrangement. Thus, for specific case the formulation is based on the two-layers rotor $\left(\mathrm{N}_l=2\right)$. The expression for generalized force for two layered rotor is shown in Eq. (3.9).

$$\begin{aligned}\{\mathbf{F}\}_{(4\mathrm{N}_d\times 1)}=&\left(\frac{a_{0_1}I_1}{b_{0_1}+b_{1_1}\mathrm{D}}+\frac{a_{0_2}I_2}{b_{0_2}+b_{1_2}\mathrm{D}}\right)\left[\mathbf{K}_B\right]\{\mathbf{q}\}+\Omega\left(\frac{a_{1_1}I_1}{b_{0_1}+b_{1_1}\mathrm{D}}+\frac{a_{1_2}I_2}{b_{0_2}+b_{1_2}\mathrm{D}}\right)\left[\mathbf{K}_C\right]\{\mathbf{q}\}\\&+\left(\frac{a_{1_1}I_1}{b_{0_1}+b_{1_1}\mathrm{D}}+\frac{a_{1_2}I_2}{b_{0_2}+b_{1_2}\mathrm{D}}\right)\left[\mathbf{K}_B\right]\{\dot{\mathbf{q}}\}\end{aligned} \tag{3.9}$$

Equation of motion is obtained by adding this force to all other force s, viz. forces from kinetic energy and external force, and is given below.

$$[\mathbf{M}]\{\ddot{\mathbf{q}}\}+[\mathbf{G}]\{\dot{\mathbf{q}}\}+\{\mathbf{F}\}=[\mathbf{P}]\{\boldsymbol{u}\} \tag{3.10}$$

In the preceding equation, $\{\boldsymbol{u}\}$ is the force vector originates due to some external disturbances, $[\mathbf{P}]$ defines the appropriate position of external forces, whose number of columns indicate the total disturbances and elements are chosen either zero or one to distribute the forces at the correct location. $[\mathbf{M}]$ is the symmetric mass matrix and $[\mathbf{G}]$ is the skew symmetric gyroscopic matrix. Those are also written in Appendix-C.

After operating the operand in denominator with other terms in Eq. (3.11), final equation of motion of the 2- layer, multi disc viscoelastic rotor, rotating at constant angular speed is written as:

$$\left[\mathbf{A}_0\right]\{\mathbf{q}\}+\left[\mathbf{A}_1\right]\{\dot{\mathbf{q}}\}+\left[\mathbf{A}_2\right]\{\ddot{\mathbf{q}}\}+\left[\mathbf{A}_3\right]\{\dddot{\mathbf{q}}\}+\left[\mathbf{A}_4\right]\{\ddddot{\mathbf{q}}\}=[\mathbf{B}]\{\boldsymbol{u}\} \tag{3.11}$$

The coefficients present in Eq. (3.11) are expressed as,

$$\left[\mathbf{A}_0\right]_{(4\mathrm{N}_d\times4\mathrm{N}_d)}=\left(a_{0_1}b_{0_2}I_1+a_{0_2}b_{0_1}I_2\right)\left[\mathbf{K}_B\right]+\Omega\left(a_{1_1}b_{0_2}I_1+a_{1_2}b_{0_1}I_2\right)\left[\mathbf{K}_C\right]$$

$$\left[\mathbf{A}_1\right]_{(4\mathrm{N}_d\times4\mathrm{N}_d)}=b_{0_1}b_{0_2}[\mathbf{G}]+\left(\left(a_{0_1}b_{1_2}I_1+a_{0_2}b_{1_1}I_2\right)+\left(a_{1_1}b_{0_2}I_1+a_{1_2}b_{0_1}I_2\right)\right)\left[\mathbf{K}_B\right]$$
$$+\Omega\left(a_{1_1}b_{1_2}I_1+a_{1_2}b_{1_1}I_2\right)\left[\mathbf{K}_C\right]$$

$$\left[\mathbf{A}_2\right]_{(4\mathrm{N}_d\times4\mathrm{N}_d)}=b_{0_1}b_{0_2}[\mathbf{M}]+\left(b_{0_1}b_{1_2}+b_{0_2}b_{1_1}\right)[\mathbf{G}]+\left(a_{1_1}b_{1_2}I_1+a_{1_2}b_{1_1}I_2\right)\left[\mathbf{K}_B\right]$$

$$\left[\mathbf{A}_3\right]_{(4\mathrm{N}_d\times4\mathrm{N}_d)}=\left(b_{0_1}b_{1_2}+b_{0_2}b_{1_1}\right)[\mathbf{M}]+b_{1_1}b_{1_2}[\mathbf{G}]$$

$$\left[\mathbf{A}_4\right]_{(4\mathrm{N}_d\times4\mathrm{N}_d)}=b_{1_1}b_{1_2}[\mathbf{M}]$$

$$[\mathbf{B}]_{(4\mathrm{N}_d\times r)}=\left(b_{0_1}b_{0_2}+\left(b_{0_1}b_{1_2}+b_{0_2}b_{1_1}\right)\mathrm{D}+b_{1_1}b_{1_2}\mathrm{D}^2\right)[\mathbf{P}];\ 'r'\text{ is the number of inputs.}$$

Equation of motion obtained by utilizing the classical approach, has its most significant importance. The size of the matrices is very small and depends only on number of discs, i.e. $\left(4\mathrm{N}_d\times4\mathrm{N}_d\right)$.

3.4 Finite element approach

Finite element method is used to discretized multilayered viscoelastic rotor where Euler-Bernoulli beam theory is used. Modelling is done on a single element and later assembling it for all elements to get the whole system behaviour. Forces due to bending action are obtained first and incorporated with other forces like inertia force, the force due to gyroscopic action to bring down equations of motion. The shear deformation effect can easily be added; however the same has been discarded at present for the sake of simplicity. The elemental length 'l' of a beam with nodal displacement variables is presented in Fig. 2.5.

Following Zorzi and Nelson (1977), the mechanical stress is incorporated in the infinitesimal element that is acting in the 'x' direction and expressed as:

$$\varepsilon_x = -r\cos\left[(\Omega-\omega)t\right]\frac{\partial^2 R(x,t)}{\partial x^2} \tag{3.12}$$

At any instant of time the bending moments 'M_{yy}' and 'M_{zz}' about 'y' and 'z' axes are as follows:

$$\begin{aligned} M_{zz} &= \int_0^{2\pi}\int_0^{r_o} -\left(v+r\cos(\Omega t)\right)\sigma_x r dr d(\Omega t) \\ M_{yy} &= \int_0^{2\pi}\int_0^{r_o} \left(w+r\sin(\Omega t)\right)\sigma_x r dr d(\Omega t) \end{aligned} \tag{3.13}$$

Expressions of 'σ_x' and 'ε_x', are substituted in Eq. (3.13), and the bending moment equations for 'N' layered rotor are rewritten as,

$$\begin{aligned} M_{zz} &= \sum_{k=1}^{N}\int_0^{2\pi}\int_{r_{i_k}}^{r_{o_k}} -\left(v+r\cos(\Omega t)\right)\frac{a_{0_k}+a_{1_k}\mathrm{D}}{b_{0_j}+b_{1_j}\mathrm{D}}\left[-r\cos(\Omega t-\omega t)\frac{\partial^2 R(x,t)}{\partial x^2}\right] r dr d(\Omega t) \\ M_{yy} &= \sum_{k=1}^{N}\int_0^{2\pi}\int_{r_{i_k}}^{r_{o_k}} \left(w+r\sin(\Omega t)\right)\frac{a_{0_k}+a_{1_k}\mathrm{D}}{b_{0_k}+b_{1_k}\mathrm{D}}\left[-r\cos(\Omega t-\omega t)\frac{\partial^2 R(x,t)}{\partial x^2}\right] r dr d(\Omega t) \end{aligned} \tag{3.14}$$

After integrating Eq. (3.14), the modified bending equation can be rewritten as follows:

$$\begin{Bmatrix} M_{zz} \\ M_{yy} \end{Bmatrix} = \begin{bmatrix} \sum_{k=1}^{N} \frac{a_{0_k} I_k}{b_{0_k} + b_{1_k} \mathrm{D}} & \sum_{k=1}^{N} \frac{a_{1_k} I_k}{b_{0_k} + b_{1_k} \mathrm{D}} \Omega \\ \sum_{k=1}^{N} \frac{a_{1_k} I_k}{b_{0_k} + b_{1_k} \mathrm{D}} \Omega & \sum_{k=1}^{N} - \frac{a_{0_k} I_k}{b_{0_k} + b_{1_k} \mathrm{D}} \end{bmatrix} \begin{Bmatrix} v'' \\ w'' \end{Bmatrix} + \begin{bmatrix} \sum_{k=1}^{N} \frac{a_{1_k} I_k}{b_{0_k} + b_{1_k} \mathrm{D}} & 0 \\ 0 & \sum_{k=1}^{N} - \frac{a_{1_k} I_k}{b_{0_k} + b_{1_k} \mathrm{D}} \end{bmatrix} \begin{Bmatrix} \dot{v}'' \\ \dot{w}'' \end{Bmatrix} \tag{3.15}$$

It is seen from the above equation that the order of differentiation 'D' is dependent on the nature of viscoelastic material likewise the number of constituent material exists in the multi layering arrangement. Thus, for simplicity the formulation is based on the two layers rotor (putting N=2).

The rotor is discretize with 2- noded beam element with four degrees of freedom per node. Four degrees of freedom are two displacements $v(x,t)$, $w(x,t)$, and two slopes $\varphi(x,t)$, $\vartheta(x,t)$ along and about $'y'$ and $'z'$ direction respectively. The nodal displacement vector is given as $\{\mathbf{q}(t)\}$.

$$\begin{Bmatrix} v \\ w \end{Bmatrix} = \left[\boldsymbol{\phi}(x) \right]^T \{\mathbf{q}(t)\}; \quad \varphi = -\frac{\partial w}{\partial x}; \quad \vartheta = \frac{\partial v}{\partial x} \tag{3.16}$$

The bending moment expression also helps to find the three common matrices (viz. stiffness, circulatory and damping matrices) of any rotating system. The diagonal elements of bending moment expression give rise to direct elements (e.g. direct stiffness, direct damping matrix) whereas the off-diagonal elements give rise to cross coupled elements i.e. circulatory matrix. The total bending energy is obtained after integrating the differential bending energy over elemental length. This contains the strain energy and dissipation function, and is expressed as,

$$P_B^e = \frac{1}{2} \int_0^l \begin{Bmatrix} v'' \\ -w'' \end{Bmatrix}^T \begin{Bmatrix} M_{zz} \\ M_{yy} \end{Bmatrix} dx \tag{3.17}$$

Putting the terms of Eq. (3.15) and Eq. (3.16) in Eq. (3.17), and Lagrangian concept is applied to obtain generalized force, which is expressed in terms of nodal displacement vector and time derivatives. For two layers rotor the generalized force vector in $'xy'$ and $'xz'$ plane are givens as:

$$\{\mathbf{F}\}=\begin{Bmatrix}\{\mathbf{F}_{xy}\}\\\{\mathbf{F}_{zx}\}\end{Bmatrix}=\left(\frac{a_{0_1}I_1}{b_{0_1}+b_{1_1}\mathrm{D}}+\frac{a_{0_2}I_2}{b_{0_2}+b_{1_2}\mathrm{D}}\right)\left[\mathbf{K}_B\right]\{\mathbf{q}\}+\Omega\left(\frac{a_{1_1}I_1}{b_{0_1}+b_{1_1}\mathrm{D}}+\frac{a_{1_2}I_2}{b_{0_2}+b_{1_2}\mathrm{D}}\right)\left[\mathbf{K}_C\right]\{\mathbf{q}\}$$
$$+\left(\frac{a_{1_1}I_1}{b_{0_1}+b_{1_1}\mathrm{D}}+\frac{a_{1_2}I_2}{b_{0_2}+b_{1_2}\mathrm{D}}\right)\left[\mathbf{K}_B\right]\{\dot{\mathbf{q}}\} \tag{3.18}$$

The expression of $\left[\mathbf{K}_B\right]$ and $\left[\mathbf{K}_C\right]$ are given as

$\left[\mathbf{K}_B\right]=\int_0^l\left[\boldsymbol{\phi}''(x)\right]\left[\boldsymbol{\phi}''(x)\right]^T dx,$ and $\left[\mathbf{K}_C\right]=\int_0^l\left[\boldsymbol{\phi}''(x)\right]\begin{bmatrix}0 & 1\\-1 & 0\end{bmatrix}\left[\boldsymbol{\phi}''(x)\right]^T dx$ in which, Hermite shape function matrix $\left[\boldsymbol{\phi}(x)\right]$, (refer to Rao (2009) is given as $\left[\boldsymbol{\phi}(x)\right]=\begin{bmatrix}\{\boldsymbol{\phi}_{xy}(x)\} & \{0\}\\\{0\} & \{\boldsymbol{\phi}_{zx}(x)\}\end{bmatrix}$, with subscripts in the elements showing the respective planes.

Following Rao (2009), inertia force and force due to gyroscopic couple are obtained after utilizing kinetic energy expression. These forces are incorporated with the above generalized force to get the equation of motion for two layered viscoelastic rotor.

$$[\mathbf{M}]\{\ddot{\mathbf{q}}\}+[\mathbf{G}]\{\dot{\mathbf{q}}\}+\{\mathbf{F}\}=[\mathbf{P}]\{\boldsymbol{u}\} \tag{3.19}$$

In the preceding equation, $\{\boldsymbol{u}\}$ is the force vector originated due to some external disturbances, $[\mathbf{P}]$ defines the nodal position of external forces, whose number of columns indicate the total disturbances and elements are chosen either zero or one to distribute the forces at the correct nodal locations. The mass matrix can be formed as,

$[\mathbf{M}]_{(8\text{x}8)}=\left[\mathbf{M}_T\right]_{(8\text{x}8)}+\left[\mathbf{M}_R\right]_{(8\text{x}8)}$,

where $\left[\mathbf{M}_T\right]_{(8\text{x}8)}$ and $\left[\mathbf{M}_R\right]_{(8\text{x}8)}$ are translational mass matrix and rotary inertia matrix respectively. $[\mathbf{G}]_{(8\times8)}$ is the gyroscopic matrix. Following Rao (2009), matrix expression used in formulation is given below,

$$\left[\mathbf{M}_T\right]=\int_0^l \rho A\boldsymbol{\phi}(x)\boldsymbol{\phi}(x)^T\,dx,$$

$$\left[\mathbf{M}_R\right]=\int_0^l \rho I\boldsymbol{\phi}'(x)\boldsymbol{\phi}'(x)^T\,dx,$$

$$\left[\mathbf{G}\right]=\int_{0}^{l}2\rho I\Omega\boldsymbol{\phi}'(x)\begin{bmatrix}0 & 1\\ -1 & 0\end{bmatrix}\boldsymbol{\phi}'(x)^{T}\,dx,$$

Utilizing all the above factors, the final equation of motion of full model at constant angular speed is rewritten as,

$$\left[\mathbf{A}_0\right]_{n\times n}\{\mathbf{q}\}_{n\times 1}+\left[\mathbf{A}_1\right]_{n\times n}\{\dot{\mathbf{q}}\}_{n\times 1}+\left[\mathbf{A}_2\right]_{n\times n}\{\ddot{\mathbf{q}}\}_{n\times 1}+\left[\mathbf{A}_3\right]_{n\times n}\{\dddot{\mathbf{q}}\}_{n\times 1}+\left[\mathbf{A}_4\right]_{n\times n}\{\ddddot{\mathbf{q}}\}_{n\times 1}=[\mathbf{B}]_{n\times r}\{\boldsymbol{u}\}_{r\times 1}\qquad(3.20)$$

where,

$$\left[\mathbf{A}_0\right]_{n\times n}=\left(a_{0_1}b_{0_2}I_1+a_{0_2}b_{0_1}I_2\right)\left[\mathbf{K}_B\right]_{n\times n}+\Omega\left(a_{1_1}b_{0_2}I_1+a_{1_2}b_{0_1}I_2\right)\left[\mathbf{K}_C\right]_{n\times n}$$

$$\left[\mathbf{A}_1\right]_{n\times n}=b_{0_1}b_{0_2}[\mathbf{G}]_{n\times n}+\left(\left(a_{0_1}b_{1_2}I_1+a_{0_2}b_{1_1}I_2\right)+\left(a_{1_1}b_{0_2}I_1+a_{1_2}b_{0_1}I_2\right)\right)\left[\mathbf{K}_B\right]_{n\times n}$$
$$+\Omega\left(a_{1_1}b_{1_2}I_1+a_{1_2}b_{1_1}I_2\right)\left[\mathbf{K}_C\right]_{n\times n}$$

$$\left[\mathbf{A}_2\right]_{n\times n}=b_{0_1}b_{0_2}[\mathbf{M}]_{n\times n}+\left(b_{0_1}b_{1_2}+b_{0_2}b_{1_1}\right)[\mathbf{G}]_{n\times n}+\left(a_{1_1}b_{1_2}I_1+a_{1_2}b_{1_1}I_2\right)\left[\mathbf{K}_B\right]_{n\times n}$$

$$\left[\mathbf{A}_3\right]_{n\times n}=\left(b_{0_1}b_{1_2}+b_{0_2}b_{1_1}\right)[\mathbf{M}]_{n\times n}+b_{1_1}b_{1_2}[\mathbf{G}]_{n\times n}$$

$$\left[\mathbf{A}_4\right]_{n\times n}=b_{1_1}b_{1_2}[\mathbf{M}]_{n\times n}$$

$$[\mathbf{B}]_{n\times r}=\left(b_{0_1}b_{0_2}+\left(b_{0_1}b_{1_2}+b_{0_2}b_{1_1}\right)\mathrm{D}+b_{1_1}b_{1_2}\mathrm{D}^2\right)[\mathbf{P}]_{n\times r}$$

$\{\mathbf{q}\}_{n\times 1}=\left\{v_1\quad \varphi_1\quad w_1\quad \vartheta_1\quad \cdots\quad v_{\mathcal{N}}\quad \varphi_{\mathcal{N}}\quad w_{\mathcal{N}}\quad \vartheta_{\mathcal{N}}\right\}^{T}$, '$\mathcal{N}$' is the total number of nodes.

With keen observation, it is noted that the order of the equation depends on the viscoelastic material model. 'n' is the total degree of freedom. The associated mass, gyroscopic and stiffness matrices are shown in Appendix-D.

3.5 State space representation

To establish the standard eigenvalue problem, Eq. (3.11) and Eq. (3.20) is conjoined with an identity equation to obtain the state space form as shown below,

$$[\mathcal{E}]\{\dot{\mathcal{X}}\}=[\mathcal{A}]\{\mathcal{X}\}+[\mathcal{B}]\{\boldsymbol{u}\}\qquad(3.21(a))$$

$$\{\mathcal{y}\} = [\mathcal{C}]\{\mathcal{x}\} + [\mathcal{D}]\{\boldsymbol{u}\} \tag{3.21(b)}$$

where,

$$[\mathcal{E}] = \begin{bmatrix} [\mathbf{I}] & [0] & [0] & [0] \\ [0] & [\mathbf{I}] & [0] & [0] \\ [0] & [0] & [\mathbf{I}] & [0] \\ [0] & [0] & [0] & [\mathbf{A}_4] \end{bmatrix}, \ [\mathcal{A}] = \begin{bmatrix} [0] & [\mathbf{I}] & [0] & [0] \\ [0] & [0] & [\mathbf{I}] & [0] \\ [0] & [0] & [0] & [\mathbf{I}] \\ -[\mathbf{A}_0] & -[\mathbf{A}_1] & -[\mathbf{A}_2] & -[\mathbf{A}_3] \end{bmatrix},$$

$$[\mathcal{B}] = \begin{bmatrix} [\mathbf{0}] \\ [\mathbf{0}] \\ [\mathbf{0}] \\ [\mathbf{B}] \end{bmatrix}, \ [\mathcal{C}] = \begin{bmatrix} [\mathbf{L}] & [\mathbf{0}] & [\mathbf{0}] & [\mathbf{0}] \end{bmatrix},$$

$$\{\mathcal{x}\} = \begin{Bmatrix} \{\mathbf{q}\} \\ \{\dot{\mathbf{q}}\} \\ \{\ddot{\mathbf{q}}\} \\ \{\dddot{\mathbf{q}}\} \end{Bmatrix}, \ \{\boldsymbol{u}\} = \begin{Bmatrix} \{\mathbf{0}\} \\ \{\mathbf{0}\} \\ \{\mathbf{0}\} \\ \{\mathbf{B}\} \end{Bmatrix},$$

$[\mathcal{E}]$ is the descriptor matrix, $[\mathcal{A}]$ is the system state matrix, $[\mathcal{B}]$ is the input matrix, $[\mathcal{C}]$ is the output matrix, $[\mathcal{D}]$ is the direct transmission matrix. $\{\mathcal{x}\}$ is the state vector. $\{\boldsymbol{u}\}$ is the vector of 'r' inputs, and $\{\mathbf{y}\}$ is the vector of output quantities. Elements of matrix $[\mathbf{L}]$ are chosen zero or one to select correct output from all states.

3.6 Model implementation

For the simulation purpose a simply supported, two-layered, two-disc rotor shaft is shown schematically in Fig. 3.3(a), of length of rotor is L, and diameter is D_r, mounted on bearings at the ends, considered to generate simply supported boundary conditions. Two discs are located at a distance of 'L_1' and 'L_2' from the left end.

On the other side of this figure (Fig. 3.3(b)) cross sectional view of two concentric layer shaft with distinct material densities 'ρ_i' and 'ρ_o' is displayed. Equivalent density and radius ratio of such cross section is expressed respectively as:

$$\rho = \rho_i \Re^2 + \rho_o \left(1 - \Re^2\right), \text{ where } \Re = \frac{r_i}{r_o} \tag{3.22}$$

For the case where inner layer is interchanged with the outer layer, keeping the respective masses unchanged, the radius ratio is represented as:

$$\mathfrak{R}' = \sqrt{1-\mathfrak{R}^2} \tag{3.23}$$

As $\mathfrak{R} \to 0$ the whole cross section is filled with the outer material of density ρ_o and $\mathfrak{R} \to 1$ signifies the cross section is made of inner material of density ρ_i. The radius ratios are used for finding out their effects and influences on the dynamics of a two layered rotor.

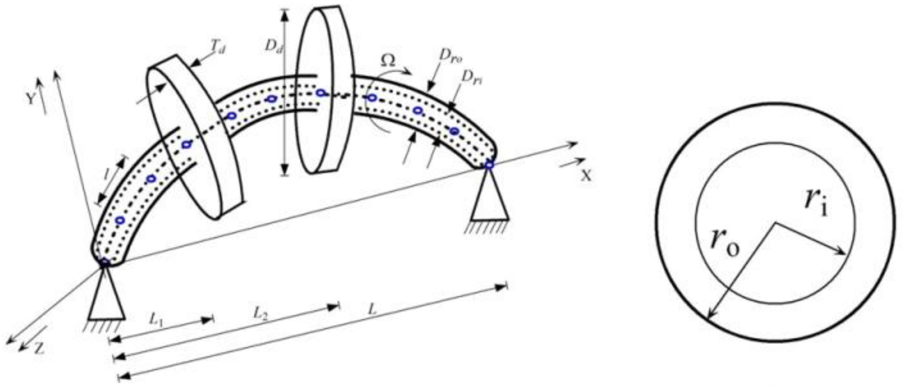

(a) A deformed rotor disc arrangement

(b) Cross-sectional view of deformed rotor

Fig. 3.3 Schematic diagram of the rotor

3.7 Result simulation and discussion

This part presents the numerical solutions to examine the dynamic behaviour of a two-layered viscoelastic rotor-shaft arrangement. A comparative study has been done for both classical model and finite element model approaches. Eigenvalue analysis has a significant role in the dynamic analysis of the rotor shaft system. Campbell diagram, decay rate plot, and modal damping factor are estimated from eigenvalues. Few such studies are described in subsequent sections. For understanding the effects of material behaviour in rotors, two sets of case studies have been shown below:

- **Case - 1:** multi layer composite rotor made of aluminium and steel, both materials are examples of low damped materials.
- **Case - 2:** multi layer composite rotor made of PVC and LORD LD-400; both materials are examples of high damped materials.

3.7.1 Simulated results obtained from aluminium and steel composite rotor: Case - 1

Two layer rotor made of aluminium and steel is considered for study, in which length of rotor is $L=1\text{ m}$, and diameter is $D_r=0.05\text{ m}$, mounted on bearings at the ends, considered to generate simply supported boundary conditions. Two identical discs are symmetrically located at distance $'L_1'$ and $'L_2'$ from the left end. The rotor shaft is made of mild steel and aluminium, but the discs are of mild steel. The various geometric dimensions of discs are considered in this analysis, those are shown in Table 3.1. The viscoelastic parameters of aluminium and steel are extracted from storage modulus and loss factor, which are clearly mentioned in Appendix-A. The extracted data are directly used here referring in Table 3.2.

Table 3.1 Discs parameter

Disc	Material	Diameter (m)	Thickness (m)	Mass un-balance (kg m)	Disc position (m)
Disc-1	Mild steel	0.20	0.05	10e-06	$L_1=0.3$
Disc-2	Mild steel	0.20	0.05	10e-06	$L_2=0.7$

Table 3.2 Material properties and extracted viscoelastic parameters

Material	Density $'\rho'$ (kg/m^3)	Storage Modulus $'E'$ (Pa)	Loss Modulus $'\eta'$	Fixed Parameters		Designed Parameters	
				a_0	b_0	a_1	b_1
Mild Steel	7800	2.1e+11	2.9e-02	2.1e+11	1	7.51e+05	1.475e-09
Aluminium	2750	7.13e+10	5.0e-02	7.13e+10	1	4.79e5	2.068e-9

A comparative study is done on various numerical results for both classical model (CM) and finite element model (FEM). Most of the results are obtained for the radius ratio $\mathfrak{R}=0.3$, otherwise it has been mentioned. For better understanding of graphs, different legends, line styles, and markers are used for representation of these models. Nice match in all figures between both models shows the correctness of this study.

A. Stability limit of spin speed

Fig. 3.4 shows the decay rate plot, where maximum real part of all eigenvalues are plotted with various spin speeds for three different radius ratio $(\mathfrak{R}=0.0,0.2,0.3)$. It is clear from figure that the SLS increases with increase in radius ratio and their values in rpm are 2280(2340), 2430(2500), and 2600(2680) for CM(FEM) respectively, when aluminium is kept as inside layer.

SLSs are calculated based on different parameters, viz. disc position, and radius ratio as shown in Fig. 3.5. SLS for various disc positions are shown in Fig. 3.5(a). Placement of first disc is changing from left end to middle of shaft, while second disc changing its position from right end to the middle of the shaft. From the figure it is noticed that, SLS of the system varies with disc position, and non-central position gives higher value than central position, which is due to stiffening effect of gyroscopic couple. It is also seen from the figure that SLS for both CM and FEM are reflecting similar values up to the range of $L^{*} = 0.2 \text{ to } 0.8$. Beyond that range classical model fails to extract the correct values of SLS as same as FE model due to data insufficiency. The stiffness coefficients for classical model predict incorrect result when L_1 is very small or L_2 is very large.

Fig. 3.5(b) shows the calculated value of SLS for various radius ratios when aluminium is kept as an inner layer and an outer layer. This study helps to understand the behaviour of the multi layering of various materials. After visualizing the figure some important conclusion can be drawn that the shaft performance measured in term of SLS is good only when the less stiffer material like aluminium is kept inside and the more stiffer material like steel forms the outside layer of the rotor. As the equivalent density increases with radius ratios, there is an involvement of critical radius ratio and after that SLS is found to go down.

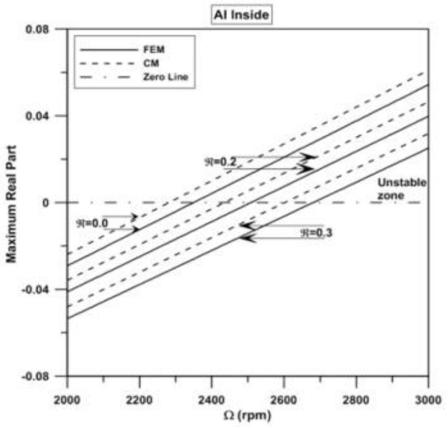

Fig. 3.4 Decay rate plot

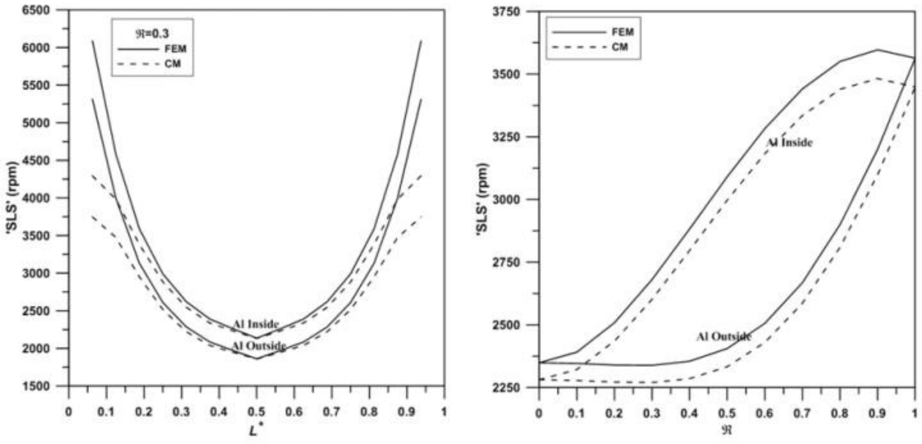

(a) For various disc positions **(b) For various radius ratio**

Fig. 3.5 Stability limit of spin speed

B. Campbell diagram

Fig. 3.6 demonstrates campbell diagram, which is plotted between the whirl-frequency and the rotor spin speed. Considering four consecutive bending modes, campbell diagram is drawn for a particular radius ratio $(\Re = 0.3)$ and keeping aluminium as an inner layer. Resonance frequencies are reflected in the campbell diagram when the whirl frequencies intersect synchronous whirl line (SWL) and corresponding spin speed is known as critical speed (Ω_{cr}). The values of 'Ω_{cr}'for four modes considering CM and FEM are given in Table 3.5. It is seen that there is very small difference (less than 1%) between CM and FEM in first two modes. But it has a little high value in higher modes. Thus, CM gives satisfactory results in lower mode.

Fig. 3.7 also shows the campbell diagram for three different radius ratios $(\Re = 0.0, 0.2, 0.3)$ and considering first displacement mode only. The first point of intersection indicates the first natural frequency of the system and is denoted by FNF. Fig. 3.7(b) reveals that the eigen-frequency and FNF both increase with the high value of radius ratio. In the present case the value of FNF in rpm for three different radius ratios are 2282(2295), 2435(2451), 2602(2620) for CM(FEM) respectively, when aluminium (Al) is considered as inside layer. But when aluminium is considered as an outside layer in Fig. 3.7(a), the values of FNF in rpm are

2282(2295), 2272(2287), 2270(2286) for CM(FEM) respectively. As aluminium is less stiffer than steel, effective stiffness of the system substantially decrease when 'Al' form the outer layer, FNF decreases with increase in radius ratio.

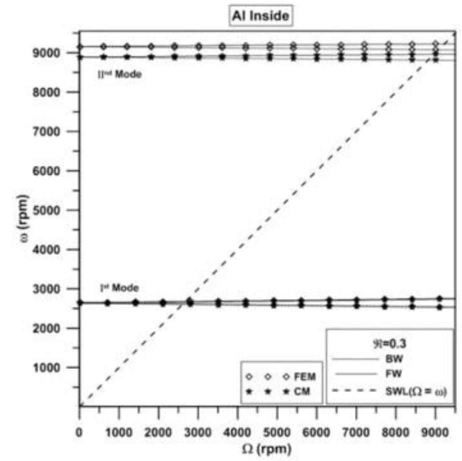

Fig. 3.6 Campbell diagram for two displacement Mode

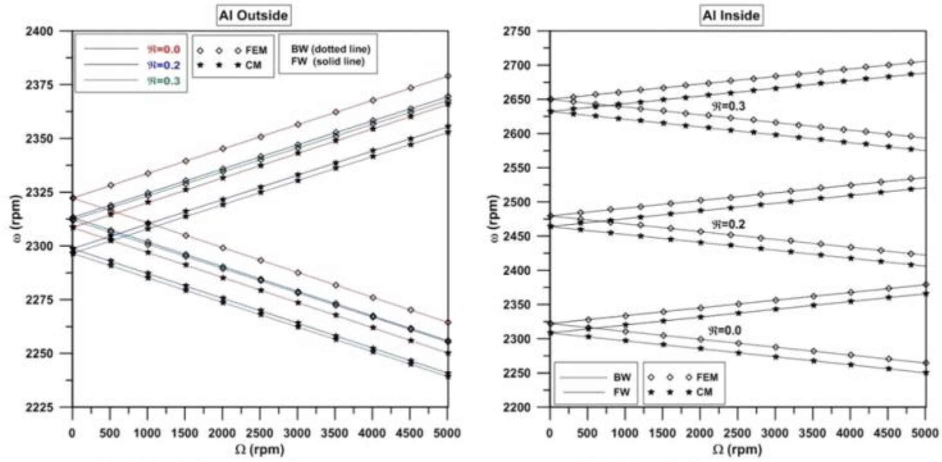

(a) Aluminium outside case

(b) Aluminium inside case

Fig. 3.7 Campbell diagram for various radius ratio

Fig. 3.8(a) shows the values of FNF for various disc positions. Two discs are symmetrically located, their positions are correlated as $L_1 = L - L_2$. If two discs are approaching from boundary to centre or vice versa, their positions are expressed by a single Non-dimensional parameter $L^* = L_1/L$. Due to the gyroscopic stiffening effect, the system FNF is high when the discs are near the boundary.

Fig. 3.8(b) draws the values of FNF for various radius ratios, when aluminium is kept as an inner and outer layer. Shaft performance in terms of FNF is good only when aluminium is kept inside and mild steel forms outside coating of rotor. As aluminium is less stiff than other material and undergoes higher deflection and velocity, when it forms an outer layer. Considering aluminium an inner layer, FNF reduces further for high value of radius ratio. It is due to enhancement of system mass. So, there should be a critical value of radius ratio for achieving the optimum performance.

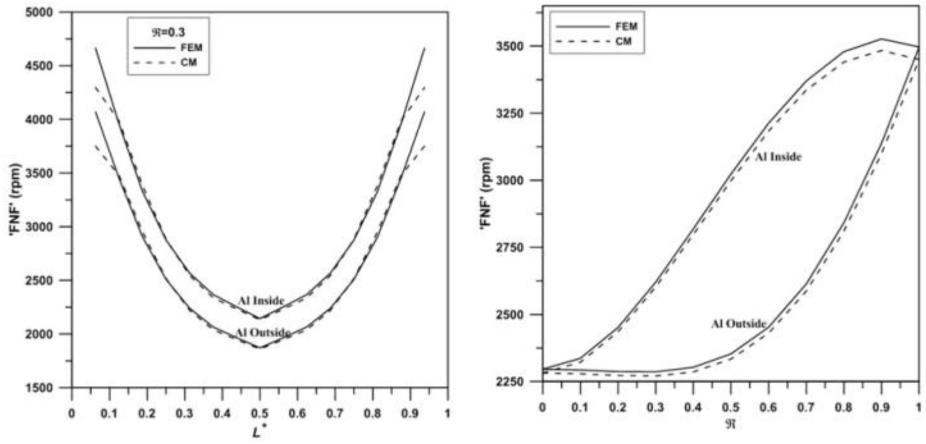

(a) For various disc positions **(b) For various radius ratio**

Fig. 3.8 First natural frequency

C. *Modal damping factor*

Assessment of SLS for various radius ratios through MDF is shown in Fig. 3.9(a). In the figure, MDF is only for two modes (first forward and first backward) and keeping aluminium as a core material. It has the incremental value for a backward whirl with spin speed, whereas it has decrementing nature for a forward whirl and after certain spin speed becomes negative. Thus, system instability initiates due to forward whirl only. It is noted that the values of SLS in rpm are 2280(2340), 2430(2500), and 2600(2680) for CM(FEM). Though SLS increases with radius ratio, but MDF for small radius ratio is high at low frequency and later intersect each other. As damping of aluminium is higher than steel, MDF gives higher value for the small radius ratio.

In Fig. 3.9(b), MDF is plotted for first four modes (two forward and two backward) at $\Re=0.3$ and aluminium is kept as an inner layer. The values of MDF reach too high for the higher side mode. Thus, lower mode has a tendency to become unstable earlier.

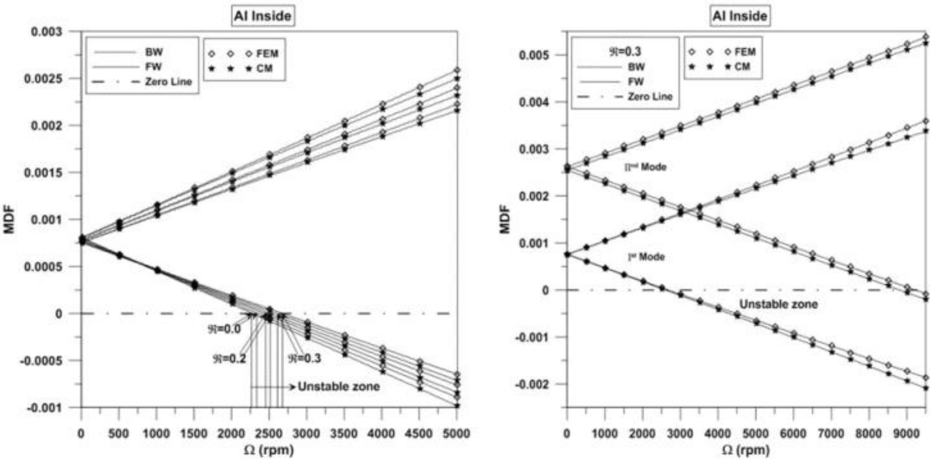

(a) For three radius ratio **(b) For four consecutive modes**

Fig. 3.9 Modal damping factor

D. Frequency response due to mass unbalance

Unbalance response (UBR) of the second disc is plotted for various rotational speeds as shown in Fig. 3.10. In which, Fig 3.10(a) shows unbalance response for three different radius ratio, when aluminium is kept as an inner layer. From the figure it is clearly visible that the resonance peak is shifted towards the right direction as the radius ratio increases, it is due to the system becoming stiffer.

Fig. 3.10(b) shows the UBR for $\Re=0.3$, aluminium inside and outside case. It is seen that there is a substantial improvement of peak shifting, when aluminium is considered as an inner layer as compared with aluminium as an outer layer. Hence the rotor performance is much better in case when the less stiff material is kept as an inner layer.

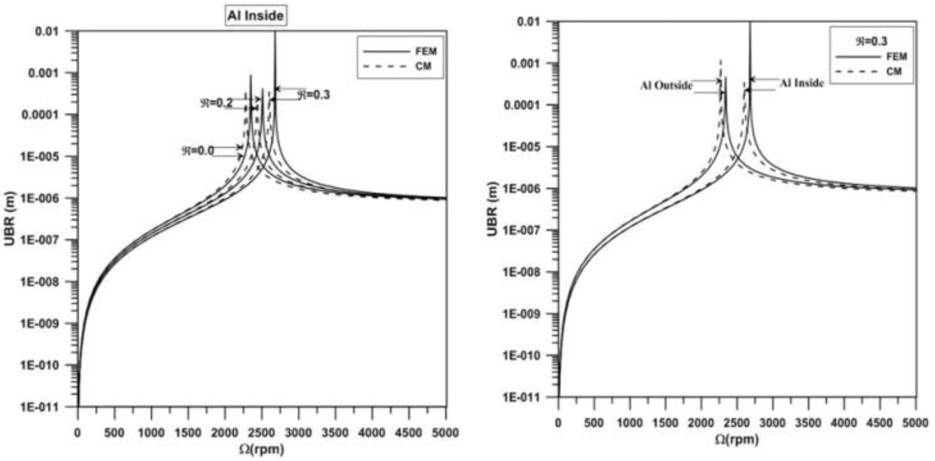

(a) For three radius ratio (b) For Aluminium inside - outside case

Fig. 3.10 Unbalance frequency response

E. Time response due to mass unbalance

Fig. 3.11 shows the steady state time response of the second disc due to unbalance for two radius ratios, viz. $\Re=0.2$ and $\Re=0.3$ considering rotor spin speed is 2500 rpm. The plot in Fig. 3.11(a) shows unstable nature as response monotonically increases. Whereas steady state stable response pattern is observed in Fig. 3.11(b). With the increase in radius ratio from $\Re=0.2$ and $\Re=0.3$, system nature becomes stiffer, thus the plot in second case shows stable nature. The initial part of steady state stable responses show combined effects of steady state and transient state response which later smoothens because the transient effect diminishes.

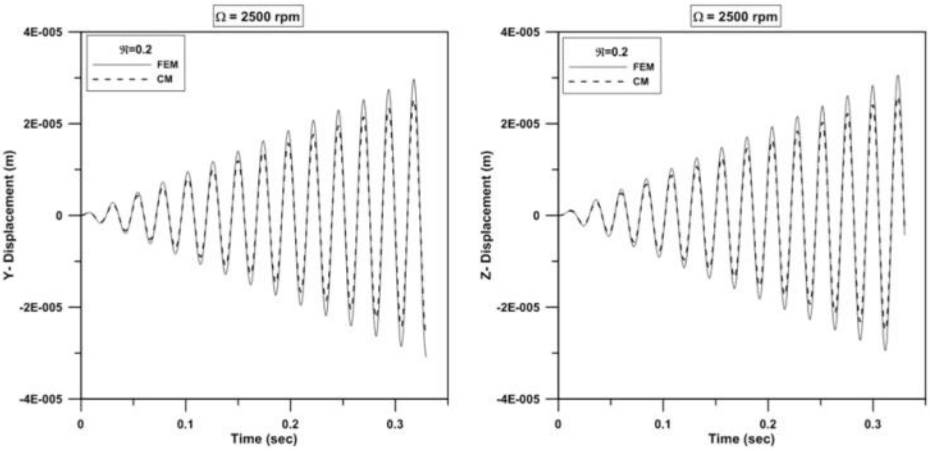

(a) Unstable zone

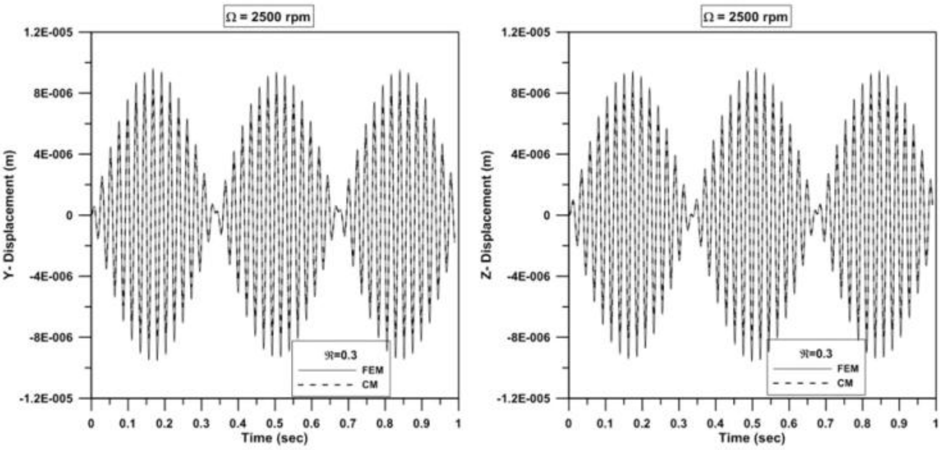

(b) Stable zone

Fig. 3.11 Time response plot

F. Whirl orbit

An orbit is a path traced by a point on rotor with time, which is obtained by plotting time response along y-direction vs. z-direction. Figs. 3.12(a) and 3.12(b) show orbit plot due to unbalance. The same time responses as discussed in previous section are used to procure orbit plot. The rotor orbit in first case increases monotonically for $\Re = 0.2$, whereas it remains constant in second case for $\Re = 0.3$. In first case rotor spin speed is above the SLS and system shows unstable behaviour.

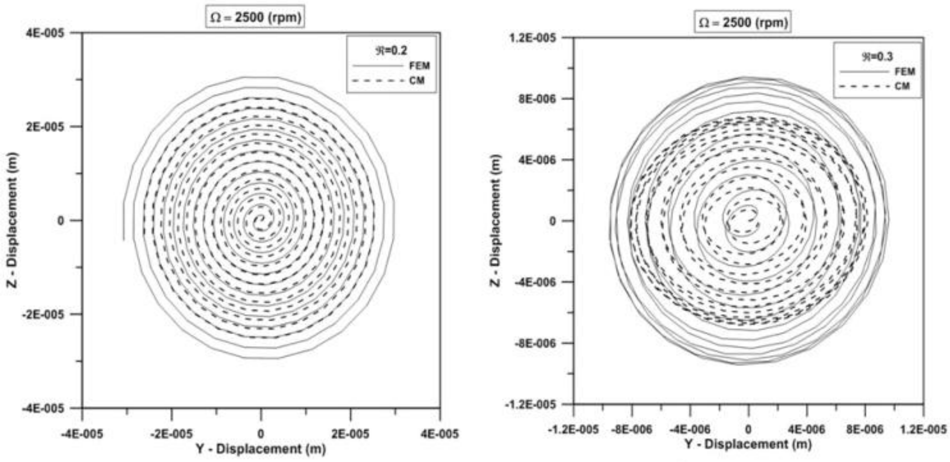

(a) Unstable zone **(b) Stable zone**

Fig. 3.12 Whirl orbit

3.7.2 Simulated results obtained from PVC and Lord LD-400 composite rotor: Case - 2

In the second example, two layered rotor made of high damped material, i.e. Poly Vinyl Chloride (PVC) as one material and Lord LD-400 polymers as second material, is chosen. Length and diameter of the shaft are 0.5 m and 0.05 m respectively. Following Roy (2008) and Roy et al. (2013), material properties of two layers are shown in Table 3.3. Two discs are mounted on the rotor shaft. The disc dimensions are given in Table 3.4 below. Both CM and FEM approaches are used to represent the numerical results.

Table 3.3 Material properties of the rotor

Material	Density 'ρ' (kg/m^3)	'a_0'	'a_1'	'b_0'	'b_1'
PVC	1390	1.3785e+06	5.0641e+03	1	0.0016
LORD LD-400	1500	4.8981e+08	3.7649e+06	1	0.0023

Table 3.4 Disc parameter

Disc	Material	Diameter (m)	Thickness (m)	Mass unbalance (kg m)	Node position
Disc-1	PVC	0.2	0.05	10e-06	3
Disc-2	PVC	0.2	0.05	10e-06	5

A. Stability limit of spin speed

Fig. 3.13 shows the decay rate plot for three different radius ratios $(\Re = 0.0, 0.2, 0.3)$. In this example, the values of SLS for the three different radius ratios are 85(90) rpm, 370(376) rpm, and 541(550) rpm for CM(FEM) respectively, when PVC is kept as inside layer. Considering same example, Fig. 3.14 shows plots between the percentage increase of SLS versus various radius ratios when PVC is kept as an inner layer and an outer layer. After visualizing the figure some important conclusion can be drawn that the SLS and the relative stability of the system increases as the system get stiffer. Shaft performance measured in terms of SLS is good only when the less stiff material like PVC is kept inside and the stiffer material like LORD forms the outside layer of the rotor. As the equivalent density increases with radius ratios, there is a decrement in SLS at some places, caused by some critical radius ratios.

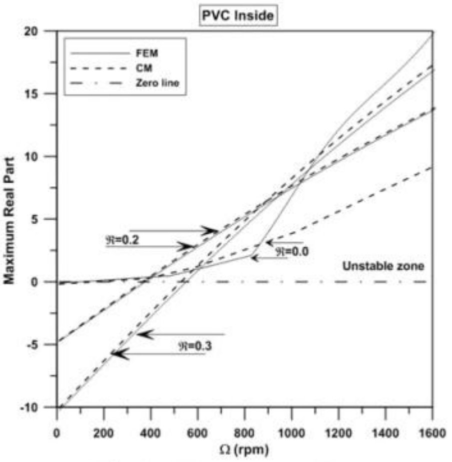

Fig. 3.13 Decay rate plot

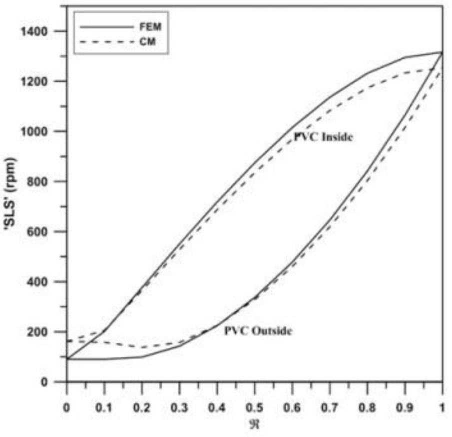

Fig. 3.14 SLS plot

B. Campbell diagram

Fig. 3.15 demonstrates the Campbell diagram for various radius ratios; here only first displacement mode has been presented. It can be seen from the figure that value of FNF increases with the high value of radius ratio. For this example, the value of FNF in rpm for three different radius ratios are 56(58), 305(310), and 443(449) for CM(FEM) respectively, when PVC is considered as inside layer. Fig. 3.16 shows the plot between the percentage increase of FNF versus various radius ratios when PVC is kept as an inner layer and an outer layer. Shaft performance in terms of FNF is good only when PVC is kept inside and LORD forms outside coating of rotor.

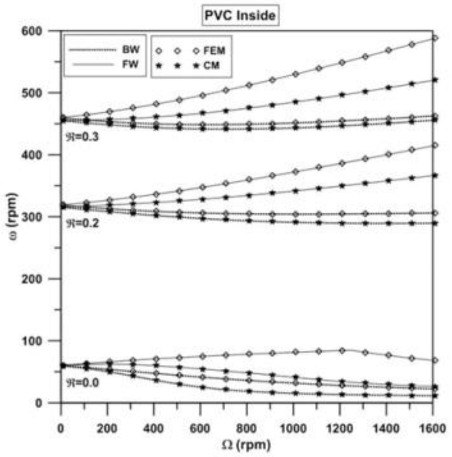

Fig. 3.15 Campbell diagram

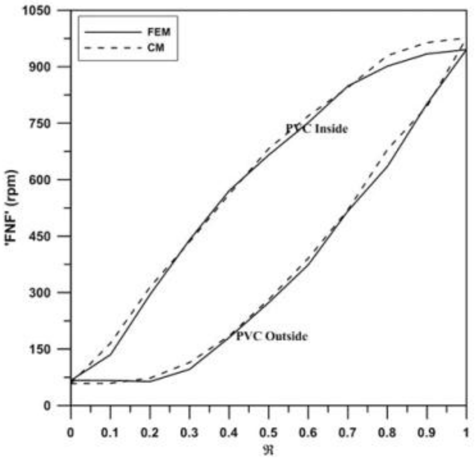

Fig. 3.16 FNF plot

C. Modal damping factor

Fig. 3.17 represents the variation of MDF with the rotor spin speed for different radius ratios. The MDF in the plot is only for first mode. At a particular spin speed, MDF for both forward and backward whirl increases with increase in radius ratio, due to enhancement in system damping. It also shows that the relative stability of the system increases with increase in radius ratio.

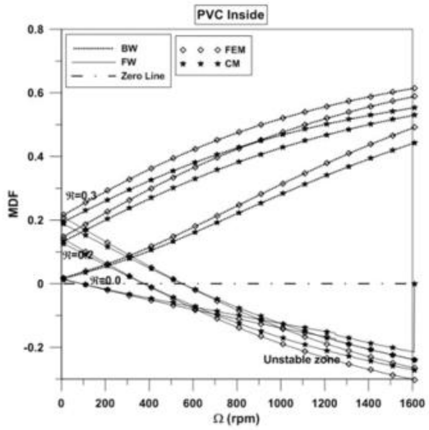

Fig. 3.17 MDF plot

D. Frequency response due to mass unbalance

Due to uncertainty in structures, unbalance mass is considered in the second disc. A simulation study has been performed to predict the unbalance frequency response at same disc for different radius ratios. An important conclusion can be drawn from the Fig. 3.18 that with increase of the radius ratio, the amplitude response decreases as well as resonance frequency increases, as the shaft becomes stiffer.

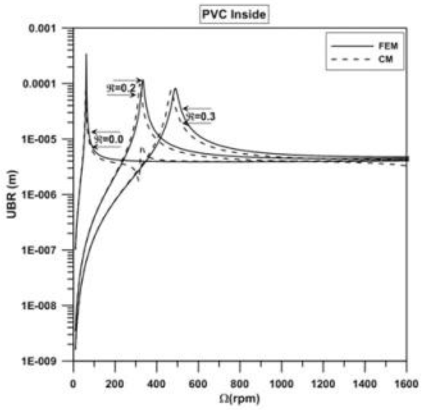

Fig. 3.18 UBR plot

E. Time response due to mass unbalance

Fig. 3.19 and Fig. 3.20 shows the steady state time response of the second disc due to unbalance for two radius ratios, viz. $\Re = 0.2$ and $\Re = 0.3$ considering rotor spin speed is 500 rpm. The plot in Fig. 3.19 shows unstable nature as response monotonically increases. In other figure, it has a stable nature as response remains constant in magnitude. With increase in radius ratio from $\Re = 0.2$ to $\Re = 0.3$, system nature become stiffer, thus the plots in second case show stable nature. The initial part of steady state stable responses show combined effects of steady state and transient state response which later smoothens because the transient effect diminishes.

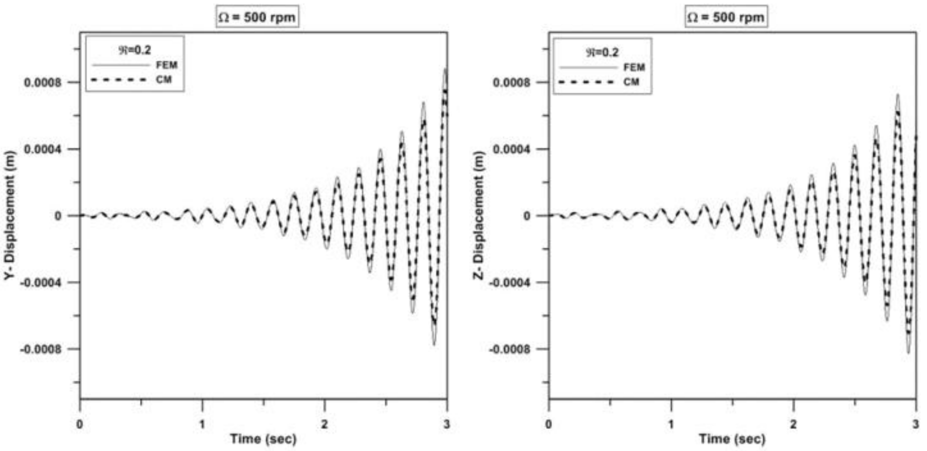

Fig. 3.19 Time response for unstable zone

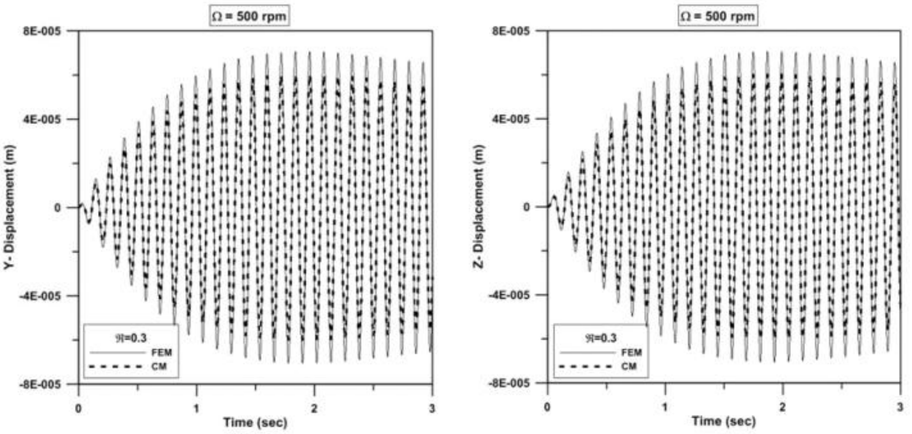

Fig. 3.20 Time response for stable zone

F. Whirl orbit

Fig. 3.21 show orbit plot due to unbalance. The same time responses as discussed in the previous section are used to procure orbit plots. The rotor orbit in the first case increases monotonically, whereas it remains constant in the second instance. In the first cas e, rotor spin speed is above the SLS and system shows unstable behaviour.

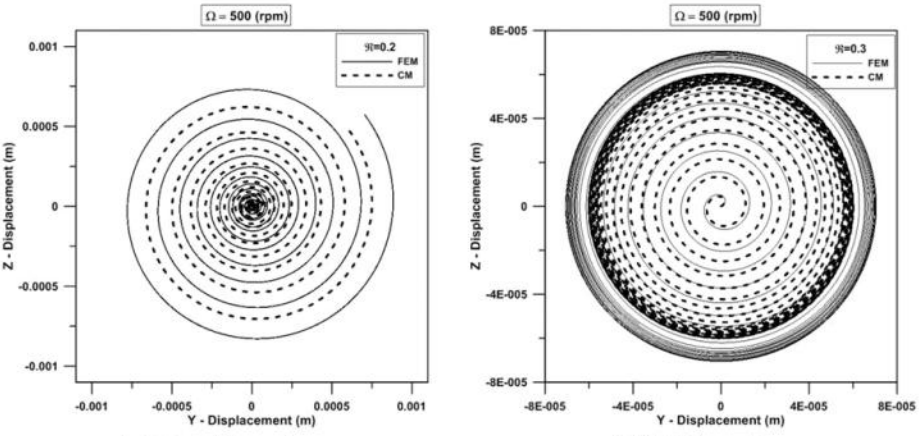

(a) Unstable region

(b) Stable region

Fig. 3.21 Whirl orbit plot

G. *Mode shapes*

Here mode shapes are plotted for the simply supported rotor for which the system's eigenvectors are used. Fig. 3.22 and Fig. 3.23 show the two consecutive bending modes for forward and backward whirl at speed of 500 rpm and radius ratio is 0.3. Clockwise rotations of the circles present in figure are considered as backward whirl and counter clockwise rotation is the forward whirl. In these plots, beginning of the whirl-locus at a plane is marked with a star and the locus is left incomplete at the end to assess the direction of whirl. Due to the existence of one node (zero displacement) at the middle of the simply supported system, the circle size is reduced in the centre in second mode as shown in Fig. 3.23.

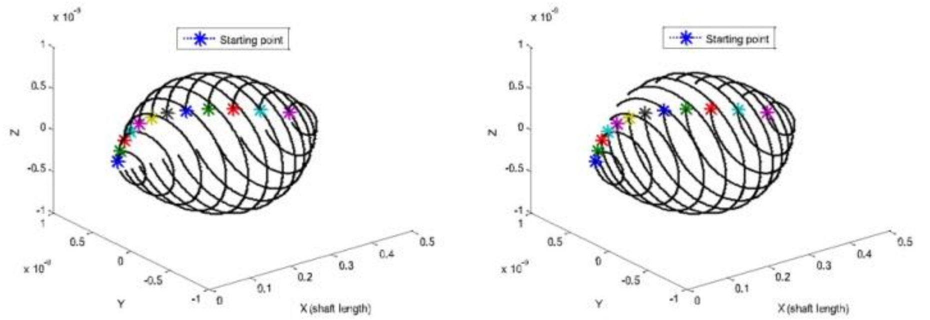

(a) Backward whirl **(b) Forward whirl**

Fig. 3.22 First mode shape at spin speed of 500 rpm

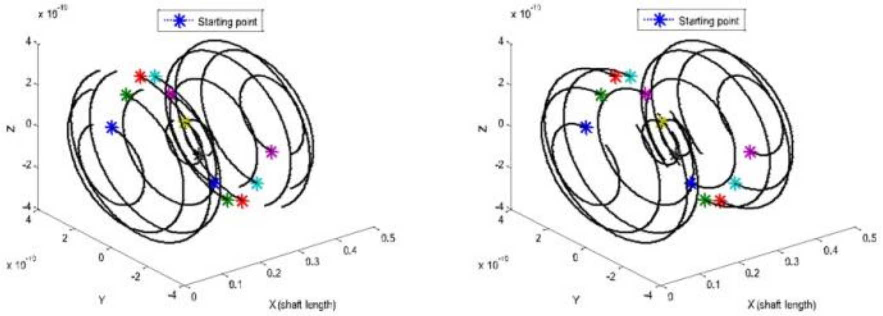

(a) Backward whirl Fig. 3.23 (b) Forward whirl

Fig. 3.23 Second mode shape at spin speed of 500 rpm

3.8 Summary

This chapter shows the most generalized mathematical modelling technique for multi layer, multi disc viscoelastic rotor system using an operator based approach. The results obtained from CM are perfectly matched with FEM, when the discs are kept within the range of $L^* = 0.2$ to 0.8. Beyond that range CM fails to predict an accurate result as compared to FEM due to its smaller matrix size and data insufficiency.

Based on the several analyses, complete databases between the two methods are tabulated below.

Table 3.5 Comparison of modal parameters for low damped material: Case - 1 $(\Re = 0.3)$

Modelling Approach	'Ω_{cr}' (rpm)				SLS (rpm)
	1st BW	1st FW	2nd BW	2nd FW	
CM	2602	2662	8813	8959	2600
FEM	2620	2680	8959	9225	2680

Table 3.6 Modal parameters for high damped material: Case - 2

Modelling Approach	FNF (rpm)			SLS (rpm)		
	$\Re = 0.0$	$\Re = 0.2$	$\Re = 0.3$	$\Re = 0.0$	$\Re = 0.2$	$\Re = 0.3$
CM	56	305	443	85	370	541
FEM	58	310	449	90	376	550

The values obtained from for both low and high damped material shows that in case of multilayer rotor it is necessary to predict stability criteria. Due to the presence of damping, the system tends to destabilize after certain critical speed.

From the dynamic analysis of multilayer rotor an important conclusion is drawn that the less stiff or soft material are kept as an inner layer and the stiffer material is used as an outer layer. This statement is valid only for two layer rotor system, but as the number of layer increases, it is necessary to check the placement arrangement of materials by keeping it in chronological order and perform from the various eigen analysis.

Chapter-4

Reduction of Higher Order Model

4.1 Introduction

Finite element formulation of the viscoelastic rotor reaches a higher order configuration, where the order of the system depends on the material properties, as shown in the previous chapters. This leads to a complicated system. In this chapter, the application of model order reduction is implemented to reduce the existing higher order differential equation. For the sake of finding the best methodology to reduce the higher order model, two different reduction techniques are used here, i.e., (a) Iterative Improved Reduction System (b) Balanced Realization method.

4.2 Higher order finite element model

For the sake of convenience, higher order differential equations of finite element model are further rewritten here.

$$\begin{aligned}\left[\mathbf{A}_0\right]_{n\times n}\{\mathbf{q}\}_{n\times 1}+\left[\mathbf{A}_1\right]_{n\times n}\{\dot{\mathbf{q}}\}_{n\times 1}+\left[\mathbf{A}_2\right]_{n\times n}\{\ddot{\mathbf{q}}\}_{n\times 1}+\left[\mathbf{A}_3\right]_{n\times n}\{\dddot{\mathbf{q}}\}_{n\times 1}&\\+\left[\mathbf{A}_4\right]_{n\times n}\{\ddddot{\mathbf{q}}\}_{n\times 1}=[\mathbf{B}]_{n\times r}\{\boldsymbol{u}\}_{r\times 1}&\end{aligned}\tag{4.1(a)}$$

Following the previous chapters, state space representation of the above equation is shown below;

$$\begin{aligned}[\mathcal{E}]\{\dot{x}\}&=[\mathcal{A}]\{x\}+[\mathcal{B}]\{\boldsymbol{u}\}\\\{y\}&=[\mathcal{C}]\{x\}+[\mathcal{D}]\{\boldsymbol{u}\}\end{aligned}\tag{4.1(b)}$$

The equations of motion (Eq. 4.1) are used in subsequent sections. Where, 'n' is the total degree of freedom.

4.3 Iterative improved reduction system

O'Callahan (1989) first presented his work based on Improved Reduction System (IRS). Later, Friswell et al. (1995) improvised the IRS concept and presented an Iterative Improved Reduction System (IIRS). In which, refinement of unwanted degree of freedom is checked by ensuring that the transformation matrix of each reduction is optimized iteratively. Further, IIRS has been explained with its mathematical formulation for the available sets of higher order differential equation. Only fourth order equations obtained from Chapter-3 are used for reduction purpose. Using the same fashion third order equation can also be reduc ed.

The IIRS method is also the modified version of Guyan reduction, as the order of differential equation changes, structural formation of the transformation matrix $[\mathcal{T}]$ is also to be modified. Following Friswell et al. (1995), coefficients $\mathbf{A}_0, \mathbf{A}_1, \mathbf{A}_2, \mathbf{A}_3$ and $\mathbf{A}_4$ are first rearranged and partitioned into separate quantities as master (retained) and slave (discarded) degree of freedom.

$$\begin{bmatrix} \mathbf{A}_{0_{mm}} & \mathbf{A}_{0_{ms}} \\ \mathbf{A}_{0_{sm}} & \mathbf{A}_{0_{ss}} \end{bmatrix}_{n\times n} \begin{Bmatrix} \mathbf{q}_m \\ \mathbf{q}_s \end{Bmatrix}_{n\times 1} + \begin{bmatrix} \mathbf{A}_{1_{mm}} & \mathbf{A}_{1_{ms}} \\ \mathbf{A}_{1_{sm}} & \mathbf{A}_{1_{ss}} \end{bmatrix}_{n\times n} \begin{Bmatrix} \dot{\mathbf{q}}_m \\ \dot{\mathbf{q}}_s \end{Bmatrix}_{n\times 1} + \begin{bmatrix} \mathbf{A}_{2_{mm}} & \mathbf{A}_{2_{ms}} \\ \mathbf{A}_{2_{sm}} & \mathbf{A}_{2_{ss}} \end{bmatrix}_{n\times n} \begin{Bmatrix} \ddot{\mathbf{q}}_m \\ \ddot{\mathbf{q}}_s \end{Bmatrix}_{n\times 1}$$
$$+ \begin{bmatrix} \mathbf{A}_{3_{mm}} & \mathbf{A}_{3_{ms}} \\ \mathbf{A}_{3_{sm}} & \mathbf{A}_{3_{ss}} \end{bmatrix}_{n\times n} \begin{Bmatrix} \dddot{\mathbf{q}}_m \\ \dddot{\mathbf{q}}_s \end{Bmatrix}_{n\times 1} + \begin{bmatrix} \mathbf{A}_{4_{mm}} & \mathbf{A}_{4_{ms}} \\ \mathbf{A}_{4_{sm}} & \mathbf{A}_{4_{ss}} \end{bmatrix}_{n\times n} \begin{Bmatrix} \ddddot{\mathbf{q}}_m \\ \ddddot{\mathbf{q}}_s \end{Bmatrix}_{n\times 1} = \begin{bmatrix} \mathbf{B}_m \\ 0 \end{bmatrix}_{n\times r} \{\boldsymbol{u}\}_{r\times 1} \tag{4.2}$$

In the above equation subscript $'m'$ and $'s'$ are representing the master and the slave degrees of freedom, respectively.

To obtain the static transformation through Guyan reduction, the displacement coefficients $\mathbf{A}_0$ is used and is written as,

$$\begin{Bmatrix} \mathbf{q}_m \\ \mathbf{q}_s \end{Bmatrix} = \begin{bmatrix} \mathbf{I} \\ -\mathbf{A}_{0_{ss}}^{-1} \mathbf{A}_{0_{sm}} \end{bmatrix} \mathbf{q}_m = \begin{bmatrix} \mathbf{I} \\ \mathbf{t}_s \end{bmatrix} \mathbf{q}_m = [\mathcal{T}_s] \mathbf{q}_m \tag{4.3}$$

Subscript 's' signifies the essence of static transformation matrix between the master coordinates and the full state vector. After substituting the master coordinate in respect of full state vector, the reduced matrices are written below,

$$\begin{aligned}
\left[\mathbf{A}_{0_r}\right] &= \left[\mathcal{T}_s\right]^T \left[\mathbf{A}_0\right]\left[\mathcal{T}_s\right], \\
\left[\mathbf{A}_{1_r}\right] &= \left[\mathcal{T}_s\right]^T \left[\mathbf{A}_1\right]\left[\mathcal{T}_s\right], \\
\left[\mathbf{A}_{2_r}\right] &= \left[\mathcal{T}_s\right]^T \left[\mathbf{A}_2\right]\left[\mathcal{T}_s\right], \\
\left[\mathbf{A}_{3_r}\right] &= \left[\mathcal{T}_s\right]^T \left[\mathbf{A}_3\right]\left[\mathcal{T}_s\right], \\
\left[\mathbf{A}_{4_r}\right] &= \left[\mathcal{T}_s\right]^T \left[\mathbf{A}_4\right]\left[\mathcal{T}_s\right],
\end{aligned} \tag{4.4}$$

It is important to notify that the frequency response calculated by this reduced coefficients is exact only for zero frequency. So, for the high-frequency range, the neglected coordinates of higher order coefficients also need to consider in the formation of transformation matrix. Mainly the inertia coefficient played a significant role at the time of higher excitation frequency; therefore, it can be incorporated in the above transformation matrix. Following Friswell et al. (1995) the transformation matrix considering inertia coefficient can be written as follows,

$$\left[\mathcal{T}_{\mathrm{IRS}}\right] = \left[\mathcal{T}_s\right] + [\mathbf{S}]\left[\mathbf{A}_2\right]\left[\mathcal{T}_s\right]\left[\mathbf{A}_{2_r}\right]\left[\mathbf{A}_{0_r}\right], \tag{4.5}$$

where,

$$[\mathbf{S}] = \begin{bmatrix} 0 & 0 \\ 0 & \mathbf{A}_{0_{ss}}^{-1} \end{bmatrix}$$

Once the modified transformation matrix is obtained, reduction of various coefficients of higher order can be performed. It is defined as,

$$\begin{aligned}
\left[\mathbf{A}_{0_{\mathrm{IRS}}}\right] &= \left[\mathcal{T}_{\mathrm{IRS}}\right]^T \left[\mathbf{A}_0\right]\left[\mathcal{T}_{\mathrm{IRS}}\right], \\
\left[\mathbf{A}_{1_{\mathrm{IRS}}}\right] &= \left[\mathcal{T}_{\mathrm{IRS}}\right]^T \left[\mathbf{A}_1\right]\left[\mathcal{T}_{\mathrm{IRS}}\right], \\
\left[\mathbf{A}_{2_{\mathrm{IRS}}}\right] &= \left[\mathcal{T}_{\mathrm{IRS}}\right]^T \left[\mathbf{A}_2\right]\left[\mathcal{T}_{\mathrm{IRS}}\right], \\
\left[\mathbf{A}_{3_{\mathrm{IRS}}}\right] &= \left[\mathcal{T}_{\mathrm{IRS}}\right]^T \left[\mathbf{A}_3\right]\left[\mathcal{T}_{\mathrm{IRS}}\right], \\
\left[\mathbf{A}_{4_{\mathrm{IRS}}}\right] &= \left[\mathcal{T}_{\mathrm{IRS}}\right]^T \left[\mathbf{A}_4\right]\left[\mathcal{T}_{\mathrm{IRS}}\right],
\end{aligned} \tag{4.6}$$

The above Eq. (4.5) expresses the IRS transformation and it also satisfies at non-zero frequencies. These improved reduced matrices from Eq. (4.6) are used to estimate dynamic properties of the system, and they compute a more accurate result. Friswell et al. (1995) suggested an iterative method to improve the accuracy of the transformation matrix up to some extent that will help the reduction technique to generate more exact result nearer to the full model. The $(\mathrm{i}{+}1)^{th}$ transformation in the IIRS algorithm may be procured from the 'i^{th}' transformation as follow,

$$\left[\mathcal{T}_{(\mathrm{i}+1)}\right]=\begin{bmatrix}\mathbf{I}\\ \mathbf{t}_{(\mathrm{i}+1)}\end{bmatrix} \tag{4.7}$$

where,

$$\mathbf{t}_{(\mathrm{i}+1)}=\mathbf{t}_{\mathrm{s}}+\left[\mathbf{A}_{0_{ss}}^{-1}\right]\left[\mathbf{A}_{2_{sm}}\quad \mathbf{A}_{2_{ss}}\right]\left[\mathcal{T}_{\mathrm{IRS}}\right]\left[\mathbf{A}_{2_{\mathrm{r}}}^{-1}\right]\left[\mathbf{A}_{0_{\mathrm{r}}}\right]$$

The above equation shows the iterative procedure when the convergence will happen and the solution will not change from one iteration to the next. Numerically it can be seen as, the iteration performing in Eq. (4.7) continues until $\left[\mathcal{T}_{(\mathrm{i}+1)}\right]=\left[\mathcal{T}_{\mathrm{i}}\right]$ or like to be $\mathbf{t}_{(\mathrm{i}+1)}$ tends to $\mathbf{t}_{\mathrm{i}}$. Then the value of $\left[\mathcal{T}_{\mathrm{i}}\right]$ is used as the final transformation matrix to get the reduced matrices.

So, the reformed transformation matrix can be written as $\left[\mathcal{T}_{\mathrm{i}}\right]=\begin{bmatrix}\mathbf{I}\\ \mathbf{t}_{\mathrm{i}}\end{bmatrix}$. Hence, utilizing the above procedure reduction can be performed again to get the desired reduced matrices in the more accurate form.

$$\begin{aligned}
\left[\mathbf{A}_{0_{\mathrm{IIRS}}}\right]&=\left[\mathcal{T}_{\mathrm{i}}\right]^{T}\left[\mathbf{A}_{0}\right]\left[\mathcal{T}_{\mathrm{i}}\right],\\
\left[\mathbf{A}_{1_{\mathrm{IIRS}}}\right]&=\left[\mathcal{T}_{\mathrm{i}}\right]^{T}\left[\mathbf{A}_{1}\right]\left[\mathcal{T}_{\mathrm{i}}\right],\\
\left[\mathbf{A}_{2_{\mathrm{IIRS}}}\right]&=\left[\mathcal{T}_{\mathrm{i}}\right]^{T}\left[\mathbf{A}_{2}\right]\left[\mathcal{T}_{\mathrm{i}}\right],\\
\left[\mathbf{A}_{3_{\mathrm{IIRS}}}\right]&=\left[\mathcal{T}_{\mathrm{i}}\right]^{T}\left[\mathbf{A}_{3}\right]\left[\mathcal{T}_{\mathrm{i}}\right],\\
\left[\mathbf{A}_{4_{\mathrm{IIRS}}}\right]&=\left[\mathcal{T}_{\mathrm{i}}\right]^{T}\left[\mathbf{A}_{4}\right]\left[\mathcal{T}_{\mathrm{i}}\right],
\end{aligned} \tag{4.8}$$

The above reduced matrices are gained after shorting the unwanted degree of freedom. After getting the reduced coefficients using IIRS method, i.e. $\mathbf{A}_{0_{\mathrm{IIRS}}},\mathbf{A}_{1_{\mathrm{IIRS}}},\mathbf{A}_{2_{\mathrm{IIRS}}},\mathbf{A}_{3_{\mathrm{IIRS}}}$ and $\mathbf{A}_{4_{\mathrm{IIRS}}}$. These desired reduced size matrices finally being used and converted to state space form to estimate eigen-analysis.

$$\begin{aligned}
\left[\mathcal{E}\right]_{\mathrm{IIRS}}\left\{\dot{\mathcal{x}}\right\}_{\mathrm{IIRS}}&=\left[\mathcal{A}\right]_{\mathrm{IIRS}}\left\{\mathcal{x}\right\}_{\mathrm{IIRS}}+\left[\mathcal{B}\right]_{\mathrm{IIRS}}\left\{\boldsymbol{u}\right\}_{\mathrm{IIRS}},\\
\left\{\mathcal{y}\right\}_{\mathrm{IIRS}}&=\left[\mathcal{C}\right]_{\mathrm{IIRS}}\left\{\mathcal{x}\right\}_{\mathrm{IIRS}}+\left[\mathcal{D}\right]_{\mathrm{IIRS}}\left\{\boldsymbol{u}\right\}_{\mathrm{IIRS}}
\end{aligned} \tag{4.9}$$

where,

$$[\mathcal{E}]_{\mathrm{IIRS}} = \begin{bmatrix} [\mathbf{I}] & [0] & [0] & [0] \\ [0] & [\mathbf{I}] & [0] & [0] \\ [0] & [0] & [\mathbf{I}] & [0] \\ [0] & [0] & [0] & \left[\mathbf{A}_{4_{\mathrm{IIRS}}}\right] \end{bmatrix},$$

$$[\mathcal{A}]_{\mathrm{IIRS}} = \begin{bmatrix} [0] & [\mathbf{I}] & [0] & [0] \\ [0] & [0] & [\mathbf{I}] & [0] \\ [0] & [0] & [0] & [\mathbf{I}] \\ -\left[\mathbf{A}_{0_{\mathrm{IIRS}}}\right] & -\left[\mathbf{A}_{1_{\mathrm{IIRS}}}\right] & -\left[\mathbf{A}_{2_{\mathrm{IIRS}}}\right] & -\left[\mathbf{A}_{3_{\mathrm{IIRS}}}\right] \end{bmatrix}, \qquad [\mathcal{B}]_{\mathrm{IIRS}} = \begin{bmatrix} [\mathbf{0}] \\ [\mathbf{0}] \\ [\mathbf{0}] \\ [\mathbf{B}]_{\mathrm{IIRS}} \end{bmatrix},$$

$$\{\mathcal{x}\} = \{\{\mathbf{q}\} \quad \{\dot{\mathbf{q}}\} \quad \{\ddot{\mathbf{q}}\} \quad \{\dddot{\mathbf{q}}\}\}^T,$$

Using the matrices $[\mathcal{E}]_{\mathrm{IIRS}}$ and $[\mathcal{A}]_{\mathrm{IIRS}}$, eigenvalues and eigenvectors is being estimated after neglecting the force matrix. Likewise, frequency response is calculated for whole system considering an unbalance at a disc.

4.4 Balanced realization system

Balanced realization technique (BRS), was first developed by Moore (1981), where an elementary tool was used for extracting the system to an acceptable reduced model. This method first involves balancing the system matrices through a nonsingular matrix. Mapping of input and output state, which is done by controllability gramians and observability gramians respectively, those are balanced in a balanced system. Reduced model via balancing is also optimal in many applications. Thus, it provides a convenient structure for model reduction.

Following Al-Saggaf et al. (1993), state space representation as shown in Eq. (4.1(b)) is transformed to another representation and is rewritten as

$$[\mathcal{E}]_{\mathrm{b}}\{\dot{\mathcal{x}}\}_{\mathrm{b}} = [\mathcal{A}]_{\mathrm{b}}\{\mathcal{x}\}_{\mathrm{b}} + [\mathcal{B}]_{\mathrm{b}}\{\boldsymbol{u}\}_{\mathrm{b}} \tag{4.10(a)}$$

$$\{\mathbf{y}\}_{\mathrm{b}} = [\mathcal{C}]_{\mathrm{b}}\{\mathcal{x}\}_{\mathrm{b}} + [\mathcal{D}]_{\mathrm{b}}\{\boldsymbol{u}\}_{\mathrm{b}} \tag{4.10(b)}$$

where, the balanced matrices are given as

$$[\mathcal{E}]_{\mathrm{b}} = [\mathcal{T}]_{\mathrm{b}}^{-1}[\mathcal{E}][\mathcal{T}]_{\mathrm{b}}, \qquad [\mathcal{A}]_{\mathrm{b}} = [\mathcal{T}]_{\mathrm{b}}^{-1}[\mathcal{A}][\mathcal{T}]_{\mathrm{b}}, \qquad [\mathcal{B}]_{\mathrm{b}} = [\mathcal{T}]_{\mathrm{b}}^{-1}[\mathcal{B}]_{\mathrm{b}},$$

$$[\mathcal{D}]_{\mathrm{b}} = [\mathcal{D}][\mathcal{T}]_{\mathrm{b}}, \qquad [\mathcal{C}]_{\mathrm{b}} = [\mathcal{C}][\mathcal{T}]_{\mathrm{b}}, \qquad [\mathcal{x}]_{\mathrm{b}} = [\mathcal{T}]_{\mathrm{b}}^{-1}[\mathcal{x}]_{\mathrm{b}},$$

$[\mathcal{T}]_{\mathrm{b}}$ is a non-singular transformation matrix, which doesn't introduce any round-off error in balancing.

The input and the output states play a key role in controllability and observability checkout. For the discrete time systems, the controllability gramian $[\mathcal{P}]$ is related to the value of minimum energy control, and observability gramian $[\mathcal{Q}]$ refers to the output energy of the free response. Controllability gramian is positive definite if an only if the system matrices and the input matrix are controllable. Similarly, the observability gramian is positive definite if and only if system matrices and output matrix are observable. The present gramians are determined by using Lyapunov equations.

$$\begin{aligned}&[\mathcal{E}][\mathcal{P}][\mathcal{A}]^T+[\mathcal{A}][\mathcal{P}][\mathcal{E}]^T+[\mathcal{B}][\mathcal{B}]^T=0\\&[\mathcal{E}][\mathcal{Q}][\mathcal{A}]^T+[\mathcal{A}][\mathcal{Q}][\mathcal{E}]^T+[\mathcal{C}][\mathcal{C}]^T=0\end{aligned}\tag{4.11}$$

For a controlled system, if any input exists, the states of the system may be driven to any random configuration. In which, gramian '$\mathcal{P}$' and '$\mathcal{Q}$' are used to measure the controllable and observable mode by checking the rank of full system. Assimilating system is observable, and then the present state vector should be rearranged and reconstructed from past and current elements of output vector to get the balanced gramian. The controllability and observability checking for stability are done by Friswell et al. (1996) and Friswell and Inman (1999).

For the new balanced system, the controllability gramian and the observability gramian can be written by using the same non-singular transformation matrix.

$$\begin{aligned}&[\mathcal{P}]_{\mathrm{b}}=[\mathcal{T}]_{\mathrm{b}}^{-1}[\mathcal{P}][\mathcal{T}]\\&[\mathcal{Q}]_{\mathrm{b}}=[\mathcal{T}]_{\mathrm{b}}^{-1}[\mathcal{Q}][\mathcal{T}]\end{aligned}\tag{4.12}$$

After transformation eigenvalues of their product, $[\mathcal{PQ}]$ will remain invariant because the gramians depend on state space coordinates. Hankel singular values of the system are the square root of the eigenvalues of $[\mathcal{PQ}]$.

For a balanced system, following conditions are to be satisfied such that, both the new balanced gramian are equal and diagonal with special arrangement.

$$[\mathcal{P}]_{\mathrm{b}}=[\mathcal{Q}]_{\mathrm{b}}=\boldsymbol{\Sigma}=\mathrm{diag}\left[\alpha_1,\alpha_2,\dots,\alpha_{4n}\right]\tag{4.13}$$

in which, $\alpha_1\geq\alpha_2\geq,\dots,\geq\alpha_{4n}>0$,

Here, 'α' are the Hankel singular values of the system, which measure the degree of controllability and observability of the states. The dominant subsystem corresponding to large Hankel singular values, which are most controllable and most observable part are retained. The remaining states were corresponding to the smallest singular values, which are least controllable and least observable, are neglected. After rearrangement the Hankel singular values are written as;

$$\Sigma = \begin{bmatrix} \Sigma_m & 0 \\ 0 & \Sigma_s \end{bmatrix} \tag{4.14}$$

where, $\Sigma_m = diag\left[\alpha_1, \; ..., \alpha_{\mathrm{r}}\right]$, and $\Sigma_s = diag\left[\alpha_{\mathrm{r}+1}, \; ..., \alpha_{4n}\right]$, Subscript '$m$' and '$s$' are known as master (retained) and slave (discarded) coordinate respectively.

On the same basis, matrices $[\mathcal{E}], [\mathcal{A}], [\mathcal{B}], [\mathcal{C}], [\mathcal{D}]$ and $\{\mathcal{X}\}$ are re-ordered and partitioned into separate quantities relating to the master and slave degrees of freedom.

$$\begin{gathered}
\begin{bmatrix} \mathcal{E}_{mm} & \mathcal{E}_{ms} \\ \mathcal{E}_{sm} & \mathcal{E}_{ss} \end{bmatrix}_{3n\times 3n} \begin{Bmatrix} \dot{\mathcal{X}}_m \\ \dot{\mathcal{X}}_s \end{Bmatrix}_{3n\times 1} = \begin{bmatrix} \mathcal{A}_{mm} & \mathcal{A}_{ms} \\ \mathcal{A}_{sm} & \mathcal{A}_{ss} \end{bmatrix}_{3n\times 3n} \begin{Bmatrix} \mathcal{X}_m \\ \mathcal{X}_s \end{Bmatrix}_{3n\times 1} + \begin{bmatrix} \mathcal{B}_m \\ \mathcal{B}_s \end{bmatrix}_{3n\times r} \begin{Bmatrix} \boldsymbol{u}_m \\ \boldsymbol{u}_s \end{Bmatrix}_{r\times 1} \\
\begin{Bmatrix} \mathbf{y}_m \\ \mathbf{y}_s \end{Bmatrix}_{p\times 1} = \begin{bmatrix} \mathcal{C}_m & \mathcal{C}_s \end{bmatrix}_{p\times 3n} \begin{Bmatrix} \mathcal{X}_m \\ \mathcal{X}_s \end{Bmatrix}_{3n\times 1} + \begin{bmatrix} \mathcal{D}_m & \mathcal{D}_s \end{bmatrix}_{p\times r} \begin{Bmatrix} \boldsymbol{u}_m \\ \boldsymbol{u}_s \end{Bmatrix}_{r\times 1}
\end{gathered} \tag{4.15}$$

Then the new reduced balanced subsystem is shown as:

$$[\mathcal{E}]_{\mathrm{br}} \{\dot{\mathcal{X}}\}_{\mathrm{br}} = [\mathcal{A}]_{\mathrm{br}} \{\mathcal{X}\}_{\mathrm{br}} + [\mathcal{B}]_{\mathrm{br}} \{\boldsymbol{u}\}_{\mathrm{br}} \tag{4.16(a)}$$

$$\{\mathbf{y}\}_{\mathrm{br}} = [\mathcal{C}]_{\mathrm{br}} \{\mathcal{X}\}_{\mathrm{br}} + [\mathcal{D}]_{\mathrm{br}} \{\boldsymbol{u}\}_{\mathrm{br}} \tag{4.16(b)}$$

Eq. (4.16) shows balance reduced model of the full-order system, which contains only the most controllable and most observable part of the system. If $\alpha_{\mathrm{r}} \neq \alpha_{\mathrm{r}+1}$, then the reduced order balance system $(\mathcal{E}_{mm}, \mathcal{A}_{mm}, \mathcal{B}_m, \mathcal{C}_m, \mathcal{D}_m, \mathcal{X}_m)$ is stable, controllable and observable (Pernebo and Silverman (1982), Saksena et al. (1984)). The eigenvalues of the reduced matrix of size $(\mathrm{r}\times\mathrm{r})$ retain approximately to the original extensive system.

4.5 Model implementation

Higher order model of viscoelastic rotor faces some difficulty in numerical analysis. To achieve a small and handy model, two reduction techniques IIRS and BRS are used here. For simulation purpose, two sets of numerical problems are considered from previous chapters to implement these two reduction techniques. A comparative study based on various dynamic parameters shows the effectiveness of the reduced model. Two examples are,

- **Case - 1:** IIRS and BRS are applied to the third order differential equation of motion obtained from Chapter-2.

- **Case - 2:** BRS is applied to the fourth order differential equation of motion as illustrated in Chapter-3.

4.5.1. Numerical illustration for reducing third order model: Case – 1

For the simulation purpose, a rotor shaft system is shown schematically in Fig. 4.1. Length and diameter of the mild steel shaft are $L = 1$ m and $D_R = 0.05$ m respectively, is mounted on bearings at the ends, considered to generate simply supported boundary conditions. Solid circles on the rotor shaft show the different nodal location. A disc of the same material is mounted in different node positions and for parametric study placement of the disc is changed from one end to another end. For any particular position, the distance of disc from left end is L_1. Non-dimensional parameters ($L^*=L_1/L$) is ratio between left end distances of disc to the total length of the shaft, is used to indicate disc position L^* varies from 0 to 1 represents left and right end respectively. Table 4.1 shows the disc dimensions considered for this analysis. While the operator parameter and material properties of rotor are shown in Table 4.2.

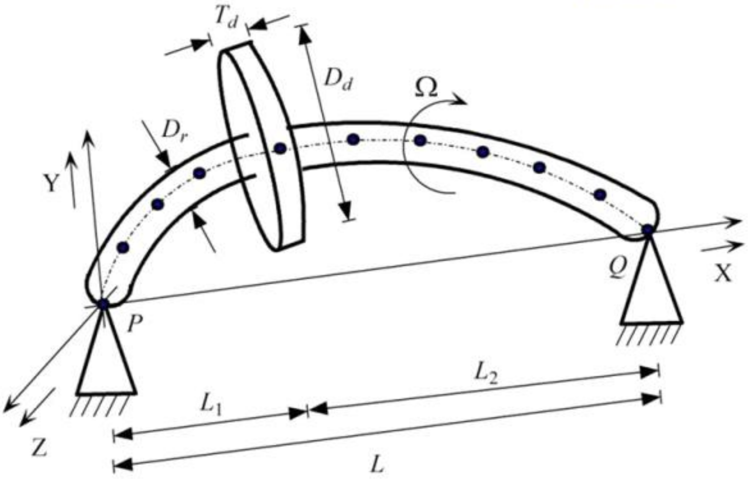

Fig. 4.1 Schematic diagram of the simply-supported rotor

Table 4.1 Disc parameter

Diameter (m)	Thickness (m)	Mass unbalance (kg-m)
0.25	0.050	10e-06

Table 4.2 Material properties of mild steel

Density	**Young's Modulus**	**Viscoelastic parameters**			
'ρ' (kg/m^3)	**'E' (Pa)**	a_0	b_0	a_1	b_1
7800	2.1e+11	2.1e+11	1	7.51e+5	1.475e-9

Two noded beam elements is considered in finite element analysis of the rotor shaft. The continuum is discretized into 10- elements or 11- nodes and each node has 4- degree of freedom, i.e. 2- displacements and 2- rotations. Calculating all facts, the total size of the global matrix becomes (44×44) for the full model. Due to simply supported ends, 2- translational degrees of freedom from first and last node are discarded from total degree of freedom. So, the remaining size of the matrix becomes (40×40). According to equation in state space representation the system matrix size enhance to three times of the initial. Thus the full model consists (120) degrees of freedom.

Applying IIRS to the present system, it is seen that a very few reduction is possible, that's why only 120th full mode, 111th and 102th reduced modes are shown in this paper.

While applying BRS technique, checking of stable modes through Hankel singular value decomposition, it is found that the maximum reduction of the system matrices is possible up to 8 degrees of freedom. In this paper, the result presented below is showing the dat a for the 120th full mode, 12th and 8th reduced mode.

Numerical results based on free and forced vibration analysis are obtained to do a comparative study between full and reduced model. Most of the results are obtained from the disc position, $L^* = 0.3$ otherwise it has been mentioned. For better understanding of graphs, different legends and line styles are used for representation. Nice match in all figures between reduced and full model shows the importance of this study.

A. Stability limit of spin speed

The decay rate is plotted between maximum real parts vs. spin speed, as shown in Fig. 4.2 and Fig. 4.4, which helps to predict the stability limit of spin speed (SLS). Fig. 4.3 and Fig. 4.5 show the SLS plot for various disc positions for both IIRS and BRS technique respectively.

It is found that the values of SLS for full mode and two reduced mode for IIRS case are 4490 rpm, 6210 rpm and 7070 rpm, respectively. After reduction the value of SLS increases rapidly, this shows that IIRS is not so suitable for reducing such type of higher order model.

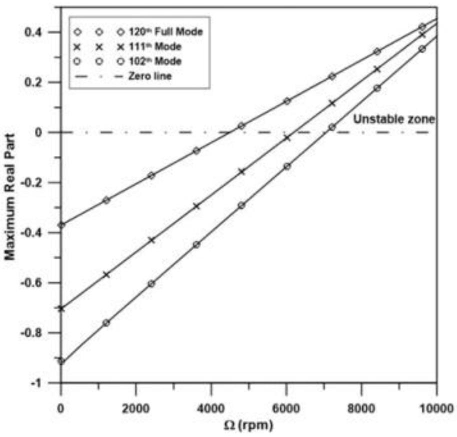

Fig. 4.2 Decay rate using IIRS

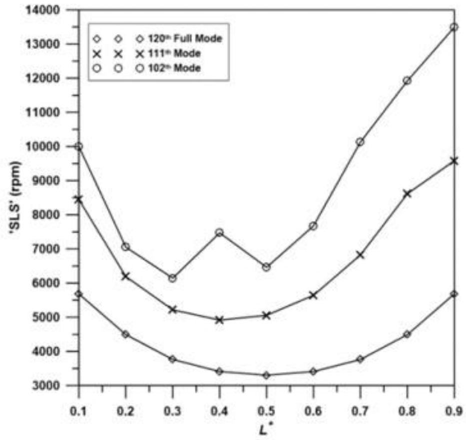

Fig. 4.3 SLS for various disc positions using IIRS

Applying BRS to the same example, the values of SLS for full mode and two reduced mode are 4490 rpm, 4495 rpm and 4498 rpm, respectively. Fig. 4.4 and Fig. 4.5 represent the decay rate and SLS for various disc positions. After visualizing the figure, a conclusion can be drawn that the SLS is not much affected by the reduction of large matrices in BRS case.

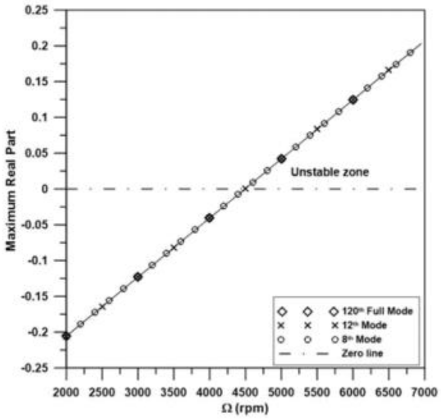

Fig. 4.4 Decay rate using BRS

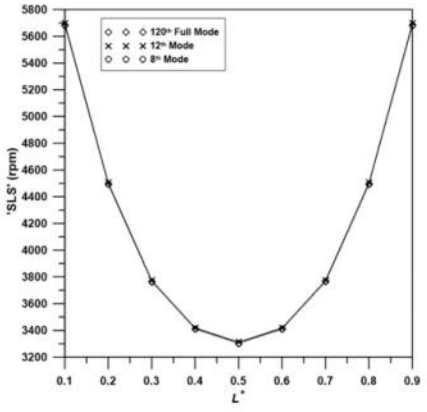

Fig. 4.5 SLS for various disc positions using BRS

B. Campbell diagram

Campbell diagram and FNF for various disc positions for IIRS technique are demonstrated in Fig. 4.6 and Fig. 4.7, which is plotted between the whirl-frequency and the rotor spin speed. It gives the information about the location of natural frequencies. The first and second natural frequency is abbreviated as FNF and SNF. Here only two displacement modes have been presented.

The value of FNF (SNF) for full mode and two reduced mode using IIRS technique are 4490 rpm (16294 rpm), 5810 rpm (22020 rpm), and 6630 rpm (27882 rpm), respectively. It is seen from figure that IIRS technique allows to reduce the full model to a little extend. While reducing the matrices the system configuration is badly affected. The transformation matrix in IIRS is formed with the iterative approach, at higher reduction, the master and slave arrangement of the inertia and stiffness matrices are distorted. Due to this the efficiency of the technique also reduces. But the quality of IIRS can be improved by increasing the iteration value, but it takes more computational time.

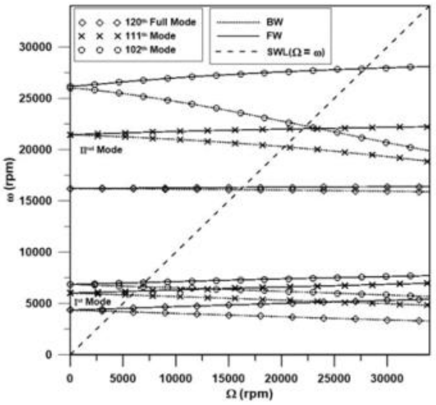

Fig. 4.6 Campbell diagram using IIRS

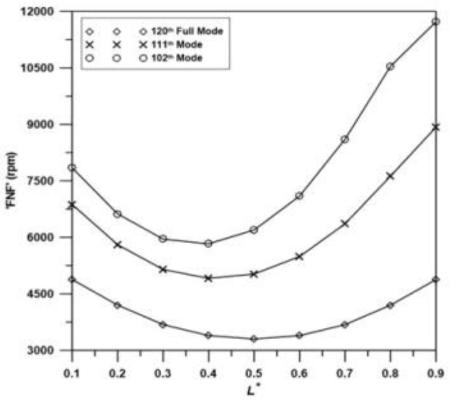

Fig. 4.7 FNF for various disc positions using IIRS

Campbell diagram and FNF for various disc position are obtained using BRS technique, are shown in Fig. 4.8 and Fig. 4.9 respectively. The value of FNF (SNF) for full mode and two reduced mode are 4490 rpm (16294 rpm), 4495 rpm (16295 rpm), and 4498 rpm (16 297 rpm), respectively. It is seen in Fig. 4.9 that value of FNF increases with change of disc position from centre to offset position. Both classical and reduced models have less matrix size. The reduced model agrees with full model at all disc position, but the classical model cannot, as shown in Chapter-2.

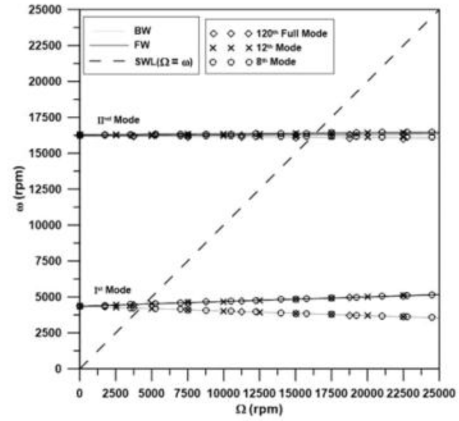

Fig. 4.8 Campbell diagram using BRS

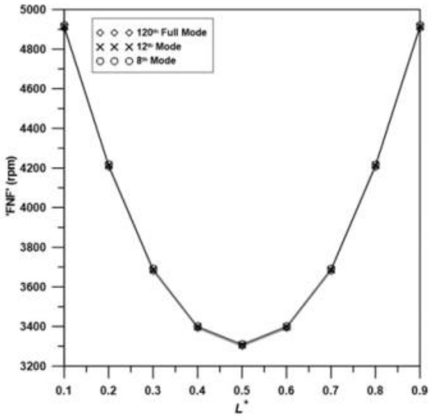

Fig. 4.9 FNF for various disc positions using BRS

C. *Modal damping factor*

The modal damping factor (MDF) is the ratio between negative real and imaginary part of an eigenvalue corresponds to any mode. The MDF is also a stability deciding parameter. Fig. 4.10 and Fig. 4.11 represent the variation of MDF with the rotor spin speed for two consecutive modes using both reduction techniques.

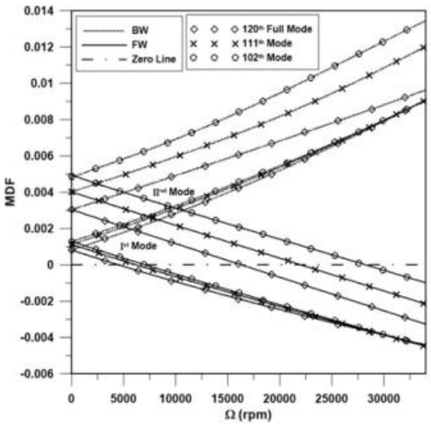

Fig. 4.10 MDF plot using IIRS

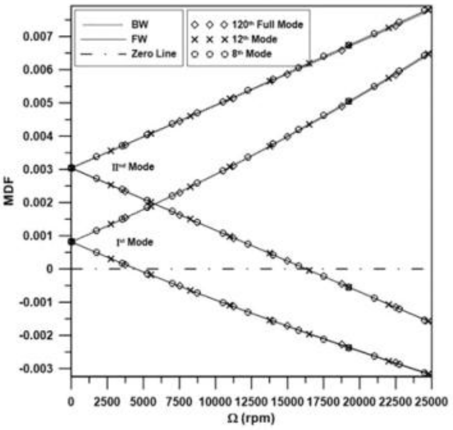

Fig. 4.11 MDF plot using BRS

D. *Frequency response due to mass unbalance*

A simulation study has been performed to predict the unbalance frequency response (UBR) at the disc for both full and reduce model. An unbalance is considered at the disc due to some irregularities in the structure. In this case, mathematical formulation from Chapter-2 is used. The matrices $\left(\mathcal{E}_{\text{IIRS}}, \mathcal{A}_{\text{IIRS}}, \mathcal{B}_{\text{IIRS}}, \mathcal{C}_{\text{IIRS}}, \mathcal{D}_{\text{IIRS}}\right)$ and $\left(\mathcal{E}_{\text{br}}, \mathcal{A}_{\text{br}}, \mathcal{B}_{\text{br}}, \mathcal{C}_{\text{br}}, \mathcal{D}_{\text{br}}\right)$ for reduced models are utilized to calculate the UBR. For both reduction techniques, UBR is presented in Fig. 4.12 and Fig. 4.13. It is seen from these figures, the response pattern has a good agreement between reduced and full model using BRS technique. These results also show the effectiveness of BRS reduced model over the finite element model.

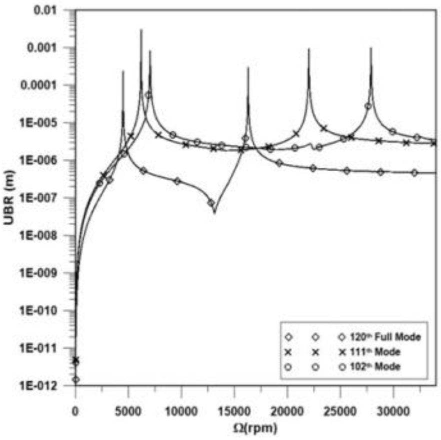

Fig. 4.12 UBR plot using IIRS

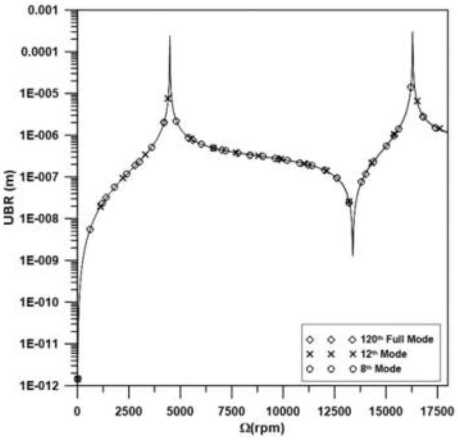

Fig. 4.13 UBR plot using BRS

E. *Time response due to mass unbalance*

For better clarity, only BRS technique is used here to estimate the steady state time response of the disc due to unbalance. Fig. 4.14 and Fig. 4.15 show the time response for two different rotational speeds, i.e. 3200 rpm and 4200 rpm, respectively. The plots in Fig. 4.15 show unstable nature as response monotonically increases. In another figure, it has a stable nature as response magnitude varies with time for a certain interval of time, but for every cycle of time nature of the response is same as the previous cycle. Which shows rotor is rotating at the same path until it achieves instability.

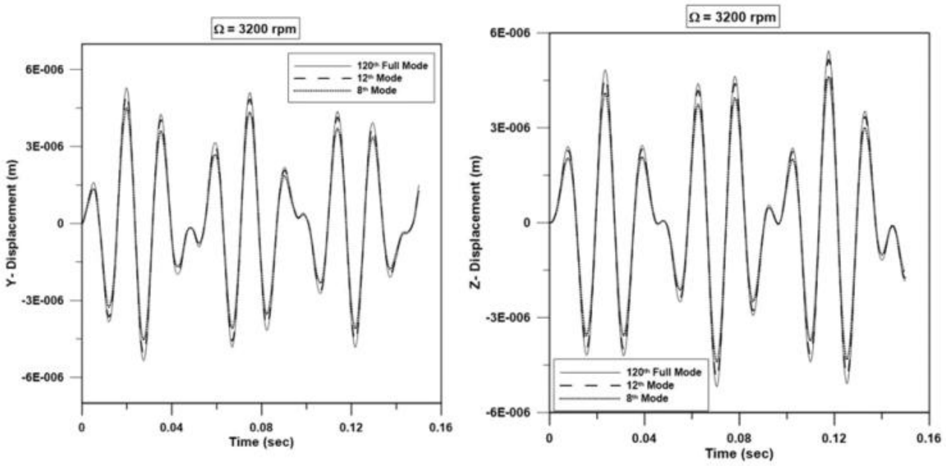

Fig. 4.14 Time response for stable zone using BRS

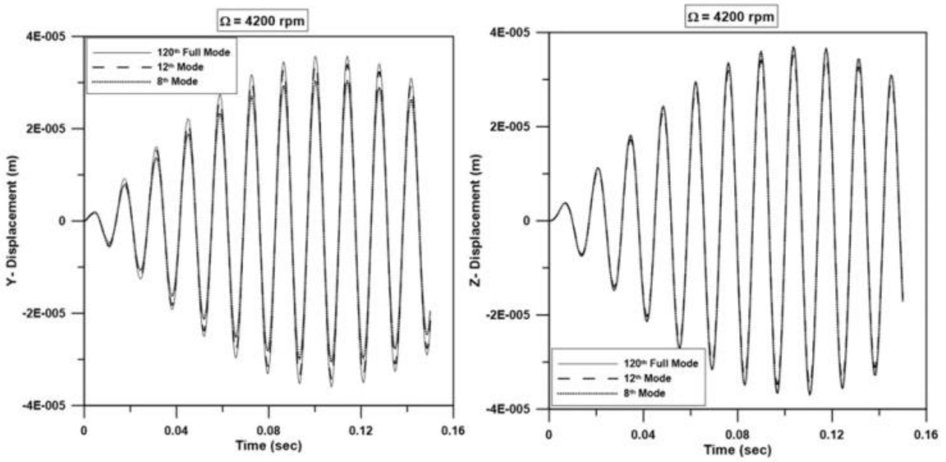

Fig. 4.15 Time response for unstable zone using BRS

F. Whirl orbit

Whirl orbit is a path traced by a point on a rotor with time, which is obtained by plotting time response along the y-direction vs. z-direction. Fig. 4.16 and Fig. 4.17 show whirl orbit due to unbalance. The same time responses as discussed in the previous section are used to procure orbit plots. The rotor orbit in the first case remains constant, whereas it increases monotonically in the second case. In the second case, rotor spin speed is above the SLS and system shows unstable behaviour.

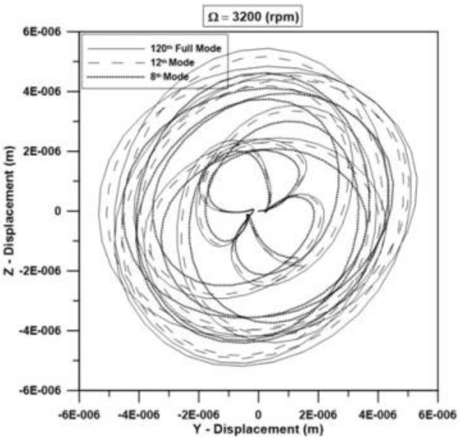

Fig. 4.16 Orbit plot in stable region using BRS

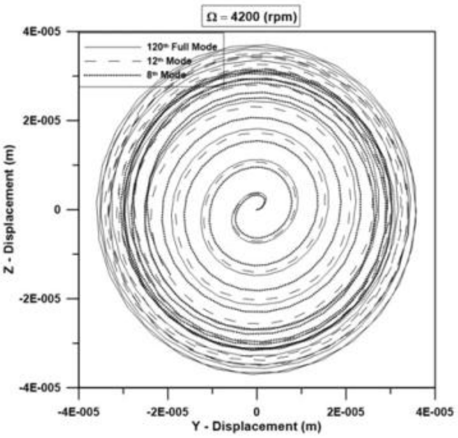

Fig. 4.17 Orbit plot in unstable region using BRS

4.5.2. Numerical illustration for reducing fourth order model: Case - 2

For the simulation purpose a simply supported, two -layered rotor shaft is considered with two-disc mounted in different node positions as shown in the Fig. 4.18. Equivalent density and radius ratio of such cross section is expressed earlier in the previous Chapter-3.

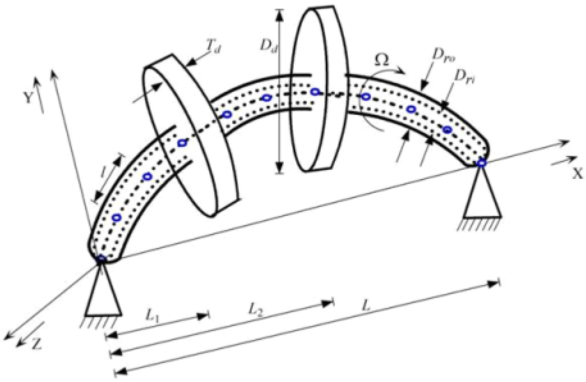

Fig. 4.18 Schematic diagram of deformed rotor disc arrangement

Parameters like, length and diameter of the shaft are 0.5 m and 0.05 m respectively considered for the present numerical example. Poly Vinyl Chloride (PVC) as one material and Lord LD-400 polymer as the second material chosen for the two layers of the multilayer rotor.

2- disc mounted on the rotor shaft are of PVC material. The disc dimensions are given in Table 4.3 below. Following Roy et al. (2013) material properties are shown in Table 4.4.

Table 4.3 Disc parameter

Disc Material	Outer Diameter (m)	Thickness (m)	Mass un-balance (kg-m)	Node position
Disc-1 (PVC)	0.15	0.030	10e-6	3
Disc-2 (PVC)	0.20	0.015	10e-6	5

Table 4.4 Material properties of the rotor

Material	Density 'ρ' (kg/m^3)	'a_0'	'a_1'	'b_0'	'b_1'
PVC	1390	9.21e+11	4.057e+07	378.30	1
LORD LD-400	1500	2.108e+11	1.621e+09	430.41	1

Two noded beam elements are considered in finite element analysis of the rotor shaft. The continuum is discretized into 6- element or 7- nodes and each node has 4- degree of freedom, i.e. 2- displacements and 2- rotations. Calculating with these facts, the total size of the global matrix becomes (28×28) for the full model. Due to simply supported ends, 2- translational degrees of freedom from first and last node are discarded from total degree of freedom. So, the remaining size of the matrix becomes (24×24). According to equation in state space representation the system matrix size enhance to four times of the initial. Thus, the full model consists 96 degrees of freedom. Checking the present system with Hankel singular value decomposition, it is found that the maximum reduction of the system matrices is possible up to 6 degrees of freedom. In this paper, the result presented below is showing the data for the 96$^{\text{th}}$ full mode, 8$^{\text{th}}$ and 6$^{\text{th}}$ reduced mode, under three different values of radius ratios viz. $\Re = 0.0,\ 0.2,\ 0.3$. Most of the results are obtained by keeping PVC as an inner layer, otherwise it has been mentioned. For better understanding of graphs, different legends and line styles are used for representation of these models. Nice match in all figures between reduced and full model shows the importance of this study.

A. Stability limit of spin speed

SLSs are obtained from decay rate plot as shown in Fig. 4.19. In this example, the values of SLS from full mode models for the three different radius ratios are 90 rpm, 376 rpm, and 550 rpm. Considering same example, Fig. 4.20 shows plots between the percentage increase of SLS versus various radius ratios when PVC is kept as an inner layer and an outer layer. The SLS and the relative stability of the system increases as the system get stiffer. The values of SLS from the reduced mode are perfectly matched with full mode. Exactness of the result shows that values obtained from BRS are good and can be used further for the easy computational simulation.

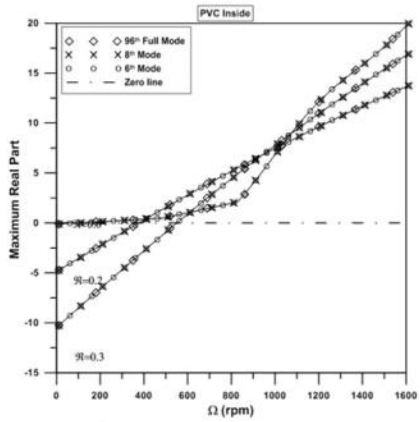

Fig. 4.19 Decay rate plot

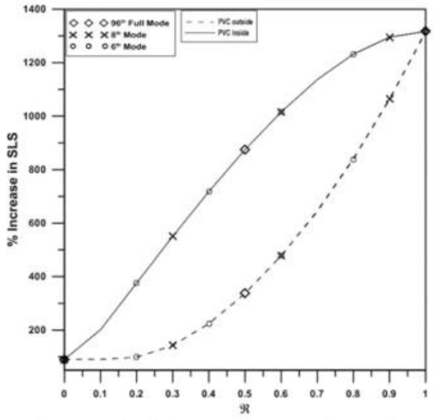

Fig. 4.20 SLS for various radius ratio

B. Campbell diagram

Fig. 4.21 demonstrates the campbell diagram for various radius ratios. For this example the values of FNF are extracted for three different values of radius ratios (i.e. 58 rpm, 310 rpm, and 449 rpm). The values obtained from the reduced model are also nearby with the full model. For the comparative study of values obtained from full and reduced mode is presented in Table 4.6. Shaft performance in terms of FNF is good only when PVC is kept inside and LORD forms outer layer and it is well justified in Fig. 4.22.

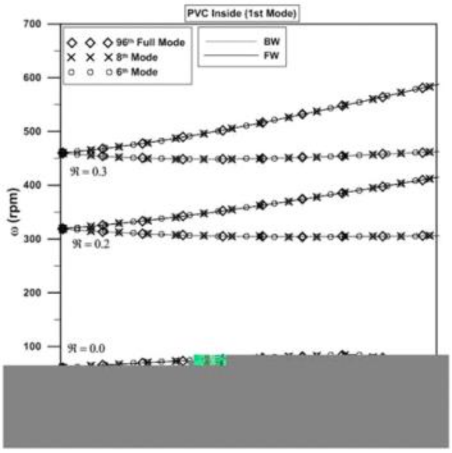

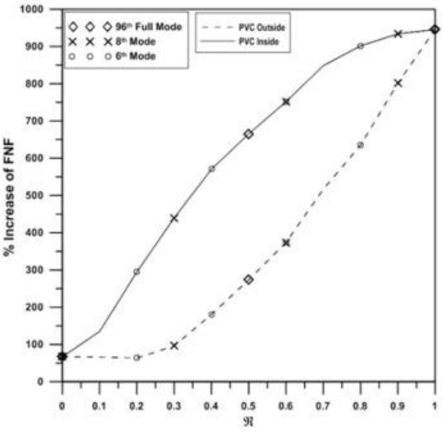

Fig. 4.21 Campbell diagram **Fig. 4.22 FNF for various radius ratio**

C. Modal damping factor

Fig. 4.23 represents the variation of MDF with the rotor spin speed for different radius ratios. The MDF in the plot is only for first mode. From the figure it is clearly visible that the SLS prediction from full mode and the reduced modes are quite similar for three different radius ratios. It also shows that the relative stability of the system increases with increase in radius ratio.

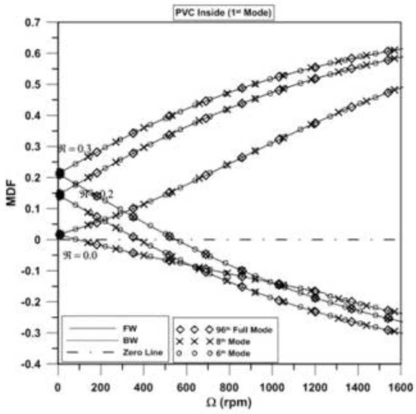

Fig. 4.23 MDF plot

D. *Frequency response due to mass unbalance*

UBR plot shown in Fig. 4.24 reveals that as the radius ratio increases the amplitude response decreases as well as resonance frequency increases, as the shaft becomes stiffer. The results obtained from full and reduced modes are identical in nature. The resonance occurred are similar as the critical speed discussed in above section for three different radius ratios.

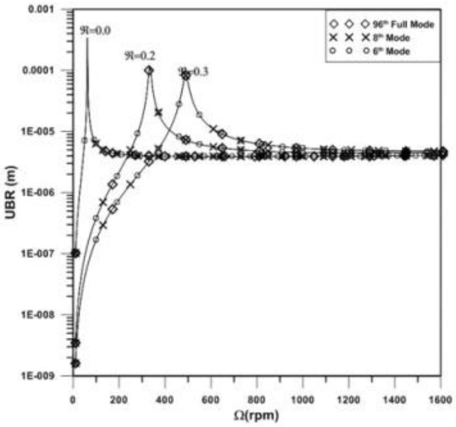

Fig. 4.24 UBR plot

E. Time response due to mass unbalance

Fig. 4.25 and Fig. 4.26 shows the steady state time response of the second disc due to unbalance for two radius ratios, viz. $\Re = 0.2$ and $\Re = 0.3$ considering rotor spin speed is 500 rpm. The nature of the response pattern estimated from the reduced model is as similar to the full model.

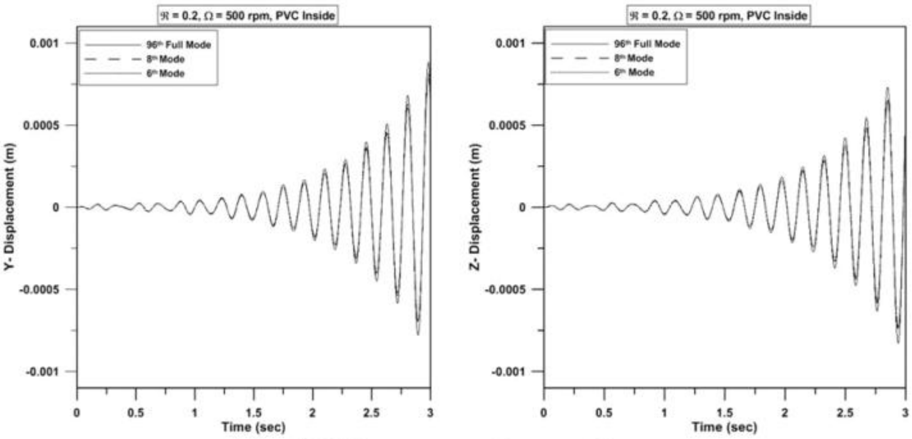

Fig. 4.25 Time response for unstable zone

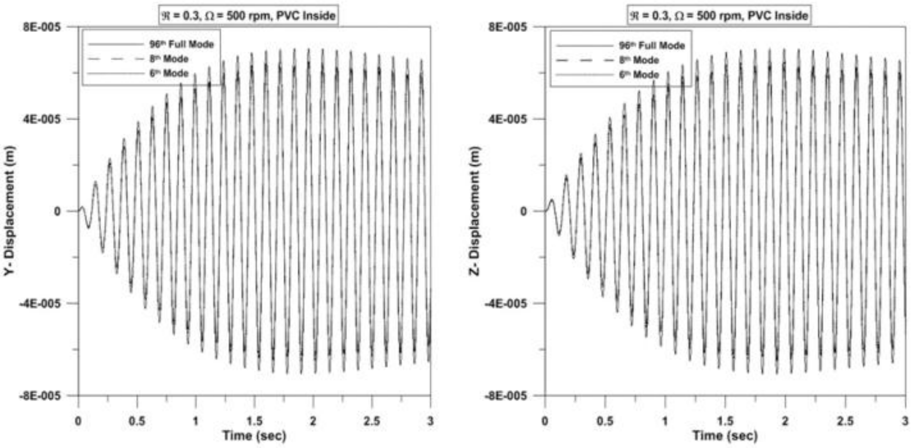

Fig. 4.26 Time response for stable zone

F. Whirl orbit

Fig. 4.27 and Fig. 4.28 show orbit plot due to unbalance. The rotor orbit in first case increases monotonically, whereas the nature of orbit quenches in second case. In first plot rotor spin speed is above the SLS and system shows unstable behaviour. At the end, it is found that there is very less distorsion in dynamic performance of the reduced model and can be reused further to overcome the difficulty of full model.

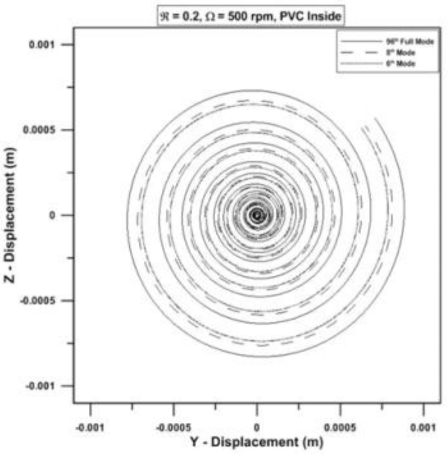

Fig. 4.27 Orbit plot showing unstable region

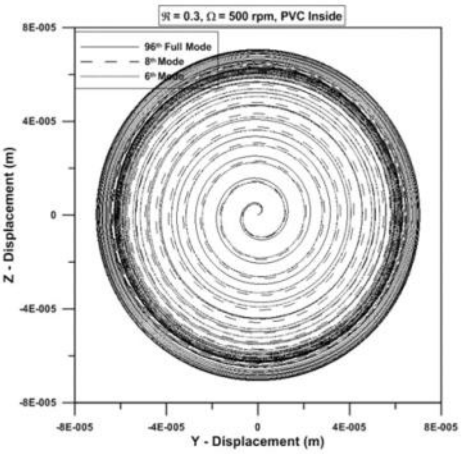

Fig. 4.28 Orbit plot showing stable region

4.6 Summary

Model order reduction is implemented to reduce the computational effort. Several reduction techniques are applied by many researchers to the second order differential equation only. In the present research work, two reduction techniques, i.e., IIRS and BRS are used for the higher order differential equation considering for both third and fourth order examples. From the present results, it is concluded that IIRS is insufficient to reduce the higher order model and the result is deteriorating abruptly when the reduction of modes are gone higher. It is due to the presence of skew-symmetric matrices in the governing equation.

Table 4.5 and Table 4.6 are presented here to show the comparison of modal parameters for the full model and the reduced models using BRS technique.

Table 4.5 Comparison of modal parameters at $L^* = 0.3$ using BRS technique: Case - 1

Mode size	**'Ω_{cr}' (rpm)**				**SLS (rpm)**
	1st BW	**1st FW**	**2nd BW**	**2nd FW**	
120th Full mode	4200	4490	16070	16294	4490
12th Reduced mode	4203	4495	16075	16295	4495
8th Reduced mode	4204	4498	16079	16297	4498

Table 4.6 Comparison of modal parameters using BRS technique: Case - 2

Mode size	**'Ω_{cr}' (rpm)**				**SLS(rpm)**	
	$\mathfrak{R} = 0.2$		$\mathfrak{R} = 0.3$		$\mathfrak{R} = 0.2$	$\mathfrak{R} = 0.3$
	1st BW	**1st FW**	**1st BW**	**1st FW**		
96th Full mode	310	332	449	486	376	550
8th Reduced mode	309	330	447	484	375	548
6th Reduced mode	306	329	446	483	372	547

After analyzing the above tables, it is proven that the balance realization system boosts reduction process by assuring that the transformation matrix for all reduced mode is controllable and observable. The benefit of implementing this technique is to tackle the problems caused due to skew-symmetric matrices that emanate for the addition of internal material damping and gyroscopic effects. Under these conditions, the comparative model order reduction is examined for the different complex modal nature of the rotor dynamic system. For better understanding, the dynamic characteristics of the various system parameters are discussed. Nice agreement between reduced and original system predict the usefulness of this study.

Chapter-5

Conclusion and Future Work

5.1 Conclusions

Based on all estimated facts from earlier discussions, some conclusions are presented here.

i. Modulus operator can be expressed with viscoelastic parameter and differential time operator. Viscoelastic parameters for various materials are found from experimentally obtained values of storage modulus and loss factor. A genetic algorithm based optimization technique has been applied for this purpose.

ii. The present work concentrates on developing a mathematical model of a general viscoelastic rotor by using two distinct approaches; a) Classical model (CM), b) Finite element model (FEM). The operator based constitutive relationship is used to bring down higher order equations of motion. The inherent material properties decide the number of viscoelastic parameters as well as the order of differential equation. Skew symmetric stiffness matrix and damping matrix are generated by considering dissipation effect through all coordinates.

iii. In the classical approach, equations of motion are drawn up by considering lumped mass approximation of the rotor-shaft-system. Whereas, in FE approach, the distributed effect of continuum is considered. The latter is elegant but needs massive computational effort. However, the former is brief, handy and may be used for a quick prediction of dynamic behaviour. But it captures few modes according to degrees of freedom. Therefore, it has some limitation and fails to predict accurate results when the discs are kept at extreme boundaries. Both the models are significant, as per their usage.

iv. For better understanding, modelling of rotor is done under consideration of both rolling and sliding contact bearings. The bearing coefficient matrices of rolling contact bearing are symmetric in nature and such type of nonrotating damping assisting to enhance stability. While considering sliding contact bearing, speed dependent cross couple terms arise in the bearing coefficient matrix and propagate instability. The higher order model also includes asymmetry in higher order terms. Dynamic analysis of such higher order model considering all sources of asymmetry is a real challenge.

v. Complex modal coordinate creates a platform to indicate the directivity of modes. The modal behaviour of higher order model differs from conventional second order model due to the presence of cross dFRFs. This important nature of higher order model is highlighted through accurate modal analysis. Thus, before explaining the exact dynamics of a rotating structure, it is essential to have a perfect model that depends exclusively on material behaviour.

vi. To fulfill modern requirement, the heavy and bulky rotors are replaced by light and stiff composite material. This is done by using multi-layer isotropic viscoelastic materials. The effect of placement of material and their radius ratio in multilayering of rotor is being well justified by taking an example of aluminium/steel (as low damped material) and PVC/LORD LD-400 (as high damped material).

vii. Considering stiffer material as an outer layer, system stiffness increases with increment in radius ratio and causes enhancement in critical frequency. Due to low stiffness and high damping property of inner material benefices the rotor system to work in high critical speed. From the equivalent density point of view, there should be a critical radius ratio, after that the dynamic performance will drop again.

viii. Multi-disc rotor considering CM approach, the size of system matrices is small and directly dependent on number of discs. The disc mass and associated shaft mass are assumed to be accumulated at each disc location. This approach is simple, but sometime becomes numerically insufficient. While, FE model needs a minimum number of elements for achieving a convergent result. As the number of elements increases size of the matrix also increases. The presence of large dimension matrices cause greater computational time as well as the problem of data post processing. This difficulty is getting prominent if the system considers a higher order model. Keeping this in mind reduction of such asymmetric system is essential.

ix. For the sake of finding best methodology to reduce the higher order model, two different reduction techniques are applied here, i.e. a) Iterative Improved Reduction System b) Balanced Realization System. In the first case, an iterative algorithm is used to improve the transformation matrix by achieving convergence. Whereas, in the second case Hankel singular value decomposition assures to predict the most controllable and most observable states, that helps to reduce the system matrices accurately. The dynamic study justifies the effectiveness of reduced model.

x. The obtained values through IIRS technique are poor and abruptly hampered as the spin speed increases; it is due to an insufficient arrangement of the transformation matrix and also due to the participation of skew-symmetric matrices in the higher order system. The errors in IIRS can be minimized up to some extent with the increase of iteration order, and apparently it increases the computation time.

xi. The observability and controllability concepts in balanced realization technique help to predict actual working modes. The reduced model via BRS can reproduce identical results to the original full model even considering higher order asymmetric system. Such reduction is difficult to achieve by some other techniques. The errors found in CM are being rectified with the use of FE model and difficulty in FE model is overcome by balance reduction techniques. Such reduced model also saves computational time significantly.

xii. In the past, most of the researchers developed a reduced model using second order system and considered only single input and single output system. Applications of IIRS and BRS to the higher order system also project a new direction of work. In the present model, there is no such bondage of input and output parameters, this will definitely help to researchers in solving their problem with less constraint.

Some specific contributions made from the research work are as follows:

- ➢ A lower degree of polynomial is sufficient to model the low damped material, whereas higher degree polynomial is essential for high damped material.
- ➢ Both CM and FEM are adequate to model the viscoelastic rotor bearing system.
- ➢ The higher order model is more elegant and predicts accurate results than conventional second order systems.
- ➢ Considering inner layer with less stiff and high damped material is more viable than the outer one in the case of multi-layering arrangement. But as the number of layers increases, it is better to predict the orientation of layers through its best dynamic behaviour.
- ➢ Limitations of CM are rectified with FEM. Similarly, drawbacks of FEM are taken care with the help of model order reduction. In which, BRS technique is superior then IIRS for higher order model.

5.2 Potential applications of present work

The presented work purely shows the mathematical modelling for various viscoelastic rotor system. The mathematical procedure and formulations can be used for any type of rotor bearing arrangements. Here some of applications are shown below.

1) **Applications of isotropic material rotors**:
    - (a) Rotors made of low damped material like metals (mild steel, aluminium) are largely used in gas turbines, turbochargers, centrifugal compressors, where the rotating machines operate with very high speed, and vibration is a major issue. Some of the vibration problems are minimized by such viscoelastic rotor.
    - (b) Rotors made of high damped material like polymers (PVC, Lord LD-400) are mainly used in light duty application and normal temperature environment, like rotors in an optical drive, quadcopter, soft toy, home mixer-grinder, etc.
2) **Applications of composite material rotors**:
    - (a) Aluminium/mild steel composite rotors are examples of low damped material, and can be used as an alternative where the weight and strength of the rotor are a major issue. This type of rotor also helps to reduce the vibration problem caused at very high speed. One real time problem is faced at NIT Rourkela campus when a high-speed differential shaft of F1 formula car is needed to be replaced with some light weight material. Here the concept of a multilayered shaft can be used to achieve the desired task.
    - (b) PVC/Lord LD-400 composite rotors are the examples of high damped material. This rotor can mainly be used in a cold environment condition where the use of metals faces severe icing problem. This type of rotor can also be utilized in a lightweight submarine application where corrosion of metals is big challenges.
3) **Application of model order reduction:** Model order reduction methods are mainly used for bulky system obtain through finite element formulation. ANSYS, MSC NASTRAN, ROTORINSA, and ADAMS are some FEM packages, used for rotor modelling. In the present research, IIRS and BRS are applied to reduce the one-dimensional rotor model. These techniques also help in reducing the computational time and global error.

5.3 Future scopes

This study has given birth to numerous other possibilities which may be taken up as future research activities in this area.

1) Effects of temperature on the viscoelastic material:
   Properties of viscoelastic material are usually dependent on the temperature of the continuum. Taking into account the temperature effect on the equation of motion of the rotor poses an interesting problem and may be pursued as a direction of future research work.
2) Effects of shear deformation:
   For the complete study, it is necessary to incorporate transverse shear stress that has been neglected in the present model for the sake of simplicity.
3) Effects of stacking sequences:
   In the present model, composite is formed by multi layering of isotropic viscoelastic materials. Operator based approach can also be adopted to model the fibre reinforced composite rotor, where the orientation of fibre may change for layer to layer.
4) Operator based approach for 2D and 3D rotor model:
   The present work is concentrated on modelling of a viscoelastic rotor using one-dimensional finite element approach. This technique can also be extended to 2D and 3D rotor models.
5) Operator based approach for particulate based composite rotors:
   One of the classifications of composite is particulate composite, and rotor made up of this type of material give rise to another field of research. Applying operator based approach to obtain constitutive relationship for particulate composite is never approached in past literature.
6) Operator based approach for non-axisymmetric rotor
   The present model considers axisymmetric rotor. But axisymmetry may be destroyed due to various reasons. Considering actual practical applicability, this can be extended to non-axisymmetric rotors.
7) Experimental validation:
   From the validation point of view, it is necessary to perform experimental validation. In immediate future, it can be accomplished by setting an experimental setup for rotor bearing model.
8) Implementation of condition monitoring:
   Various parts are attached to the rotor models, and all faces severe vibration problems. It is necessary to monitor the system by its rational behaviour. Through proper

conditioning of machines various irregularities and miss happening can be minimized. After establishing an experimental setup, condition monitoring can be smoothly done in future for the present model.

Bibliography

Al-Saggaf, U. M., Barratt, C., and Bettayeb M., (1993), "Techniques in optimized model reduction for high dimensional systems", *In: Control and Dynamic Systems: Advances in Theory and Application, New York: Academic Press*, Vol. 55, Part-1, pp. 51-109.

Alves, M. S., Buriol, C., Ferreira, M. V., Munoz, R. J. E., Sepulveda, M., and Vera, O., (2013), "Asymptotic behaviour for the vibrations modeled by the standard linear solid model with a thermal effect", *Journal of Mathematical Analysis and Applications*, Vol. 399, pp. 472-9.

Asnani, N. T., and Nakra, B. C., (1976), "Vibration damping characteristics of multilayered beams with constrained viscoelastic layers", *Journal of Engineering for Industry*, Vol. 98, No. 3, pp. 895–901.

Adhikari, S. (1999), "Modal analysis of linear asymmetric nonconservative systems." *Journal of Engineering Mechanics*, Vol. 125, No. 12, 1372–1379.

Adhikari, S., (2001), "Eigenrelations for nonviscously damped systems", *AIAA Journal*, Vol. 39, No. 8, pp. 1624-30.

Adhikari, S., (2002), "Dynamics of nonviscously damped linear systems", *Journal of Engineering Mechanics*, Vol. 128, No. 3, pp. 328-339.

Bagley, R. L., and Torvik, J., (1983), "Fractional calculus-a different approach to the analysis of viscoelastically damped structures", *AIAA Journal,* Vol. 21, pp. 741-8.

Bagley, R. L., and Torvik, J., (1985), "Fractional calculus in the transient analysis of viscoelastically damped structures", *AIAA Journal*, Vol. 23, pp. 918-25.

Bagley, R. L., and Torvik, J., (1986), "On the fractional calculus model of viscoelastic behaviour", *Journal of Rheology*, (1978), Vol. 30, pp. 133-55.

Benner, P., and Saak, J., (2011), "Efficient balancing based MOR for large scale second order systems", Mathematical and Computer Modelling of Dynamical Systems, *Mathematical and Computer Modelling of Dynamical Systems, Springer,* pp. 1–17.

Bavastri, C. A, Ferreira, E. M. D. S., Espíndola, J. J. D., and Lopes, E. M. D. O., (2008), "Modeling of dynamic rotors with flexible bearings due to the use of viscoelastic materials" *Journal of the Brazilian Society of Mechanical Science & Engineering, ABCM,* Vol. XXX, No. 1, pp. 22-29.

Bert, C. W., (1973), "Material damping an introductory review of mathematical model, measures and experimental techniques", *Journal of sound and vibration*, Vol.29, No. 2, pp. 129–153.

Bert, C. W., (1992), "The effect of bending–twisting coupling on the critical speed of a driveshafts", *Proceedings, 6th Japan–US Conference on Composites Materials, Orlando, FL. Technomic, Lancaster*, PA, pp. 29–36.

Bert, C. W., and Kim, C. D., (1995), "Whirling of composite material drive shafts including bending-twisting coupling and transverse shear deformation", *Journal of Vibration and Acoustics*, Vol. 117, No. 1, pp. 7–21.

Bland, D. R., (1960), "The theory of linear viscoelasticity", *Pergamon Press, Oxford*, pp. 1-10.

Carrera, E., Filippi, M., and Zappino, E., (2013), "Analysis of rotor dynamic by one-dimensional variable kinematic theories", *Journal of Engineering for Gas Turbines and Power*, Vol. 135, pp. 1-9.

Carrera, E. and Filippi, M., (2014), "Variable kinematic one-dimensional finite elements for the analysis of rotors made of composite materials", *Journal of Engineering for Gas Turbines and Power*, Vol. 136, No. 9, pp. 459-461.

Chandraker, S., Roy, H., and Maurya, G., (2013), "Modal analysis of multi-layer viscoelastic rotors considering higher order model", *Proceeding in GTINDIA, ASME Conference, Bangalore, India*.

Chandraker, S., and Roy, H., (2014), "A balanced IIRS model for investigating the dynamics of damped rotor bearing system", *Proceeding in GTINDIA, ASME Conference, New Delhi, India*.

Chandramouli, G., Gupta, K., Pandey, R. K., (1994), "Delamination propagation in rotating carbon-epoxy composite shaft" *Engineering Fracture Mechanics*, Vol. 49, No. 1, pp. 121-132.

Chang, M. Y., Chen, J. K., and Chang, C. Y., (2004a), "A simple spinning laminated composite shaft model", *International Journal of Solids and Structures*, Vol. 41, No. 3-4, pp. 637–662.

Chang, C. Y., Chang, M. Y., and Huang, J. H., (2004b), "Vibration analysis of rotating composite shafts containing randomly oriented reinforcements" *Composite Structures*, Vol. 63, No, 1, pp. 21–32.

Chatelet, E., Ambrosio, F. D., and Jacquet-Richardet, G., (2005), "Toward global modeling approaches for dynamic analyses of rotating assemblies of turbomachines", *Journal of Sound Vibration*, Vol. 282, pp. 163–178.

Chávez, J. P., Hamaneh, V. V., and Wiercigroch, M., (2015), "Modelling and experimental verification of an asymmetric Jeffcott rotor with radial clearance", *Journal of Sound and Vibration*, Vol. 334, pp. 86–97.

Chen, Y., and Jiang, J., (2015), "Effects of forward/backward whirl mechanism on nonlinear normal modes of a rotor/stator rubbing system", *Journal of Vibration and Acoustics*, Vol. 137, pp. 1-7.

Chouksey, M., (2012), "Studies in modal analysis, frequency response characteristics and finite element model updating of rotor systems", *Ph.D. thesis*, *Indian Institute of Technology, Delhi*, pp. 1–244.

Chouksey, M., Modak, S. V., and Dutt, J. K., (2010), "Influence of rotor-shaft material damping on modal and directional frequency response characteristics" *ISMA, Katholieke Universiteit, Leuven, Belgium*, pp. 1543–1557.

Chouksey, M., Dutt, J. K., and Modak, S. V., (2012), "Modal analysis of rotor-shaft system under the influence of rotor-shaft material damping and fluid film forces", *Mechanism and Machine Theory*, Vol. 48, pp. 81–93.

Christensen, R. M., (1982), "Theory of viscoelasticity, an introduction", Academic press, New York.

Combescure, D., and Lazarus, A., (2008), "Refined finite element modelling for the vibration analysis of large rotating machines: application to the gas turbine modular helium reactor power conversion unit," *Journal of Sound and Vibration*, Vol. 318, pp. 1262–1280.

Craig, R. and Bampton, M., (1968), "Coupling of substructures for dynamic analyses", *AIAA Journal*, Vol. 6, No.7, pp. 1313-1319.

Crandall, S. H., (1983), "Physical nature of rotor instability mechanisms", *Proceedings of the Rotor Dynamical Instability, ASME special publication, AMD,* Vol.55, pp. 1-18.

Crandall, S. H., and Yeh, N. A., 1989, "Automatic generation of component modes for rotordynamic substructures," *ASME Journal of Vibration, Acoustics, Stress, and Reliability in Design,* Vol. 111, pp. 6-10.

Das, A. S., (2009), "Active vibration control of flexible rotors with electromagnetic actuator", *Ph.D. thesis, IIT, Kharagpur, India.*

Das, A. S., and Dutt, J. K., (2008), "Reduced model of a rotor-shaft system using modified SEREP", *Mechanics Research Communications*, Vol. 35, pp. 398–407.

Das, A. S., and Dutt, J. K., (2012), "A reduced rotor model using modified SEREP approach for vibration control of rotors", *Mechanical Systems and Signal Processing*, Vol. 26, pp. 167-180.

Dimentberg, M., (1961), "Flexural vibrations of rotating shafts", *Butterworth London, England*.

Dunkerley, St., (1895), "On the whirling and vibration of shafts", *Philosophical Transaction of Royal Society*, Vol. 185, pp. 279-360.

Dutt, J. K. (1992), "Studies on dynamics of rotating systems with viscoelastically damped supports", *Ph.D thesis, Department of Mechanical Engineering IIT Delhi, India* .

Dutt, J. K., and Nakra, B. C., (1992), "Stability of rotor systems with viscoelastic supports", *Journal of sound and vibration*, Vol. 153, No.1, pp. 89-96.

Dutt, J. K., and Nakra, B. C., (1995), "Dynamics of rotor shaft-system on flexible support with gyroscopic effects", *Mechanic Research Communication*, Vol. 22, No.6, pp. 541-545.

Dutt, J. K., and Nakra, B. C., (1996), "Stability characteristics of rotating system with journal bearing on viscoelastic supports", *Journal of sound and vibration*, Vol. 31, No.6, pp. 771-779.

Dutt, J. K., and Toi, T., (2003), "Rotor vibration reduction with polymeric sectors", *Journal of sound and vibration*, Vol. 262, No.4, pp. 769-793.

Dutt, J. K., and Roy, H., (2011), "Viscoelastic modelling of rotor–shaft systems using an operator-based approach", *Journal of Mechanical Science, IMechE, Part-C*, Vol. 225, No. 1, pp. 73-87.

Ehrich, F. F., (1964), "Shaft whirl induced by rotor internal damping", *ASME, Journal of Applied Mechanics*, Vol. 31, pp. 279-282.

Ewins, D. J., (2000a), "Basics and state-of-the-art of modal testing", *Sadhana,* Vol. *25*, No. 3, pp. 207-220.

Ewins, D. J., (2000b), "Modal testing: Theory, practice and application", *Research Studies Press, Baldock, Hertfordshire, England*.

Ferry, J. D., (1980), "Viscoelastic properties of polymers", *John Wiley and Sons, New York*.

Fernando, K. V., and Nicholson, H., (1982), "Singular perturbation model reduction of balanced systems", *IEEE Transactions on Automatic Control*, Vol. AC-27, No. 2, pp. 466-468.

Foppl, A., (1895), "Das problem der lavalschen turbinenwelle", *Der Civilingenieur*, Vol. 4, pp. 335-342.

Friedrich, C. H. R., (1991), "Relaxation and retardation functions of the Maxwell model with fractional derivatives", *Rheologica Acta*, Vol. 30, pp.151-8.

Friswell, M. I., Garvey, S. D, and Penny, J. E. T., (1995), "Model reduction using dynamic and iterated IRS technique", *Journal of Vibration and Acoustics*, Vol. 186., No. 2, pp. 311–323.

Friswell, M. I., Penny, J. E. T., and Garvey, S. D., (1996), "The application of the IRS and balanced realization methods to obtain reduced models of structures with local non-linearities", *Journal of Vibration and Acoustics*, Vol. 196., No. 4, pp. 453–468.

Friswell, M. I., Garvey, S. D, and Penny, J. E. T., (1998), "The convergence of the iterated IRS method", *Journal of sound and Vibration*, Vol. 211., No. 1, pp. 123–132.

Friswell, M. I., and Inman, D. J., (1999), "Reduced-order models of structures with viscoelastic components", *American Institute of Aeronautics and Astronautics Journal*, Vol. 37., No. 10, pp. 1318–1325.

Friswell, M. I., Penny, J. E. T., and Garvey, S. D., (2000), "Model reduction for structures with damping and gyroscopic effects", *ISMA-25 Katholieke Universiteit Leuven, Belgium*, pp. 1-9.

Friswell, M. I., Dutt, J. K., Adhikari, S. and Lees, A. W., (2010a), "Time domain analysis of a viscoelastic rotor using internal variable models", *International Journal of Mechanical Sciences*, Vol. 52., No. 10, pp. 1319–1324.

Friswell, M. I., Penny, J. E. T., Garvey, S. D, and Lees, A. W., (2010b), "Rotor dynamics: Modeling and analysis of rotating machines", *Cambridge university press, USA*.

Genta, G., (2005), "Dynamics of rotating systems", *Springer*.

Genta, G., (2004), "On a persistent misunderstanding of the role of hysteretic damping in rotor dynamics", *Journal of vibration and acoustics*, Vol. 126, pp. 459-461.

Genta, G., and Amati, N., (2009), "On the equivalent viscous damping for the system with hysteretic", *Atti dell'Accademia delle Scienze di Torino*.

Genta, G., and Amati, N., (2010), "Hysteretic damping in rotordynamics: An equivalent formulation", *Journal of Sound and Vibration*, Vol. 329, pp. 4772–4784.

Golla, D. F., and Hughes, P. C., (1985), "Dynamics of viscoelastic structures—a time-domain, finite element formulation", *Journal of Applied Mechanics*, Vol. 52, pp. 897-906.

Grybos, R., (1991), "The dynamics of a viscoelastic rotor in flexible bearing", *Archive of Applied Mechanics, Springer Verlag*, Vol. 61, pp. 479-487.

Gunter, E. J. J., (1967), "The influence of internal friction on the stability of high speed rotors", *Transactions of the American Society of Mechanical Engineers, Journal of Engineering for Industry,* pp. 683-688.

Gunter, E. J. J., and Trumpler, P. R., (1969), "The influence of internal friction on the stability of high speed rotors with anisotropic supports", *ASME, Journal of Engineering for Industry,* Vol. 52, pp. 683-688.

Gupta, K. and Singh, S. P., (1998), "Damping measurement in fibre reinforced composite rotor", *Journal of Sound and Vibration,* Vol. 211, No. 3, pp. 513-520.

Guo, Y., and Parker, R. G., (2012), "Stiffness matrix calculation of rolling element bearings using a finite element/contact mechanics model", *Mechanism and Machine Theory,* Vol. 51, pp. 32-45.

Gubran, H. B. H., and Gupta, K., (2005), "The effect of stacking sequence and coupling mechanisms on the natural frequencies of composite shaft", *Journal of Sound and Vibration*, Vol. 282, No. 1–2, pp. 231–248.

Guyan, R. J., (1965), "Reduction of stiffness and mass matrices", *AIAA Journal*, Vol. 3, No. 2, pp. 320.

Hamrock, B., Schmid, S. R., and Jacobson, B. O., (2004), "Fundamentals of fluid film lubrication", *CRC Press*.

Han, J. S., (2014), "Krylov subspace-based model order reduction for Campbell diagram analysis of large-scale rotordynamic systems", *Structural Engineering and Mechanics*, Vol. 50, No. 1, pp. 19–36.

Harnoy, A., (2003), "Bearing design in machinery: Engineering tribology and lubrication", *New York: Marcel Dekker*.

Harris, T. A., (2001), "Rolling bearing analysis", *Wiley*.

Holmes, R., (1963), "Oil-whirl characteristics of a rigid rotor in 360° journal bearings", *Proceedings of the I. Mech. E*. Vol. 177, pp. 291–307.

Jalali, M. H., Ghayour, M., Rad, S. Z., and Shahriari, B., (2014), "Dynamic analysis of a high speed rotor-bearing system" *Measurement*, Vol. 53, pp. 1–9.

Jeffcott, H., (1919), "The lateral vibration of loaded shafts in the neighborhood of a whirling speed-the effect of want of balance", *Philadelphia Magazine*, Vol. 37, No. 6, pp. 301-314.

Jei Y.G. and Kim Y.J., (1993), "Modal Testing Theory of Rotor-Bearing Systems", *Journal of Vibration and Acoustics*, *ASME*, Vol. 115, pp. 165–176.

Jia, J. H., Shen, X. Y., and Hua, H. X., (2007), "Viscoelastic behavior analysis and application of the fractional derivative Maxwell model", *Journal of Vibration and Control*, Vol. 13, pp. 385-401.

Joh, C. Y., and Lee, C. W., (1996), "Use of dFRFs for diagnosis of asymmetric/anisotropic properties in rotor-bearing system", *Journal of Vibration and Acoustics*, *ASME,* Vol. 118 pp. 64–69.

Jei, Y.G., and Lee, C. W., (1992), "Does curve veering occurs in the eigenvalue problem of rotors?" *Journal of Vibration and Acoustics*, *Trans. ASME*, Vol. 114, pp. 32–36.

Kandil, M. A., (2004), "On rotor internal damping instability", *Ph.D. thesis, University of Imperial college of London, pp. 1-265.*

Kapur, A. D., Nakra, B. C., and Chawla, D. R., (1977), "Shock response of viscoelastically damped beam", *Journal of Sound and Vibration*, Vol. 55, No. 3, pp. 351-362.

Kramer, E., (1993), "Dynamics of rotors and foundation", *Springer-Verlag*.

Kessler, C. L., (1999), "Complex modal analysis of rotating machinery", *Ph.D. thesis, University of Cincinnati, United states*, pp. 1-106.

Kessler, C. L., and Kim, J., (2002), "Vibration analysis of rotors utilizing implicit directional information of complex variable descriptions", *Journal of Vibration and Acoustics, ASME* Vol. 124, pp. 340–349.

Kessler, C. L., Kim, J., (2006), "Complex modal analysis and interpretation for rotating machinery", *SEM, IMAC XVI - 16th International Modal Analysis Conference - Model Updating & Correlation*.

Kessler, C. L., Kim, J., (2007), "Complex modal analysis and modal superposition for rotating machinery", *SEM, XVII-17th International Modal Analysis Conference - Model Updating & Correlation*.

Kiciński, J., (2010), "Rotor Dynamics", *Alstom IMP Pan publishers, Gdansk, Poland*.

Kirk, R. G., and Gunter, E. J., (1972), "The effect of support flexibility and damping on the synchronous response of a single mass flexible rotor", *Transactions of the American Society of Mechanical Engineers, Journal of Engineering for Industry,* pp. 221-232.

Kim, C. D., and Bert, C. W., (1993), "Critical speed analysis of laminated composite, hollow drive shafts", Composites Engineering, Vol. 3, No. 7–8, pp. 633–643.

Ku, D. M., (1998), "Finite element analysis of whirl speeds for rotor-bearing systems with internal damping", *Mechanical Systems and Signal Processing*, Vol. 12, No. 5, pp. 599-610.

Lalanne, M. and Ferraris, G., (1998), "Rotor dynamics prediction in Engineering", *John Wiley and Sons*.

Lam, M. J., Inman, D. J., and Saunders, W. R., (1997), "Vibration control through passive constrained layer damping and active control", *Journal of Intelligent Material Systems and Structures,* Vol. 8 pp. 663-77.

Lam, M. J., Inman, D. J., and Saunders, W. R., (2000), "Hybrid damping models using the Golla-Hughes-McTavish method with internally balanced model reduction and output feedback", *Smart Materials and Structures*, Vol. 9, pp. 362.

Lam, M. J., Saunders, W. R., and Inman, D. J., (1995), "Modeling active constrained-layer damping using Golla-Hughes-McTavish approach", *International Society for Optics and Photonics*, Article ID: 2445, pp. 86-97.

Lazan, B. J., (1968), "Damping of material and members in structural mechanics", *Pergamon press, Oxford London*.

Lee, C. W., (1991), "A complex modal testing theory for rotating machinery", *Mechanical Systems and Signal Processing*, Vol. 5, No. 2, pp.119-137.

Lee, C. W., (1993), "Vibration analysis of rotors", *Kluwer Academic Publishers*.

Lee, C. W., and Jei, Y. G., (1988), "Modal analysis of continuous rotor-bearing systems", *Journal of Sound and Vibration*, Vol. 126, No. 2, pp. 345–361.

Lee, C. W., and Lee, S. K., (1997), "An efficient complex modal testing theory for asymmetric rotor systems: use of undirectional excitation method", *Journal of Sound and Vibration*. Vol. 206 pp. 327–338.

Lei, Y., Adhikari, S., and Friswell, M. I., (2013), "Vibration of nonlocal Kelvin–Voigt viscoelastic damped Timoshenko beams", *International Journal of Engineering Science*, Vol. 66–67, pp. 1-13.

Lesieutre, G. A., (1989), "Finite elements modelling of frequency-dependent material damping using augmenting thermodynamic fields", *Ph.D. Thesis, University of California, Los Angeles*.

Lesieutre, G. A., (1992), "Finite elements for dynamic modeling of uniaxial rods with frequency-dependent material properties", *International Journal of Solids and Structures,* Vol. 29, pp. 1567-79.

Lesieutre, G. A., and Mingori, D. L., (1990), "Finite element modelling of frequency-dependent material damping using augmenting thermodynamic fields", *AIAA Journal of Guidance, Control and Dynamics*, Vol. 13, No. 6, pp. 1040-1050.

Lesieutre, G. A., and Bianchini, E., (1995), "Time domain modeling of linear viscoelasticity using anelastic displacement fields", *Journal of Vibration and Acoustics*, Vol. 117, pp. 424-30.

Lesieutre, G. A., and Govindswamy, K., (1996), "Finite element modeling of frequency dependent and temperature-dependent dynamic behavior of viscoelastic materials in simple shear", *International Journal of Solids and Structures,* Vol. 33, pp. 419-32.

Lesieutre, G. A., and Lee, U., (1996), "A finite element for beams having segmented active constrained layers with frequency-dependent viscoelastic", *Smart Materials and Structures*, Vol. 5, pp. 615.

Lesieutre, G. A., Bianchini, E., and Maiani, A., (1996), "Finite element modelling of one-dimensional viscoelastic structures using anelastic displacement fields", *AIAA Journal of Guidance, Control and Dynamics*, Vol. 19, No. 3, pp. 520-527.

Lewandowski, R., and Chorazyczewski, B., (2010), "Identification of the parameters of the Kelvin–Voigt and the Maxwell fractional models, used to modeling of viscoelastic dampers", *Computers & Structures*, Vol. 88, pp. 1-17.

Liu, Y. I, and Anderson B. D. O., (1989), "Singular perturbation approximation of balanced systems", *International Journal of Control*, Vol. 50, No. 4, pp. 1379-1405.

Liu, Y., Liu, H., Yi, J., and Jing, M., (2013), "Investigation on the stability and bifurcation of a 3D rotor-bearing system" *Journal of Vibration and Acoustics*, Vol. 135, pp. 1-11.

Lu, L. Y., Lin, G. L., and Shih, M. H., (2012), "An experimental study on a generalized Maxwell model for nonlinear viscoelastic dampers used in seismic isolation", *Engineering Structures*, Vol. 34, pp. 111-23.

Mainardi, F., (2010), "Fractional calculus and waves in linear viscoelasticity: An introduction to mathematical models", *World Scientific*.

Makris, N., and Constantinou, M. C., (1991), "Fractional-derivative Maxwell model for viscous dampers", *Journal of Structural Engineering*, Vol. 117, pp. 2708-24.

Matthew, B. W., Younan, A., Paul, A., and Cogill, R., (2010), "Model reduction methods for rotor dynamic analysis: A survey and review", *International Journal of Rotating Machinery*, Article ID: 273716, pp. 1-17.

MATLAB, (2010). Version 7.8.0.347: *The MathWorks Inc*.

McTavish, D. J., (2003), "Shock response of a damped linear structure using GHM finite elements", *Proceedings of the 44th AIAA/ASME/ASCE/AHS/ASC Structures, Structural Dynamics, and Materials Conference. Norfolk, Virginia*, pp. 1681-9.

McTavish, D. J., and Hughes, P. C., (1992), "Finite element modeling of linear viscoelastic structures-The GHM method", *33rd Structures, Structural Dynamics and Materials Conference: American Institute of Aeronautics and Astronautics*.

McTavish, D. J., Hughes, P. C., Soucy, Y., and Graham, W. B., (1992), "Prediction and measurement of modal damping factors for viscoelastic space structures", *AIAA Journal*, Vol. 30, pp. 1392-9.

McTavish, D. J., and Hughes, P. C., (1993), "Modeling of linear viscoelastic space structures", *Journal of Vibration and Acoustics,* Vol. 115, pp. 103-10.

Meirovitch, L., (1986), "Elements of vibration analysis" *International Edition McGraw-Hill, New York.*

Mesquita, A. L. A, Dias, M. Jr., and Miranda, U. A., (2002), "A comparison between the traditional Frequency Response Function (FRF) and the directional Frequency Response Function (dFRF) in rotor dynamic analysis *", MECOM, First South American congress on computational mechanics*, *Santa fe-parana, Argentina*, pp. 2227–2246.

Mohiuddin, M. A., Bettayeb, M., and Khulief, Y. A., (1998), "Dynamic analysis and reduced order modelling of flexible rotor-bearing systems" *Computers and Structures*, Vol. 69, pp. 349-359.

Montagnier, O., and Hochard, C. (2014) "Dynamics of a supercritical composite shaft mounted on viscoelastic supports", *Journal of Sound and Vibration*, Vol. 333, pp. 470–484.

Moore, B. C., (1981), "Principal component analysis in linear systems: controllability, observability, and model reduction", *IEEE Transactions on Automatic Control*, Vol. AC-26, No. 1, pp. 17-32.

Muszynska, A., (1986), "Whirl and whip–rotor/bearing stability problems", *Journal of Sound and Vibration,* Vol. 110 pp. 443–462.

Muszynska, A., (2005), "Rotordynamics", *CRC press, Taylor and Francis*.

Muszynska, A., and Goldman, P., (1995), "Chaotic responses of unbalanced rotor/bearing/stator systems with looseness or rubs", *Chaos, Solitons and Fractals*, Vol. 5, No. 9, pp. 1683-1704.

Nakra, B. C., (1998), "Vibration control in machines and structures using viscoelastic damping", *Journal of Sound and Vibration*, Vol. 211, No. 3, pp. 449-465.

Nelson, H. D., (1980), "A finite rotating shaft element using timoshenko beam theory," *ASME, Journal of Mechanical Design*, Vol.102, pp. 793-804.

Nelson, H. D., and McVaugh, J. N., (1976), "The dynamics of rotor-bearing systems using finite elements," ASME, *Journal of Engineering for Industry*, Vol. 98, No. 2, pp. 593-600.

Nashif, A. D., Jones, D., and Henderson, J., (1985), "Vibration damping", *John Wiley and Sons, New York*.

Nashif, A. D., and Lewis, T. M., (1991), "Data base of the dynamic properties of materials", *Journal of Sound and Vibration*, Vol. 25, pp. 14-25.

O'Callahan, J. C., Avitabile, P., and Riemer, R., (1989), "System Equivalent Reduction and Expansion Process (SEREP)", *Proceedings of the 6th International Modal Analysis Conference, Las Vegas*, pp. 29-36.

O'Callahan, J. C., (1989), "A procedure for an Improved Reduced System (IRS) model", *Proceedings of the 6th International Modal Analysis Conference, Las Vegas*, pp. 17-21.

Ozguven, H. N. and Ozkan, Z. L., (1984), "Whirl speeds and unbalance response of multibearing rotors using finite elements", *Journal of Vibration and Acoustics*, Vol. 106, No. 1, pp. 72 -79.

Palmeri, A., and Muscolino, G., (2011), "A numerical method for the time-domain dynamic analysis of buildings equipped with viscoelastic dampers", *Structural Control and Health Monitoring*, Vol. 18, pp. 519-39.

Pernebo, L., and Silverman, L. M., (1982), "Model reduction via balanced state space representation", *IEEE Transactions on Automatic Control*, Vol. AC-27, No. 2, pp. 382-387.

Qu, Z-Q., (2004). "Model order reduction technique with application in finite element analysis", *Springer-Verlag London Berlin Heidelberg*.

Rankine, W. J. M., (1869), "On the centrifugal force of rotating shafts", *The Engineer*.

Rao, J. S., (2009), "Rotor dynamics", *New Age International Publishers, New Delhi*.

Reis, D. H. L. M., Goldman, R. B., and Verstrate, P. H., (1987), "Thin-walled laminated composite cylindrical tubes: Part III-Critical speed analysis", *Journal of Composites Technology and Research*, Vol. 9, pp. 58–62.

Roy, H., (2008), "Study of dynamics of viscoelastic rotors- A finite element approach", *Ph.D. thesis, IIT, Kharagpur, India*, pp. 1-133.

Roy, H., and Dutt, J. K., (2016), "Dynamics of polymer and polymer composite rotors – An operator based finite element approach", *accepted for publication in Applied Mathematical Modelling Journal*, Vol. 40, (2016), 1754-1768.

Roy, H., Dutt, J. K., and Datta, P. K., (2008), "Dynamics of a viscoelastic rotor shaft using augmenting thermodynamic fields — a finite element approach", *International Journal of Mechanical Sciences*, vol. 50, No. 4, pp. 845-853.

Roy, H., Dutt, J. K., and Datta, P. K., (2009), "Dynamics of mutilayer viscoelastic beams", *Structrual Engineering and Mechanics*, vol. 33, No. 4, pp. 391-406.

Roy, H., Dutt, J. K., and Datta, P. K., (2013), "Dynamic behavior of stepped multilayered viscoelastic beams – A finite element approach" *Advances in Vibration Engineering*, Vol. 12, No. 1, pp. 75-88.

Roy, H., Dutt, J. K., and Chandraker, S., (2014), "Modeling of multilayered viscoelastic rotors – An operator based approach", *Journal of Vibration Engineering and Technologies*, Vol. 2, No. 6, pp. 485-494.

Roy, H., and Dutt, J.K., (2015), "Dynamics of polymer and polymer composite rotors – An operator based finite element approach", *accepted for publication in Applied Mathematical Modelling Journal, doi:10.1016/j.apm.2015.08.021*.

Roy, H., and Chandraker, S., (2015), "A comparative study between classical and finite element model for multilayer viscoelastic rotors", *Published proceeding at ASME GTINDIA conference, Hyderabad, India, paper id- GTINDIA-1330.*

Ruhl, R. L., and Booker, J. F., (1971), "A finite element model for distributed parameter turborotor systems", *Journal of Engineering for Industry, ASME*, Vol. 94, No. 1, pp. 126-132.

Saksena, V. R, O'Reilly, J., and Kokotovic, P. V., (1984), "Singular perturbations and time scale methods in control theory: survey 1976-1983", *Automatica*, Vol. 20, pp. 273-93.

Satyanarayana, N., Tiwari, R., and Talukdar, S., (2003), "Whirling of a simple rotor with gyroscopic effects: A finite element approach based on complex coordinates", *Advances in Vibration Engineering*, Vol. 2, No. 3, pp. 270-279.

Shames, I. H., and Cozzarelli, F. A., (1992), "Elastic and inelastic stress analysis", *Prentice Hall, Englewood Cliffs, New Jersey*.

Singh, S. P., and Gupta, K., (1994), "Free damped flexural vibration analysis of composite cylindrical tubes using beam and shell theories", *Journal of Sound and Vibration,* Vol.172, No.2, pp. 171-190.

Singh, S. P., and Gupta, K., (1996), "Composite shaft rotordynamic analysis using a layerwise theory", *Journal of Sound and Vibration,* Vol.191, No.5, pp. 739-756.

Sino, R., Baranger, T. N., Chatelet, E., Jacquet, G., (2008), "Dynamic analysis of a rotating composite shaft", *Composite Science and technology*, Vol. 68, No. 2, pp. 337–345.

Stepan, G., Frank, P., Muller, T., and Szlivka, F., (1995), "Vibration problems on steamturbine - generators at low power", *Proceedings of IFToMM 9th World Congress on Theory of Machines and Mechanisms*, Milan, pp. 1344–1388.

Subbaiah, R., Bhat R. B., and Sankar, T. S., (1989), "Dynamic response of rotors using modal reduction technique", *Journal of Vibration and Acoustics, ASME* , Vol. 111, pp. 360-365.

Thomson, W. T., Dahleh, M. D., and Padmanabhan, C., (2008), "Theory of vibration with applications" *Pearson India, 5th Edition.*

Tiwari, R., (2006), "A brief history of rotor dynamics and recent trends", *Proceeding of 51th congress of the Indian society of theoretical and applied mechanics (ISTAM-2006), An international meet December 18-21, College of engineering, Andhra University, Visakhapatanam, India.*

Tiwari, R., (2013), "Theory and practice of rotor dynamics" *Web course and video course lecture under NPTEL –II, MHRD,* (http://nptel.ac.in/courses/112103024/25).

Tiwari, R., Lees, A. W., and Friswell, M. I., (2004), "Identification of dynamic bearing parameters: A review", *The Shock and Vibration Digest,* Vol. 36, No. 2, pp. 99-124.

Tondl, A., (1965), "Some problem of rotor dynamics", *Chapman and Hall, London*.

Trindade, M. A., Benjeddou, A., and Ohayon, R., (1999), "Modeling of frequency-dependent viscoelastic materials for active passive vibration damping", *Journal of Vibration and Acoustics*, Vol.122, pp. 169-74.

Vance, J. M., (1988), "Rotordynamics of turbomachinery", *John Wiley & Sons, Technology & Engineering, New York*, pp. 388.

Walford, T. L. H., & Stone, B. J., (1983), "The sources of damping in rolling element bearings under oscillating conditions", *Proceedings of the Institution of Mechanical Engineers, Part C: Journal of Mechanical Engineering Science,* Vol. 197, No. 4, pp. 225-232.

Wang, B., and Chen, L. Q., (2009), "Asymptotic stability analysis with numerical confirmation of an axially accelerating beam constituted by the standard linear solid model", *Journal of Sound and Vibration*, Vol. 328, pp. 456-66.

Wang, W., Li, Q., Gao, J., Yao, J., and Allaire, P., (2015), "An identification method for damping ratio in rotor systems", *Mechanical Systems and Signal Processing*, in press.

Zener, C., (1948), "Elasticity and anelasticity of metals", *University of Chicago Press*.

Zghal, S., Bouazizi, M. L., Bouhaddi, N., and Nasri, R., (2015), "Model reduction methods for viscoelastic sandwich structures in frequency and time domains", *Finite Elements in Analysis and Design*, Vol. 9, pp. 312–29.

Zhang, H., Wu, L., Shi, P., and Zhao, Y., (2015), "Balanced truncation approach to model reduction of Markovian jump time-varying delay systems" *Journal of the Franklin Institute*, Vol. 352, pp. 4205–4224.

Zhou, X. Q., Yu, D. Y., Shao, X. Y., Zhang, S. Q., Wang, S., (2015), "Research and applications of viscoelastic vibration damping materials: A review" *Composite Structures*, http://dx.doi.org/10.1016/j.compstruct.2015.10.014.

Zinberg, H., and Symonds, M. F., (1970), "The development of an advanced composite tail rotor driveshaft", *Presented at the 26th Annual Forum of the American helicopter Society, Washington, DC*.

Zorzi, E. S., and Nelson, H. D., (1977), "Finite element simulation of rotor-bearing systems with internal damping", *Journal of Engineering for Gas Turbine and Power*, Vol. 99, No. 1, pp. 71-76.

Zorzi, E.S., and Nelson, H. D., (1980), "The dynamics of rotor-bearing systems with axial torque," *ASME, Journal of Mechanical Design*, Vol. 102, pp. 158–161.

Appendix-A

A.1 Extraction of viscoelastic parameters

In this section, various viscoelastic parameters ('a_0', 'a_1', 'b_0', 'b_1') used in Chapter-2, have been extracted from experimentally obtained values of storage modulus and loss factor. A longitudinal vibration of a uni-axial rod (Fig. A.1) is utilized to find these parameters. Finite element method is used to discretize the rod. Vibration response due to harmonic excitation is calculated by using two methods; a) complex modulus approach b) operator based approach. In first case storage modulus and loss factor are utilized but in the second case viscoelastic parameters are used, these are unknown quantities. The unknown parameters are found out by minimizing the error of frequency response obtained from two methods. A Genetic Algorithm based optimization code has been applied for this purpose.

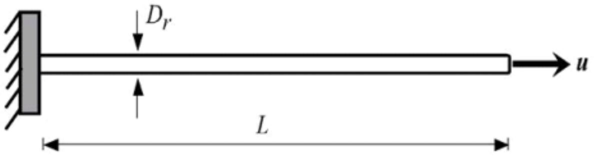

Fig. A.1 Schematic diagram of an uni-axial circular rod

The FE based equation of motion of a uni-axial rod is given by

$$[\mathbf{M}]\{\ddot{\mathbf{q}}\}+E[\mathbf{K}]\{\mathbf{q}\}=[\mathbf{P}]\{\boldsymbol{u}\} \qquad \text{(A.1)}$$

where, $\{\boldsymbol{u}\}$ is externally applied excitation force, $[\mathbf{P}]$ is nodal position of excitation, $\{\mathbf{q}\}$ is nodal coordinates, $[\mathbf{M}^e]$, and $E[\mathbf{K}^e]$ are mass and stiffness matrix of bar element respectively and their expressions are given by:

$$[\mathbf{M}^e]=\frac{\rho AL}{6}\begin{bmatrix}2 & 1\\ 1 & 2\end{bmatrix}, \qquad [\mathbf{K}^e]=\frac{A}{6}\begin{bmatrix}2 & 1\\ 1 & 2\end{bmatrix}$$

While considering material damping through complex modulus approach, elastic modulus 'E' in stiffness matrix expression is replaced by $E(1+i\eta)$, where η is loss modulus. Following Eq. (2.2(b)), it will be $\left(\dfrac{a_0+a_1\mathrm{D}}{b_0+b_1\mathrm{D}}\right)$ for operator based approach. After replacing it in Eq. (A.1) and rewritten again as-

$$[\mathbf{M}]\{\ddot{\mathbf{q}}\}+E(1+i\eta)[\mathbf{K}]\{\mathbf{q}\}=[\mathbf{P}]\{\boldsymbol{u}\} \tag{A.2(a)}$$

$$[\mathbf{M}]\{\ddot{\mathbf{q}}\}+\left(\frac{a_0+a_1\mathrm{D}}{b_0+b_1\mathrm{D}}\right)[\mathbf{K}]\{\mathbf{q}\}=[\mathbf{P}]\{\boldsymbol{u}\} \tag{A.2(b)}$$

After simplifying Eq. (A.2(b)), the modified view of equation is seen below.

$$[\mathbf{A}_0]\{\mathbf{q}\}+[\mathbf{A}_1]\{\dot{\mathbf{q}}\}+[\mathbf{A}_2]\{\ddot{\mathbf{q}}\}+[\mathbf{A}_3]\{\dddot{\mathbf{q}}\}=[\mathbf{B}]\{\boldsymbol{u}\} \tag{A.3}$$

Where, $[\mathbf{A}_0]=(a_0)[\mathbf{K}]$, $[\mathbf{A}_1]=(a_1)[\mathbf{K}]$, $[\mathbf{A}_2]=(b_0)[\mathbf{M}]$,

$[\mathbf{A}_3]=(b_1)[\mathbf{M}]$, $[\mathbf{B}]=(b_0+b_1\mathrm{D})[\mathbf{P}]$.

For steady state harmonic excitation, an assumed function $\{\boldsymbol{u}\}=\{\hat{\boldsymbol{u}}\}\mathrm{e}^{i\omega t}$ and $\{\mathbf{q}\}=\{\hat{\mathbf{q}}\}\mathrm{e}^{i\omega t}$ are employed to Eq. (A.2(a)) and Eq. (A.3), where, 'ω' is excitation frequency. The steady state frequency response for two methods are written as,

$$\{\hat{\mathbf{q}}\}=\left[-\omega^2[\mathbf{M}]+E(1+i\eta)[\mathbf{K}]\right]^{-1}[\mathbf{P}]\{\hat{\boldsymbol{u}}\} \tag{A.4(a)}$$

$$\{\hat{\mathbf{q}}\}=\left[[\mathbf{A}_0]+i\omega[\mathbf{A}_1]-\omega^2[\mathbf{A}_2]-i\omega^3[\mathbf{A}_3]\right]^{-1}(b_0+i\omega b_1)[\mathbf{P}]\{\hat{\boldsymbol{u}}\} \tag{A.4(b)}$$

From preceding Eq. (A.4), the response amplitude 'q' is calculated and are expressed as below

$$\mathrm{q}=\mathrm{Real}\left(\hat{\mathbf{q}}\,\mathrm{e}^{i\omega t}\right) \tag{A.5}$$

Viscoelastic parameters are found out by minimizing an objective function '$\mathcal{F}$', which is a square of error between frequency response obtained from two methods.

$$\mathcal{F}_{\mathrm{i}}=\mathcal{F}_{\mathrm{i-1}}+\left(\frac{\mathrm{q}_1-\mathrm{q}_2}{\mathrm{q}_1}\right)^2 \tag{A.6}$$

'q_1' and 'q_2' are the frequency response for two methods.

For simulation purpose, a one dimensional viscoelastic bar with circular cross section is considered. The bar is discretize with 10 elements and 11 nodes. Length and outer diameter are $L=1\,\mathrm{m}$, and $D_r = 0.05\ \mathrm{m}$, respectively. A steady state harmonic load of magnitude $\hat{u}=1\,\mathrm{N}$ is applied at the other end. Viscoelastic parameters for Mild steel and Aluminium are extracted here. Various properties of these two materials are taken from Lazan (1968), which are shown in Table A.1.

Considering this example, the main focus is to extract the data for the operator coefficient (a_0, a_1, b_0, b_1) with respect to the existing model shown in Eq. (A.2(a)). In optimization concepts, these parameters are also known as design variables. For ease of execution in the genetic algorithm code, two parameters, i.e., 'a_0' and 'b_0' are taken as a fixed value for all iterations. In this present work the values of 'a_0' and 'b_0' are considered as elastic modulus of material (i.e., 'E') and unity respectively. Further, a suitable initial value of other two design variables is taken to start genetic algorithm code.

The aim is to reduce the objective function through several iterations. On every iteration the function value is updated with respect to the previously obtained results and terminates when it reaches to converging point. After progressive iteration, frequency response based on those design variables will come closer to the value of frequency response through complex modulus approach. Thus 'a_1' and 'b_1' are modified. The finally extracted data are tabulated in Table A.1.

Table A.1 Material properties and extracted viscoelastic parameters

Material	Density 'ρ' (kg/m^3)	Storage Modulus 'E' (Pa)	Loss Factor 'η'	Fixed Parameters		Designed Parameters	
				a_0	b_0	a_1	b_1
Mild Steel	7800	2.1e+11	2.9e-02	2.1e+11	1	7.51e+05	1.475e-09
Aluminium	2750	7.13e+10	5.0e-02	7.13e+10	1	4.79e+05	2.068e-09

Optimize data are used to obtain various numerical results for this bar vibration considering operator based approach and complex modulus approach, are shown in successive figures. Hysteresis loop, response and energy dissipation plot for steel are shown in Figs. A.2(a), A.2(b) and A.2(c), respectively. Whereas for aluminium, those are in Figs. A.3(a), A.3(b) and A.3(c), respectively. Hysteresis loop is a time varying force-displacement plot at a particular frequency, when displacement is measured at tip of the bar. The response amplitude is the maximum displacement per cycle. While, energy dissipation has been calculated from the area enclosed by the hysteresis loop. Nice agreement in all these plots proves the correctness of the viscoelastic parameters for a broad frequency range.

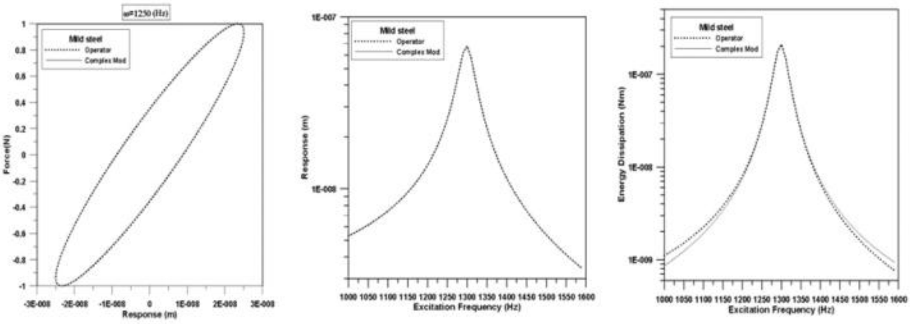

(a) Hysteresis loop (b) Response plot (c) Energy dissipation plot

Fig. A.2 Data validation for mild steel

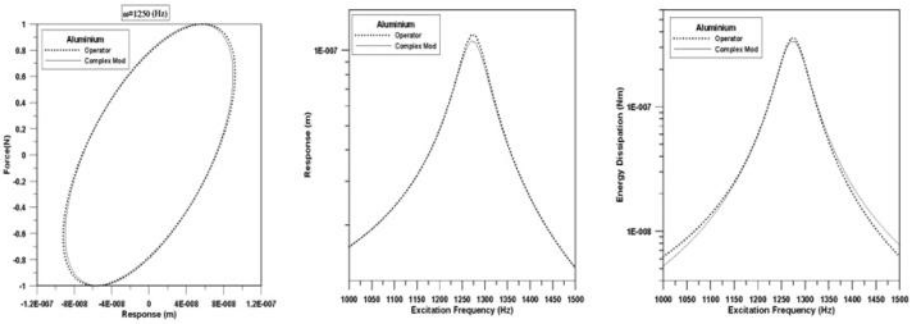

(a) Hysteresis loop (b) Response plot (c) Energy dissipation plot

Fig. A.3 Data validation for aluminium

Appendix-B

B.1 Effective mass of a simply supported beam for non-central loading

For classical modelling, a continuous system is assumed to act a lumped mass system and single degree of freedom is considered at lump mass point, the effective mass of whole system is used for further analysis. A factor is multiplied with the total mass to obtain the effective mass. This section covers to bring the factor for simply supported beam subjected to non-central loading.

A simply supported beam, as shown in Fig. B.1, is subjected to unit load at non-central position (point C), i.e. L_1 distance from left end (point A), where L is the total length.

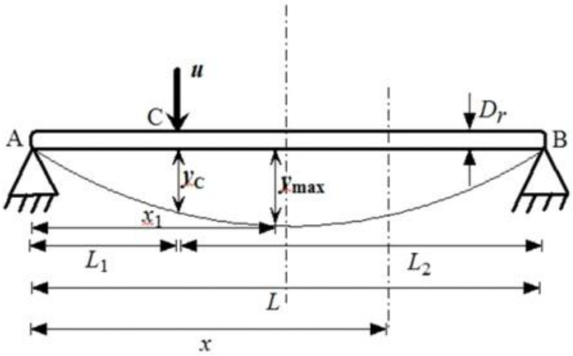

Fig. B.1 Simply supported beam with single point loading condition

Referring from several strength of material books and using the Macaulay's method, equation of the deformed beam is given by:

$$\begin{aligned} y &= y_C\left(\frac{\left(L_1^2-2LL_1\right)x}{2L_1^2\left(L-L_1\right)}-\frac{x^3}{2L_1^2\left(L-L_1\right)}+\frac{L\left(x-L_1\right)^3}{2L_1^2\left(L-L_1\right)^2}\right) \\ &= y_C\left(p_1+p_2+p_3\right) \end{aligned} \tag{B.1}$$

where, $\left(y_C\right)$ is the deflection of point C and is given as: $y_C = \frac{L_1^2\left(L-L_1\right)^2}{3EIL}$, and

$$p_1 = \frac{\left(L_1^2 - 2LL_1\right)x}{2L_1^2\left(L-L_1\right)}; \qquad p_2 = -\frac{x^3}{2L_1^2\left(L-L_1\right)}; \quad p_3 = \frac{L\left(x-L_1\right)^3}{2L_1^2\left(L-L_1\right)^2};$$

The effective mass is calculated from energy method. Kinetic energy expression of a continuous system is given as-

$$T = \frac{1}{2}\int_0^L \frac{M\left(x\right)}{L}\dot{y}^2 dx \tag{B.2(a)}$$

As the beam is subjected to non-central loading and deformation is unsymmetric, integration is performed over two domain. The kinetic energy expression for uniform cross section is rewritten as:

$$T = \frac{1}{2}M\left[\int_0^{L_1}\frac{1}{L}\dot{y}^2 dx + \int_{L_1}^{L}\frac{1}{L}\dot{y}^2 dx\right] \tag{B.2(b)}$$

To obtain effective mass, the kinetic energy is calculated based on maximum deflection of whole section $\left(y_{\max}\right)$. The maximum deflection point $\left(x_1\right)$ for non-central loading is not at mid-point of beam, depends on loading point location. The location of $\left(x_1\right)$ is found at zero slope position. When L_1 is less than half of the beam length, maximum deflection occurs in CB and left side of middle point. In other case, its position is in AC and right side of middle point. It is important to note that, the maximum deflection of other portion (AC or CB) is $\left(y_C\right)$. The expression of $\left(x_1\right)$ and $\left(y_{\max}\right)$ are written as:

$$\text{if}\left(L_1 \le L/2\right) \Rightarrow \left\{\begin{array}{l} x_1 = L\dfrac{6L^* - 2\sqrt{3\left(3L^{*2} - L^*\left(3L^{*2} + \left(1-L^*\right) - \left(1-L^*\right)^3\right)\right)}}{6L^*} \\ y_{\max} = y_C\left(\dfrac{\left(L_1^2 - 2LL_1\right)x_1}{2L_1^2\left(L-L_1\right)} - \dfrac{x_1^3}{2L_1^2\left(L-L_1\right)} + \dfrac{L\left(x_1-L_1\right)^3}{2L_1^2\left(L-L_1\right)^2}\right)\end{array}\right\} \tag{B.3(a)}$$

$$\text{else}\left(L_1 \geq {}^{L}\!/_{2}\right) \Rightarrow \left\{ \begin{array}{c} x_1 = L\sqrt{\dfrac{L^{*2} + 2L^{*}\left(1 - L^{*}\right)}{3}} \\ y_{\max} = y_C\left(\dfrac{\left(L_1^2 - 2LL_1\right)x_1}{2L_1^2\left(L - L_1\right)} - \dfrac{x_1^3}{2L_1^2\left(L - L_1\right)}\right) \end{array} \right\} \tag{B.3(b)}$$

Rearranging the kinetic energy expression on the basis of $\left(y_{\max}\right)$, Eq. (B.2(b)) is further rewritten as:

$$T = \left\{ \begin{array}{ll} \dfrac{1}{2}\left[\dfrac{1}{L}\displaystyle\int_0^{L_1}\left(p_1 + p_2\right)^2 dx + \dfrac{1}{L}\int_{L_1}^{L}\left(\dfrac{y_C}{y_{\max}}\left(p_1 + p_2 + p_3\right)\right)^2 dx\right] M\dot{y}_{\max}^2 & \text{for}\left(L_1 \leq {}^{L}\!/_{2}\right) \\ \dfrac{1}{2}\left[\displaystyle\int_0^{L_1}\dfrac{1}{L}\left(\dfrac{y_C}{y_{\max}}\left(p_1 + p_2\right)\right)^2 dx + \dfrac{1}{L}\int_{L_1}^{L}\left(p_1 + p_2 + p_3\right)^2 dx\right] M\dot{y}_{\max}^2 & \text{for}\left(L_1 \geq {}^{L}\!/_{2}\right) \end{array} \right\} \tag{B.4}$$

$$= \frac{1}{2}\beta_M M\dot{y}_{\max}^2 = \frac{1}{2}M_{eff}\,\dot{y}_{\max}^2$$

The effective mass factor $\left(\beta_M\right)$ is obtained after performing integration and is written below. β_M is plotted in Fig. B.2 for various non-dimensional loading positions $\left(L^* = {}^{L_1}\!/_{L}\right)$. It is seen that minimum value (0.4857) is at the middle and increase to 0.5446 at $L^* = 0.15$. It has a tendency to go down when approaches to boundary. Thus, it is commented again here that the classical model fails to give a correct interpretation at this location.

$$\beta_M = \left\{ \begin{array}{ll} \left[\dfrac{L_1\left(35L^2 - 56LL_1 + 23L_1^2\right)}{105L\left(L - L_1\right)^2} + \dfrac{9\left(L - L_1\right)^2\left(2L^2 + 10LL_1 + 23L_1^2\right)}{35L\left(L + L_1\right)^3}\right] & \text{for } L_1 \leq {}^{L}\!/_{2} \\ \left[\dfrac{9L_1^2\left(35L^2 - 56LL_1 + 23L_1^2\right)}{35L\left(2L - L_1\right)^3} + \dfrac{\left(2L^3 + 8L^2L_1 + 13LL_1^2 - 23L_1^3\right)}{105LL_1^2}\right] & \text{for } L_1 \geq {}^{L}\!/_{2} \end{array} \right\} \tag{B.5}$$

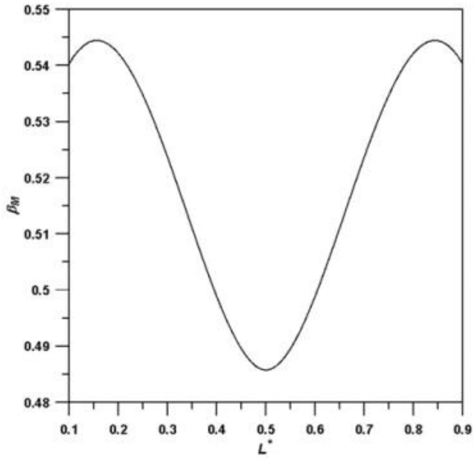

Fig. B.2 Effective mass factor for various loading positions

B.2 Effective diametral moment of inertia of a simply supported beam for non-central loading

Effective diametral moment of inertia of the beam for non-central loading is calculated by applying parallel axis theorem. The beam section rotates during deformation about an axis passing through zero slope position, where maximum deflection $(y_{\max})$ occurs. The position of $(y_{\max})$ from left end (x_1) is shown in previous section. The expression of effective diametral moment of inertia is written below.

$$J_{D_{eff}} = \int_{x_1}^{(L-x_1)} \frac{M(x)}{L} x^2 dx \tag{B.6}$$

After performing integration, Effective diametral moment of inertia for uniform cross section is written as;

$$J_{D_{eff}} = \frac{x_1^3 + (L-x_1)^3}{3L^3} ML^2 = \beta_{J_D} ML^2 \tag{B.7}$$

(β_{J_D}) is the factor used for effective diametral moment of inertia. It is plotted in Fig. B.3 for various non-dimensional loading position L^*. It is seen that the minimum value occurs at middle point of beam and increases toward the boundary.

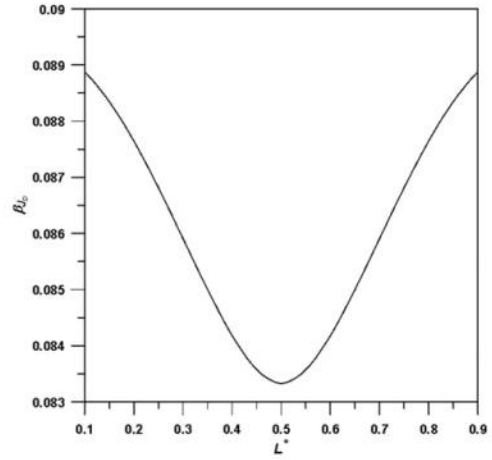

Fig. B.3 Effective diametral moment of inertia factor for various loading position

B.3 Various matrices for single disc rotor

Following Tondl (1965), the expressions of mass and gyroscopic matrices of the rotor shaft are given as,

$$\left[\mathbf{M}_r\right]=\begin{bmatrix} M_{r_{eff}} & 0 & 0 & 0 \\ 0 & J_{D_{r_{eff}}} & 0 & 0 \\ 0 & 0 & M_{r_{eff}} & 0 \\ 0 & 0 & 0 & J_{D_{r_{eff}}} \end{bmatrix},\ \left[\mathbf{G}_r\right]=\begin{bmatrix} 0 & 0 & 0 & 0 \\ 0 & 0 & 0 & \Omega J_{P_r} \\ 0 & 0 & 0 & 0 \\ 0 & -\Omega J_{P_r} & 0 & 0 \end{bmatrix}$$

The effective mass $\left(M_{r_{eff}}\right)$ and effective diametral moment of inertia $\left(J_{D_{r_{eff}}}\right)$ of shaft for non-central loading. The polar moment of inertia $\left(J_{P_r}\right)$ is written below.

$$J_{P_r}=\frac{M_r D_r^2}{8};$$

The other matrices are

$$\left[\mathbf{K}_B\right]=\begin{bmatrix} K_{11} & -K_{12} & 0 & 0 \\ -K_{12} & K_{22} & 0 & 0 \\ 0 & 0 & K_{11} & -K_{12} \\ 0 & 0 & -K_{12} & K_{22} \end{bmatrix},\ \left[\mathbf{K}_C\right]=\begin{bmatrix} 0 & 0 & K_{11} & -K_{12} \\ 0 & 0 & -K_{12} & K_{22} \\ -K_{11} & K_{12} & 0 & 0 \\ K_{12} & -K_{22} & 0 & 0 \end{bmatrix},\ \{\mathbf{q}\}=\begin{Bmatrix} v \\ \varphi \\ w \\ \vartheta \end{Bmatrix}$$

where, $\left[\mathbf{K}_B\right]$ is the stiffness due to bending and $\left[\mathbf{K}_C\right]$ is the skew symmetric circulatory matrix, and $\{\mathbf{q}\}$ represents the total degrees of freedom of system.

The mass and gyroscopic matrices for disc are written as:

$$\left[\mathbf{M}_d\right]=\begin{bmatrix} M_d & 0 & 0 & 0 \\ 0 & J_{D_d} & 0 & 0 \\ 0 & 0 & M_d & 0 \\ 0 & 0 & 0 & J_{D_d} \end{bmatrix},\qquad \left[\mathbf{G}_d\right]=\begin{bmatrix} 0 & 0 & 0 & 0 \\ 0 & 0 & 0 & \Omega J_{P_d} \\ 0 & 0 & 0 & 0 \\ 0 & -\Omega J_{P_d} & 0 & 0 \end{bmatrix}$$

In which, M_d, J_{D_d}, and J_{P_d}, are the mass, diametral and polar moment of inertia of the disc located non-centrally, and they are calculated as follows:

$$M_d=\frac{\pi\rho\left(D_d^{\,2}-D_r^{\,2}\right)T_d}{4};\ J_{D_d}=\frac{1}{12}M_d\left[\frac{3}{4}\left(D_d^{\,2}+D_r^{\,2}\right)+T_d^{\,2}\right];\ J_{P_d}=\frac{M_d\left(D_d^{\,2}+D_r^{\,2}\right)}{8};$$

Appendix-C

C.1 Stiffness coefficient of multi-disc rotor

Classical modelling of rotor shaft system uses few stiffness coefficients. Influence coefficient method is used here to calculate stiffness coefficients of flexible multi -disc rotor, supported by rigid bearings. Influence coefficient gives the relation bet ween forces, moments, linear and angular deformation.

Let us consider forces (F), moments (M) are applied at a point and corresponding lateral (ν), angular(φ) deformation respectively. Considering static linear deformation, the deformation is directly proportional to the applied force or moments. Therefore, it can be written as:

$$\nu \propto F\ ,\ \ \nu \propto M\ ,\ \ \varphi \propto F\ ,\ \ \varphi \propto M \tag{C.1(a)}$$

According to the principle of superposition theory, total lateral and angular deformation due to combined action of force and moment are expressed as,

$$\nu = \alpha_{(\mathrm{ld}/F)} F + \alpha_{(\mathrm{ld}/M)} M \quad \text{and} \quad \varphi = \alpha_{(\mathrm{ad}/F)} F + \alpha_{(\mathrm{ad}/M)} M \tag{C.1(b)}$$

$F_1, F_2, \ldots, F_{\mathrm{N}_d}$ and $M_1, M_2, \ldots, M_{\mathrm{N}_d}$ are various forces, moments acting at the position where disc 1, 2, …, N_d, are mounted. The lateral and angular deformation of shaft at different loading position are $\nu_1, \nu_2, \ldots, \nu_{\mathrm{N}_d}$ and $\varphi_1, \varphi_2, \ldots, \varphi_{\mathrm{N}_d}$ respectively. Principle of superposition theory is used again to establish net lateral and angular deformation at different disc position caused due to various forces and moments. It is achieved after expanding Eq. (C.1(b)) following Tiwari (2013).

$$\begin{Bmatrix} v_1 \\ \varphi_1 \\ v_2 \\ \varphi_2 \\ \vdots \\ v_{\mathrm{N}_d} \\ \varphi_{\mathrm{N}_d} \end{Bmatrix} = \begin{bmatrix} \alpha_{(\mathrm{ld}_1/F_1)} & \alpha_{(\mathrm{ld}_1/M_1)} & \alpha_{(\mathrm{ld}_1/F_2)} & \alpha_{(\mathrm{ld}_1/M_2)} & \cdots & \alpha_{(\mathrm{ld}_1/F_{\mathrm{N}_d})} & \alpha_{(\mathrm{ld}_1/M_{\mathrm{N}_d})} \\ \alpha_{(\mathrm{ad}_1/F_1)} & \alpha_{(\mathrm{ad}_1/M_1)} & \alpha_{(\mathrm{ad}_1/F_2)} & \alpha_{(\mathrm{ad}_1/M_2)} & \cdots & \alpha_{(\mathrm{ad}_1/F_{\mathrm{N}_d})} & \alpha_{(\mathrm{ad}_1/M_{\mathrm{N}_d})} \\ \alpha_{(\mathrm{ld}_2/F_1)} & \alpha_{(\mathrm{ld}_2/M_1)} & \alpha_{(\mathrm{ld}_2/F_2)} & \alpha_{(\mathrm{ld}_2/M_2)} & \cdots & \alpha_{(\mathrm{ld}_2/F_{\mathrm{N}_d})} & \alpha_{(\mathrm{ld}_2/M_{\mathrm{N}_d})} \\ \alpha_{(\mathrm{ad}_2/F_1)} & \alpha_{(\mathrm{ad}_2/M_1)} & \alpha_{(\mathrm{ad}_2/F_2)} & \alpha_{(\mathrm{ad}_2/M_2)} & \cdots & \alpha_{(\mathrm{ad}_2/F_{\mathrm{N}_d})} & \alpha_{(\mathrm{ad}_2/M_{\mathrm{N}_d})} \\ \vdots & \vdots & \vdots & \vdots & \ddots & \vdots & \vdots \\ \alpha_{(\mathrm{ld}_{\mathrm{N}_d}/F_1)} & \alpha_{(\mathrm{ld}_{\mathrm{N}_d}/M_1)} & \alpha_{(\mathrm{ld}_{\mathrm{N}_d}/F_2)} & \alpha_{(\mathrm{ld}_{\mathrm{N}_d}/M_2)} & \cdots & \alpha_{(\mathrm{ld}_{\mathrm{N}_d}/F_{\mathrm{N}_d})} & \alpha_{(\mathrm{ld}_{\mathrm{N}_d}/M_{\mathrm{N}_d})} \\ \alpha_{(\mathrm{ad}_{\mathrm{N}_d}/F_1)} & \alpha_{(\mathrm{ad}_{\mathrm{N}_d}/M_1)} & \alpha_{(\mathrm{ad}_{\mathrm{N}_d}/F_2)} & \alpha_{(\mathrm{ad}_{\mathrm{N}_d}/M_2)} & \cdots & \alpha_{(\mathrm{ad}_{\mathrm{N}_d}/F_{\mathrm{N}_d})} & \alpha_{(\mathrm{ad}_{\mathrm{N}_d}/M_{\mathrm{N}_d})} \end{bmatrix} \begin{Bmatrix} F_1 \\ M_1 \\ F_2 \\ M_2 \\ \vdots \\ F_{\mathrm{N}_d} \\ M_{\mathrm{N}_d} \end{Bmatrix} \tag{C.2}$$

$$= \left[\boldsymbol{\alpha}_{ij}\right] \begin{Bmatrix} F_1 \\ M_1 \\ F_2 \\ M_2 \\ \vdots \\ F_{\mathrm{N}_d} \\ M_{\mathrm{N}_d} \end{Bmatrix}; \quad i, j = 1, 2, \ldots, 2\mathrm{N}_d$$

where, $\left[\boldsymbol{\alpha}_{ij}\right]$ is known as compliance matrix and its elements are called as influence coefficients.

$\alpha_{(\mathrm{ld}_{\mathrm{N}_d}/F_{\mathrm{N}_d})}$ Lateral deformation at disc-N_d due to unit force acting at disc-N_d

$\alpha_{(\mathrm{ld}_{\mathrm{N}_d}/M_{\mathrm{N}_d})}$ Lateral deformation at disc-N_d due to unit moment acting at disc-N_d

$\alpha_{(\mathrm{ad}_{\mathrm{N}_d}/F_{\mathrm{N}_d})}$ Angular deformation at disc-N_d due to unit force acting at disc-N_d

$\alpha_{(\mathrm{ad}_{\mathrm{N}_d}/M_{\mathrm{N}_d})}$ Angular deformation at disc-N_d due to unit moment acting at disc-N_d

Following Maxwell reciprocal theorem, $\alpha_{(\mathrm{ld}_{\mathrm{N}_d}/M_{\mathrm{N}_d})} = \alpha_{(\mathrm{ad}_{\mathrm{N}_d}/F_{\mathrm{N}_d})}$ thus $\left[\boldsymbol{\alpha}_{ij}\right]$ is a symmetric matrix.

In the present study, a problem of two disc flexible rotor with simply supported ends, is considered. For deriving the stiffness coefficients, it can be treated as a simply supported beam, as shown in Fig. (C.1), subjected to two point loading at the disc positions. Point C and D are the two loading position at a distance L_1 and L_2 from the left end, where L is the total length of the beam. Dutt (1992) found stiffness coefficients of simply supported beam under a single point loading. So this is the extension of Dutt (1992) work.

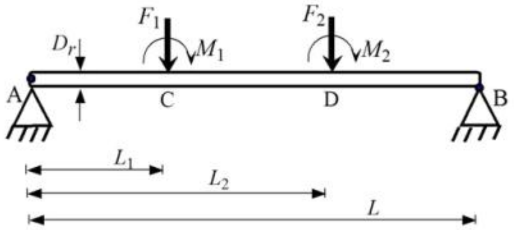

Fig. C.1 Simply supported beam at two point loading condition

$v_1, v_2, \varphi_1, \varphi_2$ are two lateral and two angular deformation at point C and D, caused due to the combined effect of F_1, F_2, M_1, M_2. Their relation is expressed after rewriting Eq.(C.2) for two point loading $\left(\mathrm{N}_d = 2\right)$ and is given as:

$$\begin{Bmatrix} v_1 \\ \varphi_1 \\ v_2 \\ \varphi_2 \end{Bmatrix} = \begin{bmatrix} \alpha_{11} & \alpha_{12} & \alpha_{13} & \alpha_{14} \\ \alpha_{21} & \alpha_{22} & \alpha_{23} & \alpha_{24} \\ \alpha_{31} & \alpha_{32} & \alpha_{33} & \alpha_{34} \\ \alpha_{41} & \alpha_{42} & \alpha_{43} & \alpha_{44} \end{bmatrix} \begin{Bmatrix} F_1 \\ M_1 \\ F_2 \\ M_2 \end{Bmatrix} \tag{C.3}$$

Expressions of the various influence coefficients are obtained using deflection of beam theory and given below:

$$\alpha_{11} = \frac{1}{EIL}\left(\frac{L_1\left(L^2-\left(L-L_1\right)^2\right)\left(L-L_1\right)}{6} - \frac{L_1^3\left(L-L_1\right)}{6}\right),$$

$$\alpha_{21} = \frac{1}{EIL}\left(\frac{L_1^3}{6} - \frac{L_1\left(L^2-3\left(L-L_1\right)^2\right)}{6}\right),$$

$$\alpha_{22} = \frac{1}{EIL}\left(\frac{L_1^2}{2} - \frac{L^2}{6} + \frac{\left(L-L_1\right)^2}{2}\right),$$

$$\alpha_{31} = \frac{1}{EIL}\left(\frac{L_1\left(L^2-(L-L_2)^2\right)(L-L_2)}{6} - \frac{L_1^3(L-L_2)}{6}\right),$$

$$\alpha_{32} = \frac{1}{EIL}\left(\frac{\left(L^2-(L-L_2)^2\right)(L-L_2)}{6} - \frac{L_1^2(L-L_2)}{2}\right),$$

$$\alpha_{33} = \frac{1}{EIL}\left(\frac{L_2\left(L^2-(L-L_2)^2\right)(L-L_2)}{6} - \frac{L_2^3(L-L_2)}{6}\right),$$

$$\alpha_{41} = \frac{1}{EIL}\left(\frac{L_1^3}{6} - \frac{L_1\left(L^2-3(L-L_2)^2\right)}{6}\right),$$

$$\alpha_{42} = \frac{1}{EIL}\left(\frac{L_1^2}{2} - \frac{L^2}{6} + \frac{(L-L_2)^2}{2}\right),$$

$$\alpha_{43} = \frac{1}{EIL}\left(\frac{L_2^3}{6} - \frac{L_2\left(L^2-3(L-L_2)^2\right)}{6}\right),$$

$$\alpha_{44} = \frac{1}{EIL}\left(\frac{L_2^2}{2} - \frac{L^2}{6} + \frac{(L-L_2)^2}{2}\right),$$

As $\left[\boldsymbol{\alpha}_{ij}\right]$ is a symmetric matrix, so $\alpha_{12} = \alpha_{21}$, $\alpha_{13} = \alpha_{31}$, $\alpha_{14} = \alpha_{41}$, $\alpha_{23} = \alpha_{32}$, $\alpha_{24} = \alpha_{42}$, $\alpha_{34} = \alpha_{43}$. Where, E and I are the young's modulus and the moment of inertia of the section respectively.

Stiffness matrix is obtained after inverting Eq. (C.3) and written as,

$$\begin{Bmatrix} F_1 \\ M_1 \\ F_2 \\ M_2 \end{Bmatrix} = \left[\boldsymbol{\alpha}_{ij}\right]^{-1} \begin{Bmatrix} v_1 \\ \varphi_1 \\ v_2 \\ \varphi_2 \end{Bmatrix}, \qquad \text{(C.4)}$$

$$= \left[\mathbf{C}_{ij}\right] \begin{Bmatrix} v_1 \\ \varphi_1 \\ v_2 \\ \varphi_2 \end{Bmatrix},$$

Here, $\left[\mathbf{C}_{ij}\right]=\left[\boldsymbol{\alpha}_{ij}\right]^{-1}$ is known as stiffness matrix of system.

After finding the inverse of compliance matrix, expression of the various stiffness coefficients for simply supported beam under two point loading are given as follows.

$$C_{11}=-EIL\frac{3\left(3L_1^4-6L_1^2L_2^2+4L_1L_2^3-L_2^4\right)}{L_1^3\left(L_1-L_2\right)^4},$$

$$C_{21}=EIL\frac{3\left(L_1^2+2L_1L_2-L_2^2\right)}{L_1^2\left(L_1-L_2\right)^2},$$

$$C_{22}=-EIL\frac{L_1+3L_2}{L_1\left(L_1-L_2\right)},$$

$$C_{31}=EIL\frac{12}{\left(L_1-L_2\right)^3},$$

$$C_{32}=-EIL\frac{6}{\left(L_1-L_2\right)^2},$$

$$C_{33}=EIL\frac{3\left(-4L^3+12L^2L_2-12LL_2^2+L_1^3-3L_1^2L_2+3L_1L_2^2+3L_2^3\right)}{\left(L-L_2\right)^3\left(L_1-L_2\right)^3},$$

$$C_{41}=EIL\frac{6}{\left(L_1-L_2\right)^2},$$

$$C_{42}=-EIL\frac{2}{\left(L_1-L_2\right)},$$

$$C_{43}=-EIL\frac{3\left(2L^2-4LL_2-L_1^2+2L_1L_2+L_2^2\right)}{\left(L-L_2\right)^2\left(L_1-L_2\right)^2},$$

$$C_{44}=EIL\frac{\left(3L_1-4L+L_2\right)}{\left(L-L_2\right)\left(L_1-L_2\right)},$$

$\left[\mathbf{C}_{ij}\right]$ is also a symmetric matrix, thus $C_{12}=C_{21}, C_{13}=C_{31}, C_{14}=C_{41}, C_{23}=C_{32}, C_{24}=C_{42}$, $C_{34}=C_{43}$

C.2 Various matrices for double disc rotor

Following Tondl (1965), the expressions of mass and gyroscopic matrix are given as

$$\left[\mathbf{M}_r\right]=\begin{bmatrix} M_{r_1} & 0 & 0 & 0 & 0 & 0 & 0 & 0 \\ 0 & J_{D_{r_1}} & 0 & 0 & 0 & 0 & 0 & 0 \\ 0 & 0 & M_{r_1} & 0 & 0 & 0 & 0 & 0 \\ 0 & 0 & 0 & J_{D_{r_1}} & 0 & 0 & 0 & 0 \\ 0 & 0 & 0 & 0 & M_{r_1} & 0 & 0 & 0 \\ 0 & 0 & 0 & 0 & 0 & J_{D_{r_2}} & 0 & 0 \\ 0 & 0 & 0 & 0 & 0 & 0 & M_{r_1} & 0 \\ 0 & 0 & 0 & 0 & 0 & 0 & 0 & J_{D_{r_2}} \end{bmatrix},$$

$$\left[\mathbf{G}_r\right]=\begin{bmatrix} 0 & 0 & 0 & 0 & 0 & 0 & 0 & 0 \\ 0 & 0 & 0 & \Omega J_{P_{r_1}} & 0 & 0 & 0 & 0 \\ 0 & 0 & 0 & 0 & 0 & 0 & 0 & 0 \\ 0 & -\Omega J_{P_{r_1}} & 0 & 0 & 0 & 0 & 0 & 0 \\ 0 & 0 & 0 & 0 & 0 & 0 & 0 & 0 \\ 0 & 0 & 0 & 0 & 0 & 0 & 0 & \Omega J_{P_{r_2}} \\ 0 & 0 & 0 & 0 & 0 & 0 & 0 & 0 \\ 0 & 0 & 0 & 0 & 0 & -\Omega J_{P_{r_2}} & 0 & 0 \end{bmatrix}$$

where,

$$M_{r_1}=\frac{\frac{L_1}{2}+\left(\frac{L}{2}-L_1\right)}{L}M_r, \qquad M_{r_2}=\frac{\left(L_2-\frac{L}{2}\right)+\left(\frac{L-L_2}{2}\right)}{L}M_r,$$

$$J_{D_{r_1}}=\frac{M_r\left(\left(\frac{L_1}{2}\right)^3+\left(\frac{L}{2}-L_1\right)^3\right)}{3L}+\frac{J_{P_{r_1}}}{2}, \qquad J_{D_{r_2}}=\frac{M_r\left(\left(L-\frac{L_2}{2}\right)^3+\left(L_2-\frac{L}{2}\right)^3\right)}{3L}+\frac{J_{P_{r_2}}}{2},$$

$$J_{P_{r_1}}=\frac{M_{r_1}D_r^2}{8}, \qquad J_{P_{r_2}}=\frac{M_{r_2}D_r^2}{8},$$

in which, $M_r = \dfrac{\pi\rho D_r^2 L}{4}$, is total mass of the rotor. M_{r_1}, and M_{r_2}, are the mass, $J_{D_{r_1}}$, and $J_{D_{r_2}}$ are diametral moment of inertia and $J_{P_{r_1}}$ and $J_{P_{r_2}}$ are polar moment of inertia of shaft at a particular zone where the corresponding discs are located.

The expression of bending stiffness matrix, skew symmetric circulatory matrix and generalized coordinates are given below.

$$\left[\mathbf{K}_B\right] = \begin{bmatrix} K_{11} & K_{12} & 0 & 0 & K_{13} & K_{14} & 0 & 0 \\ K_{12} & K_{22} & 0 & 0 & K_{23} & K_{24} & 0 & 0 \\ 0 & 0 & K_{11} & K_{12} & 0 & 0 & K_{13} & K_{14} \\ 0 & 0 & K_{12} & K_{22} & 0 & 0 & K_{23} & K_{24} \\ K_{13} & K_{23} & 0 & 0 & K_{33} & K_{34} & 0 & 0 \\ K_{14} & K_{24} & 0 & 0 & K_{34} & K_{44} & 0 & 0 \\ 0 & 0 & K_{13} & K_{23} & 0 & 0 & K_{33} & K_{34} \\ 0 & 0 & K_{14} & K_{24} & 0 & 0 & K_{34} & K_{44} \end{bmatrix},$$

A.

$$\left[\mathbf{K}_C\right] = \begin{bmatrix} 0 & 0 & K_{11} & K_{12} & 0 & 0 & K_{13} & K_{14} \\ 0 & 0 & K_{12} & K_{22} & 0 & 0 & K_{23} & K_{24} \\ -K_{11} & -K_{12} & 0 & 0 & -K_{13} & -K_{14} & 0 & 0 \\ -K_{12} & -K_{22} & 0 & 0 & -K_{23} & -K_{24} & 0 & 0 \\ 0 & 0 & K_{13} & K_{23} & 0 & 0 & K_{33} & K_{34} \\ 0 & 0 & K_{14} & K_{24} & 0 & 0 & K_{34} & K_{44} \\ -K_{13} & -K_{23} & 0 & 0 & -K_{33} & -K_{34} & 0 & 0 \\ -K_{14} & -K_{24} & 0 & 0 & -K_{34} & -K_{44} & 0 & 0 \end{bmatrix}, \quad \{\mathbf{q}\} = \begin{Bmatrix} v_1 \\ \varphi_1 \\ w_1 \\ \vartheta_1 \\ v_2 \\ \varphi_2 \\ w_2 \\ \vartheta_2 \end{Bmatrix}$$

The mass and gyroscopic matrices of the two discs are written as

B.

$$\left[\mathbf{M}_d\right] = \begin{bmatrix} M_{d_1} & 0 & 0 & 0 & 0 & 0 & 0 & 0 \\ 0 & J_{D_{d_1}} & 0 & 0 & 0 & 0 & 0 & 0 \\ 0 & 0 & M_{d_1} & 0 & 0 & 0 & 0 & 0 \\ 0 & 0 & 0 & J_{D_{d_1}} & 0 & 0 & 0 & 0 \\ 0 & 0 & 0 & 0 & M_{d_2} & 0 & 0 & 0 \\ 0 & 0 & 0 & 0 & 0 & J_{D_{d_2}} & 0 & 0 \\ 0 & 0 & 0 & 0 & 0 & 0 & M_{d_2} & 0 \\ 0 & 0 & 0 & 0 & 0 & 0 & 0 & J_{D_{d_2}} \end{bmatrix},$$

$$\left[\mathbf{G}_d\right]=\begin{bmatrix}0 & 0 & 0 & 0 & 0 & 0 & 0 & 0\\ 0 & 0 & 0 & \Omega J_{P_{d_1}} & 0 & 0 & 0 & 0\\ 0 & 0 & 0 & 0 & 0 & 0 & 0 & 0\\ 0 & -\Omega J_{P_{d_1}} & 0 & 0 & 0 & 0 & 0 & 0\\ 0 & 0 & 0 & 0 & 0 & 0 & 0 & 0\\ 0 & 0 & 0 & 0 & 0 & 0 & 0 & \Omega J_{P_{d_2}}\\ 0 & 0 & 0 & 0 & 0 & 0 & 0 & 0\\ 0 & 0 & 0 & 0 & 0 & -\Omega J_{P_{d_2}} & 0 & 0\end{bmatrix}$$

where, $M_{d_1}=\dfrac{\pi\rho\left(D_{d_1}^2-D_r^2\right)T_{d_1}}{4}$, $\quad M_{d_2}=\dfrac{\pi\rho\left(D_{d_2}^2-D_r^2\right)T_{d_2}}{4}$,

$$J_{P_{d_1}}=\frac{M_{d_1}\left(D_{d_1}^2+D_r^2\right)}{8},\qquad J_{P_{d_2}}=\frac{M_{d_2}\left(D_{d_2}^2+D_r^2\right)}{8},$$

$$J_{D_{d_1}}=\frac{M_{d_1}}{12}\left(\frac{3}{4}\left(D_{d_1}^2+D_r^2\right)+T_{d_1}\right),\qquad J_{D_{d_2}}=\frac{M_{d_2}}{12}\left(\frac{3}{4}\left(D_{d_2}^2+D_r^2\right)+T_{d_2}\right),$$

where, M_{d_1}, M_{d_2}, $J_{P_{d_1}}$, $J_{P_{d_2}}$, and $J_{D_{d_1}}$, $J_{D_{d_2}}$ are the respective mass, polar and diametral moment of inertia of two different discs.

Appendix-D

E.1. Different matrices in finite element approach

Various expressions are given below, which are used to obtain the finite element matrices considering Eular-Bernoulli beam theory.

The Hermite shape functions in x-y plane are given by

$$\phi_1 = 2\left(\frac{x}{l}\right)^3 - 3\left(\frac{x}{l}\right)^2 + 1, \qquad \phi_2 = \frac{x^3}{l^2} - 2\frac{x^2}{l} + x,$$

$$\phi_3 = -2\left(\frac{x}{l}\right)^3 + 3\left(\frac{x}{l}\right)^2, \qquad \phi_4 = \frac{x^3}{l^2} - \frac{x^2}{l},$$

The Hermite shape functions in z- x plane are given by

$$\phi_1 = 2\left(\frac{x}{l}\right)^3 - 3\left(\frac{x}{l}\right)^2 + 1, \qquad \phi_2 = -\frac{x^3}{l^2} + 2\frac{x^2}{l} - x,$$

$$\phi_3 = -2\left(\frac{x}{l}\right)^3 + 3\left(\frac{x}{l}\right)^2, \qquad \phi_4 = -\frac{x^3}{l^2} + \frac{x^2}{l},$$

The expressions of mass, gyroscopic, bending stiffness and skew symmetric circulatory matrix are given as:

Translational mass matrix $\left[\mathbf{M}_T\right]$:

$$\left[\mathbf{M}_T\right] = \frac{\rho A l}{420} \times \begin{bmatrix} 156 & 0 & 0 & 22l & 54 & 0 & 0 & -13l \\ 0 & 156 & -22l & 0 & 0 & 54 & 13l & 0 \\ 0 & -22l & 4l^2 & 0 & 0 & -13l & -3l^2 & 0 \\ 22l & 0 & 0 & 4l^2 & 13l & 0 & 0 & -3l^2 \\ 54 & 0 & 0 & 13l & 156 & 0 & 0 & -22l \\ 0 & 54 & -13l & 0 & 0 & 156 & 22l & 0 \\ 0 & 13l & -3l^2 & 0 & 0 & 22l & 4l^2 & 0 \\ -13l & 0 & 0 & -3l^2 & -22l & 0 & 0 & 4l^2 \end{bmatrix}$$

Rotary inertia matrix $\left[\mathbf{M}_R\right]$

$$\left[\mathbf{M}_R\right]=\frac{\rho I}{30l}\times\begin{bmatrix} 36 & 0 & 0 & 3l & -36 & 0 & 0 & 3l \\ 0 & 36 & -3l & 0 & 0 & -36 & -3l & 0 \\ 0 & -3l & 4l^2 & 0 & 0 & 3l & -l^2 & 0 \\ 3l & 0 & 0 & 4l^2 & -3l & 0 & 0 & -l^2 \\ -36 & 0 & 0 & -3l & 36 & 0 & 0 & -3l \\ 0 & -36 & 3l & 0 & 0 & 36 & 3l & 0 \\ 0 & -3l & -l^2 & 0 & 0 & 3l & 4l^2 & 0 \\ 3l & 0 & 0 & -l^2 & -3l & 0 & 0 & 4l^2 \end{bmatrix}$$

Skew symmetric gyroscopic matrix $\left[\mathbf{G}\right]$:

$$\left[\mathbf{G}\right]=\frac{2\Omega\rho I}{30l}\times\begin{bmatrix} 0 & -36 & 3l & 0 & 0 & 36 & 3l & 0 \\ 36 & 0 & 0 & 3l & -36 & 0 & 0 & 3l \\ -3l & 0 & 0 & -4l^2 & 3l & 0 & 0 & l^2 \\ 0 & -3l & 4l^2 & 0 & 0 & 3l & -l^2 & 0 \\ 0 & 36 & -3l & 0 & 0 & -36 & -3l & 0 \\ -36 & 0 & 0 & -3l & 36 & 0 & 0 & -3l \\ -3l & 0 & 0 & l^2 & 3l & 0 & 0 & -4l^2 \\ 0 & -3l & -l^2 & 0 & 0 & 3l & 4l^2 & 0 \end{bmatrix}$$

Bending stiffness matrix $\left[\mathbf{K}_B\right]$:

$$\left[\mathbf{K}_B\right]=\frac{I}{l^3}\times\begin{bmatrix} 12 & 0 & 0 & 6l & -12 & 0 & 0 & 6l \\ 0 & 12 & -6l & 0 & 0 & -12 & -6l & 0 \\ 0 & -6l & 4l^2 & 0 & 0 & 6l & 2l^2 & 0 \\ 6l & 0 & 0 & 4l^2 & -6l & 0 & 0 & 2l^2 \\ -12 & 0 & 0 & -6l & 12 & 0 & 0 & -6l \\ 0 & -12 & 6l & 0 & 0 & 12 & 6l & 0 \\ 0 & -6l & 2l^2 & 0 & 0 & 6l & 4l^2 & 0 \\ 6l & 0 & 0 & 2l^2 & -6l & 0 & 0 & 4l^2 \end{bmatrix}$$

Skew symmetric circulatory stiffness matrix $\left[\mathbf{K}_C\right]$:

$$\left[\mathbf{K}_C\right]=\frac{I}{l^3}\times\begin{bmatrix} 0 & 12 & -6l & 0 & 0 & -12 & -6l & 0 \\ -12 & 0 & 0 & -6l & 12 & 0 & 0 & -6l \\ 6l & 0 & 0 & 4l^2 & -6l & 0 & 0 & 2l^2 \\ 0 & 6l & -4l^2 & 0 & 0 & -6l & 2l^2 & 0 \\ 0 & -12 & 6l & 0 & 0 & 12 & 6l & 0 \\ 12 & 0 & 0 & 6l & -12 & 0 & 0 & -6l \\ 6l & 0 & 0 & -2l^2 & -6l & 0 & 0 & 4l^2 \\ 0 & 6l & -2l^2 & 0 & 0 & 6l & -4l^2 & 0 \end{bmatrix}$$

Appendix-E

D.1. Coefficients of sliding contact bearing

In this section, bearing coefficients for short sliding contact bearing (L/D << 1, L and D being the length and diameter of the bearing respectively) are calculated. Rao (2009) and Friswell et al. (2010b), among others may be referred for the derivation of bearing coefficients. Fig. E.1 shows the bearing geometry, where 'R' is the bearing radius (D/2), 'c' is the bearing clearance, and 'ε' is the eccentricity.

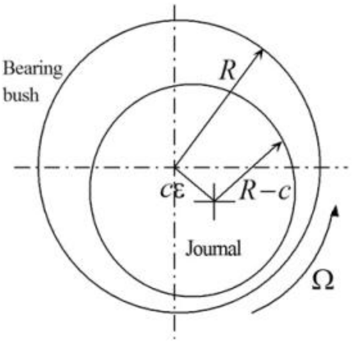

Fig. E.1 Bearing geometry

The equation of bearing forces (Eq. 2.25(b)) is written as,

$$\begin{bmatrix} C_{yy} & C_{yz} \\ C_{zy} & C_{zz} \end{bmatrix} \begin{Bmatrix} \dot{v} \\ \dot{w} \end{Bmatrix} + \begin{bmatrix} K_{yy} & K_{yz} \\ K_{zy} & K_{zz} \end{bmatrix} \begin{Bmatrix} v \\ w \end{Bmatrix} = \begin{Bmatrix} \mathbf{F}_{brg_y} \\ \mathbf{F}_{brg_z} \end{Bmatrix} \tag{E.1}$$

The bearing coefficients are calculated by the radial and tangential forces which are denoted f_r and f_t respectively.

$$f_r = -\frac{\mathrm{D}\Omega\eta\mathrm{L}^3\varepsilon^2}{2c^2\left(1-\varepsilon^2\right)^2}, \quad \text{and} \qquad f_t = -\frac{\pi\mathrm{D}\Omega\eta\mathrm{L}^3\varepsilon}{8c^2\left(1-\varepsilon^2\right)^{3/2}},$$

The resultant force is given by

$$f=\sqrt{f_r^2+f_t^2}=-\frac{\pi \mathrm{D}\Omega\eta \mathrm{L}^3\varepsilon}{8c^2\left(1-\varepsilon^2\right)^2}\left(\left(\frac{16}{\pi^2}-1\right)\varepsilon^2+1\right)^{1/2} \tag{E.2}$$

If the magnitude of this load is known then the bearing eccentricity may be obtained by rearranging Eq. (E.2) to give the following quartic equation in Eq. (E.3),

$$\varepsilon^8-4\varepsilon^6+\left(6-S_s^2\left(16-\pi^2\right)\right)\varepsilon^4-\left(4+\pi^2 S_s^2\right)\varepsilon^2+1=0 \tag{E.3}$$

Where, $S_s=\dfrac{\mathrm{D}\Omega\eta \mathrm{L}^3}{8fc^2}$

'S_s' is called the modified Sommerfeld number or the Ocvirk number, and is known for a particular speed, load and oil viscosity. The smallest root of Eq. (E.3) is taken, and is always between 0 and 1. A more general non-dimensional parameter is called the Sommerfeld number or duty parameter, S, which is typically defined as.

$$S=\frac{S_s}{\pi}\left(\frac{\mathrm{D}}{\mathrm{L}}\right)^2=\frac{\mathrm{D}^3\Omega\eta \mathrm{L}}{8\pi fc^2}$$

From Eq. (E.2) the load carrying capacity of a particular short bearing for any rotational speed and eccentricity may be determined. Conversely, if the applied load and rotational speed are known the eccentricity may be determined from Eq. (E.3).

Only short bearings are considered here, where the matrices are (2×2) and the shaft rotation about x and y is unconstrained. The stiffness and damping matrices may be written in closed form in terms of the eccentricity and load.

$$K_{yy}=\left(\frac{f}{c}\right)h_0\times 4\left(\pi^2\left(2-\varepsilon^2\right)+16\varepsilon^2\right),$$

$$K_{yz}=\left(\frac{f}{c}\right)h_0\times\frac{\pi\left(\pi^2\left(1-\varepsilon^2\right)^2-16\varepsilon^4\right)}{\varepsilon\sqrt{1-\varepsilon^2}},$$

$$K_{zy}=-\left(\frac{f}{c}\right)h_0\times\frac{\pi\left(\pi^2\left(1-\varepsilon^2\right)\left(1+2\varepsilon^2\right)+32\varepsilon^2\left(1+\varepsilon^2\right)\right)}{\varepsilon\sqrt{1-\varepsilon^2}},$$

$$K_{zz}=\left(\frac{f}{c}\right)h_0\times 4\left(\pi^2\left(1+2\varepsilon^2\right)+\frac{32\varepsilon^2\left(1+\varepsilon^2\right)}{\left(1-\varepsilon^2\right)}\right),$$

$$C_{yy}=\left(\frac{f}{c\Omega}\right)h_0\times\frac{2\pi\sqrt{1-\varepsilon^2}\left(\pi^2\left(1+2\varepsilon^2\right)\right)-16\varepsilon^2}{\varepsilon},$$

$$C_{yz} = C_{zy} = -\left(\frac{f}{c\Omega}\right) h_0 \times 8\left(\pi^2\left(1+2\varepsilon^2\right)-16\varepsilon^2\right),$$

$$C_{zz} = \left(\frac{f}{c\Omega}\right) h_0 \times \frac{2\pi\left(\pi^2\left(1-\varepsilon^2\right)^2+48\varepsilon^2\right)}{\varepsilon\sqrt{1-\varepsilon^2}},$$

where, $h_0 = \dfrac{1}{\left(\pi^2\left(1-\varepsilon^2\right)+16\varepsilon^2\right)^{3/2}}$

It is clear that the stiffness matrix is not symmetric and thus hydrodynamic bearings introduce anisotropic supports into the machine model.

Dissemination

List of Publications:

Journal:

1) H. Roy, J. K. Dutt, and S. Chandraker, (2014), "Modeling of multilayered viscoelastic rotors – An operator based approach", *Journal of Vibration Engineering and Technologies,* Vol. 2, No. 6, pp. 485-494.

2) H. Roy, **S. Chandraker**, J. K. Dutt, and T. Roy, (2016), "Dynamics of Multilayer, Multidisc Viscoelastic Rotor – An Operator Based Higher Order Classical Model", *Accepted for publication in the Journal of Sound and Vibration, Elsevier.* DOI10.1016/j.jsv.2015.12.047.

3) **S. Chandraker**, and H. Roy, "A balanced reduced model of multilayer viscoelastic rotors considering higher order system", Communicated for publication in the Journal of Vibration and Acoustics, transaction to ASME, (Under review).

4) H. Roy, and **S. Chandraker,** "Dynamic Study of Viscoelastic Rotor: Validation of Classical and Finite Element Model Considering Higher Order System", Communicated for publication in the Journal of vibration and control, Sage, (Under review).

5) **S. Chandraker**, and H. Roy, "Dynamic Study of Viscoelastic Rotor: Reduction of Higher Order Model Using Different Techniques", Communicated for publication in the Journal of Journal of Mechanics Research Communication, Elsevier, (Under review).

6) H. Roy, and **S. Chandraker,** "Dynamic Study of Viscoelastic Rotor: Modal Analysis of Higher Order Model Considering Various Asymmetries" Communicated for publication in the Journal of Mechanism and Machine Theory, Elsevier, (Under review).

7) H. Roy, A. Khare, **S. Chandraker**, and J. K. Dutt, "Fatigue based design and prognosis of viscoelastic rotors - a Finite Element Approach" Communicated for publication in the Aircraft Engineering and Aerospace Technology: An International Journal, (Under review).

Conferences:

1) H. Roy, J. K. Dutt, **S. Chandraker**, (2012), "Modelling of multilayered viscoelastic rotors – An operator based approach", *proceedings of VETOMAC VIII International Conference, Polish Academy of Science, Gdansk, Poland*, September 03-05, pp. 219-231.
2) **S. Chandraker**, G. Maurya, H. Roy, (2012), "Optimization of discs position for high stability of damped multi-disc rotor", *proceedings of ICCMS, IIT Hyderabad, India*, December 09-12, Paper id–122.
3) P. Mutalikdesai, **S. Chandraker**, and H. Roy, (2013), "Modal analysis of damped rotor using finite element method", *published in proceedings of (AMAAS), March 01-02, NIT Rourkela, India.*
4) **S. Chandraker**, P. Mutalikdesai, and H. Roy, (2013), "Complex modal analysis of damped rotor using finite element method" *published in proceedings of (ICAME), May 29-31, COEP Pune, Maharashtra, India,* Paper id: S16/P4.
5) **S. Chandraker**, G. Maurya, and H. Roy, (2013), "Parameterized optimization of disc for a damped rotor model using LMI approach", *proceeding of ICOVP, Lisbon, Portugal*, September 09-12, paper id– 551.
6) **S. Chandraker**, H. Roy, and G. Maurya, (2013), "Modal Analysis of multilayer viscoelastic rotor consider higher order mode", *proceedings of the ASME GTINDIA conference, Bangalore, India*, December 04-05, paper id- GTINDIA-3670.
7) **S. Chandraker**, and H. Roy, (2014), "A Balanced IIRS Model for Investigating the Dynamics of Damped Rotor Bearing System", *proceedings of the ASME GTINDIA conference, NewDelhi, India*, December 15-17, paper id- GTINDIA-8279.
8) H. Roy, and **S. Chandraker**, (2015), "A Comparative study between classical and finite element model for Multilayer viscoelastic rotors", *proceedings of the ASME GTINDIA conference, Hyderabad, India*, December 01-03, paper id- GTINDIA-1330.

Vitae

Saurabh Chandraker was born on August 1st, 1986 in Dalli-Rajhara, India. He graduated from the Department of Mechanical Engineering, from Pt. Ravi Shankar Shukla University, Raipur in year 2008. After his graduation he completed his Masters in Mechanical Engineering degree (Specialization: Machine Design) from Chhattisgarh Swami Vivekananda Technical University, Bhilai in the year 2011. He also worked as Assistant Professor in the Department of Mechanical Engineering at CSVTU, Bhilai for duration of 3 years. Presently, he is pursuing his Ph.D. in the Department of Mechanical Engineering, National Institute of Technology, Rourkela.

"Rate yourself every time; you will reach to your unrevealed question and answer"

Saurabh Chandraker
Email: saurabh01anizer@gmail.com
C/338 DBA Hall,
NIT Rourkela
India